

Atomic force microscopy study of interactions of silica surfaces in aqueous solutions with different salt concentrations

Joseph French



Doctor of Philosophy
The University of Edinburgh

January 2024

0.1 Abstract

This thesis presents a comprehensive study of the interplay of forces at the nanoscale in colloidal systems, utilizing Atomic Force Microscopy (AFM) as the primary investigative tool. The research explores a solution of 50:50 water glycerol solution across a range of different LiCl salt concentrations. Detailed examinations of surface imaging and force curve analysis are conducted, highlighting the intricacies of colloidal interactions and their practical implications for colloidal physics. Through a series of methodical AFM experiments, the work delves into the operational parameters and their implications, culminating in a profound analysis of approach and retract force curves. The study not only contributes to the fundamental understanding of colloidal dynamics but also bridges the gap between theoretical knowledge and practical applications, paving the way for innovations in materials science, biotechnology, and environmental sustainability.

0.2 Lay Abstract

In this thesis, we explore the tiny forces that act on microscopic particles suspended in liquids, known as colloids. These particles, which are often too small to see with the naked eye, play a critical role in everyday products like paints, foods, and medicines. By using a sophisticated tool called Atomic Force Microscopy, we can “feel” the forces as these tiny particles come close to or move away from each other. Our research shows how these forces change from pushing the particles apart to pulling them together, and how this delicate balance affects the behavior of colloids in different environments. Understanding these forces helps us not only to appreciate the complexities of microscopic world but also to develop better materials and technologies for everyday use, from smarter drugs to more sustainable practices in industries.

0.3 Declaration

I declare the following:

- (a) That the thesis, research project or dissertation has been composed by myself, and
- (b) either that the work is my own, or, if the student has been a member of a research group, that the student has made a substantial contribution to the work, such contribution being clearly indicated, or
- (c) that the work has not been submitted for any other degree or professional qualification except as specified, and
- (d) that any included publications are my own work, except where indicated throughout the thesis and summarised and clearly identified on the declarations page of the thesis.

Signed:

Joseph French, January 2024

0.4 Acknowledgements

I owe this thesis to a great many people and groups.

Firstly, to the University of Edinburgh, and the wider SOFI CDT community, I thank you. The support and community I was given from the members of the University of Edinburgh will always be a fond part of my life. The wider SOFI-CDT community as well is one I cherish, particularly cohort 2 (best cohort).

I'd like to thank my Professors, particularly Vasileios for never giving up on me even when I made it difficult. With your help my thesis transformed from something I felt incredible guilt about, to something I have found pride in. From the research group I would also like to thank Teun and John, both of whom inspired me during and afterwards.

I would also like to thank the Edinburgh Innovations student enterprise team. Your unflinching belief in me helped to build myself back up from my lowest point and gave me the support I needed to persevere, and the strength required to slay this PhDragon.

Also I would like to thank the ss13 community, you showed me the value I had in coding and developing complex systems, a skill I otherwise not have realised. And to the growing community around Whimsylabs, thank you for supporting me and believing in me.

To my family, friends and partners, I thank you for supporting my chaotic self as I muddled through my PhD, and only offered support instead of judgement. To those who body doubled me, you made this thesis a reality. To my life long friend Alex, I would like to thank you specifically, as you not only gave me a home and a space to write this, you were by my side through this challenge right from the beginning.

Contents

0.1	Abstract	1
0.2	Lay Abstract.....	1
0.3	Declaration.....	2
0.4	Acknowledgements	3
0.5	Introduction to the Thesis.....	25
1	Introduction to surface forces	27
1.1	Interparticle Colloidal forces	28
1.1.1	Electrostatic interactions.....	30
1.1.2	Van der Waals Forces	35
1.2	The Interplay of Attractive and Repulsive Forces on Colloidal Systems	38
1.2.1	Lennard-Jones potential	39
1.2.2	DLVO theory.....	40
1.3	Dynamic forces.....	44
1.3.1	Hydrodynamic Interactions	44
1.3.2	Steric Forces.....	45
1.4	Bulk interactions and properties	46
1.4.1	Rheology	46
1.4.2	Non-Newtonian Fluids	46
1.4.3	Shear Thinning and Thickening	46
1.4.4	Lubrication Forces	47
1.4.5	Simple Viscous Drag in Colloidal Systems	47

1.4.6	Rheology of suspended colloidal particles	47
1.5	Considering reality	48
1.5.1	Attaching spherical putty to the ceiling	48
2	Atomic force microscopy	50
2.1	Introduction	50
2.2	Basic overview of AFM operation	51
2.3	Tip Calibration	56
2.4	Common artifacts in AFM	58
2.4.1	The tip	59
2.4.2	Scanner error	60
2.4.3	Vibrations	61
2.4.4	Incorrect user parameters and feedback errors	61
2.5	Imaging mode AFM	61
2.5.1	Mathematical alignment and error correction of AFM images	63
2.6	Surface Force profiling	65
2.6.1	Anatomy of a force curve	65
2.6.2	Error correction of force curves	67
3	Surface Imaging	69
3.1	Introduction	69
3.2	Surface analysis	70
3.2.1	Measuring the surface of mica	70
3.2.2	Silica Surface Analysis	71
3.3	Silica particle surface resolution	76
4	Atomic force spectroscopy analysis	80
4.1	Introduction	80
4.2	MFP-1D	80
4.2.1	Experimental setup	82

4.2.2	Connection with Rheology	86
4.2.3	MFP-1D force-distance curves acquisition and processing....	86
4.2.4	Validation of results	94
4.3	Nanowizard	95
4.3.1	Analysis differences for JPK NanoWizard.....	95
4.4	Development and Significance of the Force Curve Analysis Software	96
5	Analysis of Approach Force Curves in Colloidal Systems	98
5.1	MFP-1D contact force derivation	98
5.1.1	A note on rejected curves	98
5.1.2	Contact force calculations.....	99
5.1.3	Diversity and Range of Data Points	100
5.1.4	0.6mM Site 1	101
5.1.5	0.6mM Site 2	102
5.1.6	0.6mM Site 3	103
5.1.7	1.6mM Site 1	104
5.1.8	1.6mM Site 2	105
5.1.9	5mM Site 1	107
5.1.10	5mM Site 2	108
5.1.11	5mM Site 3	109
5.1.12	10mM Site 1.....	111
5.1.13	10mM Site 2.....	112
5.1.14	10mM Site 3.....	113
5.1.15	25mM Site 1.....	114
5.1.16	25mM Site 2.....	115
5.1.17	25mM Site 3.....	116
5.1.18	50mM Site 1.....	117
5.1.19	50mM Site 2.....	118
5.1.20	230mM Site 1	119

5.1.21	230mM Site 2	120
5.1.22	550mM Site 1	121
5.1.23	550mM Site 2	122
5.1.24	550mM Site 3	123
5.2	Overall force vs LiCl concentration graph	124
5.3	Discussion of Force Measurements and Salt Concentration Effects ..	125
6	Analysis of Retract Force Curves in Colloidal Systems	127
6.1	Introduction	127
6.2	MFP-1D contact force derivation	128
6.2.1	0.6mM Site 1	129
6.2.2	0.6mM Site 2	130
6.2.3	0.6mM Site 3	131
6.2.4	1.6mM Site 1	132
6.2.5	1.6mM Site 2	133
6.2.6	5mM Site 1	134
6.2.7	5mM Site 2	135
6.2.8	5mM Site 3	136
6.2.9	10mM Site 1	137
6.2.10	10mM Site 2	138
6.2.11	10mM Site 3	139
6.2.12	25mM Site 1	140
6.2.13	25mM Site 2	141
6.2.14	25mM Site 3	142
6.2.15	50mM Site 1	143
6.2.16	50mM Site 2	144
6.2.17	230mM Site 1	145
6.2.18	230mM Site 2	146
6.2.19	550mM Site 1	147

6.2.20	550mM Site 2	148
6.2.21	550mM Site 3	149
6.3	Overall force vs LiCl concentration graphs	149
7	Operational parameter exploration and their implications	152
7.1	Introduction	152
7.2	Tip speed analysis.....	153
7.3	Dwell time.....	174
7.4	pH analysis.....	176
7.5	JPK ForceMapping.....	178
8	Further analysis and discussion	183
8.1	Approach force curves	183
8.2	Retract force curves.....	184
8.3	Shelf analysis	185
8.4	Overcoming the noise in data.....	189
8.5	Temporal Dynamics in Force Measurements	191
8.5.1	The Influence of Tip Velocity	191
8.5.2	Dielectric Relaxation, Ion Mobility and Measurement Fi- delity	191
8.5.3	Implications for Measurement Strategy	191
8.6	Comparing results to DLVO theory	193
9	Conclusion	197
9.1	Future work.....	198
10	Appendix	200
	Bibliography	201

List of Figures

(1.1) A schematic of counter ion distribution under the Gouy-Chapman model. This demonstrates how positive counter ions will arrange themselves around a negative surface.	32
(1.2) The Electrostatic potential of a counter ion, where distance is the distance between the negative surface and positive ion.	32
(1.3) The Electrical double layer model highlighting the transition between the Stern and diffuse layers.	33
(1.4) A basic schematic of Keesom interacting forces.	35
(1.5) A basic schematic of Debye interacting forces. The orange dipole represents an non permanent sudden gradient.	36
(1.6) A basic schematic of dispersion interacting forces.	36
(1.7) The Lennard-Jones potential function. The potential energy between the two particles is given as a function of distance. As the particles begin to get closer, the experience attraction. As the distance between the two shortens, the attraction eventually gives way to a infinitely increasing repulsive force.	39
(1.8) A graphical demonstration of the competing forces between colloidal particles. The electrostatic repulsion ($U_E(h)$) and the van der Waals attraction $U_{vdW}(h)$ combine together the sum interplay known as DLVO theory (bold line).	41
(1.9) A graphical representation of h	42
(1.10) Polymeric brushes on the surface of colloidal particles create steric hindrance, preventing close contact with neighboring particles. . .	45
(1.11) A diagram demonstrating a 2mm radius putty sphere attached to the ceiling.	49
(2.1) A basic schematic of an set up AFM. Image adapted from [86]. . .	52
(2.2) Above is shown the potential difference between tip shapes and types - where the tip with a circular geometry on the end is unable to enter fully into the crevasse on the sample, the thinner triangular one is. This will the be reflected on the output data.	54

(2.3) A diagram demonstrating the basic feedback loop control for an AFM. In this case an example for an AFM operating in imaging scanning mode is shown, which is elaborated in the next section. Image adapted from [2]	55
(2.4) A Van-der-Waals potential with corresponding regions imposed over the curve to demonstrate the ranges each of the modes have in relation to the forces applied to the cantilever. Image adapted from [32].	55
(2.5) An example of a thermal tuning calibration software interface. The blue line is the raw signal from the AFM and the red line is the fit over that data. The operation itself is automatic, requiring the user to only press the run thermal noise button for the spring constant to be given.	57
(2.6) A diagram demonstrating the translation of InvOLS to force, A demonstrates the raw data plotted, B demonstrates the data adjusted with InvOLS into a force. Adapted from [60]	58
(2.7) As the damaged tip interacts with a sample surface an artificial lump is measured by the cantilever in scanning mode. This is due to the double prong defect in the probe head limiting the range of movement, incorrectly reporting a secondary feature.	59
(2.8) Creeping drift can occur across the motion of a scan. In the x, y direction this manifests as a bending motion, whereas in the z plane this can result in an overshoot of driven motion. In both cases the effects are exaggerated to convey the effects.	60
(2.9) A diagram demonstrating the model setup for a sample. The geometry of each of the layers in the sample setup is an example in this case and can vary with application and requirements. The scanning window is non physical and is a projection of the area scanned by an AFM upon the surface of a sample.	62
(2.10)A figure demonstrating a standard mathematical operation applied to raw data. A demonstrates the array shown direct without any processing, B has had a mean field plane subtraction applied and C has had a row alignment applied to it. The image itself is of a freshly cleaved mica surface which is reflected in the final image C.	63
(2.11)A figure demonstrating different errors and operations on the output images produced from an AFM. A. demonstrates a physical complications known as the double tip effect produced by tip damage. B. highlights an example of the zigzag patterns that can be produced from operation error, as well as the blank areas where the tip is not in contact with the surface.	64

(2.12)A diagram showing a model force curve event. The leftmost image corresponds to the trace (aka approach) curve the first part of the force profiling event. The trace force curve proceeds from the bottom right up to the top left, passing through the A,B and C events in order. After this motion the piezo movement reverses, retracting the cantilever away from the surface, this begins the start of the retrace curve. In reverse fashion the cantilever progresses through the D,E and F sections in order. . .	66
(2.13)A theoretical demonstration of a rough AFM tip interacting with an imperfect surface. Due to the differences in topology between the two surfaces the interacting areas generate a different sum force experienced by the tip than expected.	67
(2.14)A demonstration of the theoretical movement that a cantilever tip will undergo when slipping along a surface profile.	68
(3.1) Photograph of the operational setup for the Bruker Nanoscope 2, which was used for image measurements.	69
(3.2) Time-lapse AFM tapping mode images of a mica surface showing progressive hydration. The first image was taken roughly 10 minutes after cleavage, with each subsequent image taking about 30 minutes to take. The changes in surface texture and color intensity suggest the absorption of water from the air, leading to a more pronounced hydration pattern, as seen in the increased contrast and the development of distinct features over time. . .	70
(3.3) A diagram demonstrating how the glass capillary was broken and how samples were extracted from the capillary.	71
(3.4) Two sample AFM images of untreated borosilicate glass at two different scan sizes: (a) displays an image with a scan size of $10 \mu\text{m} \times 10 \mu\text{m}$, while (b) demonstrates a scan size of $2 \mu\text{m} \times 2 \mu\text{m}$. .	72
(3.5) Four AFM images of untreated borosilicate glass on two different glass surfaces, with two sites per glass slide. The image has a scan size of $10 \mu\text{m} \times 10 \mu\text{m}$	73
(3.6) Four AFM images of untreated borosilicate glass on two different glass surfaces, with two sites per glass slide. The image has a scan size of $2 \mu\text{m} \times 2 \mu\text{m}$	73
(3.7) Four AFM images of untreated borosilicate glass on two different glass surfaces, with two sites per glass slide. The image has a scan size of $10 \mu\text{m} \times 10 \mu\text{m}$	74
(3.8) Four AFM images of untreated borosilicate glass on two different glass surfaces, with two sites per glass slide. The image has a scan size of $2 \mu\text{m} \times 2 \mu\text{m}$	74

(3.9) Four AFM images of untreated borosilicate glass on two different glass surfaces, with two sites per glass slide. The image has a scan size of $10 \mu\text{m} \times 10 \mu\text{m}$	75
(3.10) Four AFM images of untreated borosilicate glass on two different glass surfaces, with two sites per glass slide. The image has a scan size of $2 \mu\text{m} \times 2 \mu\text{m}$	75
(3.11) The output image of the 2D cross correlation function between the two images. The two smaller images are the input images into the script. The x and y values are the location of the z values in the 2D matrix dataset. The z scale is labeled respectively.	77
(3.12) The observed surface of a silica sphere.	78
(3.13) The flattened surface of a silica sphere.	79
(3.14) The flattened surface of a silica sphere with a uniquely seen feature. The RMS roughness of this image was 0.72 nm, the highest one in the dataset.	79
(4.1) Operation setup for the MFP-1D AFM that was used for force measurements.	81
(4.2) Operational setup for the MFP-1D AFM that was used for force measurements. Adapted from [60]	82
(4.3) Experimental schematic of MFP-1D during operation. The AFM is abstracted away into a back box to highlight the motion that the cantilever takes with respect to the surface. The stage control provides horizontal control, and therefore moves the projected site of contact along the petri dish surface.	83
(4.4) The view of a damaged chip from sequential plasma treatment. Normally a clean chip presents an observed silver colour on the outside, but from over-treatment the surface has worn away, resulting in the presentation seen above.	85
(4.5) An example of a individual graph produced at this point. Minimal processing has been done with only the deflection converted into force (nN) vs piezo z position (μm)	88
(4.6) An example of a individual graph produced for a single approach curve. The orange region of the graph is the area used in the farfield drift reduction and used to set the floor of the data to 0. .	89
(4.7) An example plot of an approach curve. The area used to help define contact is highlighted by the purple dots overlaying the raw curve.	90

(4.8) An example plot of the averaged approach gradient. The "approach gradient" in this context refers to the slope of the deflection as the AFM tip approaches the surface. Specifically, it is the rate at which the deflection changes as the AFM piezoelectric element moves the cantilever closer to the sample surface. This gradient provides insight into the force interactions occurring as the tip nears the surface, which is critical for understanding phenomena like the "jump to contact." This graph focuses specifically on the region after contact and the area used to define contact is highlighted by vertical dotted black lines (aka the defined contact region). The horizontal black line indicates the extrapolation of the data. in this case the data is binned to reduce noise. The height of each blue bar indicates the standard deviation for each point.	91
(4.9) An example plot of all the curves for a given site processed up until this point. A reference black line is overlaid demonstrating what a curve would look like with only terminal electrostatic repulsion. This figure represents about 100 curves aligned atop one another.	93
(4.10)An example plot of the final processed force curve. The y axis has been translated to show the distance from contact, with a black line highlighting the defined point of contact. The datapoint used to define the force at contact is highlighted in red.	93
(4.11)An example of a histogram produced from a set of curves for specific site. The mean force is given at the top with the standard deviation.	94
(4.12)A preliminary graph produced to investigate the expected Debye length vs the recorded Debye length at different salt concentrations. The black line indicates the approximated κ , whereas site one and two are two different recording areas on the glass surface.	95
(4.13)Operation setup for the Nanowizard AFM that was used for force measurements [3].	96
(5.1) A graph demonstrating a rejected curve. In this case the AFM failed to reach the surface for the recorded data, leading to a single up and down motion.	99
(5.2) A graph demonstrating the binned average curve post fit for 0.6mM LiCl at contact site 1.	101
(5.3) A log-linear plot of the force as a function of the Z-piezo position, highlighting the interaction phase for 0.6mM LiCl at contact site 1.	101
(5.4) A graph demonstrating the force histogram calculated from the range of curves for 0.6mM LiCl at contact site 1. The averaged contact force with the standard deviation is given above.	102

(5.5) A graph demonstrating the binned average curve post fit for 0.6mM LiCl at contact site 2	102
(5.6) A log-linear plot of the force as a function of the Z-piezo position, highlighting the interaction phase for 0.6mM LiCl at contact site 2.	103
(5.7) A graph demonstrating the force histogram calculated from the range of curves for 0.6mM LiCl at contact site 2. The averaged contact force with the standard deviation is given above.	103
(5.8) A graph demonstrating the binned average curve post fit for 0.6mM LiCl at contact site 3.	104
(5.9) A log-linear plot of the force as a function of the Z-piezo position, highlighting the interaction phase for 0.6mM LiCl at contact site 3.	104
(5.10)A graph demonstrating the force histogram calculated from the range of curves for 0.6mM LiCl at contact site 3. The averaged contact force with the standard deviation is given above.	104
(5.11)A graph demonstrating the binned average curve post fit for 1.6mM LiCl at contact site 1.	105
(5.12)A log-linear plot of the force as a function of the Z-piezo position, highlighting the interaction phase for 1.6mM LiCl at contact site 1.	105
(5.13)A graph demonstrating the force histogram calculated from the range of curves for 1.6mM LiCl at contact site 1. The averaged contact force with the standard deviation is given above.	105
(5.14)A graph demonstrating the binned average curve post fit for 1.6mM LiCl at contact site 2.	106
(5.15)A log-linear plot of the force as a function of the Z-piezo position, highlighting the interaction phase for 1.6mM LiCl at contact site 2.	106
(5.16)A graph demonstrating the force histogram calculated from the range of curves for 1.6mM LiCl at contact site 2. The averaged contact force with the standard deviation is given above.	106
(5.17)A graph demonstrating the binned average curve post fit for 5mM LiCl at contact site 1.	107
(5.18)A log-linear plot of the force as a function of the Z-piezo position, highlighting the interaction phase for 5mM LiCl at contact site 1.	107
(5.19)A graph demonstrating the force histogram calculated from the range of curves for 5mM LiCl at contact site 1. The averaged contact force with the standard deviation is given above.	108
(5.20)A graph demonstrating the binned average curve post fit for 5mM LiCl at contact site 2.	108
(5.21)A log-linear plot of the force as a function of the Z-piezo position, highlighting the interaction phase for 5mM LiCl at contact site 2.	108

(5.22)A graph demonstrating the force histogram calculated from the range of curves for 5mM LiCl at contact site 2. The averaged contact force with the standard deviation is given above.	109
(5.23)A graph demonstrating the binned average curve post fit for 5mM LiCl at contact site 3.	109
(5.24)A log-linear plot of the force as a function of the Z-piezo position, highlighting the interaction phase for 5mM LiCl at contact site 3.	109
(5.25)A graph demonstrating the force histogram calculated from the range of curves for 5mM LiCl at contact site 3. The averaged contact force with the standard deviation is given above.	110
(5.26)A graph demonstrating the binned average curve post fit for 10mM LiCl at contact site 1.	111
(5.27)A log-linear plot of the force as a function of the Z-piezo position, highlighting the interaction phase for 10mM LiCl at contact site 1.	111
(5.28)A graph demonstrating the force histogram calculated from the range of curves for 10mM LiCl at contact site 1. The averaged contact force with the standard deviation is given above.	111
(5.29)A graph demonstrating the binned average curve post fit for 10mM LiCl at contact site 2.	112
(5.30)A log-linear plot of the force as a function of the Z-piezo position, highlighting the interaction phase for 10mM LiCl at contact site 2.	112
(5.31)A graph demonstrating the force histogram calculated from the range of curves for 10mM LiCl at contact site 2. The averaged contact force with the standard deviation is given above.	112
(5.32)A graph demonstrating the binned average curve post fit for 10mM LiCl at contact site 3.	113
(5.33)A log-linear plot of the force as a function of the Z-piezo position, highlighting the interaction phase for 10mM LiCl at contact site 3.	113
(5.34)A graph demonstrating the force histogram calculated from the range of curves for 10mM LiCl at contact site 3. The averaged contact force with the standard deviation is given above.	113
(5.35)A graph demonstrating the binned average curve post fit for 25mM LiCl at contact site 1.	114
(5.36)A log-linear plot of the force as a function of the Z-piezo position, highlighting the interaction phase for 25mM LiCl at contact site 1.	114
(5.37)A graph demonstrating the force histogram calculated from the range of curves for 25mM LiCl at contact site 1. The averaged contact force with the standard deviation is given above.	114
(5.38)A graph demonstrating the binned average curve post fit for 25mM LiCl at contact site 2.	115

(5.39)A log-linear plot of the force as a function of the Z-piezo position, highlighting the interaction phase for 25mM LiCl at contact site 2.	115
(5.40)A graph demonstrating the force histogram calculated from the range of curves for 25mM LiCl at contact site 2. The averaged contact force with the standard deviation is given above.	115
(5.41)A graph demonstrating the binned average curve post fit for 25mM LiCl at contact site 3.	116
(5.42)A log-linear plot of the force as a function of the Z-piezo position, highlighting the interaction phase for 25mM LiCl at contact site 3.	116
(5.43)A graph demonstrating the force histogram calculated from the range of curves for 25mM LiCl at contact site 3. The averaged contact force with the standard deviation is given above.	116
(5.44)A graph demonstrating the binned average curve post fit for 50mM LiCl at contact site 1.	117
(5.45)A log-linear plot of the force as a function of the Z-piezo position, highlighting the interaction phase for 50mM LiCl at contact site 1.	117
(5.46)A graph demonstrating the force histogram calculated from the range of curves for 50mM LiCl at contact site 1. The averaged contact force with the standard deviation is given above.	117
(5.47)A graph demonstrating the binned average curve post fit for 50mM LiCl at contact site 2.	118
(5.48)A log-linear plot of the force as a function of the Z-piezo position, highlighting the interaction phase for 50mM LiCl at contact site 2.	118
(5.49)A graph demonstrating the force histogram calculated from the range of curves for 50mM LiCl at contact site 2. The averaged contact force with the standard deviation is given above.	118
(5.50)A graph demonstrating the binned average curve post fit for 230mM LiCl at contact site 1.	119
(5.51)A log-linear plot of the force as a function of the Z-piezo position, highlighting the interaction phase for 230mM LiCl at contact site 1.	119
(5.52)A graph demonstrating the force histogram calculated from the range of curves for 230mM LiCl at contact site 1. The averaged contact force with the standard deviation is given above.	120
(5.53)A graph demonstrating the binned average curve post fit for 230mM LiCl at contact site 2.	120
(5.54)A log-linear plot of the force as a function of the Z-piezo position, highlighting the interaction phase for 230mM LiCl at contact site 2.	120
(5.55)A graph demonstrating the force histogram calculated from the range of curves for 230mM LiCl at contact site 2. The averaged contact force with the standard deviation is given above.	121

(5.56)A graph demonstrating the binned average curve post fit for 550mM LiCl at contact site 1.	121
(5.57)A log-linear plot of the force as a function of the Z-piezo position, highlighting the interaction phase for 550mM LiCl at contact site 1.	122
(5.58)A graph demonstrating the force histogram calculated from the range of curves for 550mM LiCl at contact site 1. The averaged attractive force with the standard deviation is given above.	122
(5.59)A graph demonstrating the binned average curve post fit for 550mM LiCl at contact site 2.	122
(5.60)A log-linear plot of the force as a function of the Z-piezo position, highlighting the interaction phase for 550mM LiCl at contact site 2.	123
(5.61)A graph demonstrating the force histogram calculated from the range of curves for 550mM LiCl at contact site 2. The averaged attractive force with the standard deviation is given above.	123
(5.62)A graph demonstrating the binned average curve post fit for 550mM LiCl at contact site 3.	123
(5.63)A log-linear plot of the force as a function of the Z-piezo position, highlighting the interaction phase for 550mM LiCl at contact site 3.	124
(5.64)A graph demonstrating the force histogram calculated from the range of curves for 550mM LiCl at contact site 3. The averaged attractive force with the standard deviation is given above.	124
(5.65)All sites' calculated force at contact with standard deviation error bars. There is an observed trend of increasing LiCl concentration leading to a decrease in repulsive force, until the repulsive force becomes attractive.	125
(6.1) A graph demonstrating the binned average curve post fit for 0.6mM LiCl at contact site 1.	129
(6.2) A linear plot of the force as a function of the Z-piezo position, highlighting the contact phase alignment for 0.6mM LiCl at contact site 1.	129
(6.3) A graph demonstrating the force histogram calculated from the range of curves for 0.6mM LiCl at contact site 0.6. The averaged attractive force with the standard deviation is given above.	129
(6.4) A graph demonstrating the binned average curve post fit for 0.6mM LiCl at contact site 2.	130
(6.5) A linear plot of the force as a function of the Z-piezo position, highlighting the contact phase alignment for 0.6mM LiCl at contact site 2.	130

(6.6) A graph demonstrating the force histogram calculated from the range of curves for 0.6mM LiCl at contact site 0.6. The averaged attractive force with the standard deviation is given above.	130
(6.7) A graph demonstrating the binned average curve post fit for 0.6mM LiCl at contact site 3.	131
(6.8) A linear plot of the force as a function of the Z-piezo position, highlighting the contact phase alignment for 0.6mM LiCl at contact site 3.	131
(6.9) A graph demonstrating the force histogram calculated from the range of curves for 0.6mM LiCl at contact site 0.6. The averaged attractive force with the standard deviation is given above.	131
(6.10)A graph demonstrating the binned average curve post fit for 1.6mM LiCl at contact site 1.	132
(6.11)A linear plot of the force as a function of the Z-piezo position, highlighting the contact phase alignment for 1.6mM LiCl at contact site 1.	132
(6.12)A graph demonstrating the force histogram calculated from the range of curves for 1.6mM LiCl at contact site 1.6. The averaged attractive force with the standard deviation is given above.	132
(6.13)A graph demonstrating the binned average curve post fit for 1.6mM LiCl at contact site 2.	133
(6.14)A linear plot of the force as a function of the Z-piezo position, highlighting the contact phase alignment for 1.6mM LiCl at contact site 2.	133
(6.15)A graph demonstrating the force histogram calculated from the range of curves for 1.6mM LiCl at contact site 1.6. The averaged attractive force with the standard deviation is given above.	133
(6.16)A graph demonstrating the binned average curve post fit for 5mM LiCl at contact site 1.	134
(6.17)A linear plot of the force as a function of the Z-piezo position, highlighting the contact phase alignment for 5mM LiCl at contact site 1.	134
(6.18)A graph demonstrating the force histogram calculated from the range of curves for 5mM LiCl at contact site 5. The averaged attractive force with the standard deviation is given above.	134
(6.19)A graph demonstrating the binned average curve post fit for 5mM LiCl at contact site 2.	135
(6.20)A linear plot of the force as a function of the Z-piezo position, highlighting the contact phase alignment for 5mM LiCl at contact site 2.	135

(6.21)A graph demonstrating the force histogram calculated from the range of curves for 5mM LiCl at contact site 5. The averaged attractive force with the standard deviation is given above.	135
(6.22)A graph demonstrating the binned average curve post fit for 5mM LiCl at contact site 3.	136
(6.23)A linear plot of the force as a function of the Z-piezo position, highlighting the contact phase alignment for 5mM LiCl at contact site 3.	136
(6.24)A graph demonstrating the force histogram calculated from the range of curves for 5mM LiCl at contact site 5. The averaged attractive force with the standard deviation is given above.	136
(6.25)A graph demonstrating the binned average curve post fit for 10mM LiCl at contact site 1.	137
(6.26)A linear plot of the force as a function of the Z-piezo position, highlighting the contact phase alignment for 10mM LiCl at contact site 1.	137
(6.27)A graph demonstrating the force histogram calculated from the range of curves for 10mM LiCl at contact site 10. The averaged attractive force with the standard deviation is given above.	137
(6.28)A graph demonstrating the binned average curve post fit for 10mM LiCl at contact site 2.	138
(6.29)A linear plot of the force as a function of the Z-piezo position, highlighting the contact phase alignment for 10mM LiCl at contact site 2.	138
(6.30)A graph demonstrating the force histogram calculated from the range of curves for 10mM LiCl at contact site 10. The averaged attractive force with the standard deviation is given above.	138
(6.31)A graph demonstrating the binned average curve post fit for 10mM LiCl at contact site 3.	139
(6.32)A linear plot of the force as a function of the Z-piezo position, highlighting the contact phase alignment for 10mM LiCl at contact site 3.	139
(6.33)A graph demonstrating the force histogram calculated from the range of curves for 10mM LiCl at contact site 10. The averaged attractive force with the standard deviation is given above.	139
(6.34)A graph demonstrating the binned average curve post fit for 25mM LiCl at contact site 1.	140
(6.35)A linear plot of the force as a function of the Z-piezo position, highlighting the contact phase alignment for 25mM LiCl at contact site 1.	140

(6.36)A graph demonstrating the force histogram calculated from the range of curves for 25mM LiCl at contact site 25. The averaged attractive force with the standard deviation is given above.	140
(6.37)A graph demonstrating the binned average curve post fit for 25mM LiCl at contact site 2.	141
(6.38)A linear plot of the force as a function of the Z-piezo position, highlighting the contact phase alignment for 25mM LiCl at contact site 2.	141
(6.39)A graph demonstrating the force histogram calculated from the range of curves for 25mM LiCl at contact site 25. The averaged attractive force with the standard deviation is given above.	141
(6.40)A graph demonstrating the binned average curve post fit for 25mM LiCl at contact site 3.	142
(6.41)A linear plot of the force as a function of the Z-piezo position, highlighting the contact phase alignment for 25mM LiCl at contact site 3.	142
(6.42)A graph demonstrating the force histogram calculated from the range of curves for 25mM LiCl at contact site 25. The averaged attractive force with the standard deviation is given above.	142
(6.43)A graph demonstrating the binned average curve post fit for 50mM LiCl at contact site 1.	143
(6.44)A linear plot of the force as a function of the Z-piezo position, highlighting the contact phase alignment for 50mM LiCl at contact site 1.	143
(6.45)A graph demonstrating the force histogram calculated from the range of curves for 50mM LiCl at contact site 50. The averaged attractive force with the standard deviation is given above.	143
(6.46)A graph demonstrating the binned average curve post fit for 50mM LiCl at contact site 2.	144
(6.47)A linear plot of the force as a function of the Z-piezo position, highlighting the contact phase alignment for 50mM LiCl at contact site 2.	144
(6.48)A graph demonstrating the force histogram calculated from the range of curves for 50mM LiCl at contact site 50. The averaged attractive force with the standard deviation is given above.	144
(6.49)A graph demonstrating the binned average curve post fit for 230mM LiCl at contact site 1.	145
(6.50)A linear plot of the force as a function of the Z-piezo position, highlighting the contact phase alignment for 230mM LiCl at contact site 1.	145

(6.51)A graph demonstrating the force histogram calculated from the range of curves for 230mM LiCl at contact site 230. The averaged attractive force with the standard deviation is given above.	145
(6.52)A graph demonstrating the binned average curve post fit for 230mM LiCl at contact site 2.	146
(6.53)A linear plot of the force as a function of the Z-piezo position, highlighting the contact phase alignment for 230mM LiCl at contact site 2.	146
(6.54)A graph demonstrating the force histogram calculated from the range of curves for 230mM LiCl at contact site 230. The averaged attractive force with the standard deviation is given above.	146
(6.55)A graph demonstrating the binned average curve post fit for 550mM LiCl at contact site 1.	147
(6.56)A linear plot of the force as a function of the Z-piezo position, highlighting the contact phase alignment for 550mM LiCl at contact site 1.	147
(6.57)A graph demonstrating the force histogram calculated from the range of curves for 550mM LiCl at contact site 550. The averaged attractive force with the standard deviation is given above.	147
(6.58)A graph demonstrating the binned average curve post fit for 550mM LiCl at contact site 2.	148
(6.59)A linear plot of the force as a function of the Z-piezo position, highlighting the contact phase alignment for 550mM LiCl at contact site 2.	148
(6.60)A graph demonstrating the force histogram calculated from the range of curves for 550mM LiCl at contact site 550. The averaged attractive force with the standard deviation is given above.	148
(6.61)A graph demonstrating the binned average curve post fit for 550mM LiCl at contact site 3.	149
(6.62)A linear plot of the force as a function of the Z-piezo position, highlighting the contact phase alignment for 550mM LiCl at contact site 3.	149
(6.63)A graph demonstrating the force histogram calculated from the range of curves for 550mM LiCl at contact site 550. The averaged attractive force with the standard deviation is given above.	149
(6.64)Site one calculated attractive force retained from contact with standard deviation error bars.	150
(7.1) Approach force-current histogram at 0.6mM at 2Hz	154
(7.2) Retract force-amplitude histogram at 0.6mM at 2Hz	155
(7.3) Approach curve for 1.6mM, S2 at 2Hz	155

(7.4) Retract curve for 1.6mM, S2 at 2Hz	155
(7.5) Approach curve for 5mM, S1 at 2Hz	156
(7.6) Retract curve for 5mM, S1 at 2Hz	156
(7.7) Approach curve for 5mM, S2 at 2Hz	157
(7.8) Retract curve for 5mM, S2 at 2Hz	157
(7.9) Approach curve for 5mM, S3 at 2Hz	158
(7.10) Retract curve for 5mM, S3 at 2Hz	158
(7.11) Approach curve for 10mM, S1 at 0.1Hz	159
(7.12) Retract curve for 10mM, S1 at 0.1Hz	159
(7.13) Approach curve for 10mM, S1 at 2Hz	160
(7.14) Retract curve for 10mM, S1 at 2Hz	160
(7.15) Approach curve for 10mM, S2 at 0.1Hz	161
(7.16) Retract curve for 10mM, S2 at 0.1Hz	161
(7.17) Approach curve for 10mM, S2 at 2Hz	162
(7.18) Retract curve for 10mM, S2 at 2Hz	162
(7.19) Approach curve for 10mM, S3 at 0.1Hz	163
(7.20) Retract curve for 10mM, S3 at 0.1Hz	163
(7.21) Approach curve for 10mM, S3 at 2Hz	164
(7.22) Retract curve for 10mM, S3 at 2Hz	164
(7.23) Approach curve for 25mM, S1 at 2Hz	165
(7.24) Retract curve for 25mM, S1 at 2Hz	165
(7.25) Approach curve for 25mM, S2 at 2Hz	166
(7.26) Retract curve for 25mM, S2 at 2Hz	166
(7.27) Approach curve for 25mM, S3 at 2Hz	167
(7.28) Retract curve for 25mM, S3 at 2Hz	167
(7.29) Approach curve for 230mM, S1 at 2Hz	168
(7.30) Retract curve for 230mM, S1 at 2Hz	168
(7.31) Approach curve for 230mM, S2 at 2Hz	169
(7.32) Retract curve for 230mM, S2 at 2Hz	169
(7.33) Approach curve for 550mM, S2 at 2Hz	170
(7.34) Retract curve for 550mM, S2 at 2Hz	170
(7.35) Approach curve for 550mM, S3 at 2Hz	171
(7.36) Retract curve for 550mM, S3 at 2Hz	171

(7.37)Averaged approach curve with the range of tip speeds. 0.5Hz represents the standard dataset, whereas 0.1Hz and 2Hz represent the modified speeds under investigation.	172
(7.38)Averaged retract curve with the range of tip speeds. 0.5Hz represents the standard dataset.	172
(7.39)Averaged approach standard deviation between points. 0.5Hz represents the standard dataset.	173
(7.40)Averaged retract standard deviation between points. 0.5Hz represents the standard dataset.	174
(7.41)A graph demonstrating the averaged retract forces felt by the AFM tip at different LiCl concentrations with 5s dwell time and 0s dwell time respectively.	175
(7.42)A graph demonstrating the averaged approach forces felt by the AFM tip at different LiCl concentrations with 5s dwell time and 0s dwell time respectively.	176
(7.43)A graph demonstrating the differences in approach and retract forces at differing pHes. pH 5 is the deviation and pH 7 is the standard.	177
(7.44)Approach force histogram for 0.5mM concentration.	178
(7.45)Approach heatmap for 0.5mM concentration.	179
(7.46)Retract force histogram for 0.5mM concentration.	180
(7.47)Retract heatmap for 0.5mM concentration.	180
(7.48)Retract heatmap for 0.5mM concentration.	181
(7.49)Approach heatmap for 10mM concentration.	181
(7.50)Retract heatmap for 0.5mM concentration.	182
(7.51)Retract heatmap for 10mM concentration.	182
(8.1) An example of a derived deflection slope vs z separation processed curve. This curve is used to help guide the user to optimise the fitting parameters. The purple region indicates the region used to define contact, and to help straighten the contact region.	185
(8.2) The fitted curve from the values above. The back is relatively straight.	186
(8.3) An example of a derived deflection slope vs z separation processed curve. The purple region indicates the region used to define contact, and has specifically been placed onto the shelf area.	186
(8.4) The fitted curve from the values above. The back is wonky, but the shelf feature prevails.	186

(8.5) Demonstrating the fitting range for the shelf analysis. The two red dots highlight the end points of the range. The shelf force is calculated by the average force for the points within the range, and the shelf range is calculated by the width of the two points in nm.	187
(8.6) Demonstrating the range of self force and self range. For the range of data, there was no significant change in the datapoints due to salt concentration for both features.	188
(8.7) An example of an unprocessed curve (except force flooring) from the JPK forcemapping. The "shelf" can clearly be seen, with a sudden jump down to contact. The difference between this and the MFP could be due to the higher resolution the newer AFM offers.	188
(8.8) An example of a zoomed in portion of a raw curve. The noise is intense. The shelf feature can be somewhat seen in the curve, but could easily be discounted by the background noise.	189
(8.9) An example of an adjusted and overlapped portion of multiple curves. The shelf is clearly visible and highlighted throughout the multiple movements throughout the noise floor.	190
(8.10) Critical surface energy values deduced from AFM (red circles) and rheological experiments (black squares) at different ionic strengths.	193
(8.11) Force at contact from AFM experimental data (red circles) compared against calculated DLVO at different ionic strengths.	195
(8.12) Force at contact from AFM experimental data (red circles) compared against calculated DLVO with respect to surface roughness at different ionic strengths.	196

0.5 Introduction to the Thesis

This thesis delves into the complex world of colloidal interactions, focusing on the microscale forces that govern the behavior of particles in various environments. The thesis begins with a curiosity about the forces affecting colloidal particles and extends into a comprehensive exploration of their impacts in real-world scenarios, bridging theoretical knowledge with practical experiments.

Chapter 1: Introduction to Surface Forces

The first chapter sets the stage by examining the fundamental interactions between particles, exploring the theoretical understand of colloidal stability. Initially various forms of explaining colloidal behaviour is discussed, such as electrostatic repulsion and van der Waals attraction. This culminates in the defining theory for colloidal physics; DLVO theory.

An example is given of DLVO in action, and explores how these interactions influence the stability and behavior of colloidal suspensions, contributing to advancements in materials science and biotechnology.

Chapter 2: Atomic Force Microscopy

This chapter delves into the history and development of microscopy, leading up to the modern techniques of Atomic Force Microscopy (AFM). It covers the basic operational principles of AFM, including tip calibration, common artifacts, and imaging modes. This chapter is essential for understanding the detailed methodologies used in subsequent experimental analyses as the majority of the data generated in the thesis is from AFM.

Chapter 3: Surface Imaging

In this chapter, the focus shifts to the practical application of AFM in surface imaging. Initially an example with mica is used to demonstrate some of the methods and results of imaging AFM. Borosilica surfaces are explored using surface analysis techniques, discussing the resolution of silica particle surfaces. This chapter lays the groundwork for understanding the surface roughnesses of the probing colloidal particle at the surface level, as well as providing a surface roughness analysis of the borosilica glass surface used, which is crucial for the later analysis of force curves.

Chapter 4: Atomic Force Spectroscopy Analysis

This chapter describes the experimental setup and methods used for force curve collection in AFM studies. It explains the computational methods for interpreting these curves, ensuring a repeatable method across a consistent experimental

setup. The chapter is critical in the detailed examination of approach force curves for the following chapters and lays the foundation of the script used, as well as the intensive validation methods used. Said script was designed to process high volumes of data automatically, and is provided on Github as FOSS software. It also overviews the two AFMs used in the force curve analysis.

Chapter 5: Analysis of Approach Force Curves in Colloidal Systems

Here, the thesis focuses providing a clear method for extracting the force at contact from raw data in colloidal systems. The chapter focuses on presenting and justifying the contact forces calculated for each concentration site. For each site, a snapshot of the analytical curves is shown to highlight where the data points are derived from, justifying the averaged force curve. Additionally, the range of contact forces is calculated, giving an averaged approach force with standard deviation for each site and concentration combination. Finally the chapter is finished with an analysis of the ionic strength vs approach force analysis.

Chapter 6: Analysis of Retract Force Curves in Colloidal Systems

Following a similar trajectory to chapter 5, this chapter focuses on the retract curves, Once again justifying the individual fits and providing an averaged force curve and retract force. This retract force is then analysed in a similar manner at the end of the chapter.

Chapter 7: Operational Parameter Exploration and Their Implications

This chapter explores various operational parameters in AFM studies and their implications. It includes analysis of tip speed, dwell time, pH, and force mapping. The chapter builds upon the foundational data presented earlier to further understand and interpret the results of AFM force curve analysis under different conditions to highlight potential differences and implications..

Chapter 8: Further Analysis and Discussion

The final chapter analyzes and discusses the findings presented in the previous chapters, focusing on the details and implications of AFM force curve analysis. This chapter also delves into the interesting quirks seen in the dataset, such as the “shelf” feature present in some of the curves. Further reflection is also done on the implications and success of the open source script and the impact of investigating a range of operation parameters. Additionally, the data generated is compared against rheological data, as well as DLVO itself to draw further conclusions and implications.

Chapter 1

Introduction to surface forces

The methods of how particles interact with one another have been a longstanding area of interest in physics. As matter encroaches upon one another, there is an interplay of attractive and repulsive forces, which is particularly evident on the microscale of colloidal particles. This transition from repulsive to attractive forces within solutions marks a pivotal point essential for understanding and manipulating the behavior of these colloidal systems. Such knowledge is not only of academic interest but also has significant practical implications, especially in how the rheological properties of solutions can shift given different conditions.

This deep dive into the realm of particle interactions has far-reaching effects that ripple through numerous industries. For instance; the paint and coatings industry, the food industry, the biotech industry and the cosmetic industry, all industries dependant on understanding this interplay where stability and consistency are necessary variables. Furthermore, in the pharmaceutical domain, the implications are even more striking. The efficacy and stability of drugs for health and well-being are fundamentally anchored in these particle behaviors. On a larger canvas, the insights from this research catalyze innovations in smart materials, such as those used in the automotive sector for shock absorption. Beyond the immediate technological triumphs, the environmental aspect is non-trivial. A refined understanding of these interactions paves the way for more sustainable practices and materials, aligning with a global imperative to minimize waste and conserve energy.

Furthermore, the exploration of particle interactions in colloidal systems extends its significance to the realm of biology, shedding light on the fundamental mechanics of microscopic life. Bacteria, along with a myriad of other microorganisms, can be modelled as simplistic colloids. Their interactions, survival, and behavior in various environments are intricately tied to the same principles of repulsive and attractive forces that govern inanimate colloids. Understanding how these biological colloids interact with each other and their surroundings provides invaluable insights into microbial life. This knowledge is not just theoretical but has practical implications in areas like biotechnology and medicine. For instance, deciphering how bacterial colonies form, adhere to surfaces, disperse,

or respond to different environmental conditions can inform the development of new antibiotics and treatments, as well as contribute to the understanding of biofilm formation and its prevention. Additionally, this understanding aids in the development of biosensors and other biotechnological applications where microbial interaction with their environment is key.

Moreover, the stability and behavior of colloidal suspensions are deeply influenced by these particle interactions. In industries where such suspensions are fundamental, the transition between repulsive and attractive forces directly impacts product stability and performance. Knowledge of where and when this transition occurs is instrumental in developing lasting products, or making a breakthrough in research.

Additionally, these force transitions are central to the study of rheology, particularly concerning shear thickening phenomena. The shift from repulsive to attractive interactions among particles in a shear-thickening fluid is key to understanding the increase in viscosity under stress. A deeper understanding of this transition is critical for uncovering the physics that underlie this behavior, leading to the development of advanced materials with specifically tailored properties.

This PhD, born from a simple desire to understand the forces influencing colloidal interactions on the nanoscale, covers a story started from the simple curiosity of what forces affect colloidal particles when they come in contact with one another. How does this force lead into the wider observed behaviour? Where do these shifts come from and what causes them? Can we model and develop tools to predict their behavior? How do these effects relate to real world life environments and systems? and what breakthroughs can we share with the world? My aim, in truth, was partially to bridge theoretical knowledge with practical application, provide an independent contribution to science and to scale the giant that is modern physics and stand atop the giant's shoulders.

But to first discuss the journey, we must first describe the mountain, and thus this brings us to the fundamental theory behind colloidal particles.

1.1 Interparticle Colloidal forces

The interactions between colloidal particles are predominantly governed by a complex interplay of various forces. These forces dictate the stability, behavior, and ultimate fate of colloidal systems in different environments. Understanding these forces is fundamental to understanding what directs colloidal systems.

The term colloid, coined in 1861 from the Greek word (*kolla*), meaning glue, reflects Thomas Graham's observations of particle aggregation[35]. Today, a colloid is a mixture comprising a dispersed phase of minute particles or droplets suspended in a continuous phase. The nature of these phases can vary, with examples including solid particles in liquids, liquids in gases (aerosols), and gases in liquids (foams).

Consider the idea of marbles kept within a liquid. At rest, they would lie upon the bottom of the container, yielding to the force of gravity[66]. However, as you scale down these marbles, to smaller and smaller sizes, the kinetic energy of the system is enough for keep the marbles dispersed within the liquid, due to Brownian motion[17].

At micrometer sizes however, the marbles begin to affect one another; when two marbles are brought together by Brownian motion, provided the interactions between the two of them are attractive, they will attract towards each other, and eventually aggregate, until they are large enough to sediment again. If there is no attraction, or indeed there is repulsion between the marbles, they will stay suspended within the solution.

On the macro scale, these interactions ultimately contribute to bulk properties. As this system is disturbed by external forces, a characteristic relaxation time is observed, dependent on the ions in solution and surface properties of the solid phase particles. These properties give rise to the time dependent effects seen in colloidal systems.

The various interactions between the marble surfaces can be combined to give a force profile, describing the strength of the interaction between the marbles with respect to the distance between them.[48][62]

These forces are not merely determined by chemical composition; they are a web of multiple interactions shaped by the colloidal environment. Specifically, van der Waals forces, electrostatic interactions, and steric hindrances play significant roles in a solution's stability and organization. van der Waals forces, although weak individually, collectively contribute to significant attractions or repulsions (more rarely) at the nanoscale. Electrostatic interactions, governed by the surface charge of the particles and the ionic composition of the medium, further influence particle behavior. Steric hindrance, resulting from the physical size and shape of the particles, adds another layer to this complex interplay.

In addition to these effects solvation forces can also affect colloidal systems. When a colloid is introduced into a solvent, the solvent molecules rearrange around the colloid, leading to a structured layer of solvent molecules at the colloid's surface. This structuring can lead to either attraction or repulsion between colloids, depending on the nature of the colloidal surface and the solvent. Solvation forces are particularly significant in polar solvents like water, where the solvent molecules can form hydrogen bonds and other directional interactions with the colloid surface. Additionally, hydrodynamic forces can affect the distribution of stability of a colloidal system. These forces are governed by factors such as the viscosity of the fluid, the relative velocity between the particle and the fluid, and the size and shape of the particles. Hydrodynamic interactions play a significant role in determining the behavior of colloids under dynamic conditions, such as in suspension flow or by perturbation by a cantilever. These forces arise from the movement of colloidal particles relative to the suspension, resulting in effects like drag and flow-induced reorientation.

Hydrophobic interactions, especially in amphiphilic systems, arise from hydropho-

bic molecules or groups in aqueous environments. This tendency drives the aggregation of hydrophobic regions, playing a key role in the self-assembly of micelles, vesicles, and the organization of cellular membranes. In these structures, hydrophobic tails cluster away from water, while hydrophilic heads interact with the aqueous environment, creating a dynamic interface.

When profiling colloidal interactions, it can be fruitful to imagine such interactions as a dynamic interplay of forces that resolve with one another dependant on distance. As two colloids move towards one another, the forces shift and change between the attractive and repulsive regime. As one expects with a dynamic system such as this, the particle will settle into distinct energy wells. The colloid can be destabilised from this energy well by influential forces overcoming the entrapping energy barriers. These can take the form of kinetic impulses (i.e. a 3rd party physical force applied upon the system), hydrodynamic forces or changes in the suspending medium. In the following sections, each of these forces will be examined in detail, unraveling their individual contributions and collective interplay in shaping the fascinating behavior of colloidal systems

1.1.1 Electrostatic interactions

Electrostatic interactions are fundamental in the study of colloidal systems, governing the behavior and stability of charged particles in various media. The understanding of these interactions dates back to ancient Greek philosophers, but it was the 18th-century physicist Charles-Augustin de Coulomb who formalized the concept. His work on what is now known as Coulomb's Law provided a framework for comprehending the forces between charged particles. This understanding is particularly vital in colloid science, where electrostatic interactions play a key role in the stability of colloids. [41]

In colloidal systems, when two phases mix, ions often arrange along the phase boundary, seeking the lowest energy configuration. This arrangement can create electric fields that induce polarization in nearby molecules, resulting in an electric potential difference between the phases. Such electrostatic phenomena are central to understanding the behavior of colloids, as they influence particle aggregation, stability, and the overall properties of the system. For example, in aqueous colloids, the balance of electrostatic repulsion and attraction among particles can determine whether the colloid remains stable or aggregates.

Coulomb's law provides a basis for understanding these forces in colloidal contexts. The equation demonstrates the force experienced between two electrically charged particles, known as the electrostatic or Coulombic force. The force is governed by the equation:

$$F = \frac{q_1 q_2}{4\pi\epsilon_r\epsilon_0 r^2} \quad (1.1)$$

In this formulation: F represents the electrostatic force between the particles. q_1 and q_2 are the electric charges of the particles. The force's attraction or repulsion

depends on these charges. If both charges are of the same sign (either positive or negative), the resulting force is repulsive, pushing the particles away from each other. In contrast, if the charges are of opposite signs, they attract each other. h is the distance between the two charged particles. The strength of the force diminishes with increasing distance; it weakens as the square of the distance. ϵ_0 is known as the vacuum permittivity. It is a measure of the resistance offered by the vacuum of space to the formation of an electric field. ϵ_r , is the relative permittivity. Unlike in a vacuum, colloidal interactions occur in a medium (such as water), which affects the electric field. The relative permittivity indicates how much the medium reduces the electric field compared to a vacuum. It accounts for the medium's ability to absorb or dampen the electrostatic interactions.

This law thus provides a foundational understanding of how charged colloidal particles interact within a medium. The inclusion of ϵ_r in the equation adjusts Coulomb's Law from the idealized context of a vacuum to the more complex reality of colloidal systems in diverse environments. In a vacuum, the electric field lines travel without much resistance, but in other mediums like water, air, or any material, these field lines encounter more resistance. This resistance is due to the medium's ability to partially absorb or slow down the electric field. $4\pi\epsilon_0$ is sometimes simplified to the electrostatic constant.

Charges on surfaces in colloidal systems can arise from several phenomena. The innate surface chemistry of the particles often dictates their initial charge characteristics. For instance, surfaces may naturally possess acidic or basic groups that can gain or lose protons, depending on the pH of the surrounding solution. Additionally, the adsorption of ions from the solution onto the particle surface and the dissociation of surface-bound ions into the solution also contribute to the overall surface charge.

The ionization of surface groups is highly dependent on the pH of the solution. In acidic conditions, basic surface groups tend to gain protons, leading to a positive charge on the surface. Conversely, in basic conditions, acidic surface groups tend to lose protons, resulting in a negative surface charge. This pH-dependent behavior can modify the surface charge characteristics of colloidal particles, thus influencing their stability and interaction in the solution.

Furthermore, the presence of a charge on the colloidal particle surface attracts counter charged ions from the surrounding medium. These counter ions associate towards the charged surface, forming a layer that screens the original surface charge. This is known as charge screening, and is influenced by the concentration and type of ionic salts within the suspending solution. The effectiveness of charge screening plays a significant role in modulating electrostatic interactions between colloidal particles. [88] [39] [47]

Charge screening

Charge screening in colloidal systems is a phenomenon where charged surfaces become surrounded by a cloud of counter-ions of opposing charge, leading to the

formation of what is known as the electrical double layer. As ionic species diffuse within a solution tending towards a reduction in the free energy of the system, charged surfaces will tend to become surrounded by a cloud of counter-ions of opposing charge. This layer plays a pivotal role in colloidal stability by influencing the electrostatic interactions between particles.

When oppositely charged ions in the solution approach the charged surface, they tend to reduce the net surface charge, creating an electrostatic potential that decreases with distance from the surface. This process leads to a distribution of ions, known as the Gouy-Chapman-Stern model, which describes the behavior of ions near the charged surface. As such the concentration, charge and valence of the ionic salts will change the repulsive forces upon interacting colloids.[5]

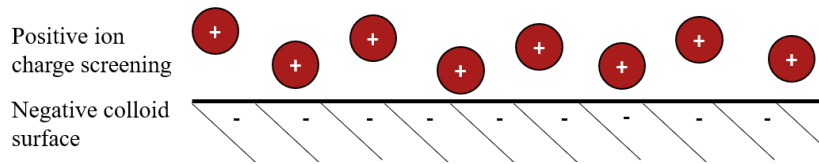


Figure 1.1 A schematic of counter ion distribution under the Gouy-Chapman model. This demonstrates how positive counter ions will arrange themselves around a negative surface.

These ions are subjected to an electrostatic potential (Ψ) as they get closer towards the oppositely charged surface. The positive counter-ions (see fig 1.1) are attracted by the electric field generated from the negatively charged surface producing a potential seen in fig 1.2.

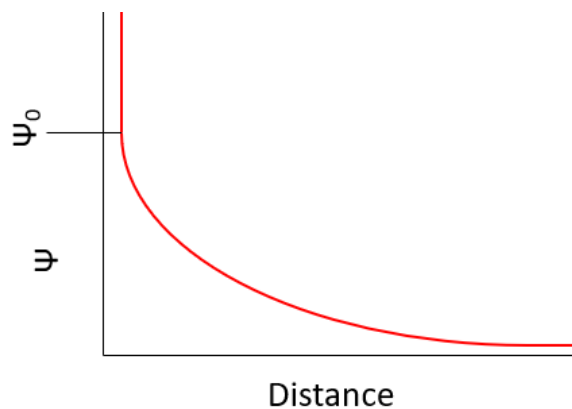


Figure 1.2 The Electrostatic potential of a counter ion, where distance is the distance between the negative surface and positive ion.

In addition to the electrostatic attraction, ions in colloidal systems are also subjected to thermal motion. This thermal motion leads to a random distribution of ions uniformly, counterbalancing their electrostatic attraction to the charged surface. As a result, the concentration of counterions decreases with increasing

distance from the surface. This leads to the formation of the diffuse electrical double layer which also includes the Stern layer.

The concept of the electrical double layer has been explained through several historical models. The Helmholtz model, proposed in 1853, suggested a simple planar distribution of charges directly opposite the surface charge, akin to a parallel plate capacitor. This distribution is a function of the distance away from the surface, and thus surface charge. While this model provided a basis of understanding the interactions between solvent ions and surface charges as a function of distance, it was unable to account for the effects of kinetics on the system.

The Gouy-Chapman model developed between 1910 and 1913 introduced a more dynamic understanding. This model considered the impact of thermal motion, leading to a diffuse distribution of ions. It relies on the linearized Poisson-Boltzmann equation, which correlates the electrostatic potential with the charge density around the colloidal particle, allowing for a theoretical description of the diffuse layer. This model assumes a uniform surface charge and a homogeneous dielectric constant for the solution, implying that ions form a diffuse point charge region rather than discrete binding sites.

Within this region there is a volume of liquid that is unique to the bulk properties of the liquid phase. This region with a higher concentration of counter ions is called the Helmholtz region and is further split up into two parts. The closest to the surface being the inner Helmholtz plane - where ions are adsorbed onto the surface, and the outer Helmholtz layer contains solvated ions. Afterwards the diffuse layer is made up of unbound free ions influenced by Brownian motion.

The Diffuse layer is characterized by a gradual reduction in counterion concentration until it reaches the bulk concentration level. The Stern layer comprises specifically adsorbed ions in the inner Helmholtz plane and more loosely associated solvated ions in the outer Helmholtz plane. This layer represents the initial structuring of ions influenced by the surface charge before transitioning into the more diffuse arrangement of the bulk solution.” The distribution of ions in this layer is highly dependent on the electrolytes present in the solution.

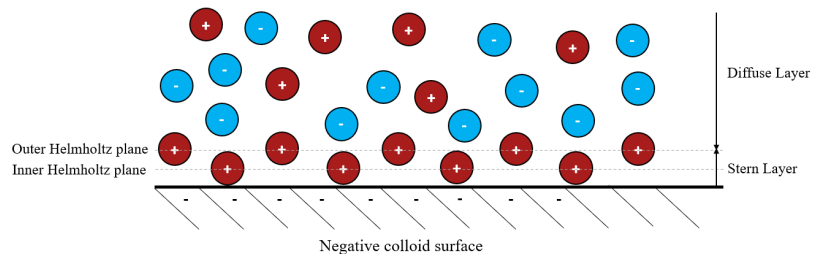


Figure 1.3 The Electrical double layer model highlighting the transition between the Stern and diffuse layers.

The Debye length (λ_D) is a measure of the distance over which the electrostatic influence of a colloidal surface charge extends into the surrounding solution. It

represents the characteristic distance at which the electrostatic potential decays by a factor of (e^{-1}). The Debye length is given by:

$$\lambda_D = \kappa^{-1} = \sqrt{\frac{2N_A e^2 I}{\epsilon_0 \epsilon_r k_B T}}, \quad (1.2)$$

Where κ is the inverse Debye length, ϵ_0 is the vacuum permittivity, N_A is Avogadro's constant, k_B is the Boltzmann constant, T is temperature in degrees Kelvin (K), ϵ_r is the relative dielectric constant, e is the elementary charge, Where I (the ionic strength) is calculated using:

$$I = \frac{1}{2} c_i z_i^2 \quad (1.3)$$

Where c_i is the concentration of the i ionic species, and z_i is the valency or charge of the i ionic species.

The Debye length measures the effective thickness of this diffuse layer. It represents the distance beyond which the electrostatic influence of the surface charge becomes insignificant. The Debye length is dependent on factors such as temperature, the dielectric constant of the medium, and the ionic strength of the solution. The ionic strength, in turn, affects the distribution and concentration of ions in the diffuse layer.

Electrostatic repulsion

Electrostatic repulsion plays a significant role in maintaining the stability of colloidal suspensions. When two colloidal particles in a suspension approach each other, their respective electrical double layers begin to overlap and repel one another. Without this repulsion attractive van der Waals forces (detailed in the next section) would dominate, leading to particle aggregation. The nature of this electrostatic repulsion is closely linked to the presence of the electrical double layer surrounding each colloidal particle. As detailed previously, the double layer consists of surface-bound charges and a diffuse layer of counterions, which create a repulsive force when two colloidal particles approach each other. This repulsion counterbalances the attractive van der Waals forces, thereby stabilizing the colloidal system.[45] The electrostatic energy of this repulsion is given by:

$$U_E(h) = \frac{64\pi\epsilon\epsilon_0 k_B T \Psi_0^2}{\kappa^2} e^{-\kappa h} \quad (1.4)$$

$U_E(h)$ represents the electrostatic repulsion energy as a function of the distance (h) between the particles. ϵ_r is the relative permittivity of the medium, and ϵ_0 is the vacuum permittivity. Ψ_0 is the surface potential of the colloidal particles. κ is the inverse Debye length and determines how quickly the potential decays with distance, related to the thickness of the electrical double layer. $e^{-\kappa h}$ is an

exponential term that describes how the repulsion decreases with the distance between the particle surfaces. T represents the absolute temperature and k_B is the Boltzmann constant. [70] [8]

The Debye length is a key factor that governs the range of electrostatic interactions. In solutions with high ionic strength, the Debye length is shorter, leading to a more compressed double layer. Consequently, the electrostatic repulsion decreases more rapidly with distance, allowing particles to come closer before experiencing significant repulsive forces. In contrast, in low ionic strength solutions, the Debye length is longer, and particles experience repulsive forces over greater distances, contributing to the stability of the suspension by preventing aggregation.

The other factor that affects colloids in suspensions is the attractive component. This component derives from van der Waals forces.

1.1.2 Van der Waals Forces

The strongest attractive forces acting on the solid phase of a colloidal system are described by van der Waals theory. Originally recognized by Johannes Diderik van der Waals in 1873 [85], these forces were further refined by London in 1930 [27] almost 60 years later, leading to the concept of London dispersion forces.

Van der Waals forces can be categorized into three types: Keesom forces (permanent dipole-permanent dipole interactions), Debye forces (permanent dipole-induced dipole interactions), and London dispersion forces (induced dipole-induced dipole interactions) [40].

Keesom forces derive from the permanent charge nature of atoms, where a static dipole induces an attraction between two particles, due to their stable differences in charge (see fig 1.4). These forces follow an inverse sixth power law ($1/h^6$) with respect to the distance between the dipoles, reflecting their short-range nature in colloidal systems.

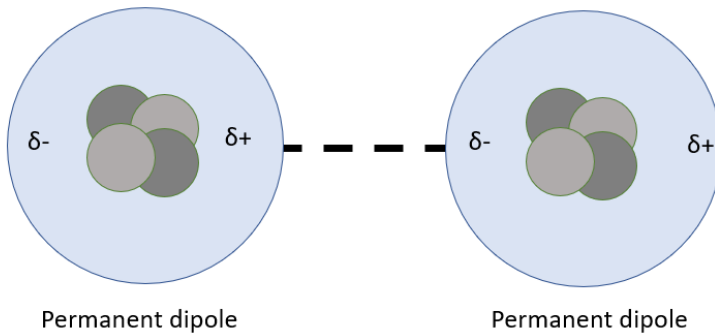


Figure 1.4 A basic schematic of Keesom interacting forces.

Debye forces result from the influence of an instantaneous dipole on a permanent

the interaction between the electronic fields results in a force between the dipoles, initially without a dipole moment. This interaction, illustrated in Figure 1.5, stems from the influence of the fluctuating electronic field of the permanent dipole on its neighboring particles.

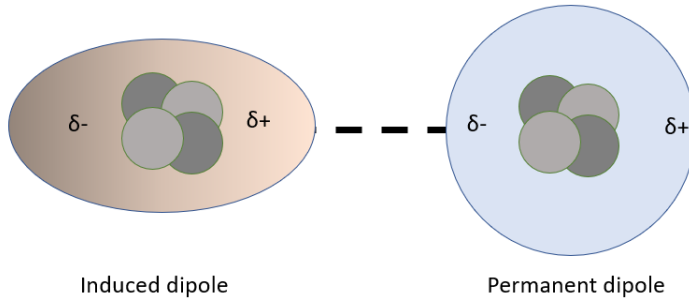


Figure 1.5 A basic schematic of Debye interacting forces. The orange dipole represents an non permanent sudden gradient.

Dispersion forces (see fig 1.6) act between all atoms and molecules, even those in neutrally charged elements. These forces arise due to fluctuations in electron density around the nucleus, as a consequence of the Heisenberg uncertainty principle.[43] [36] This dispersion force is caused by an electronic charge flux inducing a dipole moment and is unique in that it does not require the presence of permanent dipoles, unlike Keesom and Debye forces, which depend on their permanent dipole properties and the nature of the medium. [62] To understand the origin of these forces, consider an atom with a time-averaged dipole moment of zero. Fluctuations in the electron density around the nucleus result in a non-zero instantaneous dipole moment. This fluctuating instantaneous dipole moment generates a fluctuating electric field on any neighboring neutral atoms. The interaction between the instantaneous dipole moment in one atom and the induced dipole in another, averaged over orientation to account for the fluctuating nature of the instantaneous dipole, gives rise to an attractive interaction between the two atoms.

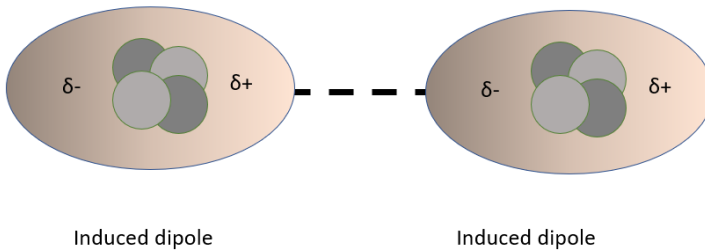


Figure 1.6 A basic schematic of dispersion interacting forces.

The intensity of the induced electric field from instantaneous dipole moments

decreases with distance, which can be described by the equation:

$$E_{\text{ins}} \propto \frac{1}{h^3} \quad (1.5)$$

This reflects that as the distance (h) increases, the intensity of the induced electric field, generated due to instantaneous dipole moments, diminishes significantly.

The induced dipole moment is proportional to this electric field, where the proportionality constant is the polarizability (α) of the second atom:

$$p_{\text{ind}} \propto \alpha E_{\text{ins}} \quad (1.6)$$

Here, p_{ind} represents the induced dipole moment, which is formed in response to the external electric field (E_{ins}). The polarizability, α , measures how easily the electron cloud of the atom is distorted to form this dipole moment.

Consequently, the interaction energy between the two atoms, which arises from these induced dipoles, follows an inverse sixth power law with respect to the distance:

$$U \propto \frac{\alpha}{h^6} \quad (1.7)$$

This equation signifies that the interaction energy (U) decreases very rapidly as the distance between the atoms or molecules increases, following an inverse sixth power law. This rapid decrease is important, as it places a high impact on the distance between particles influencing the resulting attractive force.

These equations collectively describe the fundamental mechanism of dispersion forces, highlighting how forces arise from instantaneous dipole-induced dipole interactions and lead to an attractive force between atoms or molecules. This attraction occurs even in the absence of permanent dipole moments, leading to an attractive force seen between colloidal particles.

The stability of colloids is significantly influenced by van der Waals forces, which govern the attractive interactions between particles. These forces can lead to particle aggregation especially when they overpower repulsive forces such as electrostatic interactions in charged colloids. The phenomenon of aggregation resulting from dominant van der Waals attractions can reduce colloidal stability, potentially causing sedimentation or phase separation.

These van der Waals forces, comprising Keesom, Debye, and London dispersion forces, play a pivotal role in the behavior of colloids. Their predominance in short-range interactions is essential for understanding the stability and dynamics of colloidal systems [57][39][62][48].

Mathematical basis of dispersion forces

The van der Waals interaction energies in colloidal systems can be represented mathematically through various equations. Two such expressions for the van der Waals potential energy (U_{vdW}) are:

$$U_{vdW} = -\frac{A_H R}{6h^2} \quad (1.8)$$

In these equations, U_{vdW} is the attractive cohesive energy, A_H is the Hamaker constant, R is the radius of the colloidal particle, and h is the distance between the two particles. Equation 1.8 is derived to use for sphere-plane interactions, and for different geometries different equations are often used. The Hamaker constant (A), a fundamental parameter in these equations, is influenced by the material properties of the colloidal particles and the medium. The Hamaker constant is given by:

$$A = \pi^2 C p_1 p_2 \quad (1.9)$$

Where C is the interaction parameter, given by the coefficient in the particle-particle pair interaction, and p_1 and p_2 represent the number densities of the two interacting particle types. [48] The interaction parameter C is determined as follows:

$$C = -w(h)h^6 \quad (1.10)$$

where $w(h)$ denotes the pair interaction energy between two particles.

One striking element of these interactions is their short range - their significance only felt up to tens of nanometers. This is significant in colloidal systems particularly in solvent environments, where the Hamaker constant (A) assumes characteristic values depending on the colloidal and solvent properties. The interaction range significantly influences colloidal properties such as aggregation, stability, and rheology, highlighting the importance of understanding these forces.[47]

1.2 The Interplay of Attractive and Repulsive Forces on Colloidal Systems

The intricate balance between attractive and repulsive forces plays a pivotal role in determining the stability of colloidal systems. This interplay between van der Waals forces and electrostatic interactions, forms the theoretical foundation of colloidal behavior. While van der Waals forces tend to draw particles together, potentially leading to aggregation, it is the counteracting electrostatic repulsion that often dictates whether a colloidal system remains stable or not. The stability of colloids thus depends on the equilibrium between these competing forces. Delving deeper into this complex interaction, the subsequent sections will explore the Lennard-Jones potential and the DLVO theory. The Lennard-Jones potential provides a fundamental model for understanding the balance of attraction and repulsion at a molecular level, while the DLVO theory offers a comprehensive framework that elucidates how this equilibrium contributes to the overall stability of colloidal systems and provides the main theoretical basis of understanding this practical thesis.

1.2.1 Lennard-Jones potential

The Lennard-Jones potential stands as an introduction in modeling intermolecular forces within colloidal systems. By illustrating the equilibrium between attractive and repulsive forces, this model provides a fundamental understanding of how colloids arrange themselves at a characteristic distance, giving rise to colloidal stability.

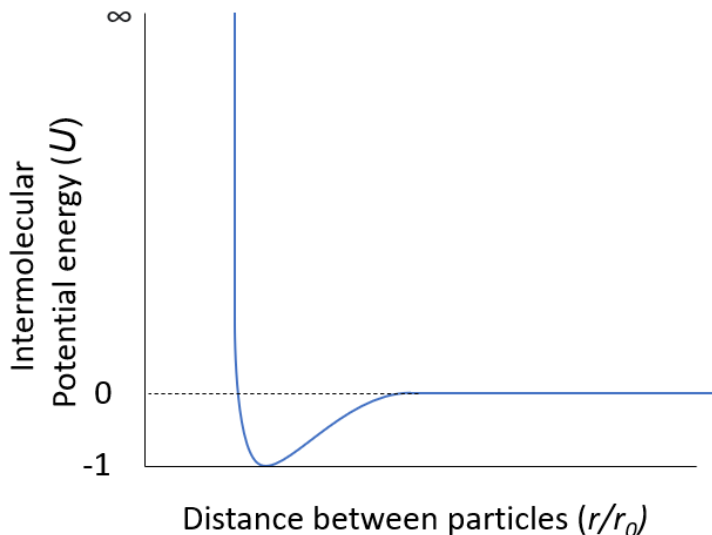


Figure 1.7 The Lennard-Jones potential function. The potential energy between the two particles is given as a function of distance. As the particles begin to get closer, the experience attraction. As the distance between the two shortens, the attraction eventually gives way to a infinitely increasing repulsive force.

The Lennard-Jones potential offers a useful visual representation of intermolecular forces. This model is particularly useful for visualizing the variation of potential energy as a function of the distance between particles. At the nadir of this curve lies the energy well, a concept that illustrates the balance between attractive and repulsive forces, and demonstrates the optimal distance location between interacting particles under no external forces. This balance occurs at a specific inter-particle distance where the system achieves its minimal potential energy and thus equilibrium state. The Lennard-Jones potential is given by:

$$U(h) = 4\epsilon \left[\left(\frac{\sigma}{h}\right)^{12} - \left(\frac{\sigma}{h}\right)^6 \right] \quad (1.11)$$

Where ϵ is the depth of the potential well, representing the strength of the attraction at the equilibrium distance. σ is the finite distance at which the inter-particle potential is zero; it represents the distance at which the potential between the two particles changes from repulsive to attractive. h is the distance

between the particles. The first term is the repulsive forces, which are strong at very short distances and decay rapidly with distance. The second term represents the attractive forces, which decay relatively slower with distance.

The graphical representation of the Lennard-Jones potential (see Figure 1.7) serves as a visual representation of the concepts discussed earlier, combining the effects of electrostatic repulsion and van der Waals attraction into a singular curve. The curve demonstrates how these two forces interplay to create a stable configuration at the energy well. This model also shares the form of an atomic force microscopy (AFM) force curve, further emphasizing its practical relevance.

This originally sought to model interactions between two noble gas atoms by describing Pauli repulsion coupled with an attractive long range term. This provides a simplistic view by assuming all interactions between all particles are the same and thus the solution is homogeneous. This is done by summing the contributions from all particles interacting with one another. However, this simplification also introduces limitations. The Lennard-Jones potential does not account for solvent effects and assumes particles are in a vacuum. Additionally, it overlooks the role of charge, which is particularly important when ions are present in the solvent. In reality, particles immersed in a solvent experience modified forces leading to a reduced attractive interaction than vacuum conditions. [39]

These limitations highlight the need for more comprehensive models which leads us into DLVO theory. DLVO theory, which integrates electrostatic repulsion and van der Waals attraction, addresses some of the shortcomings of the Lennard-Jones potential by considering the specific conditions of colloidal systems, including the presence of a solvent and the role of ionic strength.[54]

1.2.2 DLVO theory

DLVO theory, named after its developers Derjaguin, Landau, Verwey, and Overbeek in the mid-20th century, describes the complex interplay of forces within colloidal systems. This theory represents a dance of forces where electrostatic repulsions $U_E(h)$ and van der Waals attractions $U_{vdW}(h)$ continually sway between dominance, impacting the stability and behavior of colloids.[47] [83] [24]

The context of the initial theory was done upon lyophobic colloids, which is to say a colloidal suspension of particles in a medium that does not precipitate. Particles are prevented from merging (coalescence) and separating via repulsive forces present between one another, and as a result in an equilibrated state it is stable. This repulsion is produced due to the repulsive electrostatic forces described in 1.1.2, present due to the surface charges of the colloid. The attractive forces of the equation result from van der Waals forces present from the electron distribution of the atomic core, from the molecular surface of the colloid, described in 1.1.2.[69]

These two forces combine to produce a defining interaction potential:

$$U_{DLVO}(h) = U_{vdW}(h) + U_E(h) \quad (1.12)$$

This equation expresses the total interaction potential within DLVO theory, where $U_{\text{DLVO}}(h)$ is the sum of van der Waals and electrostatic forces at distance h . This interplay can be visually illustrated by 1.8.

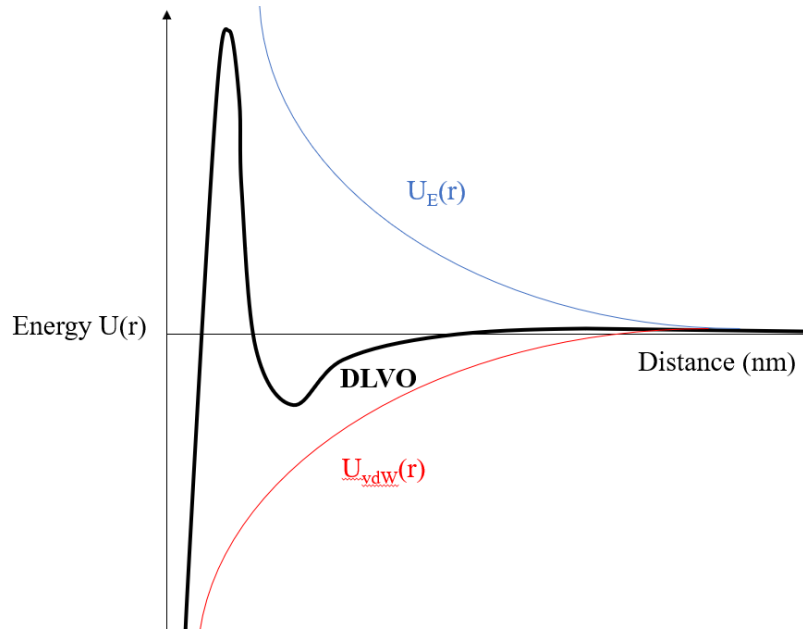


Figure 1.8 A graphical demonstration of the competing forces between colloidal particles. The electrostatic repulsion ($U_E(h)$) and the van der Waals attraction $U_{vdW}(h)$ combine together the sum interplay known as DLVO theory (bold line).

One key feature of DLVO is the repulsive barrier that is seen from the initial dip. This energy barrier prevents colloids from agglomerating. The van der Waals forces are generally attractive due to the nature of their interactions at longer ranges, giving rise to the initial dip, before the electrostatic repulsion dominates, producing said barrier. However, after this energy barrier is broken, the attraction descends to infinity, demonstrating a very strong attraction. If this barrier is substantial enough to offset the kinetic energy from Brownian motion, colloidal stability is achieved. In the absence of sufficient repulsion, particles may overcome this barrier, leading to aggregation.

While DLVO has proven itself a functional and applicable model for the description of interacting colloids, there remains a few assumptions that can limit its accuracy. DLVO assumes that the interacting surfaces is perfectly flat, expanding in all directions, and that the surface charge density is uniformly distributed along said surface. Additionally, it assumes that the surface electric potential is constant, and that any counter ions remain static and uniformly distributed too, with any interactions between said ions or solvent being purely born from their dielectric constant. While some of these assumptions aren't true for particle-particle interactions, DLVO holds up as one of the main theories for predicting interactions. [23] [87] [55] [76] [68]

This assumes that the interacting objects are flat planes, and not spherical

objects. In order to apply this theory to spherical colloids their geometry has to be considered. To this effect the Derjaguin approximation is used to approximate the DLVO force between differing geometries. This approximation adapts DLVO principles to spherical geometries, allowing for a more accurate representation of force interactions in many real-world colloidal systems.

Derjaguin approximation

The Derjaguin approximation is a useful approximation in colloidal science, particularly for calculating the interaction forces between particles with non-linear geometries. It simplifies the complex interactions in colloidal systems to a more manageable form, particularly useful when dealing with spherical particles or sphere-plane interactions.

In the Derjaguin approximation, The force F experienced by two interacting spherical colloidal particles is given by the free energy (W) of two plates per unit area with respect to the distance between the two (h). This relationship is expressed as:

$$F(h) = 2\pi R_{eff} W(h) \quad (1.13)$$

$W(h)$ represents the interaction energy per unit area between two surfaces as a function of their separation distance h , R_{eff} is the effective radius calculated using the radii of the two particles, given by:

$$R_{eff} = \frac{R_1 R_2}{R_1 + R_2} \quad (1.14)$$

Where R_1 and R_2 are the radii of the two interacting particles. In systems where the radius is homogeneous R_{eff} can be modified to $\frac{r}{2}$. For a system with a sphere and a plane, R_{eff} can be altered to simply equal R .

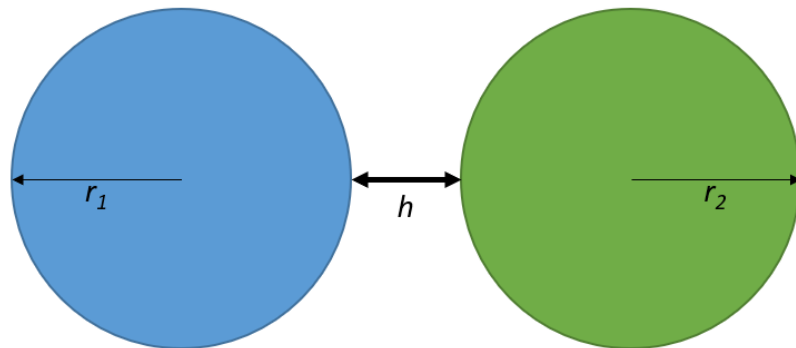


Figure 1.9 A graphical representation of h .

The Derjaguin approximation is most effective when the interacting surfaces are significantly curved, and the size of the particles is large relative to the interaction

range of the forces. This approximation simplifies the complex geometry of interacting curved surfaces by treating them as a series of infinitesimal parallel planes, making it more approachable for understanding and predicting the forces at play in colloidal interactions. This method is particularly useful when direct calculations of forces between complex geometries are challenging, as it leverages the geometry of the interacting bodies to estimate the interaction forces rather than directly comparing magnitudes of forces and distances.

[1] [83] [62] [52][19]

Limitations of DLVO Theory

DLVO theory provides our current understanding of particle interactions. However, as research in this field has progressed, the need for theoretical refinements has become increasingly apparent. The theory while robust in its basic form fails to account for several complex behaviors observed in colloidal systems, highlighting the necessity for a more comprehensive approach.

Despite its wide applicability DLVO theory has several limitations. It assumes that particle interactions are predominantly governed by electrostatic and van der Waals forces, overlooking other potential influences such as steric, hydration, and specific ion effects. Additionally the theory relies on idealized conditions, like perfectly smooth and homogeneously charged surfaces, which often diverges from the reality of more complex and heterogeneous colloidal systems. These limitations become particularly evident when considering dynamic colloidal interactions, as opposed to the static view provided by DLVO.

A key area where DLVO theory's limitations are pronounced is in the reversibility of particle contacts. Contrary to the theory's predictions of irreversible aggregation upon overcoming the energy barrier, experimental evidence often demonstrates that colloidal particles can separate after coming into contact. [11] This phenomenon is starkly evident in graphical representations of interaction forces, where the expected permanent adhesion does not always materialize.

Reversibility of Particle Contacts

Several theories have been proposed to explain the reversible nature of particle contacts:

Non uniform surface profiles: Colloidal particles are rarely homogenous. Surface irregularities, varying in chemical composition, charge, and surface roughnesses can lead to non-uniform adhesive forces. These heterogeneities can create scenarios where the calculated interaction is not accurate at certain surface points.

Dynamic Interactions and Brownian Motion: The perpetual motion of particles due to Brownian motion introduces dynamic forces, which can occasionally counteract the adhesive forces. Post-collision, this kinetic energy can facilitate the separation of particles, especially if adhesive forces are not overwhelmingly dominant.

Hydration and Steric Forces: In aqueous colloids, hydration forces, attributed to water molecules associated with particle surfaces, can induce repulsion at close distances. Similarly, steric forces from adsorbed polymers or surfactants can act as a buffer, reducing effective adhesion and enabling separation.

Electrostatic Repulsion and Ionic Strength Variations: The assumption of constant ionic strength in DLVO theory often doesn't hold in real systems. Fluctuations in ionic strength can alter electrostatic forces, potentially leading to a post-collision reduction in attraction and subsequent particle separation.

AFM provides a direct and precise way to measure the forces between colloidal particles and would provide valuable experimental data into how these surfaces come into contact, thus elucidating the true nature of this limitation. By examining AFM force curves the interplay of forces at play can be physically realised, contributing to our understanding of particle interactions beyond the scope of DLVO theory. This thought acts as the foundation for the main focus of this thesis, which is the investigation of colloidal interactions through AFM force curves. [26] [6] [47]

1.3 Dynamic forces

1.3.1 Hydrodynamic Interactions

In contrast to the thermodynamically driven forces discussed earlier, which are prevalent in systems under no external force, hydrodynamic interactions become significant when an external force induces movement within the colloidal system. This applied force generates local movement, propagating through the system via hydrodynamic effects. As particles move within a fluid, they create a flow in their wake that exerts forces on nearby particles and the container's walls.

Assuming conditions of linear flow and a constant velocity v_0 , the hydrodynamic force exerted on each particle can be quantified. This force, known as Stokes drag, is especially relevant when particles are sufficiently spaced apart, allowing for the assumption that interparticle hydrodynamic effects are negligible. The Stokes drag on a single particle is given by:

$$F_H = 6\pi\eta Rv_0 \quad (1.15)$$

Where, η represents the viscosity of the fluid, and R is the radius of the colloidal particle. This force known as Stokes drag assumes that particles are sufficiently spaced apart to negate interparticle hydrodynamic effects is valid under solution conditions of low Reynolds number and with spherical particles.[64]

Hydrodynamic interactions highlights the complexity of colloidal behavior, particularly when external forces are in play outside of the realm of DLVO. It highlights the need for a multifaceted consideration to understanding colloidal systems, beyond the descriptions of purely thermodynamic or static interaction

models.

1.3.2 Steric Forces

Steric hindrance plays an additional role in the stability and behavior of colloidal systems. It refers to the physical prevention of close contact between colloids, either due to polymeric brushes, large molecules on the particle surface, large molecules within the medium or surface roughness. These elements act as barriers, maintaining a distance between particles and thus preserving the stability of the colloid.

In colloidal suspensions steric hindrance often arises from polymers grafted onto the surface of particles forming what are commonly referred to as 'polymer brushes'. These brushes extend outwards from the particle surface reducing the system's free energy. This process results in a loss of entropy as the freedom of movement of colloids is restricted by the physical presence of the brushes. This entropy loss leads to an increase in the free energy of the system, encouraging colloids to move away from each other. Additionally, molecules and particles upon the surface can physically prevent movement of particles towards each other, preventing the distance between particles from reaching 0.

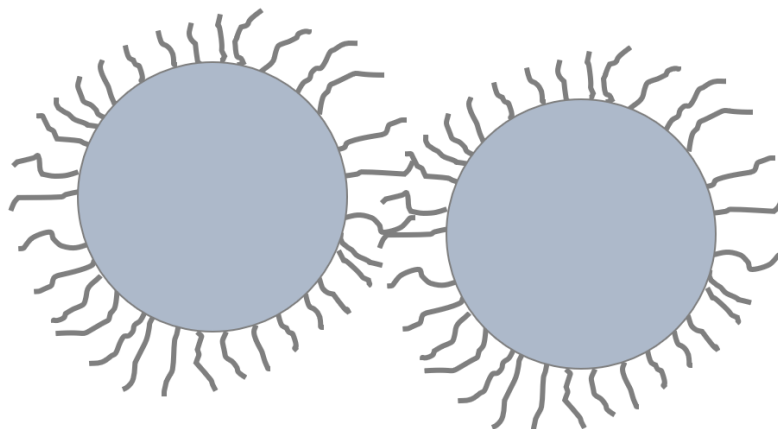


Figure 1.10 *Polymeric brushes on the surface of colloidal particles create steric hindrance, preventing close contact with neighboring particles.*

These molecular-scale interactions accumulate to define the distance-force relationship between particles in colloidal systems. As the perspective expands from individual particle interactions to larger-scale multi-colloid systems the principles of rheology become increasingly relevant. However, the effects of the microscale lead to the effects seen on the macroscale interactions and as such is critical in understanding the comprehensive behavior of colloidal suspensions. [61]

1.4 Bulk interactions and properties

1.4.1 Rheology

Rheology, the study of flow and deformation in materials, is the standard way of examining colloidal systems at the bulk level. In such systems, the clarity of individual particle interactions becomes obscured due to the multitude of forces acting in various directions. These forces, including van der Waals, electrostatic, and steric interactions, govern the dynamics of particles in the colloidal suspension and consequently shape their bulk properties. Rheological techniques, both experimental and through simulations, provide insights into how these individual behaviors accumulate into rheological properties. Oobleck, a well known non-newtonian solution, displays shear thickening properties under shear stress, born from the interplay of forces between the colloidal nature of the solution.

1.4.2 Non-Newtonian Fluids

Colloidal particle suspensions often form non-Newtonian fluids. Unlike Newtonian fluids, their behaviors do not conform to Newton's law of viscosity. Instead, their properties arise from the interplay between the particles and the suspending medium. These fluids exhibit intriguing behaviors, such as shear thinning and thickening, which can be attributed to the complex interactions at the particle level.[22]

Non-Newtonian behavior in colloidal suspensions arises from the complex interplay of these intermolecular forces. For example, in shear thinning, the alignment or structural rearrangement of particles under shear stress reduces internal resistance, a phenomenon deeply rooted in the balance of attractive and repulsive forces at the molecular level.[22]

1.4.3 Shear Thinning and Thickening

Shear thickening in colloidal suspensions occurs when an increase in shear force leads to an increase in viscosity. Shear thinning consequently is when the same suspension decreases it's viscosity from shear forces. While it may be intuitive to expect that the effects draw from the same mechanical interaction, it has yet to be proven. The current theory is that shear thinning derives from small structural changes in the suspended system. The decrease in viscosity seen in shear thinning emulsions under shear stress can be attributed to the reorientation of particles from reducing the effective area of intermolecular resistance. This reorientation is facilitated by the delicate balance of forces acting at the nanoscale.

Shear thickening presents a more complex scenario. The addition of salt to a colloidal suspension can suppress electrostatic repulsion between particles, a factor that can significantly influence the transition from shear thinning to thickening. By reducing electrostatic repulsion, salt can promote closer

particle interactions, leading to hydroclustering under high shear, resulting in increased viscosity. Where particles form temporary immobilized clusters under compression, and order-to-disorder transitions, where applied forces disrupt the structured flow of particles, increasing viscosity. [12, 30]

1.4.4 Lubrication Forces

This layer is thought to prevent physical contact, and thus frictional forces, between two interacting colloids. From this postulation, the infinite force at contact problem is solved, as the colloids never come into contact, instead separated by the viscous, lubricating layer between them during flocculation.

Lubrication forces are thought to be the dominant force regarding inter-colloidal interactions, causing their observed behaviour and structure (for systems with a high colloidal concentration). These forces arise from thin lubricating layers between particles, preventing direct contact and thus reducing friction. These layers, influenced by van der Waals and electrostatic forces, prevent direct particle contact, facilitating movement and contributing to the unique rheological properties of the suspension. This mechanism potentially resolves the infinite force at $h = 0$ issue in theoretical models, as particles never physically touch but are separated by the lubricating layer. Such forces allow particles to disperse once the applied shear force is removed causing the characteristic shift in viscosity. [47]

This theory assumes spherical particles, which may not always be the case in real systems.

1.4.5 Simple Viscous Drag in Colloidal Systems

Simple viscous drag is a critical aspect of hydrodynamic interactions in colloidal systems. This drag arises from the resistance experienced by colloidal particles as they move through a fluid, heavily influenced by the fluid's viscosity and the particle's velocity. It, along with hydrodynamic forces mentioned before, draws from fluid dynamics, and influences particle movement. With one focusing on individual particle behaviour, and the current focusing on bulk effects. Viscous drag is always in the direction opposite to the motion of the particle, whereas other hydrodynamic forces might have different directions based on flow patterns and particle shape.

This relationship assumes low Reynolds number conditions, where the flow of fluid around the particle is laminar and the effects of inertia are negligible compared to viscous forces.

1.4.6 Rheology of suspended colloidal particles

As you scale up the viscosity of a liquid and start applying these forces from the microscale to a collective sum on the macroscale you start to see interesting

behaviours arise from the inter-molecular forces.

While Rheology relies on deriving its understanding of such systems from a macroscopic lens, simulations take the current theory underpinning current scientific understanding to build up a theoretical landscape imitating reality. This *in silico* landscape often relies on equations used to simulate particle-particle interactions across all of the simulation. Simulations work by drawing a defined box with either periodic or constrained boundary conditions, in two or three dimensions, where each particle's sum force is calculated based upon the other particles within the box. Then, afterwards, the frame of reference is shifted forwards a certain amount of time, with the particle's positions moved based upon the last frame's force. This tick happens over and over, with the total time and accuracy dependent on the delta timestep.[31]

As a result it is important to experimentally verify the results of simulations as the limits of mathematical models can influence the results. As such it is a powerful visualising tool to express how a system is functioning, however, as such it is imperative that the equations used to power this simulation are accurate.

Experimental verification of these simulations is important, as current models have discussed limitations. Therefore, an experimentalists can contribute to simulations indirectly by verifying and probing the interface of colloids, both in terms of physicality, by directly probing with a cantilever, and probing the interface of theory, by exploring the unknowns of said system. [22, 25]

1.5 Considering reality

Whenever considering a mathematical model of reality it is always worth testing it against an assumed case to see whether or not it would hold up. One such case is understanding how single-particle interactions can scale to influence multi-particle interactions within a system. This concept is particularly important in colloidal rheology, where the collective behavior of particles under shear stress determines the materials macroscopic properties.

1.5.1 Attaching spherical putty to the ceiling

Consider the common experience of sticking spherical Blu Tack to a ceiling. This everyday occurrence is a testament to the complex interplay of forces that operate at the microscale. When Blu-Tack is pressed against a ceiling, the viscoelastic properties of the material allow it to deform and maximize the contact area, enhancing adhesion. This interaction is governed by van der Waals forces at the surface, a form of single-particle interaction.

However, in a colloidal suspension, similar single-particle forces, such as van der Waals attraction and electrostatic repulsion, are at play. When many such particles are present, these forces collectively influence the suspension's rheological properties, such as shear thinning and thickening. For instance,

in shear thickening systems, as shear stress increases, particles may form hydroclusterstemporary multi-particle assemblies where the collective behavior results in a noticeable increase in viscosity.

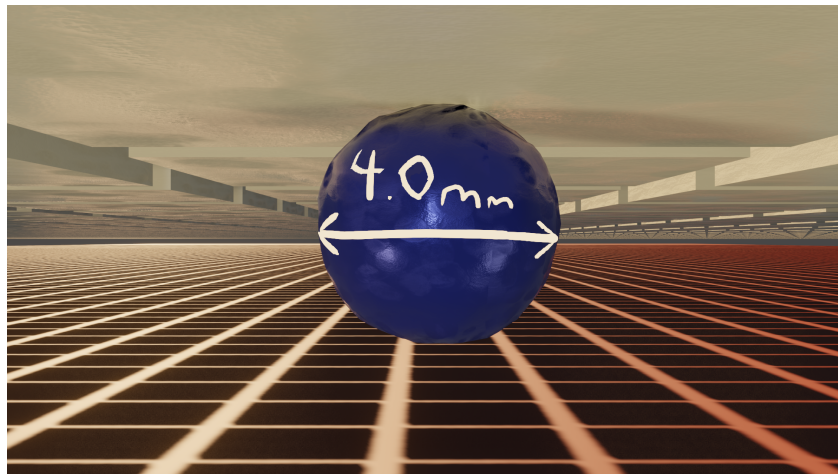


Figure 1.11 A diagram demonstrating a 2mm radius putty sphere attached to the ceiling.

This example serves as an analogy for how single-particle forces can scale in a suspension. Just as the Blu Tack conforms to surface irregularities to increase adhesion, particles in a suspension may aggregate or disperse based on similar forces, affecting the material's bulk properties. Thus, understanding single-particle interactions is a stepping stone to predicting and controlling multi-particle interactions, particularly in complex fluids and colloidal systems.

The ability of Blu Tack to adhere to the ceiling without falling off under its own weight suggests that the combined effects of its viscoelastic properties and surface conformability are crucial. These physical characteristics allow Blu Tack to maintain a firm grip on the ceiling, defying gravity and providing an excellent example of adhesion that goes beyond the scope of classical models. This observation encourages us to consider additional factors such as the material's properties and surface topography in our understanding of colloidal and surface interactions.

Through this practical lens, we see the value of questioning and expanding upon established theories like DLVO. It is through the curiosity-driven inquiry into such everyday phenomena that we can deepen our understanding of the fundamental principles governing material adhesion and surface interactions.

Chapter 2

Atomic force microscopy

2.1 Introduction

The origins of microscopy are believed to date back to the thirteenth century, stemming from the development of eyeglasses and spectacles. The first practical microscope, which utilized the visible spectrum to image samples through photonic light, evolved over centuries into what is known today as the light optical microscope. However as the optical microscopy design improved, it eventually hit a major limitation - the diffraction limit of photons. New techniques and designs were created using methods to overcome this limitation, circumventing the limitations of photons. These novel methods expanded the scope of microscopy beyond its initial reliance on emissions from the visible spectrum. Some such examples include phase contrast microscopy, electron microscopy and local probe microscopy. While these techniques share a name and history, there are major practical differences between them.

Local probe microscopy particularly differentiates itself from other microscopy techniques as it does not rely on a trans-migratory radiation particular source to convey information on the exposed sample. Instead, an image is generated by physically probing the surface with a specialized tip, wherein the tip's physical location becomes the key means of conveying information about the sample. This is in contrast to various microscopy techniques, which generally use some form of radiation to interact with a sample. The differences between these two results in different data structures for each respective technique. [33]

The first progenitor of the probing microscopy family was invented in 1981, then known as the scanning tunneling microscope (STM). The defining feature of all the probing microscopes is their ability to map topology of a sample by tracing a probe over the surface of a sample. In STM, the probe's location is tracked by passing a current through the probe and down into the surface. When the conductive probe is brought within 1 nm of the surface it allows electrons to "tunnel" to the surface from the probe. The recorded current between the two elements decreases exponentially with distance, giving a measurement of distance

between the two interacting elements as well.

Atomic force microscopy (AFM) is based on the force between the tip and the sample and tracks the physical location of the probe tip via a reflected laser. This enables the analysis of both non-conducting samples and samples that need to be in liquids. It is this versatility and adaptability that AFM allows that gives it one of its greatest strengths. The method is novel compared to conventional microscopy techniques as it does not rely on lenses for observation; instead the position of the stylus is detected by a laser reflecting off the surface of the cantilever. Equally, issues of absorbance or transparency are negated, as the results are of a physical contact nature. By probing the surface of a specimen the surface characteristics can be observed, such as the hardness or elasticity of a sample, all while remaining a relatively non-destructive method of imaging. AFM can be specialised further with specific tips or attaching specific molecules to detect surface chemistry, adhesion or arrangement of ions on a surface[28].

As a result of these phenomena, AFM stands out when compared to light microscopy. Its intrinsic ability to resolve images at nanometer length scales, overcoming the optical diffraction limit of standard microscopy techniques, means that it is one of the best methods to view and interact with samples non destructively. Since AFM's resolving power is limited by the radius of the tip, different tips can be used depending on the application such as nanometer sharp tips to resolve on the atomic scale, tips with a specialised surface chemistry or tips for use in liquid conditions. A further strength is the ability to image specimens under different conditions; within air, water, or especially in the case of biological samples; within buffers to reduce the adverse effects of observing samples. [42].

Another benefit that AFM provides to its operator is the ability to measure small forces acting between the tip and the probed surface. This interaction is particularly useful in measuring single particle interactions, and is one of the major methods used in this thesis described below.

With all these benefits there comes a cost. There is a large amount of interplay between each of the different forces, geometries and mechanisms; meaning that interpretation of recorded data is usually more complicated compared to an image produced by light microscopy. As a result, there is an art to AFM that every operator has to learn and master in order to gain meaningful data. Furthermore, it is on the operator to prove that their interpretation is accurate and avoid some of the common pitfalls in using the technique.

2.2 Basic overview of AFM operation

In order to describe in detail the methods used in this thesis for data collection, a basic understanding of how AFMs work must be understood. While some AFMs differ in design and implementation, they all rely on largely the same fundamental design and principles.

All local probe microscopes rely on the same mechanism, the information gathered

from a sample comes from an interacting probe. Consider the example of a blindfolded person using a cane to map out the surface in front of them: the map they put together in their mind would represent the topology of the space around them. AFM works in largely the same way, but in place of a mind is a computer, and the cane itself is a much smaller cantilever. Instead of the surface being felt out by hand it instead uses a few sensors to determine the sample's properties. While the range of output variables is relatively small compared to other methods, these can be greatly expanded upon by transforming this information to give properties such as elasticity, attractive and repulsive forces and more. This interaction is then processed across the sample window, giving a map of different information with respect to lateral position.

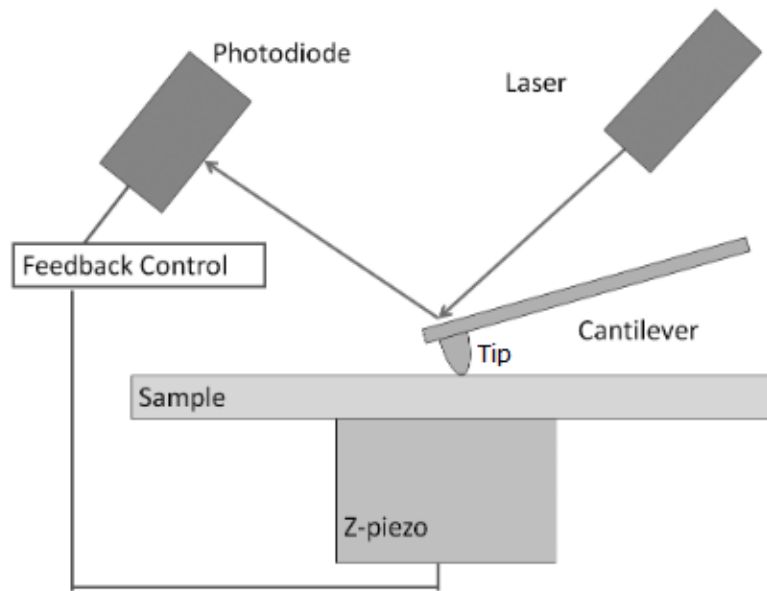


Figure 2.1 A basic schematic of an set up AFM. Image adapted from [86].

The general schematic of an AFM is shown above (figure 2.1). The only directly interacting point upon the sample is the tip (which is mounted on a cantilever), keeping the interaction between the sample and mechanism to a minimum. A laser is emitted and aligned to the head of the cantilever above the tip. This laser is then reflected off the back side of the cantilever into a photodiode which converts input light into an output electrical signal. Initially the laser is set up to reflect into the origin position (the center) of the photo diode. This ensures that it has the maximum amount of room to translate across the surface as the cantilever deflects. As the tip is brought into contact with the surface the cantilever bends and relaxes as it processes over the sample. These translations alter the reflected angle off the cantilever, depending on the underlying sample surface topography. This reflected light then changes the positioning of the detected light on the photodiode, translating its x, y component relative to the alterations of the cantilever. The cantilever itself is moved across the surface by a piezoelectric motor with a high degree of precision. In some implementations, the piezo is

singularly used to control the height position (z axis) of either the stage, or the tip. However, particularly in imaging mode AFMs, the piezo can additionally accommodate lateral and horizontal (x and y axes) movement. Generally, an emphasis on accuracy is placed on z-axis sensitivity (with most AFMs citing the operational error on the z-axis to be within the order of magnitude of an Ångstrom, whereas the x/y-axis component error is within a nanometer). From this basis, the accuracy of the piezo controller may be one of the more important capabilities of any AFM, as all data and features fundamentally rely on fine position control and piezovoltage output readings. The piezo controller fundamentally controls the rate in which the AFM can operate as well.

The feedback mechanism from these position controls relies on a laser reflected off the back of the cantilever. To aid this effect, the back of the cantilever is coated in a reflected material, such as gold or antimony. As the laser is reflected off and detected using the photodiode the changes from origin are measured and fed into the feedback control system. It is this feedback mechanism that directs the piezo's movements in the next cycle, as it controls the force applied on the surface. Generally during imaging the force applied is set to a specific magnitude, with the controller aiming to keep that constant across the whole operation. Movement across a whole dataset can vary depending on the type of operation being performed - such as imaging recording across a 2d area, and force profiling recording across a single x, y point in sample space.

Additionally, the cantilevers themselves have a wide range of options in terms of their properties. The spring constant, the length of the cantilever, geometry, tip shape, surface chemistry and more are some of the options that a operator has to consider. In some cases, the chip that the cantilever is attached to has multiple different cantilevers off the end of it, allowing a range of cantilever parameters, either to determine the best one for the case, or for probing a range of conditions. The spring constant and the length of the cantilever is used to control the cantilever's sensitivity to smaller forces (as force will bend a softer cantilever more than a hard one), or for probing surfaces. The geometry of the cantilever can be used to control for any rotation or lateral bending the cantilever may be subjected to, or for use in cases where a specific shape is needed. For example, a V shaped cantilever prevents any flexing or bending laterally.

Tip shape is also another consideration for operators as it can influence the output data. If a tip is unable to physically reach a portion of the sample due to steric interference then that portion of the sample is measured as an imprint of the tip's surface. Figure 2.2 shows an example of two tip types interacting with a pit on a sample. The circular one is unable to enter the pit fully, giving a circular artifact equal to its imprinted geometry instead, whereas the triangular one probes the depths fully, giving the correct output impression. These sorts of gaps can also influence the forces felt by a tip as it interacts with it, as a "gap" of sample will not provide the expected sum of interactions.

As this tip is brought into contact with the surface it is subjected to various forces. As an example the total force applied to the cantilever is a combination of van-der-Waals attractions and electrostatic repulsion as described in chapter

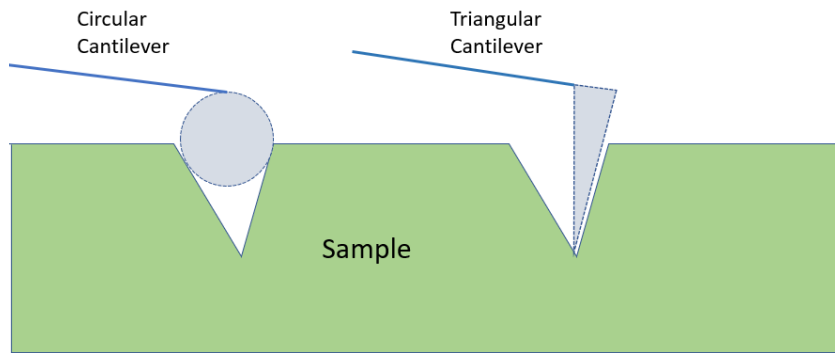


Figure 2.2 Above is shown the potential difference between tip shapes and types - where the tip with a circular geometry on the end is unable to enter fully into the crevasse on the sample, the thinner triangular one is. This will be reflected on the output data.

1. The resultant force scales with the separation distance of the tip from the surface, h . When the tip is in direct contact with the surface, the elasticity of a surface can be directly probed. When the tip is physically in contact with the sample, piezo movement into the surface is directly translated into bending as the cantilever is forced away. This process can also be used to determine the elasticity of surfaces by intentionally pressing the tip into a surface.

For the majority of AFMs in use today, the raw unprocessed data given by a machine boils down to the piezo extension and position of the reflected laser on the photodiode, as well as the piezo's z positional height, which is tied to its total operational range. This data is fed into the feedback control loop in order to adjust the tip's position to stay within operational parameters. This process is tied to the software's main cycle loop time, which occurs faster than the operator can respond to it - on the order of milliseconds, or even less. The operator instead of having a direct involvement in the cantilevers positioning and control instead sets boundaries for a range of variables depending on the operation type, but in general the speed, the force applied to the surface and the operational window (the start distance to intended end distance).

From these parameters, the cantilever is controlled in a feedback loop. First a reference signal is generated and cross referenced against the cantilever deflection. From this the gain is tweaked to attempt to apply a constant force to the tip across measurements (known as the setpoint).

From this loop, the tip position and the cantilever deflection is recorded. This loop helps to ensure that a constant force is applied to the tip, to reduce tip and sample damage as well as the reduction of errors in the system, as AFMs usually operate at a rate faster than human control. [32][2]

Using this loop the tip can then be exposed to various ranges, with corresponding forces acting upon it. These ranges are used to define various modes of operation such as: contact mode; where the tip comes into full contact with the surface, tapping mode; where the tip only lightly grazes the surface and non contact

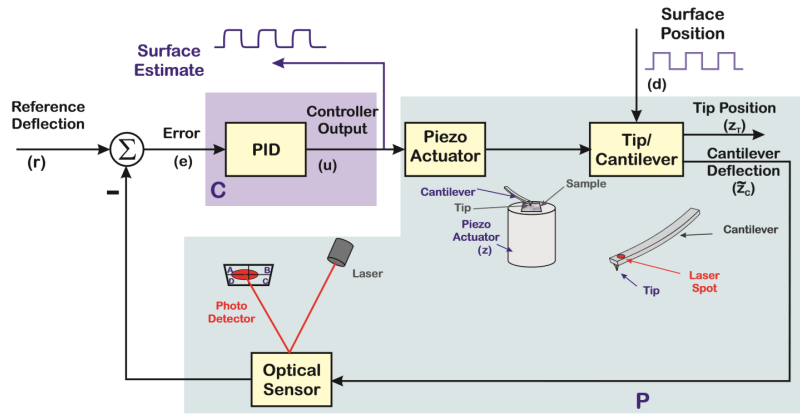


Figure 2.3 A diagram demonstrating the basic feedback loop control for an AFM. In this case an example for an AFM operating in imaging scanning mode is shown, which is elaborated in the next section. Image adapted from [2]

mode; where the tip is only affected by the long range forces. As you move the tip further away from the surface the force applied on the surface is reduced, which is particularly useful for softer samples. For force curves however, the force measured is generally across the spectrum. [32][2]

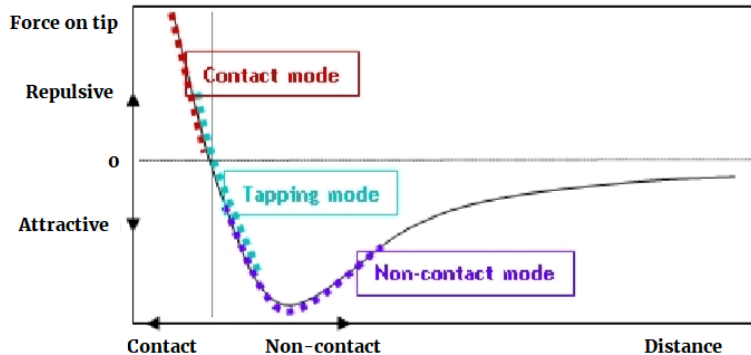


Figure 2.4 A Van-der-Waals potential with corresponding regions imposed over the curve to demonstrate the ranges each of the modes have in relation to the forces applied to the cantilever. Image adapted from [32].

For the non-contact modes the probe is set to oscillate at the resonance frequency of the cantilever. When the tip comes close enough to the sample to be affected by the surface forces it causes a dampening of the oscillation, resulting in a phase shift. Using this method, the speed and accuracy of mapping is improved. Tapping mode is similar, except that the nadir of the oscillation is brought into contact with the sample.

From these methods and mechanisms AFM has branched out into performing a

range of functions, the two most common being imaging and force profiling which rely on this tip-surface interaction to generate the surface and interaction profiles of samples respectively.

2.3 Tip Calibration

Tuning a cantilever for use under imaging mode is generally one of the simplest methods of calibrating an AFM. By sweeping a cantilever over a range of drive frequencies a maximum peak of cantilever amplitude can be found. From this the resonance frequency is assumed. However issues can arise when calibrating a tip for use under liquid as the viscous drag of the liquid dampens the oscillations of the cantilever. As a result non contact methods are generally not applicable for imaging samples under a solution and rely on contact methods.

In general however, for cantilevers used in air the thermal noise spectra can be mapped to a simple harmonic oscillator, with a noise floor added to compensate for the baseline noise found in the system. This relies on the cantilever being longer than it is wide, and the quality factor being greater than the sum of the oscillation. The power spectral density $PSD(\omega)$ as a function of angular frequency is a function that describes how the power of a signal or time series is distributed with respect to frequency.

The $PSD(\omega)$ is used to analyze the cantilever's thermal noise spectrum. The cantilever, when not being externally driven, will still oscillate due to thermal energy (Brownian motion). These thermal oscillations create a noise spectrum that can be analyzed to extract useful information about the cantilever, such as its resonant frequency and quality factor.

the $PSD(\omega)$ is given by:

$$PSD(\omega) = A_{white} + \frac{A_0\omega^4}{(\omega^2 - \omega_r^2)^2 + \frac{\omega^2\omega_r^2}{Q^2}} \quad (2.1)$$

where ω is the Angular frequency, ω_r is the resonant angular frequency of the cantilever, A is the Peak amplitude of oscillation, A_0 is a scaling factor for the peak amplitude, A_{white} is the noise floor, a constant representing the baseline PSD, and Q is the ratio of energy stored to energy dissipated in one cycle. The quality factor is a dimensionless term which correlates to how underdamped said oscillation is - i.e. it is the loss of energy across one oscillation period.

Generally for imaging mode AFM the thermal tune method of calibration for cantilevers is adequate. One of the major benefits to this method is how it is non damaging to the tip and relies on the thermal energy driving the oscillation of the tip itself in air. From this the spring constant of the cantilever can be detected by using the equipartition theorem which relates the thermal energy of a cantilever to it's spring constant. The output value is then generally sanity checked by cross referencing with the manufacturer's ranges, or in the case of a

cantilever created by the operator themselves, a more in depth calibration may be used. Calibration can also be used as a rudimentary method to detect damage to the tip during processing - as degradation of the tip will alter the oscillation of the cantilever leading to results outside of expectations.

The spring constant of the cantilever is calculated using:

$$\frac{1}{2}k_B T = \frac{1}{2}kx^2 \quad (2.2)$$

Which can be simplified to:

$$k = \frac{k_B T}{\langle x^2 \rangle} \quad (2.3)$$

where k_B is Boltzmann's constant ($1.38064852 \cdot 10^{-23} \text{ m}^2 \text{ kg s}^{-2} \text{ K}^{-1}$) and T is temperature in Kelvin. x^2 is distance in respect to the power spectral density (PSD), which is fit to the simple harmonic oscillator mentioned above. [18, 58]

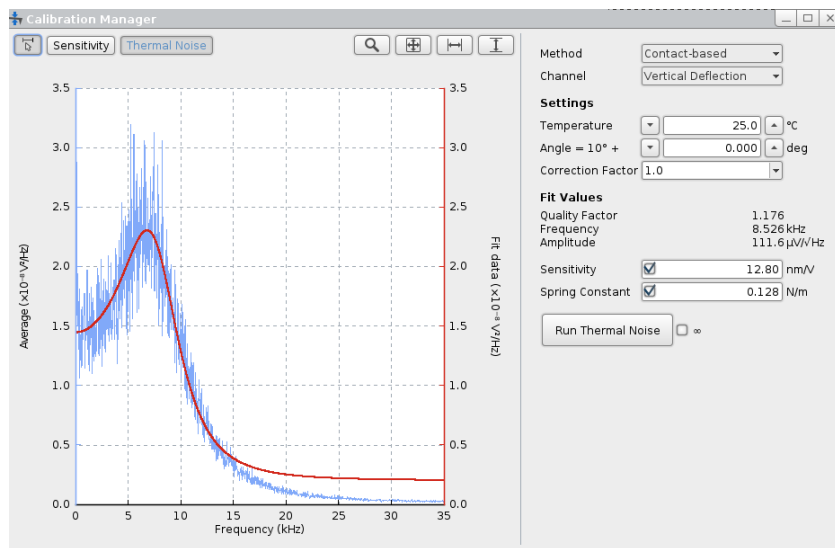


Figure 2.5 An example of a thermal tuning calibration software interface. The blue line is the raw signal from the AFM and the red line is the fit over that data. The operation itself is automatic, requiring the user to only press the run thermal noise button for the spring constant to be given.

After the laser has been aligned the system can detect changes in the cantilever, in particular bending. However, for this bending to be converted into force applied to the cantilever and/or surface, the system itself must be able to translate bending into force. Unlike imaging mode where the peak resonance is the main factor in determining a good calibration, the force instead relies more on a spring constant coupled with the inverse optical lever sensitivity (InvOLS). This is due to the force being calculated, rather than imaging producing a height map based off the

cantilever deflection. In the case of force;

$$F = kz \quad (2.4)$$

where k is the spring constant of the cantilever and z is the cantilever deflection. The cantilever deflection is in turn calculated using:

$$z = InvOLS\Delta V \quad (2.5)$$

Where $InvOLS$ is the Inverse optical lever sensitivity (m/V), and ΔV is the change in the voltage measured by the photodiode. ΔV is given as a raw value from the machine.

$InvOLS$ is dependant on a range of different factors such as spot size, position, cantilever length and electronic gains in the system, however this calculation can be bypassed by taking the slope of the curve on a hard surface, then finding the difference needed to convert said slope to be equal to one (Figure 2.6).

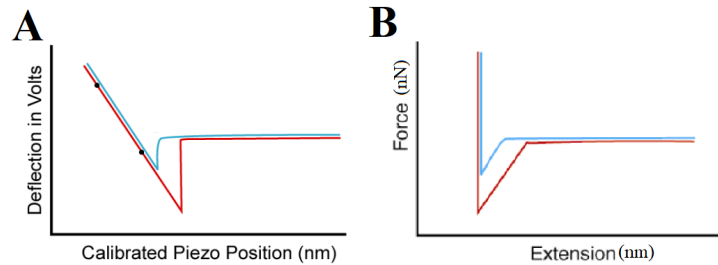


Figure 2.6 A diagram demonstrating the translation of $InvOLS$ to force, A demonstrates the raw data plotted, B demonstrates the data adjusted with $InvOLS$ into a force. Adapted from [60]

Both of these methods assume that cantilevers are motionless, or do not contribute any motion to the input motions dictated by the piezo controllers. In reality this is not the case, as cantilevers are always moving. Even a baseline measurement of lever deflection will deviate by 2 nm in vacuums, air and water by thermal noise.[60] [9, 46]

2.4 Common artifacts in AFM

One of the greatest strengths of AFM can quickly turn into a double edged sword in the wrong hands. Due to how the AFM physically interacts with the surface this means there is a lot more potential for unexpected interaction and unique artifacts when compared with traditional microscopy. Over the history of use of AFM certain recurring artifacts have been identified and recognised. These sources of artifacts in AFM generally come from either the tip, the scanner, vibrations, the feedback circuit, and the image processing software.

2.4.1 The tip

The geometry of the tip is an important factor in AFM sample preparation and experimental design. This was briefly touched on earlier in figure 2.2. However there are further aspects to the geometry that can influence the results. These examples include when the tip itself is either damaged, contaminated or when the tip is dulled from excessive use. A damaged tip will cause an artificial shape up on the surface of the image as seen in figure 2.7.

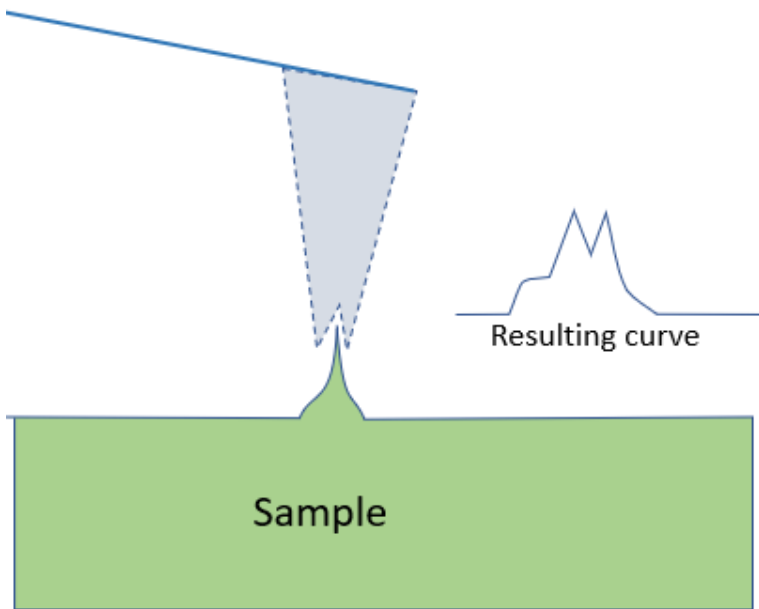


Figure 2.7 As the damaged tip interacts with a sample surface an artificial lump is measured by the cantilever in scanning mode. This is due to the double prong defect in the probe head limiting the range of movement, incorrectly reporting a secondary feature.

Contaminated tips equally will affect results, but in an irregular way - as contaminants can be gained or lost during an operation. Whilst on a tip they alter the interacting geometry and chemistry of a probe. Additionally, these contaminants can change the surface profile of the sample, leading to inaccurate measurements. For example, if a sample was covered by a contaminant during force profiling, the resulting force curves would be altered by the contaminants interaction with the probe. Contaminants are generally very difficult to remove and usually require some kind of cleaning procedure to remove, hence the use of clean rooms for some sensitive AFM operations.

A dull tip from overuse will decrease the sharpness and potentially the length of the tip - essentially widening its interaction profile. This causes the interacting surface area to widen as well as widening any topology measured by the system. As such it's standard practice to regularly use fresh tips.

Generally these sorts of artifacts provide a repetitive and unusual profile upon the surface, and can be checked by using multiple tips to profile the same sample. If

the results are consistent across tips then it's unlikely to contain artifacts created by the tip itself.

2.4.2 Scanner error

The source of scanner error fundamentally derives from the piezoelectric scanner's physical properties. A piezo electric scanner will increase in sensitivity from constant use, or will slowly depolarise and increase in sensitivity when left idle. As a result, piezo electric scanners require regular maintenance to compensate for these effects. In addition to this phenomenon the extension of a scanner in any direction is not linear with its driving signal, which affects all z and x, y movements. When a piezo electric scanner is not properly calibrated this is usually reflected in dimensional distortion in the data. These sorts of artifacts have a constant presence and adjustment to any data generated and as such mandate the proper maintenance of any AFM.

Correcting for these artifacts is either done by software or hardware and are usually not performed by the operator, instead handled by the manufacturer. Though nonlinearity effects are much less pronounced on the Z axis due to the reduced range of movement and these sort of effects only matter for very precise measurements when height profiling.

Hysteresis is also a consideration when AFMs are cyclically scanned across a profile - these can cause a lateral shift along a trace and retrace curve causing an asymmetric step height. In the same vein rows can have drift, though this is due to a disconnect between in time steps between voltage driving movements. This usually presents itself as a bending drift across rows shown in figure 2.8. Equally, this is why "zooming" into a scanned profile is difficult - these effects will displace the frame of reference by a certain offset when moving due to the change in cantilever scan velocity.

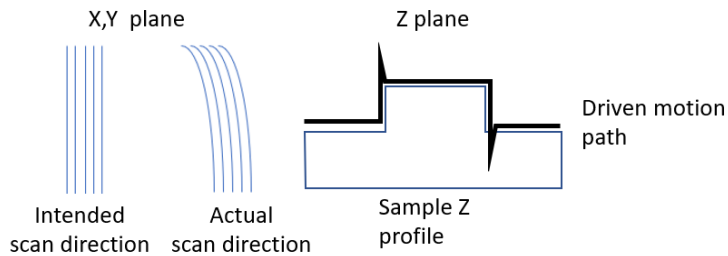


Figure 2.8 Creeping drift can occur across the motion of a scan. In the x, y direction this manifests as a bending motion, whereas in the z plane this can result in an overshoot of driven motion. In both cases the effects are exaggerated to convey the effects.

In some cases of AFMs there is a parabolic arc attached to the x and y axis component of the piezo movement, which will cause bowing in the resultant

image. Additionally, the sample itself cannot be atomically flat when inserted into the AFM. These two effects combine to cause an intrinsic tilt on the resultant image.

Finally thermal drift can cause changes in physical properties which will cause deviations from a thermally calibrated cantilever and the new properties. In the case of high resolution images small areas of thermal flux can cause issues, requiring the operator to wait until thermal equilibrium is reached.

The majority of these effects are dealt with either by hardware/software compensations outside of the standard use of AFM. During the data interpretation phase several mathematical transformations are performed on the data set to adjust for these effects.

2.4.3 Vibrations

Vibrations in the building, either due to foot traffic, wind, or even speech can cause physical displacements between the tip and sample. These vibrations can cause sudden shifts in the trace/retrace profile of a cantilever - leading to dramatic changes in the data. These are relatively easy to isolate as one time events however, and can be managed by operating the AFM in a quiet room with minimised background noise.

2.4.4 Incorrect user parameters and feedback errors

A large part of the AFM operation relies on the user to correctly set parameters during use. Generally these parameters are concluded during the operation to ensure that the output images are satisfactory. If incorrect parameters are set, then erroneous results can be easily produced. For example soft samples' profiles may be incorrectly compressed from a contact force too high, leading to a shorter than true height. As part of the feedback and correction mechanism relies on these input parameters the automatic corrections can further conflate errors in the resulting dataset.

For the majority of cases these artifacts are ironed out and compensated for over the course of sample familiarisation and as a result AFM tends to have a higher difficulty curve when compared to other microscopy techniques. Whereas other microscopy techniques will generally provide some sort of visual representation the sample imaging, improper use of AFM can result in phantasmagorical images without the appropriate care and consideration, leading to incorrect conclusions. [15]

2.5 Imaging mode AFM

Imaging mode focuses on using the AFM operation to measure the z-height of a sample across an x, y scan range. The positions are recorded in a three

dimensional array, with the distance between each x, y entry value being constant. The major operation is much the same as described above, with the requirement of a piezo controlling x, y movement as well as z movement. The surface of the sample is imaged across using a raster pattern. This raster motion attempts to keep the respective z height at a specific force/deflection value as it progresses along the surface. In the case of non contact or tapping methods the oscillation dampening effect is kept constant across each position. The resultant array is often converted mathematically into a height map to display the surface profile of the imaged sample.

Some AFM setups also provide other images during scanning; a phase image, an amplitude (or deflection) image and a friction image depending on the operational mode of the AFM. Generally two operational modes are available for the operator; contact and non-contact mode. Contact mode physically brings the tip in contact with the surface, then drags it across the surface. This is useful for measuring friction, reducing current effects on the tip in a liquid AFM situation and physically interacting with surface objects on the nanoscale. However this does have a shear force effect on the sample, and can damage particularly sensitive samples, such as biological material. Non-contact mode oscillates the cantilever above the surface, only allowing the tip to touch the surface gently at the nadir of the oscillation. By subtracting the input oscillation from the physical oscillation of the cantilever the phase can be determined. This indicates the softness of a surface, as harder surfaces dampen the movement to a greater degree, reducing the angle of the reflected laser.

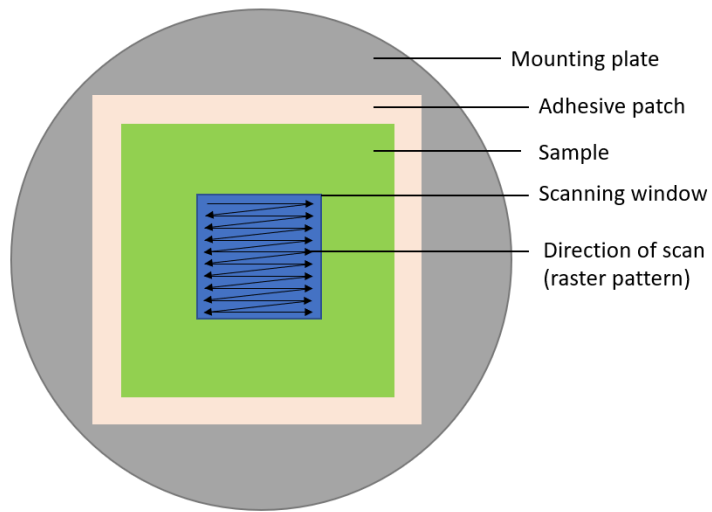


Figure 2.9 A diagram demonstrating the model setup for a sample. The geometry of each of the layers in the sample setup is an example in this case and can vary with application and requirements. The scanning window is non physical and is a projection of the area scanned by an AFM upon the surface of a sample.

During use the operator defines a field of view (aka the scanning window) - a range of coordinates that the AFM will take points of. This field of view is

then broken up into number of points per line, which defines the aforementioned distance between each data point.

The raw export data is generally saved as a file, either to be adjusted in software or externally. This final data export however isn't reflective of the surface profile yet however - as the geometry and the local angle of the surface will alter the resultant output array. To compensate for the drift in the AFM and for the angle of the surface below the cantilever probe a few mathematical transformations are generally applied.

2.5.1 Mathematical alignment and error correction of AFM images

The use of AFM has proliferated across the sciences due to its wide range of applications and data output. However in some cases the image produced is assumed to perfectly reflect the surface of the sample, when in reality there are a number of mathematical, physical and operational effects that can vastly affect the output image. Mathematical transformations are applied to the raw data via image processing. Physical errors can occur from the situations the tip is exposed to and the condition of the tip. Finally operational errors can occur from improper use. As a result it is important to consider where these transformations and errors can arise to ensure that the image produced from the machine is a reflection of the true surface of the sample.

A part of the image processing process is done to compensate for the unavoidable artifacts discussed in section 2.4. However this can be a source of error itself, as over reliance on multiple correction methods can introduce artificial profiles into the image. Other filters, such as a low pass filter can smooth out or remove sharper features in a data set. As such it is important for the operator to justify and consider any transformations upon the underlying data set.

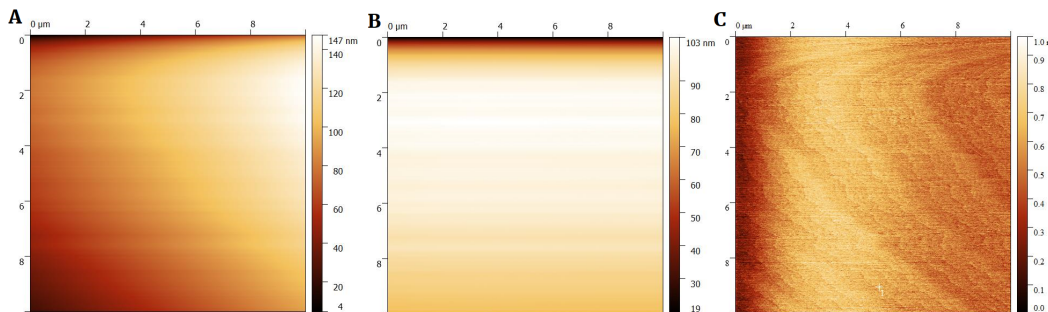


Figure 2.10 A figure demonstrating a standard mathematical operation applied to raw data. A demonstrates the array shown direct without any processing, B has had a mean field plane subtraction applied and C has had a row alignment applied to it. The image itself is of a freshly cleaved mica surface which is reflected in the final image C.

Mathematical operations are performed on all images as the data generated

does not account for the tilt of the surface, therefore a degree of mathematical transformation is required. Initially a heatmap of the the output will look similar to Figure 2.10. A mean field plane subtraction is used to determine the plane on which the data was generated, this is then removed across the dataset. This is to normalise the raw height data on a theoretical flat plane as an attempt to remove the tilt present on the sample stage. Next the rows of data are aligned by taking the representative height of each row and aligning each row to that height, this is done by several different methods, such as polynomial or median methods. As a result the features on the surface of a sample are kept intact, but it is possible that sharp differences observed on a row by row basis can be obfuscated due to image processing. The size of a pixel is dependant on the scan size (for example a $10\mu\text{m}$ by $10\mu\text{m}$ image with 512 data points per line means that each pixel is approximately worth 20 nm). Though, this does not represent the interacting surface area between the tip sample surface. In order to reduce errors like these and to resolve features that may be hidden by pixel weight larger scan sizes are often coupled with smaller scan sizes to give both the larger order topography with the smaller detail analysis. It is important for an user to not perform too much image processing without explanation and reasoning as each additional correction can be a further abstraction from the truth.

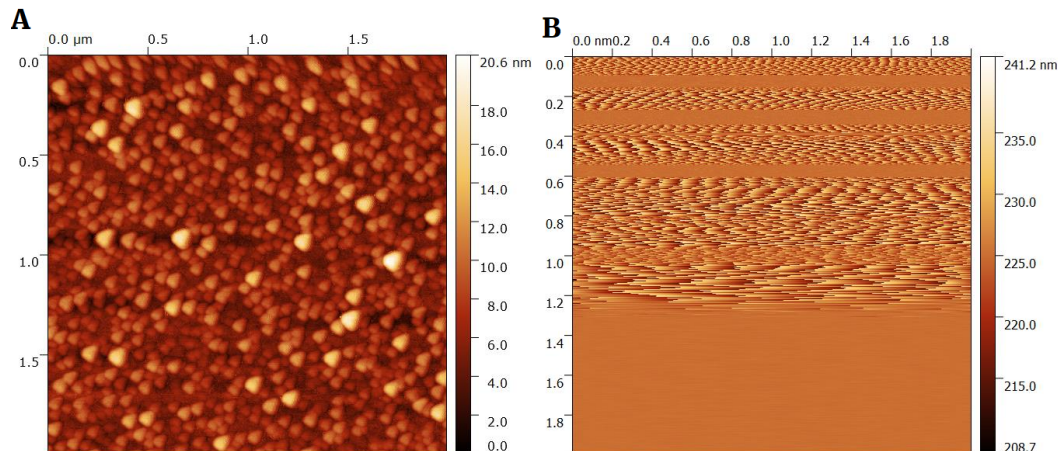


Figure 2.11 A figure demonstrating different errors and operations on the output images produced from an AFM. A. demonstrates a physical complications known as the double tip effect produced by tip damage. B. highlights an example of the zigzag patterns that can be produced from operation error, as well as the blank areas where the tip is not in contact with the surface.

Another consideration with AFM is that since the image is scanned over time rather than instantly there is a degree of physical error introduced during operation. Thermal fluctuations, piezo-error, vibrations and air fluctuations. Generally the error of an AFM in imaging mode is given to be $+/-1$ nm on the x and y length scale and $+/-1$ Ångstrom on the z length scale. Issues are made worse within liquid conditions where current effects induced by probe

movement, vibrations, sample setup and approaching the surface can frustrate results. The change in refractive index in the liquid means that the laser has to be realigned and re-calibrated in more difficult conditions. Additionally it is important to assess images produced for unusual mechanical errors, such as the double tip effect, where the tip becomes damaged during scanning and the defect in the tip's geometry is reflected onto a sample. There runs the risk of papers being published with potential double tip effects within their AFM analysis to an unknowing operator, the double tip effect is shown in Figure 2.11.A.

The operator is able to adjust several variables whilst operating an AFM. How much force is exerted on the surface as a result of the tip's proximity is altered; too light and the output image is unclear, but increasing force causes increased tip degradation rate. The scan rate is how fast the AFM scans, faster speeds increase image production, reducing the effects of drift, piezo error and thermal fluctuations. However, a high scan rate can result in unclear images and an increase in tip degradation. Finally gain can be adjusted, the values of which vary on the sample, setup and device. Images produced with incorrect settings can result in wavy mechanical patterns or poor image quality. An example of a tip that hasn't engaged the surface properly, therefore resulting in a poor pattern is shown in Figure 2.11.B. [15, 84]

2.6 Surface Force profiling

Force microscopy operation of an AFM differs from imaging mode in that the x, y movement of the piezo is removed, and instead a static sample is placed underneath, with several curves taken of a single site. This uses the mechanical nature of AFM to quantify forces applied upon the tip of the cantilever. These forces cause the cantilever to bend away in the event of repulsive forces, or towards the surface in the event of an attractive force. The interacting surface chemistry and profiles of both the tip and sample determine these force interactions. This contact area is also influenced by the solution that this area is immersed in, such as ions within the solution screening charges between the two profiles.

Having an accurate spring constant of the cantilever is paramount for these kinds of operations, as the measured parameter is the deflection of the cantilever reported by the photo diode. This can be then translated into force using the calibration methods discussed in section 2.3. This is one of the reasons why calibration is still performed for manufactured tips with given spring constants.

2.6.1 Anatomy of a force curve

A force curve is fundamentally the force "felt" by a cantilever as it is moved along a z axis. From this seemingly simple motion, several events commonly occur across this simple motion.

Given above in figure 2.12 is an unprocessed model force profile across one single

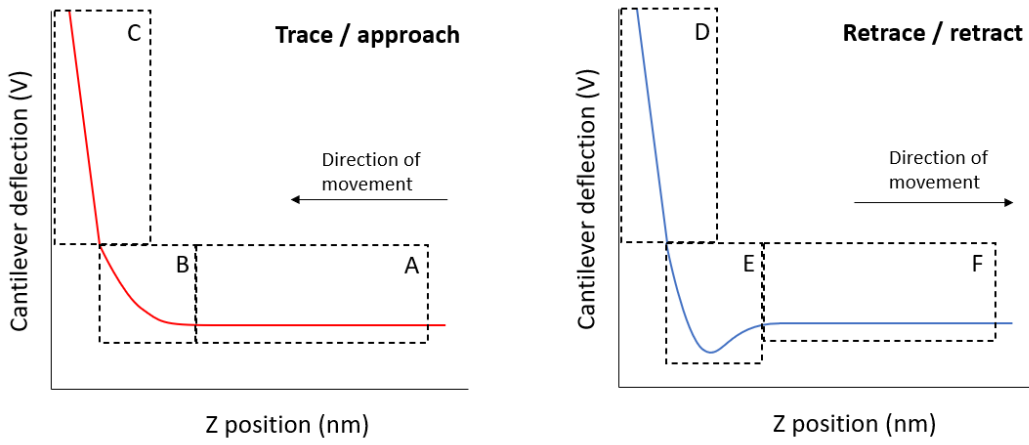


Figure 2.12 A diagram showing a model force curve event. The leftmost image corresponds to the trace (aka approach) curve the first part of the force profiling event. The trace force curve proceeds from the bottom right up to the top left, passing through the A,B and C events in order. After this motion the piezo movement reverses, retracting the cantilever away from the surface, this begins the start of the retrace curve. In reverse fashion the cantilever progresses through the D,E and F sections in order.

scan. The first event labelled as A is the approach part of the curve - where the tip and sample are too far away for any forces to be detected by the cantilever. When the surface begins to apply force upon the cantilever it enters phase B; where the curve begins to bend away. This bending is indicative of a repulsive force between the two surfaces. When the cantilever is finally brought into contact with the surface the curve transitions into a linear profile, where any z movement is directly translated into deflection. The tilt intrinsic to this phase can be transformed away by converting deflection into force given in section 2.3.

In some cases it is possible for the operator to set a delay time to retain the tip upon the surface of a sample between the two curves. This is known as a delay period. Afterwards the retrace curve follow the same pattern as the trace, but in reverse, going through D,E,F. Region E indicates an attractive force between the sample and tip, bending the tip downwards. As these sample-tip bonds break the cantilever will snap up from the stress applied from bending. This can cause multiple snap up events if the interacting surface can unfold.

2.6.2 Error correction of force curves

Since force profiling is restricted to a single axis in movement, the potential for error is reduced. The majority of artifacts and errors come from contaminants in the system, tip defects, or incorrect operational parameters. Of particular note any error incurred by scanner artifacts such as drift is reduced when compared to imaging from the reduced dimensionality. Though one additional aspect does influence results that does not affect imaging mode - the relative topological differences between the interaction areas aka roughness. [29]

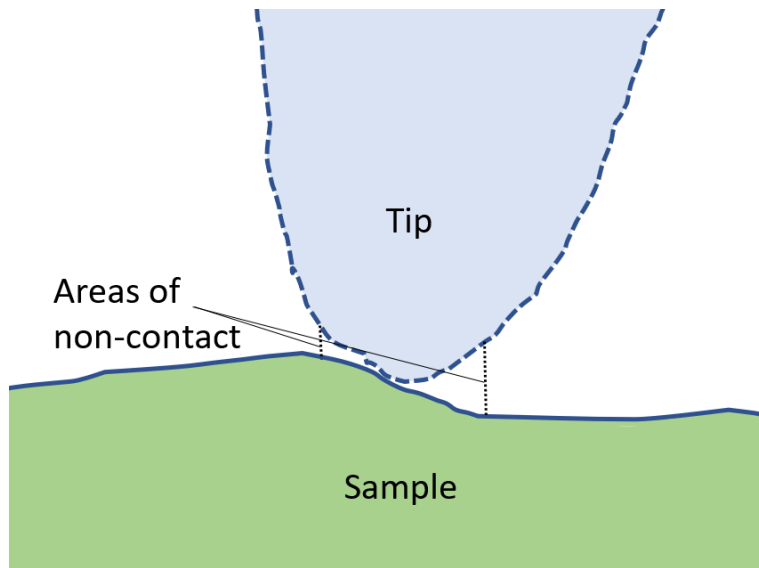


Figure 2.13 A theoretical demonstration of a rough AFM tip interacting with an imperfect surface. Due to the differences in topology between the two surfaces the interacting areas generate a different sum force experienced by the tip than expected.

These differences can cause the sum force applied on the tip to be different than expected, leading to an adjusted force curve. This is due to the DLVO force profile resulting in different force effects along the different points within the contact area as shown in figure 2.13.

In addition to this, because of the unstable geometry of the local area, as driving force increases, forcing the cantilever further into the sample, the tip itself can slip along the surface into a new more stable minima along the profile. This can cause sudden changes in the C/D regions mentioned in figure 2.12. This effect is described in figure 2.14. [4]

To deal with these effects multiple force curves are generally taken across a range of sites to ensure that any localised profiles are averaged out.

One other consideration is the effects of hydrodynamic forces which will have a constant effect on the tip during motion (phases A/B and E/F in figure 2.12). This only is present in samples immersed in a liquid, and generally doesn't impact the final curve too much. This effect can be profiled by running the machine in

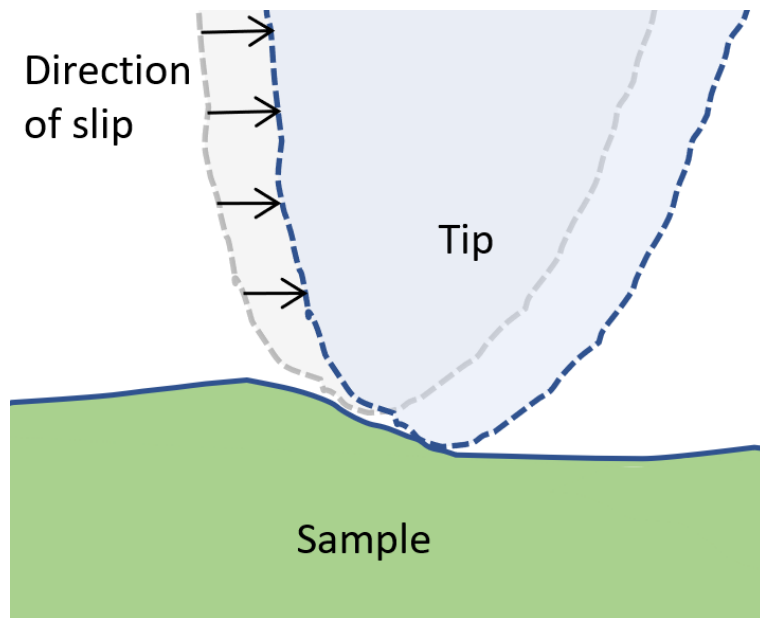


Figure 2.14 A demonstration of the theoretical movement that a cantilever tip will undergo when slipping along a surface profile.

different driving speeds.

One other effect upon the resulting data profile is the driving speed of the cantilever during profiling. Depending on the measuring tick rate some nuance to the data can be smoothed out as a faster speed will have less time to measure each point in the curve. An operator will generally tune the machine and setup to find an acceptable middle ground between data points and time taken.[56]

Chapter 3

Surface Imaging

3.1 Introduction

Atomic force microscopy (AFM) is a powerful tool for surface imaging, providing high-resolution topographical maps of sample surfaces. This technique is pivotal for understanding the morphology and texture of materials at the nanoscale. In this study, AFM was employed at various stages to quantitatively analyze the surface roughness of different materials.



Figure 3.1 *Photograph of the operational setup for the Bruker Nanoscope 2, which was used for image measurements.*

For the imaging purposes, we utilized the Bruker Nanoscope 2 AFM system

shown in 3.2. This system is designed with a sample stage capable of securing a 1cm disc, integrated with the J scanner piezoelectric stage for precise movement. The optical alignment of the laser onto the cantilever is achieved using a finely adjustable mirror mechanism, with the head unit being stabilized by tension springs to ensure accurate tracking of surface contours.

3.2 Surface analysis

3.2.1 Measuring the surface of mica

In order to assess the capabilities of the AFM a freshly cleaved mica surface was scanned under the AFM. As mica is assumed to be atomically flat [21, 72]. The cleavage of mica along its basal plane typically results in a smooth and featureless topography, making it an ideal substrate for AFM calibration and analysis.

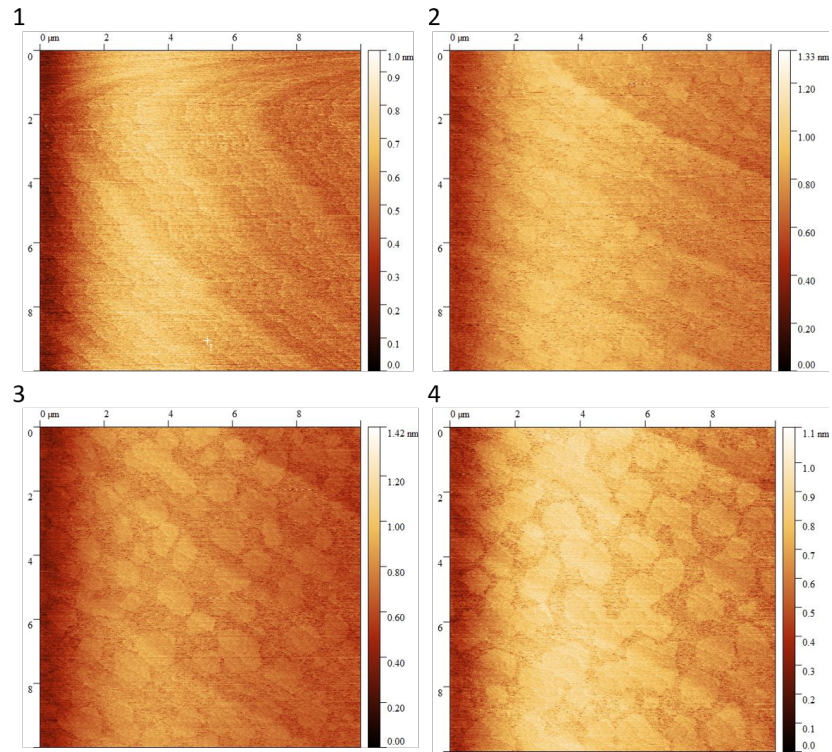


Figure 3.2 Time-lapse AFM tapping mode images of a mica surface showing progressive hydration. The first image was taken roughly 10 minutes after cleavage, with each subsequent image taking about 30 minutes to take. The changes in surface texture and color intensity suggest the absorption of water from the air, leading to a more pronounced hydration pattern, as seen in the increased contrast and the development of distinct features over time.

When a mica surface is freshly cleaved and exposed to air, it is expected to present

an initially smooth and flat surface at the atomic level due to its layered crystalline structure, which allows for easy cleavage along the basal plane. However, when exposed to ambient air, the mica surface can begin to adsorb water molecules due to its hygroscopic nature, leading to the formation of a hydration layer from the hydration process. This process is gradual and can be observed as an increasing surface roughness or the development of hydration-related features in AFM images over time. [21, 51, 65]

3.2.2 Silica Surface Analysis

One common sample that was regularly imaged across the entire investigation was silica, be it a silica sphere or borosilica glass surface. A range of different types of silica surfaces was investigated as well as surface treatment techniques performed on the same glass surface. Initially borosilicate glass capillaries were investigated. This investigation intended to resolve the uniformity of a borosilicate capillary across multiple capillaries by profiling the surface topology and roughness across a range of different points. This glass capillary was then cross referenced against the petri dish in use, to ensure that the surface of the petri dish was representative of borosilicate glass. This surface was then referenced against scanning electron microscopy images of the tips, alongside inverted AFM imaging of the tip.

Initially the inside of a glass capillary was imaged. The inside of the capillary was imaged by scoring the glass with a diamond tipped pen, with pressure applied on the outside to break the glass cleanly open 3.3. This glass reference was used as a representation for the borosilica glass roughness used in Chapter 4 and 8, as the petri dish used in chapter 4 was too large to fit into the AFM. This borosilicate capillary was used due to the ability to modify the geometry into a suitable shape to fit into the imaging AFM available. As the imaging AFM is head mounted, the ability to image larger objects was not possible as this solution was reached due to availability of said capillaries.

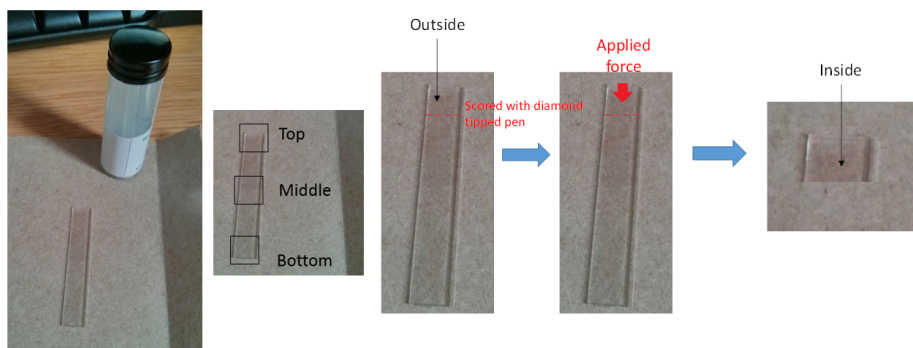


Figure 3.3 A diagram demonstrating how the glass capillary was broken and how samples were extracted from the capillary.

The sample was then loaded inside up into the AFM under tapping mode operation in air. Multiple antimony doped silicon tips (Bruker RFESP-40 tips)

were used to scan several samples each, giving a range of tips used for imaging. This was done to reduce any tip artifacts or degradation of tips so that image quality was retained throughout. A constant scan rate of 0.4Hz across all samples with the integral and proportional gain determined using the initial sample, then kept constant at 0.22 and 0.63 respectively. This was done to produce images that were similar as possible to one another from a parameter point of view. Large hysteresis effects present in the pizeo was negated by a small dummy scan window, where the AFM was left to run for a few seconds then reset to the origin of the scan. Each capillary was imaged 12 times at a $10 \mu\text{m} \times 10 \mu\text{m}$ scan size followed by a $2 \mu\text{m} \times 2 \mu\text{m}$ scan size. Images were taken at the top, the middle and the bottom of the capillary with a repeat image taken per site. Finally, two capillaries were imaged giving a total of 24 images. Scan sizes were chosen to give a larger view of the surface, while also scanning an area similar in size to the cantilever head used during the preliminary exploratory experiments ($1.6 \mu\text{m} \times 1.6 \mu\text{m}$). The bead size was later increased to $6.6 \mu\text{m}$ during the course of the exploration, representing the final dataset (see chapter 4).

In the case where dust was present in the images, to allow the applicability of a wider dataset, a standard method was used to handle dust. This involved two steps: image processing and visual inspection. After mean plane subtraction to correct for image tilt and alignment using a 5th order polynomial transformation, the images are closely examined. Dust is recognized by its consistency across all open-air images. To isolate and remove dust from the analysis, the z-axis range is adjusted, effectively minimizing the prominence of the dust in the visual representation. This method enhances the clarity of the underlying surface topology in the resultant images. Dust was only present in a small selection of the images.

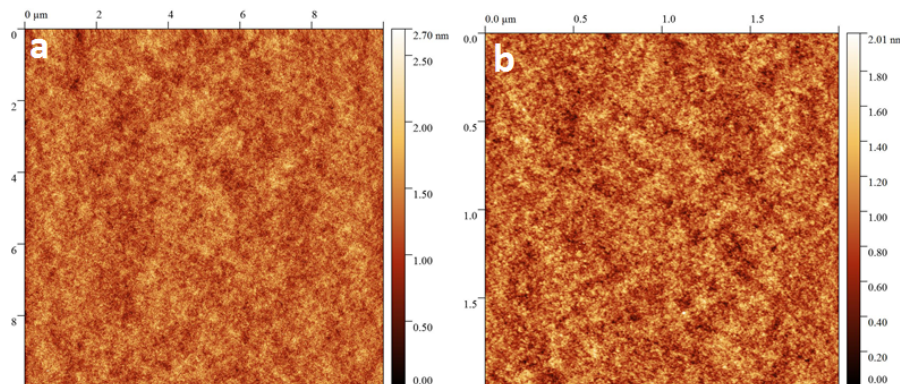


Figure 3.4 Two sample AFM images of untreated borosilicate glass at two different scan sizes: (a) displays an image with a scan size of $10 \mu\text{m} \times 10 \mu\text{m}$, while (b) demonstrates a scan size of $2 \mu\text{m} \times 2 \mu\text{m}$.

Results

The images for the inside top part of the capillary shown in 3.3 are shown below:

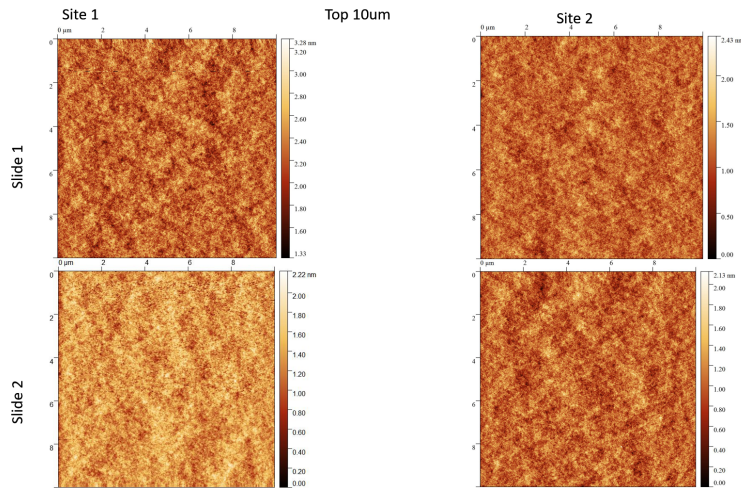


Figure 3.5 Four AFM images of untreated borosilicate glass on two different glass surfaces, with two sites per glass slide. The image has a scan size of $10 \mu\text{m} \times 10 \mu\text{m}$.

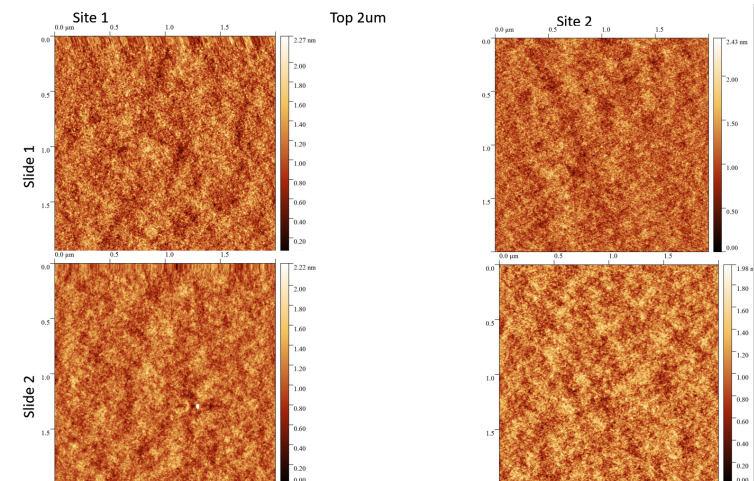


Figure 3.6 Four AFM images of untreated borosilicate glass on two different glass surfaces, with two sites per glass slide. The image has a scan size of $2 \mu\text{m} \times 2 \mu\text{m}$.

The images for the inside middle part of the capillary shown in 3.3 are shown below:

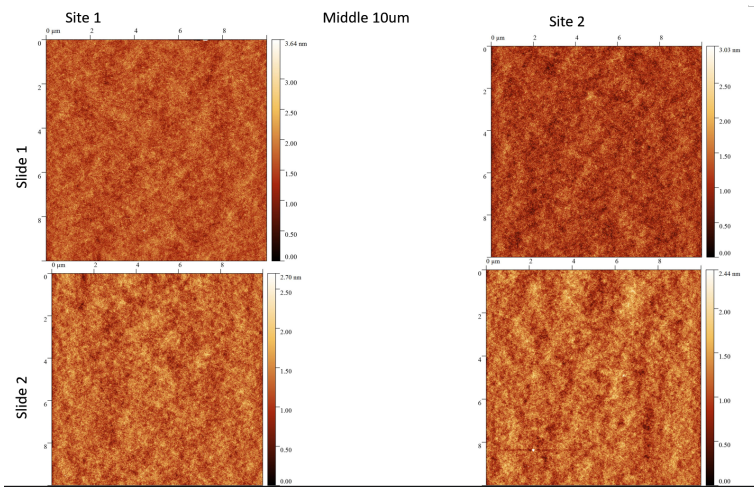


Figure 3.7 Four AFM images of untreated borosilicate glass on two different glass surfaces, with two sites per glass slide. The image has a scan size of 10 μm x 10 μm .

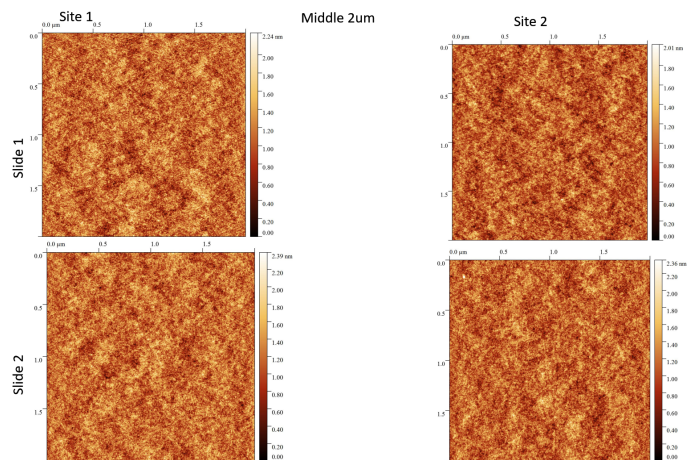


Figure 3.8 Four AFM images of untreated borosilicate glass on two different glass surfaces, with two sites per glass slide. The image has a scan size of 2 μm x 2 μm .

The images for the inside bottom part of the capillary shown in 3.3 are shown below:

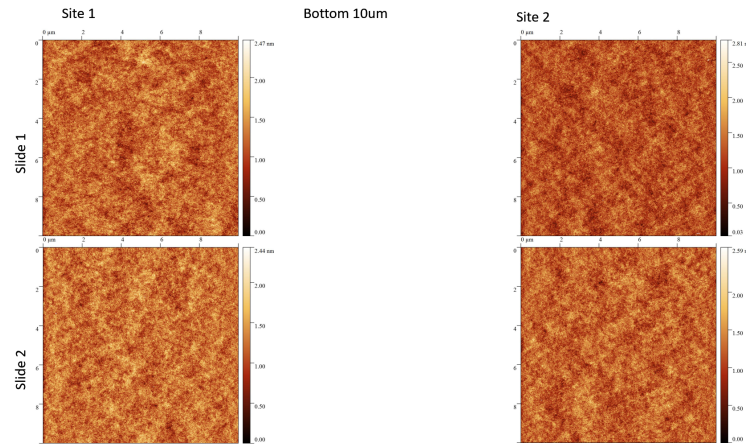


Figure 3.9 Four AFM images of untreated borosilicate glass on two different glass surfaces, with two sites per glass slide. The image has a scan size of $10 \mu\text{m} \times 10 \mu\text{m}$.

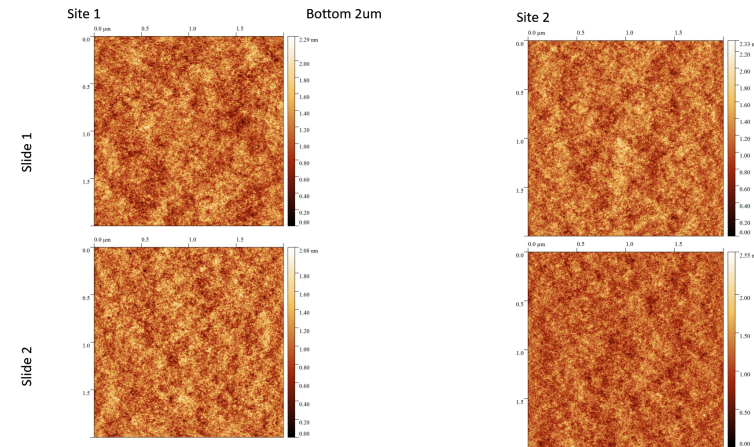


Figure 3.10 Four AFM images of untreated borosilicate glass on two different glass surfaces, with two sites per glass slide. The image has a scan size of $2 \mu\text{m} \times 2 \mu\text{m}$.

Gwyddion, an AFM analysis software, was used to process the resulting data from the imaging process and produce the images given in the figures above.[67]

The AFM analysis of borosilicate glass surfaces demonstrated remarkable uniformity across the dataset of 24 images. The root mean square (RMS) roughness is a statistical measure of surface texture, calculated from the height data obtained in AFM imaging. RMS roughness is determined by taking the square root of the average of the squares of the height deviations from the mean plane of the surface within the scanned area. This gives a quantitative assessment of the surface's vertical irregularities. Additionally, peak-to-peak roughness in Gwyddion refers

to the difference in height between the highest and lowest points within the scanned area, providing a direct measure of the surface's vertical variation.

Notably, the maximum peak-to-peak roughness average across the 24 image dataset was measured at 3.6 nm for images with a scan size of $10 \mu\text{m} \times 10 \mu\text{m}$, and 2.6 nm for those at $2 \mu\text{m} \times 2 \mu\text{m}$. The average root mean square (RMS) roughness values, calculated from the height variations across the scanned area, were 0.24 nm +/- 0.01 nm for $10 \mu\text{m} \times 10 \mu\text{m}$ images and 0.2 nm +/- 0.02 nm for $2 \mu\text{m} \times 2 \mu\text{m}$ images. These RMS values reflect the average height deviations from the mean plane with the standard deviation, providing a quantifiable measure of surface texture. Together the RMS was 0.2 nm +/- 0.02 nm. The consistency of the RMS roughness across both image sizes and sites indicates a homogenous surface texture irrespective of the scan area. Figure 3.10 presents representative images from each scan size category, illustrating the general surface topology observed. The consistent topology and roughness throughout the capillary's length and across multiple capillaries suggest that the surfaces used in the main investigation bear a similar structure to those depicted in Figure 3.10.[75]

Drift analysis

In order to ensure that any error incurred by physical drift was accounted for an investigation into the x, y and z axis drift was explored. The AFM was left to image the same glass sample repeatedly in order to produce the same image several times. This image was then two dimensionally cross correlated with the next image in the sequence and the difference removed between the two z data points. The results are displayed in Figure 3.11.

Due to the drift experienced while scanning, the rows were found to be increasingly misaligned towards the bottom of the image. The result of this is shown by the gradient seen from the top of the image downwards, as the first image scanned from the bottom up, then the second image was scanned from the top down. The process was repeated on a row by row alignment basis and the resultant drift between the two images was found to be approximately 1 Ångstrom on the z axis, 8 nm on the y axis and 28 on the x axis. However given the speed of the scan was low at 0.4 Hz each image took approximately 40 minutes to image, giving an approximate drift of 0.1 nm by 0.5 nm drift per minute.

It was concluded from this analysis that the artificial effects of drift on the measured surface roughness would ultimately be negligible. Due to the small drift observed over time the influence of the resulting plane angle at points drifted towards would not have a large enough influence to impact the calculated roughness.

3.3 Silica particle surface resolution

In order to determine the surface roughness of a silica sphere, a range of $1.5 \mu\text{m}$ silica spheres were placed upon a suitable surface and imaged. The objective was

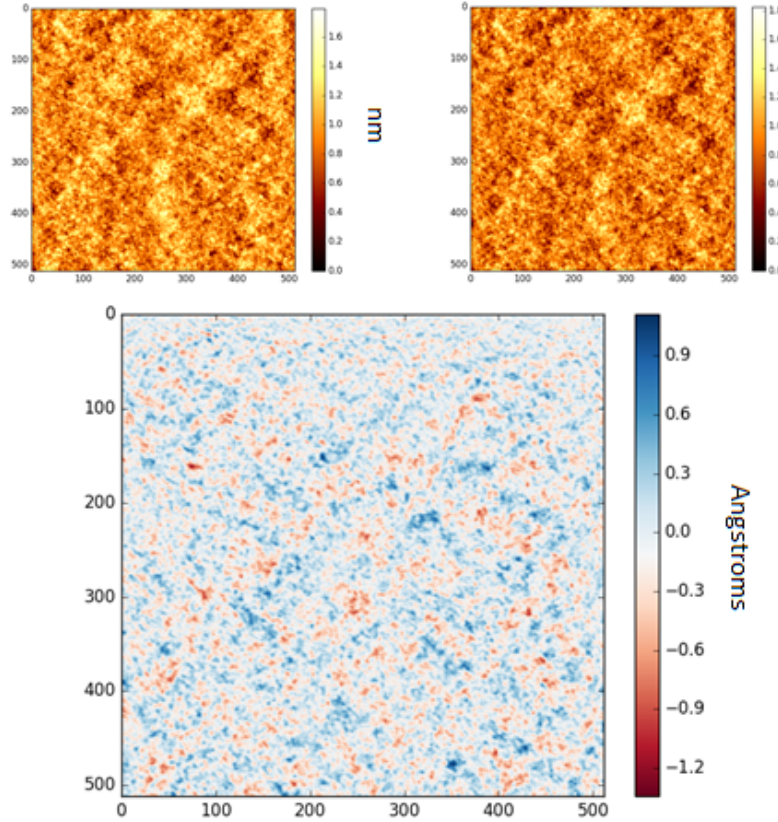


Figure 3.11 The output image of the 2D cross correlation function between the two images. The two smaller images are the input images into the script. The x and y values are the location of the z values in the 2D matrix dataset. The z scale is labeled respectively.

to discern any roughness variances between a flat silica surface and a spherical one. The methodology was influenced by the AFM tips used in Chapter 4, which involved cantilevers with silica spheres attached.

Initially, several scans were required in order to "zoom in" on an individual sphere. Due to the AFM's limit of 512 data points per line, the resolution of an individual sphere suffered unless it was the focus of the scanning frame. However, due to the drift in location due to pizeo error, attempting to suddenly zoom into a specific surface would dislocate the frame of reference from the intended area. As a result, an individual sphere was slowly zoomed in until it was the focus of the frame. This greatly reduced the range of images that could be taken and used.

Another feature of these spheres is their hexagonal appearance under AFM. This is due to the tip's geometry, which limits the area it can reach, and therefore probe. As the geometry of the tip is pyramidal in shape and the true shape of the sphere is spherical, the areas that are unreachable by the probe are reported with a straight line and the height around the sphere are erroneously high. However,

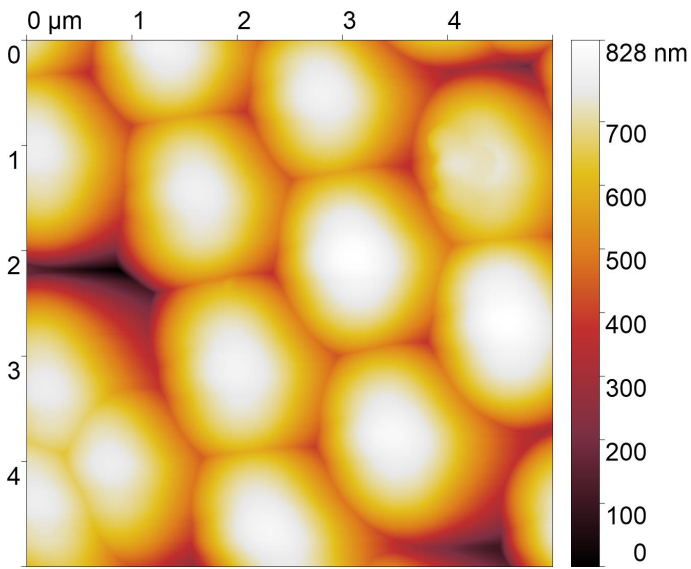


Figure 3.12 The observed surface of a silica sphere.

due to the intent of the procedure being focused on mapping the surface of a sphere, this does not affect the results as an area outside of this interference was chosen.

The curvature inherent to the spherical geometry of silica beads presents a unique challenge for AFM analysis. Subsequent to imaging, any dataset inclinations or plane shifts were computationally rectified to ensure an accurate representation of the surface topology. This step was performed to remove any systematic tilt or distortion that could obscure the genuine surface features being studied. To isolate the surface characteristics accurately, advanced image processing techniques were employed. A 5th order polynomial fit was applied to 3.12 in order to produce 3.13, effectively removing the curvature and normalizing the data to a flat plane. Further refinement was achieved by cropping the image, ensuring that only the relevant surface area remained within the data frame.

An AFM imaging of 3 $1.5 \mu\text{m}$ silica spheres was performed, and spherical deconvolution was subsequently executed using Gwyddion software [67]. From three functional sites across different spheres, an average RMS roughness of 0.65 nm was discerned, highlighting a notable difference in roughness compared to borosilicate glass. This suggests that silica spheres exhibit a higher degree of surface roughness.

The unique feature observed in 3.14 could originate from various sources: a surface defect, an impurity, manufacturing-induced irregularities like bubbles or pits, or possibly artifacts related to the AFM process, such as tip convolution effects. Further investigative work is suggested to understand the adhesive interactions between silica particles and to determine if the central “pit” seen in the images is a consequence of sonication used to disperse the silica spheres during the creation process. [50]

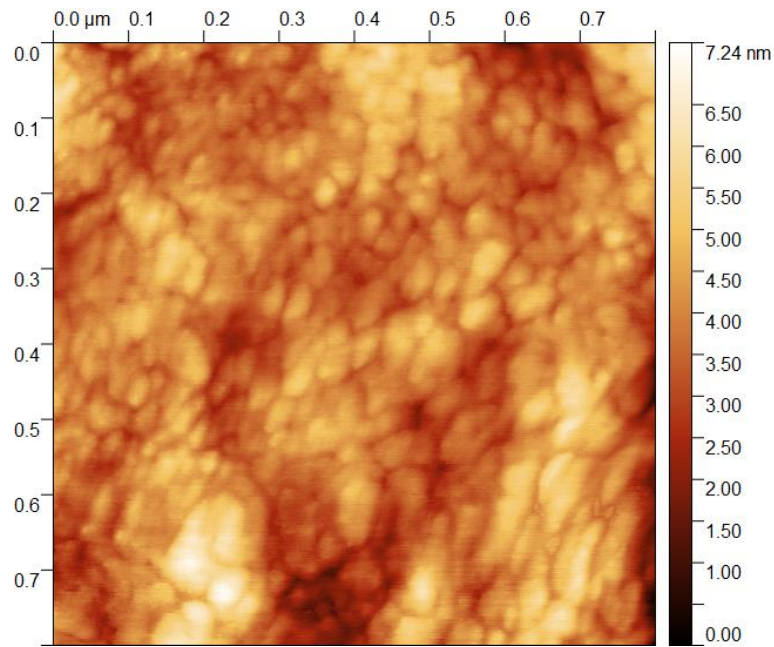


Figure 3.13 The flattened surface of a silica sphere.

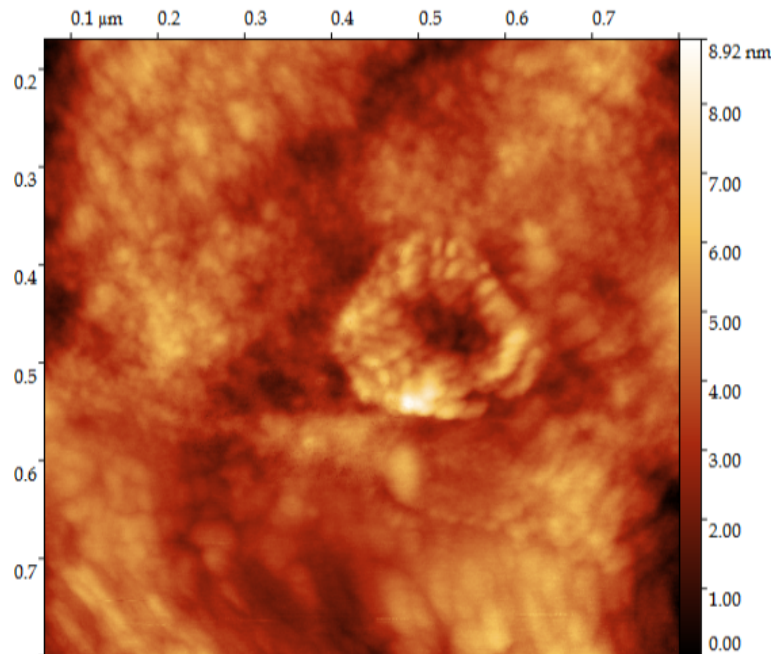


Figure 3.14 The flattened surface of a silica sphere with a uniquely seen feature. The RMS roughness of this image was 0.72 nm, the highest one in the dataset.

Chapter 4

Atomic force spectroscopy analysis

4.1 Introduction

This chapter explains the experimental methods used for force curve collection as well as the computational methods used to interpret them. Over the course of data collection the process was refined to a repeatable method across a consistent experimental setup. While two different AFMs were used across the analysis, encouraged by technical limitations, they were used in such a way to complement one another. Both of these AFMs were used to produce force curves, and were interpreted using the same scripts.

4.2 MFP-1D

For the force spectroscopy setup a MFP-1D from Asylum Research was used. The MFP-1D is an AFM mounted on top of an inverted light microscope, with the sample placed between the scanning head and the stage of the light microscope. In the AFM head the cantilever is mounted using tweezers in a holding apparatus. This head is immobile in the X,Y direction, horizontal movement is instead controlled by manipulation of the stage. In the Z direction there are two possible movements - the 3 legs of the head can be moved vertically using the wheels for coarse movement, either to bring the tip in contact with the sample, or to level the head so the contact of the tip with the surface is uniform. The other control over the vertical height is via the piezoelectric transducer (piezo) mounted in the center of the head. This piezo has a travel range of roughly 15 μm . A laser is then emitted from inside the head and directed onto the cantilever, towards the sample. (See fig 4.2)

For laser alignment on the AFM head an inverted microscope is used. First the cantilever is brought into focus under the microscope, then the position of the laser is aligned atop of the intended cantilever. Afterwards the laser is focused upon the center of the tip using the sum output given by the photosensitive diode.



Figure 4.1 Operation setup for the MFP-1D AFM that was used for force measurements.

The diode converts incident light into an output voltage, this allows the position of the laser focal point to be determined with respect to the diode boundaries. Finally the deflection of the laser is set to 0; a central position between the positive and negative extremes. Deviation of the laser's focal point from the center point of the photodiode allows movements of the cantilever to be detected. This detects any bending (and thus attraction/repulsion) of the cantilever.

In terms of the structure of the device, it differs slightly to the imaging AFM explained in the previous chapter; the components are more tightly packed, mounted atop of the z-piezo directly, which then brings the apparatus down onto the sample, unlike the z-piezo raising the sample up to be imaged. In addition a linear variable differential transformer (LVDT) sensor is mounted inside of the head to correct the movement of the z-piezo (closed-loop piezo) thus improving z-piezo accuracy (See fig 4.2).

Due to this feedback loop from the LVDT relying on previous data to define the voltage control from the next approach, the peak force (the intended maximum force applied on the cantilever per curve) was set to a relatively low number 8 nN. This was done to limit the amount of tip damage during operation. In cases where the tip fails to engage with the surface in the previous approach, this low peak force ensured re-engagement of the tip with the surface in the current loop was as gentle as possible. Noise in the data was attributable to the effect of

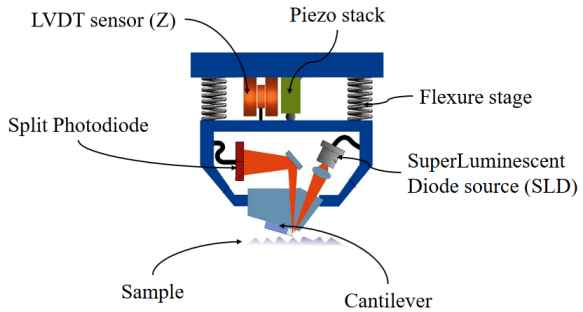


Figure 4.2 Operational setup for the MFP-1D AFM that was used for force measurements. Adapted from [60]

vibrations on the operation of the instrument. When errant vibrations reach the AFM, this energy is transferred through to the cantilever, which then causes it to oscillate. This oscillation usually presents itself as a sudden spike in deflection on the curve. It is these sorts of curves that are selected and removed from the dataset. In most cases the total amount of removed curves is minimal, usually 1 or 2 per site, with a total of 100 or more curves used for processing. While it was rare that any datasets were rejected for purely noise based reasons, there is one notable set that was repeated at a later date due to a storm causing significant, persistent errors in the data. While the AFM was mounted on an anti-vibration table, the noise observed in the machine is still present.

Additionally, the standard speed of tip movement was set to $1\text{ }\mu\text{m/s}$ (unless otherwise stated). This was done to compromise between the total dataset recording time and reduction of strain upon the cantilever and tip.

4.2.1 Experimental setup

Initial Setup and Challenges

Initially the experimental setup was focused on investigating the interactions between two silica particles. Given the difficulty in aligning two micron sized particles for interaction, the geometry of a silica particle and a flat silica surface was chosen. In order to facilitate this approach a silica particle was glued to a cantilever (see fig 4.3). These types of cantilevers are produced commercially, with the gluing process as part of the manufacturing, and were purchased to reduce experimental setup time. This cantilever was then brought into contact with a silica surface, with the results transformed using the Derjaguin approximation (See chapter 1).

The first setup involved a $1.6\text{ }\mu\text{m}$ diameter tip brought into contact with a silica surface glued to the inside of a plastic petri dish. This setup allowed for a liquid solution to be placed on top of the surface, contained within the plastic petri dish. A 50:50 (by volume) solution of deionised water and glycerol with a

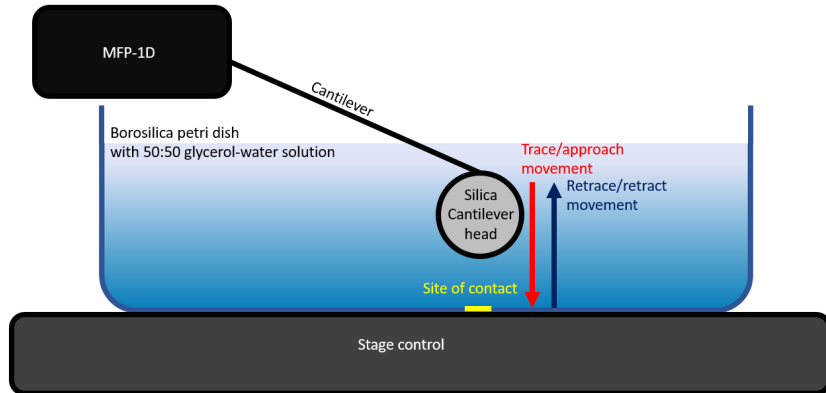


Figure 4.3 Experimental schematic of MFP-1D during operation. The AFM is abstracted away into a back box to highlight the motion that the cantilever takes with respect to the surface. The stage control provides horizontal control, and therefore moves the projected site of contact along the petri dish surface.

controlled concentration of LiCl was added. This ratio was chosen by volume to ensure consistent mixing and ease of preparation, given the liquid nature of both components. Glycerol was chosen for its high viscosity and low volatility, which help stabilize the solution during AFM measurements by reducing evaporation and maintaining a consistent environment for the silica particles. The increased viscosity allows for more controlled measurements of the forces between particles, providing insights into how these forces scale from single-particle interactions to multi-particle interactions within a viscous medium. This solution was brought up to completely cover the tip, ensuring the head of the AFM was submerged.

The initial setup involved calibrating the cantilever tip on a separate calibration surface (see chapter 2), then removing this surface and replacing it with the experimental one. Initially approaching the glass surface in air was of little issue, but the greatest difficulty arose in finding contact with the glass surface under liquid. Given that the liquid in use was of similar optical density to glass, the interface between the two was no longer visible under the microscope. As a result; the initial approach was slow, methodical and careful, as recklessness would break the tip.

Issues Identified and Interim Solutions

Problems with the setup were identified after a test run, after a sweep of 4 different concentrations it was found that the resulting Debye lengths for all the curves were above 6 nm. These were directly contrary to the expectation that Debye length should decrease to theoretically 0 at increasing salt concentrations. The anomalous readings were considered to be the result of unidentified contaminants. Given the setup with the AFM was open by necessity as well as the difficulty in getting the sample under the tip in an expedient manner, there was little

protection against airborne contaminants. Additionally, contaminants originating from the plastic of the petri dish and glue were identified as a source of problems. The method of cleaning the surface was also called into question.

In order to address these issues, a few changes were implemented over a series of experiments. The surface used was exposed to an improved washing protocol. This washing protocol used deionised water to clean the surface over a greater period of time. Ethanol was considered, but due to the glue holding the surface down, there were concerns over the surface having a stable platform. Additionally the method of approach was revised slightly, with a large part of the distance between the surface and the tip performed in air, with the liquid solution injected using a glass pipette slowly. This injection relied on the surface tension of the water to slowly fill the dish, resulting in a slightly higher volume use. This was done to minimize any dramatic flow from damaging the tip, emulating a normal approach submerging mechanics.

Contamination issues were still present after these revisions. In order to maximise contaminant removal, the plastic petri dish was replaced with a borosilicate glass one. Instead of gluing a surface on top of the petri dish, the surface of the dish itself became the sampled area. While there had been previous considerations of the stability of the glue influencing the resulting force curve, the approach had been focused on solving the contaminant problem first. By using the surface of the dish itself, any concerns regarding glue induced artifacts could be laid to rest. This new dish permitted the use of ethanol in the cleaning procedure, as well as plasma treatment of the surface. The silica bead diameter on the cantilever was also increased to $6.6\text{ }\mu\text{m}$ to increase the area of contact.

Plasma cleaning was performed under a vacuum within a sealed chamber. After the chamber was evacuated a low quantity of pure oxygen gas is flowed across the surface at 0.4 bar, with the vacuum pump still active. This plasma cleaning technique cleans off any residual organic matter, resulting in water and carbon dioxide by-products. These byproducts are pumped away by the constant vacuum. [74] [89] [13]

Final Protocol

In response to the ongoing contamination problems, a final protocol was established to ensure the integrity and reliability of the experimental results. The plastic petri dish was replaced with a borosilicate glass dish. Rather than gluing a surface on top of the petri dish, the surface of the dish itself was used as the sampled area. This change removed concerns related to glue-induced artifacts and facilitated a more thorough, efficient and effective cleaning method.

The glass petri dish and lid were cleaned with ethanol and water, then followed by plasma treatment. The plasma cleaning process was conducted under a vacuum within a sealed chamber, with a controlled flow of pure oxygen gas at 0.4 bar. This procedure removed residual organic matter, further minimizing potential sources of contamination.

During the AFM setup and operation, the cantilever was carefully mounted into the AFM head, and the laser was aligned as precisely as possible to the center of the photodiode. The petri dish was then placed under the AFM head, and its surface was utilized to calibrate and calculate the spring constant of the cantilever. Following this, the cantilever was retracted by a known amount, and the liquid solution was pipetted in. After the liquid had settled, the laser was recentered to account for the change in optical density, and the tip was brought into contact with the utmost care, relying on deflection readouts due to limited visibility. When contact was established, between 100 and 200 curves were collected for each site. In cases where multiple sites were sampled, the tip was slowly retracted, the dish was repositioned, and the approach phase was repeated to ensure consistency.

When transitioning between different electrolyte concentrations, to manage contaminants and maintain tip reusability, the tip was retracted, cleaned with water, and plasma-treated along with the petri dish. Each tip was plasma-treated no more than twice to prevent excessive damage done to the tip from the procedure (see fig 4.4). For fresh tips, they were used as supplied from the manufacturer. Direct imagining of the petri dish was not possible due to incompatible geometry at the time of collection.

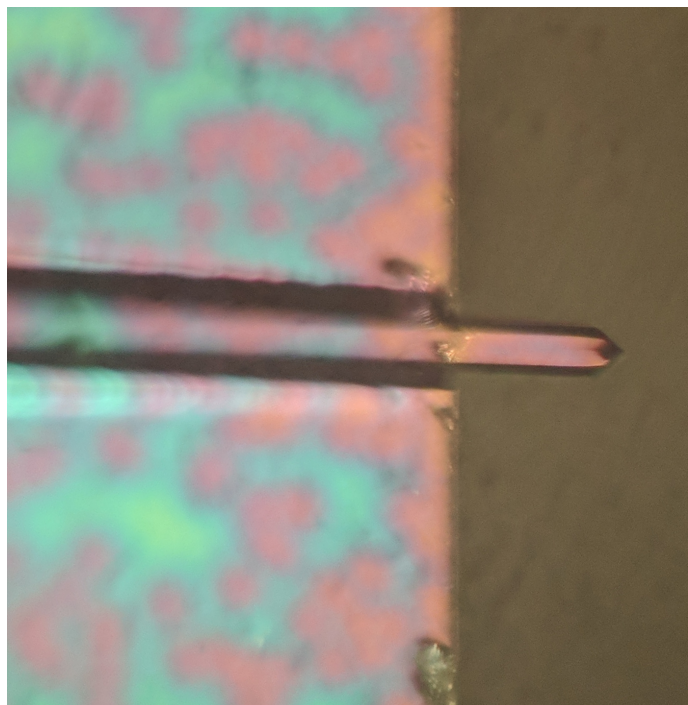


Figure 4.4 *The view of a damaged chip from sequential plasma treatment. Normally a clean chip presents an observed silver colour on the outside, but from over-treatment the surface has worn away, resulting in the presentation seen above.*

4.2.2 Connection with Rheology

The choice of experimental setup, particularly the use of glycerol and the attention to contaminant control, is essential not only for the accuracy of force measurements but also for drawing connections to rheology. The increased viscosity of the glycerol solution simulates environments similar to those found in industrial or biological systems, where the rheological properties of colloidal suspensions significantly influence their behavior under shear forces. Understanding the transition from single-particle interaction forces to multi-particle interactions in these systems can provide valuable insights into the design and optimization of products and processes that rely on controlled rheology, such as in pharmaceuticals, food science, and materials engineering.

The results from this setup are intended to bridge the gap between microscopic forces and macroscopic rheological properties, demonstrating how the behavior of individual particles can scale up to influence the bulk properties of a suspension. This connection is vital for applying the findings of this study to real-world systems, where controlling rheology is key to achieving desired product performance.

4.2.3 MFP-1D force-distance curves acquisition and processing

Acquisition

A minimum of 100 force curve readings per site was taken for each measurement site, with the raw data saved in a single file. The columns alternated with the raw deflection reading for one curve, followed by the corresponding z-piezo value. The majority of readings measured both the approach and retract in one single motion, combining both these curves into one whole column. In the case where the cantilever was held at a certain location for a period of time, a new set of columns is appended, with another one starting after it begins movement again, thus fracturing the data whenever the cantilever is stationary between periods.

From this each curve was broken down into two lists of raw unprocessed data given by the machine; the piezo height and the deflection. The piezo height is the recorded height of the end of the piezo (where the cantilever is mounted on) on a scale of 0 μm to 15 μm . This range corresponds to the effective movement of the base of the cantilever in the z direction, and is thus variable between datasets, as contact can be anywhere within this range. For example, if the piezo moves the cantilever down by 5 μm , and then comes into contact with the surface at that area, the recorded value will be 5 μm , not 0 μm . It is worth noting that the z height controlled by the legs of the AFM is independent, and is not measured by the machine. Contact is a combination of the leg height being set by the operator manually, and the piezo coming into contact within its 15 μm range. The cantilever deflection is the deviation in nm from the equilibrium position, which corresponds approximately to the center of the photodiode. No

deflection (i.e. no force) is associated (by appropriate alignment) with the laser beam hitting the centre of the photosensitive two-segment diode (corresponding to 0 Volts). Deviation from the center arises from when the cantilever is bent in a certain direction, reflecting laser off the top of the cantilever to drift along the photodiode's sensory range. This voltage is recorded as either a positive or negative voltage corresponding to upwards or downwards deflection due to repulsive or attractive forces, respectively. This deflection is saved alongside the height in individual data files during operation automatically, with any derivative graphs following the same naming convention defined by the input file, with respect to the unpacked raw curves.

In some cases the resultant curve is not typical. This can arise when the cantilever doesn't move far enough down to find the surface, or when the cantilever starts in contact with the surface at the start of the movement. While these curves were rare, they did occur during standard use of the AFM. These curves were removed during processing. These erroneous movements were usually corrected automatically by the AFM via error correction feedback for the successive curves afterwards. In some cases, due to imperfections of the control mechanism of the AFM, tremors/ vibrations in the building or other uncontrollable factors the frame of reference can shift up, resulting in an unusable curve, simply due to the lack of a data in a specific area. These fluctuations in the system cause the AFM to "lose" track of the surface and command an increase to the voltage sent to the piezo, over-correcting its movement, shifting the captured area further up. After this the error correction the peizo controller reduces the control voltage until it stabilises around the maximum force specified by the operator. In addition, in the case of an uncontrollable error (primarily vibration based) the noise of a specific curve can throw off the normal processing of the script. It is in these instances that these curves are identified and removed.

Using Python[82], an automated script was constructed to process the large volume of data generated by the MFP-1D AFM, given that each site generated around 100-200 approach and retract curves, and that multiple sites were used for each concentration, this produced a sizeable volume of data of around 6,000 curves which would be unmanageable without some form of automation.

Processing

Using numpy[71] an array was created from the data present in the raw data file for a specific site. Each of the curves for a given site was then split up into individual numpy arrays in preparation for the following functions. As it stands, this raw data requires at the bare minimum translation from a deflection vs distance graph into a force vs distance graph. This corresponding graph of force (nN) vs z-piezo position (μm) was produced. The raw deflection was converted into force using the spring constant of the cantilever with the following equation:[20].

$$F = K_c(\delta - \delta_{offset}) \quad (4.1)$$

Where F is force, K_c is the spring constant, δ is the deflection and δ_{offset} is the deviation intrinsic to the cantilever under no force (taken from the start of the curve).

Similarly the z-piezo position is converted into micrometers from meters (See fig 4.5). This produces an individual data file for each curve. From these curve several fitting runs were performed on this unpacked dataset to hone down the script's operational parameters (ensuring areas defined as contact and non-contact were as accurate as possible).

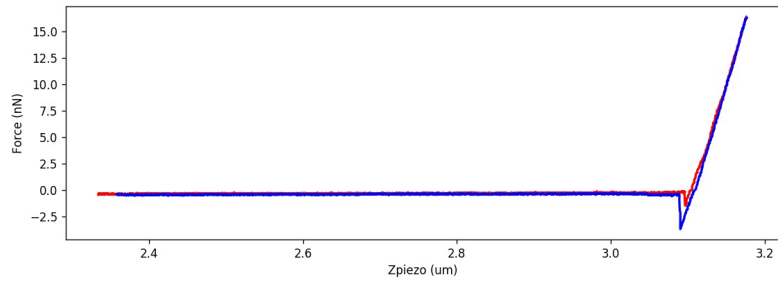


Figure 4.5 An example of a individual graph produced at this point. Minimal processing has been done with only the deflection converted into force (nN) vs piezo z position (μm)

In order for the script to perform correctly on each of the curves, there needs to be a long enough stretch of data for the approach and a long enough contact region. In the vast majority of cases this is true; there are a few cases where during normal operation an over correction occurs, resulting in the captured range of data to be shifted. For a given curve there are 3 identifiable regions; the approach phase, with no identifiable forces applied on the tip, the interaction phase, where the tip is either repulsed or attracted to the surface, and the contact phase, where the tip is in contact with the surface. These phases are shown in figure 2.12 as A, B and C respectively. A good curve will include all of these phases in it's snapshot of data, thereby allowing a clear representation of the variable forces applied upon the tip. The operational parameters of the AFM defined by the user are done so in a way to collect the most amount of data (aka setting the snapshot) during acquisition around the transitional point while reducing the amount of unneeded movement towards the surface, and equally reducing the amount of strain forced upon the cantilever during the contact region. At high strains the surface of the cantilever or petri dish can become damaged, or the cantilever can become damaged or break. As the conversion of deflection into force requires the spring constant to remain the same, and damage can cause this conversion to no longer remain true, any damage over the operation is considered by reviewing the curves over time. If there is a significant drift in the shape of the curve over the process of a site, then this is highlighted, and the experiment repeated. In the event of the cantilever breaking the AFM ceases to function and therefore data collection stops. As the retract curve immediately follows the approach curve, the retract

curve inherits the same snapshot of data range.

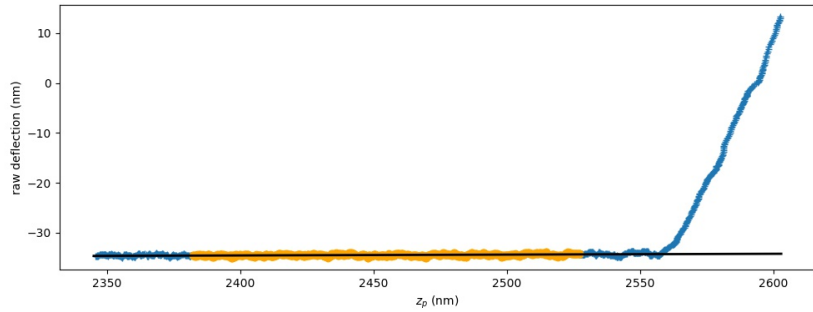


Figure 4.6 An example of a individual graph produced for a single approach curve. The orange region of the graph is the area used in the farfield drift reduction and used to set the floor of the data to 0.

Each curve is then processed individually. The first step taken is to address some of the background noise. This is done by taking a linear portion of the curve (see fig 4.6), where any movement done by the piezo is far enough away that any forces acting between the surface and the cantilever are zero. This removes any farfield drift.

This area is defined by a region along this curve, set to use points away from the initial contact area of the curve. Initially the distance traveled per datapoint is calculated by taking the adjusted range of data divided by the total number of datapoints. Based on a combination of user input and backward estimation of the contact area, the data window is carefully aligned along this linear regime. A corresponding graph is then generated to clearly highlight this selected region. This linear horizontal region is then normalised at 0, with the whole dataset translated up or down accordingly.

Afterwards the data is binned into a set of variable sized bins to produce a smoother curve and reduce the effects of noise intrinsic to the system. The size of this set is determined on a case-by-case basis through an iterative process, with a bin size of 5 being most commonly used. In earlier curves where the total number of data points taken was 2000 per curve, the bin size was smaller. Subsequently the size of the data collected was larger which improved the resolution and this enhanced the data analysis. It was determined that increasing the total number of data points to 8000 was optimal. Smoothing the curve in this manner improved the accuracy in which the contact point is defined. A graph was additionally produced with a bin size sweep of ± 2 to ensure that any features were not lost during binning.

Once binning was complete attention was given to the selection of the data which best represented the area in which the tip has made contact with the surface, i.e. where any piezo movement was translated into cantilever deflection. In general, this selection was defined by reviewing the graphical output from the previous steps. This selection aims to include as much as the graph as possible after the contact point, though it should be highlighted that the deflection is not a

purely linear event in practice. In order to ensure that the contact region was estimated reliably, the upper and lower boundaries of the range were swept by ± 5 arbitrary units producing an additional series of curves with this range. This ensured that the final estimated force at contact is within a local parameter minima, i.e. the estimated contact force wasn't independently produced because of a sole artifact, but agreed with the contact forces reported from similar input values.

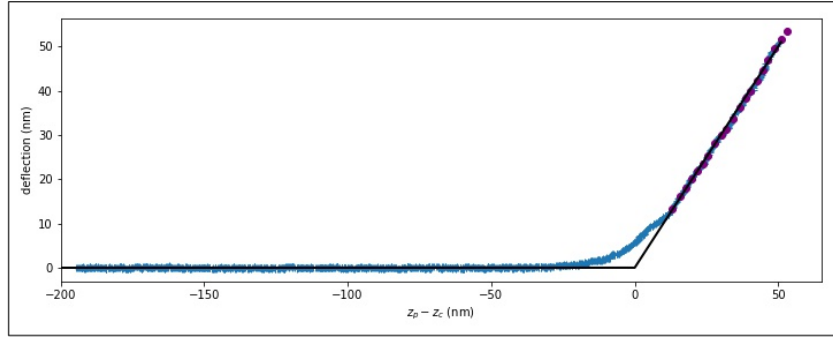


Figure 4.7 An example plot of an approach curve. The area used to help define contact is highlighted by the purple dots overlaying the raw curve.

Using this defined region, the data is extrapolated back to the intercept with the horizontal 0 force line. In the case that there is a jump to contact, the jump point is used instead of the interpolated z_c . Where the extrapolation intercepts the normalized floor line (i.e. where $y = 0$) is where z_c is defined. Each curve is then normalised to 0 using z-piezo position (z_p) minus z-piezo contact point ($z_p - z_c$) at the point of contact (see fig 4.7). This term is defined as z-separation (z_{sep}). By defining the contact point as 0 the force at contact can be extrapolated from the curve - by taking the equivalent y-axis value when x is 0.

In some cases, particularly in the measurements made with the JPK NanoWizard AFM (see Section 8.3), intermediate data points through the jump to contact were successfully captured, providing further insights into this phase of the force profile. These data points offer a more detailed understanding of the transition and are discussed in greater depth later in the thesis.

$$z_{sep} = z_p - z_c \quad (4.2)$$

In conceptual terms $z_{sep} = 0$ is the point in which the cantilever would come into contact with the surface under no outside stress. In some cases, when a high degree of cantilever movement is applied in the contact phase, the cantilever can bend beyond the non-linear region of the photodiode detector. This is only present at high deflections, and thus care is taken to ensure that the analysis is done within the linear response region of the photodiode. The non-linear region is where the laser reaches the limits of the photovoltaic cells and the overall signal strength is reduced. Additionally, at higher stresses the cantilever can be subjected to non linear deformation. As the system itself assumes a constant

translation from piezo movement during the contact phase into linear deflection recorded by the photodiode, these abnormal data points at the end of the curve are a result of the photodiode's limits. It is in these cases that said recorded can interfere with the processing. As a result, where the behaviour of the curve is inconsistent with the known behaviour of the machine, that said data is removed, though it is important to highlight that said abnormal data only appears after an expected linear contact phase, when the limits of the machine are met. This curve then displayed expected behaviour throughout the approach, interaction and contact phases.

Later in the thesis, particularly in Section 7.5, measurements made with the JPK NanoWizard AFM reveal additional aspects of this part of the force profile, including the "jump to contact" phenomenon. These subsequent findings provide a more nuanced understanding of the force interactions and should be considered alongside the observations presented here for a more complete picture.

After all this processing an averaged curve is generated by taking all of the individual curves and averaging them together. This is done by progressing along the z_{sep} list, combining their points into a binned point, averaging each bin, then calculating the standard deviation of each bin.

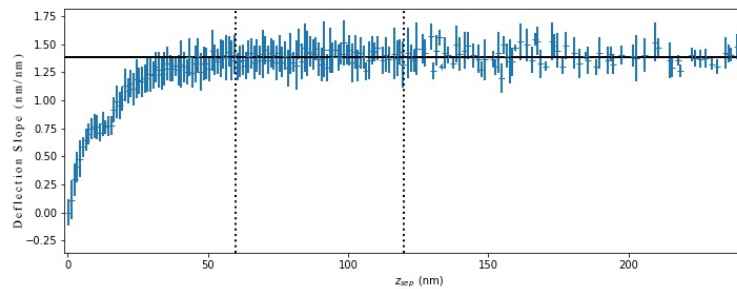


Figure 4.8 An example plot of the averaged approach gradient. The "approach gradient" in this context refers to the slope of the deflection as the AFM tip approaches the surface. Specifically, it is the rate at which the deflection changes as the AFM piezoelectric element moves the cantilever closer to the sample surface. This gradient provides insight into the force interactions occurring as the tip nears the surface, which is critical for understanding phenomena like the "jump to contact." This graph focuses specifically on the region after contact and the area used to define contact is highlighted by vertical dotted black lines (aka the defined contact region). The horizontal black line indicates the extrapolation of the data. In this case the data is binned to reduce noise. The height of each blue bar indicates the standard deviation for each point.

In order to ensure that the region defined by the operator is correct, a number of diagnostic graphs were produced in order to aid the selection process. The gradient of the deflection is calculated with respect to the stage height in order to highlight the transition between the movement phase and the contact phase

of the graph. This is done for individual curves as well as an averaged curve (see 4.8).

These curves are then all plotted on top of one another to check that all curves follow the same rough shape (see fig 4.9).

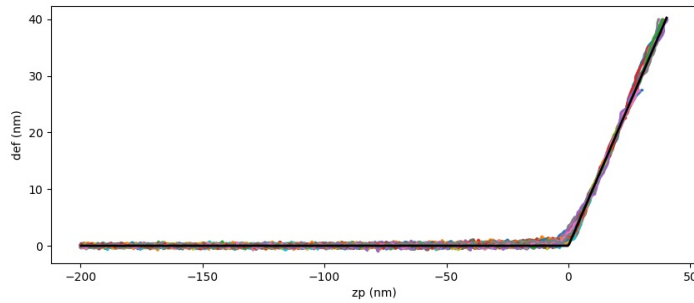


Figure 4.9 An example plot of all the curves for a given site processed up until this point. A reference black line is overlaid demonstrating what a curve would look like with only terminal electrostatic repulsion. This figure represents about 100 curves aligned atop one another.

This resolves in a final averaged and binned force curve (see fig 4.10)

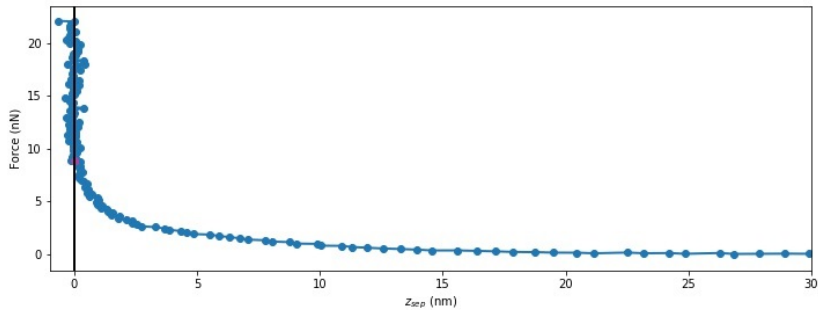


Figure 4.10 An example plot of the final processed force curve. The y axis has been translated to show the distance from contact, with a black line highlighting the defined point of contact. The datapoint used to define the force at contact is highlighted in red.

Afterwards the focus of the script changes to calculating the force applied at contact. Positive forces indicate a repulsive force, negative forces indicate an attractive force. A Savitzky–Golay filter is applied to the data to reduce the noise intrinsic to the data. [77] Then the curve is followed algorithmically until it passes over the threshold point - by default, this threshold is defined as the point where the separation between the AFM tip and the surface is 0 nanometers, indicating physical contact.

This is done for each individual curve, eventually resulting in a histogram of contact forces (see fig 4.11). This provided an insight into the variance between each of the curves, with a wide distribution indicating improper calibration settings for some of the curves. In the cases of outliers, their individual curves were reviewed and used to improve the fitting parameters.

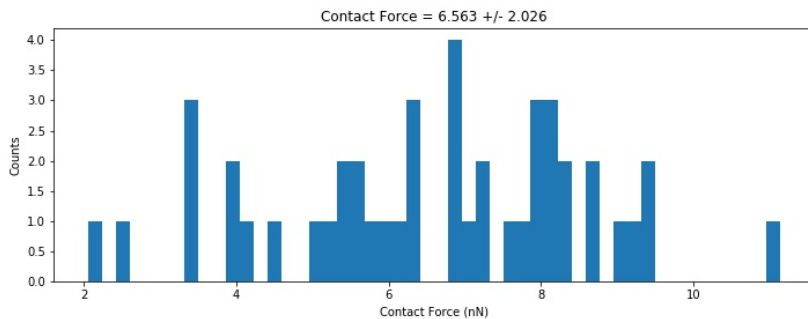


Figure 4.11 An example of a histogram produced from a set of curves for specific site. The mean force is given at the top with the standard deviation.

Contact force refers to the force exerted when the AFM tip makes physical contact with the sample surface. This force is measured at the precise moment when the separation between the AFM tip and the surface reaches zero. It can be either repulsive or attractive depending on the nature of the interaction between the tip and the sample. Positive values indicate a repulsive force, often due to surface stiffness or electrostatic repulsion, while negative values signify an attractive force, such as van der Waals forces or adhesion.

In all cases the total number of individual graphs per final force datapoint is between 80-200 curves.

4.2.4 Validation of results

In order to validate that the data produced by the procedure met the precedence set by theory, the Debye length was experimentally determined. This approximation of the Debye length (κ) was calculated using the equation outlined in chapter 1 (see eqn 1.2). The experimentally calculated value was then checked against the approximated Debye length across a sweep of concentrations. This was in part to ensure that the procedure gave sensible results as well as a means of detecting invisible sources of contamination.

This procedure produced sensible Debye length measurements according to the preliminary data (see fig 4.12). As a result this procedure was used for subsequent experiments. The Debye length of the interacting silica sphere was calculated by calculating the equation of the curve during the interaction phase and extracting the exponent component (i.e. between the approach and contact phases).

This Debye length measurement procedure indicates strongly that the chosen experimental and processing protocol is appropriate. Additionally the influence of contaminants have been reduced to a minimum from said revised protocol.

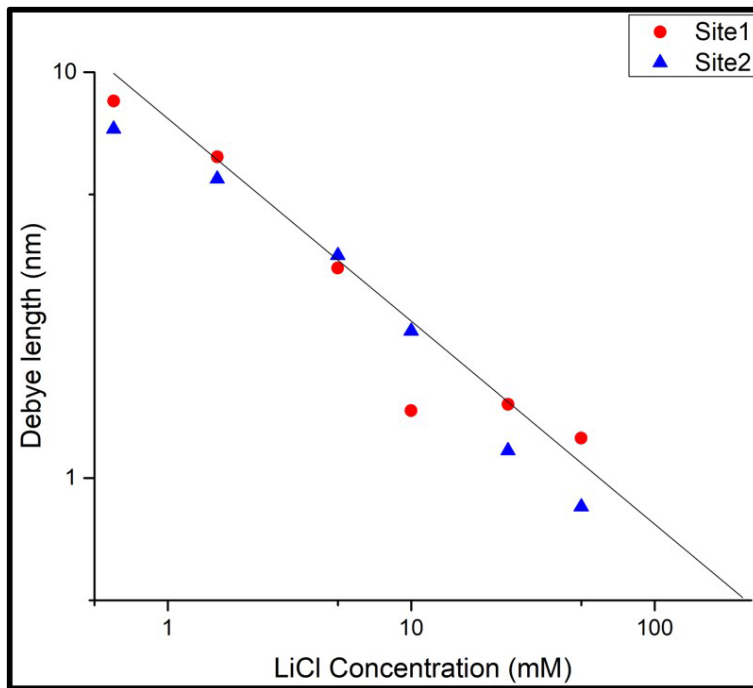


Figure 4.12 A preliminary graph produced to investigate the expected Debye length vs the recorded Debye length at different salt concentrations. The black line indicates the approximated κ , whereas site one and two are two different recording areas on the glass surface.

4.3 Nanowizard

Over the course of the investigation the availability of an alternative AFM became available. When compared to the MFP-1D, the setup is very similar, with one notable exception. This AFM allows for free horizontal control coupled to the AFM head, instead of requiring the operator to disengage each time. Aside from the time saved between changing sites, this allows for techniques such as force mapping to be used (See chapter 2). The setup procedure remained the same as defined before during use with this AFM with any difference being software based, and thus an unnecessary detail for this report.

Fortunately the previously established sample preparation and cleaning procedure was adapted with little difficulty with the experimental throughput considerably increased. The tip speed was set to the previously defined speed, 1 $\mu\text{m/s}$ as well as the peak force at 8 nN, unless otherwise stated.

4.3.1 Analysis differences for JPK NanoWizard

The output from the Nanowizard was exported from the proprietary JPK file format and refitted to work with the script described above. While the differences in output data structure is dramatic, this was handled by a short reformatting

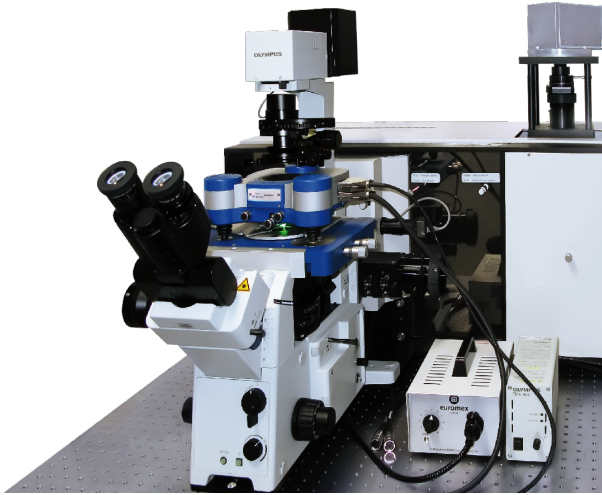


Figure 4.13 Operation setup for the Nanowizard AFM that was used for force measurements [3].

script to translate the data into a usable format. The only differences of note between the two is that the JPK format has fewer significant figures compared to the previous methods.

In the case of force mapping, there are considerably less curves per site. At this point, the previously established curves produced by the MFP-1D for each concentration were used for comparison. Each of the curves is then processed by the script, with a note taken of its $x,y \mu\text{m}$ offset. Afterwards the averaged contact force (for approach) or adhesive force (for retract) is plotted on a heat map. For each heat map a 10×10 grid was processed, with at minimum 3 curves per site taken, with a $1 \mu\text{m}$ distance between each site. It should be noted that the software processes an entire grid first, which is to say each site is repeated after all sites of the current grid are done.

4.4 Development and Significance of the Force Curve Analysis Software

The analysis software developed during this research plays a pivotal role in the extraction and interpretation of force curves obtained via Atomic Force Microscopy (AFM). The ability to automatically process large volumes of data with high accuracy and consistency is a key contribution of this thesis, making the software not just a tool, but a significant contribution to the field.

Traditional methods of AFM data analysis often rely on manual interpretation of force curves, which can introduce variability and error due to human judgment. While earlier software tools provided some level of automation, they often lacked the flexibility to handle complex datasets or adapt to the specific needs of different experiments. Equally, the availability of the software is often tied to

specific manufacturers and distributors, which limits accessibility. The software developed in this thesis builds on these earlier approaches by offering a more robust, adaptable, and user-friendly platform that can be adapted to any set of results.

This software was designed to address several key challenges. Firstly, by incorporating advanced smoothing techniques, such as the Savitzky-Golay filter, the software effectively reduces intrinsic noise while preserving critical features of the data, such as the 'shelf' observed in certain force profiles. Secondly, the variable-size binning approach allows for more precise control over data smoothing, enabling the detection of subtle force interactions that might be lost in more rigid binning protocols. Finally, the software automates curve fitting to theoretical models, reducing the need for manual intervention and ensuring that the analysis is both consistent and reproducible across different datasets.

One of the significant improvements brought by this software is its robustness against the variability inherent in AFM data. This robustness is particularly evident when comparing the software's performance with older systems that may produce noisier data. The ability to extract meaningful information from such data extends the lifespan of older AFMs, making them viable for current research without the immediate need for expensive upgrades.

The softwares robustness was validated through the analysis in this thesis, given in the following chapters. The consistency of the Debye length calculations across different concentrations, as well as the successful extraction of the 'shelf' feature in noisy data, are testaments to its reliability.

By making this software open source and accessible to the broader scientific community, this thesis not only contributes to the field of AFM but also democratizes access to high-quality data analysis tools. The flexibility of the software allows researchers to adapt it to their specific needs, potentially leading to new discoveries and innovations in surface force studies. It bridges the gap between traditional manual methods and the need for high-throughput, consistent analysis in modern AFM studies.

Chapter 5

Analysis of Approach Force Curves in Colloidal Systems

This chapter aims to serve a simple goal. To provide a clear route to extract the force at contact from raw data. As the raw unprocessed data is severely voluminous the scope of this chapter is kept to one goal, provide the data and justification for the contact forces calculated for each concentration, site and parameter. The results of this analysis is then concluded in Chapter 7, which, is free of the need to justify every data point and thus focuses on the conclusions from this data.

This data, along with the further analysis provided in chapter 7 is expanded upon, and insights are drawn from this in turn. In order to aid readability/referenceability, this chapter focuses on the data collected during the

5.1 MFP-1D contact force derivation

For the data collected from the MFP-1D the analytical approach to this elucidation is given in Chapter 4. This section will overview the results for the following LiCl concentrations: 0.6mM, 1.6mM, 5mM, 10mM, 25mM, 50mM, 230mM, 550mM. For each concentration multiple sites are analysed, highlighting features of each curve in preparation for analysis.

5.1.1 A note on rejected curves

During the process, several curves were rejected from the data set as part of the processing method. Due to the sheer volume of curves involved in this analysis. This was either due to machine failure to engage in the surface, or due to significant noise due to mechanical failure (over-correction in piezo movement by the AFM or vibrations in the building.) While the initial curves taken on the machine were too noisy, further repeats and refinements to the procedure eventually resulted in usable curves. In some of the data collected, the impact

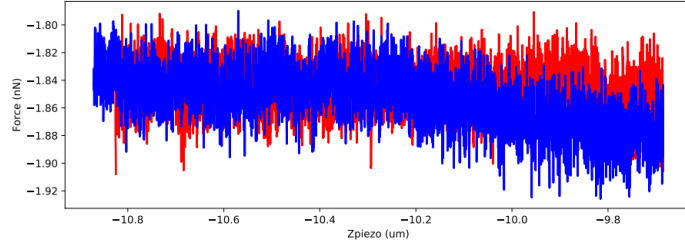


Figure 5.1 A graph demonstrating a rejected curve. In this case the AFM failed to reach the surface for the recorded data, leading to a single up and down motion.

from residual vibrations was mitigated in later datasets by operating the AFM in the night. Other improvements were found by optimising the AFM parameters - such as tip speed, data collection rate and target force. The optimal parameters found were 0.5Hz for tip speed, setting the data collection rate to maximum and a target force of 8-12 nN.

The other reason for rejected curves was due to the shift of the snapshot window providing too little data in either the approach phase or the contact phase (covered in Chapter 4).

5.1.2 Contact force calculations

In this results section, the contact force graphs displayed represent only a subset of the total analyzed graphs, selected to illustrate the most significant aspects of the analysis procedure. The ones chosen here represent the typical majority of the curves, with outliers not reflected in the dataset. Outliers may be demonstrated, and will be commented on if presented. The remainder of the curves, not shown here, played an instrumental role in guiding the parameter optimization process for the data processing script. This process involved the review and refinement of several hundred thousand curves in order to deal with the noise intrinsic to the system. Ensuring a good fit for these curves is paramount; otherwise, one risks obtaining erratic and misleading graphs that could compromise the integrity of the data interpretation. The selection process for the resulting curves involved the exclusion of certain outliers and repeat measurements, a necessary step taken to refine the data and enhance the clarity of the observed trends. Three types of graphs were chosen for their analysis of the fitting parameters and results: the histogram of contact forces provides a statistical view of the interaction forces at the point of contact, demonstrating the range of forces across the graph. The log-linear plot of the force as a function of the Z-piezo position (in nanometers), highlighting of the separation distance between the AFM tip and the sample surface during the interaction phase. At the top of the graph the transition to the contact phase can be seen. This point of transition is the contact force. The logarithmic scale for force highlights the sensitivity of the AFM in detecting forces at the nanoscale. Finally the overall approach force curve derived from binned

data presents a view of the resulting averaged force curve behavior during the approach phase. Each graph was selected for its ability to support the chosen parameters and thus the resulting contact force.

5.1.3 Diversity and Range of Data Points

Each site and corresponding graph included in Chapter 5 were selected to represent the wide range of experimental conditions explored in this study. The diversity of salt concentrations (ranging from 0.6mM to 550mM) provides a comprehensive view of how the interactions between colloidal particles change under different ionic strengths. By including data from various sites, the results shown are not biased by localized effects, but are reflective of the overall behavior of the system. This approach highlights trends across the dataset, such as the transition from repulsive to attractive forces as the salt concentration increases, which is required for understanding the underlying mechanisms governing colloidal stability.

The "shelf" feature observed in some of the following force profiles is of particular interest because it indicates a potential secondary interaction mechanism that might not be explained by traditional DLVO theory alone. The inclusion of these specific sites and graphs where the shelf feature is prominent was intentional. Highlighting this phenomenon is important because it may suggest the presence of complex surface interactions, possibly related to surface roughness or heterogeneities, which could have significant implications for the interpretation of force measurements in colloidal systems.

The presence of the shelf at different concentrations and its persistence across various sites suggest that it is not a random artifact but a consistent phenomenon that warrants deeper analysis. Including these graphs provides a more complete picture of the force interactions at play and challenges us to consider additional factors that may influence colloidal stability beyond those traditionally considered in DLVO theory. A dedicated analysis of this observation is provided later in section 8.3. This shelf feature isn't without literature precedent however, as it has been observed previously. [49] [37]

5.1.4 0.6mM Site 1

Site one demonstrates one of the difficulties with collecting the data at the lower ranges of the molar concentrations. As the repulsive force is over a wider range there is a smaller window captured of the contact phase. This means that when trying to fit to the data, there is less data available to provide a solid fit. As such, a slight bowing effect is seen in the binned average curve.

38 curves in total were processed. Of these processed curves the average contact force was $5.2 \text{ nN} \pm 1.5 \text{ nN}$.

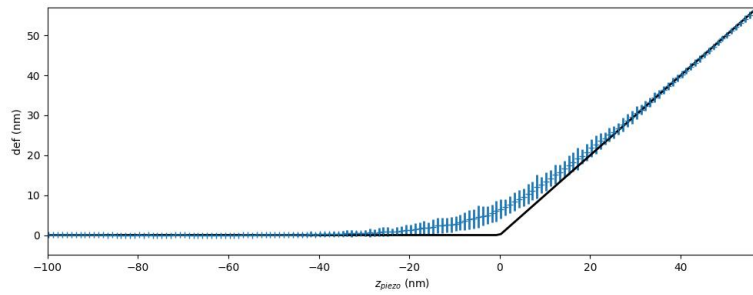


Figure 5.2 A graph demonstrating the binned average curve post fit for 0.6mM LiCl at contact site 1.

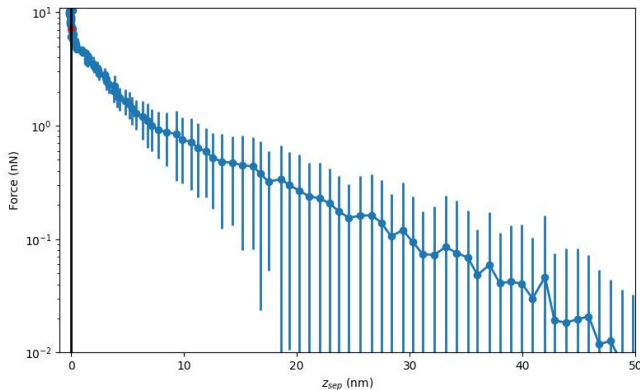


Figure 5.3 A log-linear plot of the force as a function of the Z-piezo position, highlighting the interaction phase for 0.6mM LiCl at contact site 1.

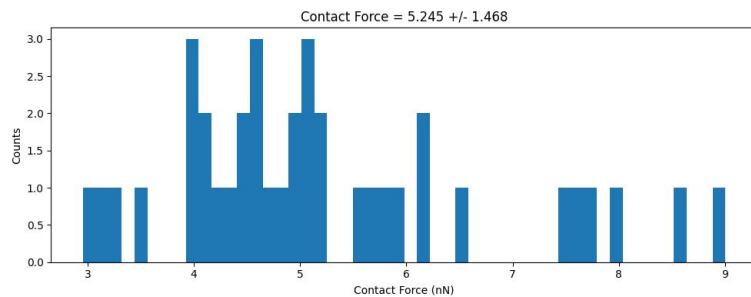


Figure 5.4 A graph demonstrating the force histogram calculated from the range of curves for 0.6mM LiCl at contact site 1. The averaged contact force with the standard deviation is given above.

5.1.5 0.6mM Site 2

Site two demonstrates the lowest observed force for this concentration, highlighting a high degree of variability between sites. However, this may be due to difficulty in finding a good fit. As the maximum contact force was capped, some of the curves ended within the contact region, or just after, limiting the number of viable curves.

13 curves in total were processed. Of these processed curves the average contact force was $3.6 \text{ nN} \pm 0.3 \text{ nN}$.

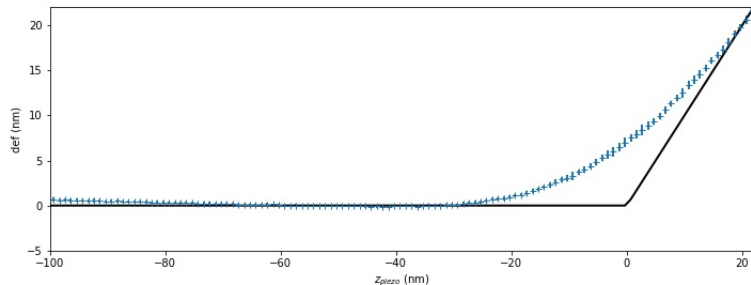


Figure 5.5 A graph demonstrating the binned average curve post fit for 0.6mM LiCl at contact site 2.

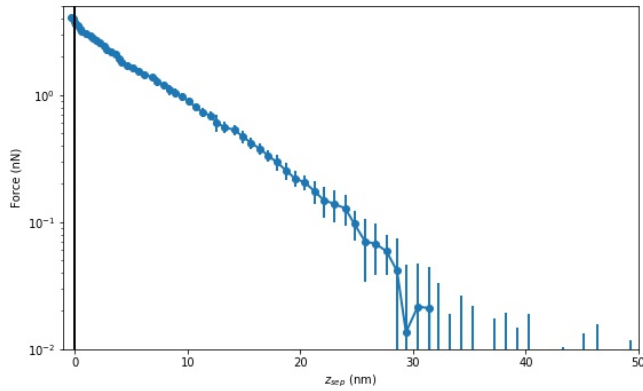


Figure 5.6 A log-linear plot of the force as a function of the Z-piezo position, highlighting the interaction phase for 0.6mM LiCl at contact site 2.

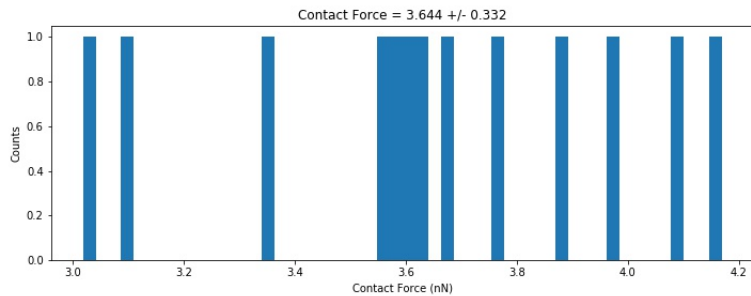


Figure 5.7 A graph demonstrating the force histogram calculated from the range of curves for 0.6mM LiCl at contact site 2. The averaged contact force with the standard deviation is given above.

5.1.6 0.6mM Site 3

Site three demonstrates an ideally fitted curve, however in the log-linear plot an irregularity is seen - the point in which the contact force area is raised up the graph. This is due to the large amount of noise seen during this interface phase, giving a large variation in the contact force histogram.

29 curves in total were processed. Of these processed curves the average contact force was $4.7 \text{ nN} \pm 1.4 \text{ nN}$.

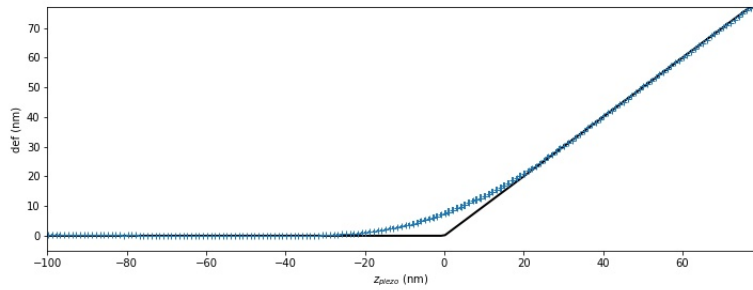


Figure 5.8 A graph demonstrating the binned average curve post fit for 0.6mM LiCl at contact site 3.

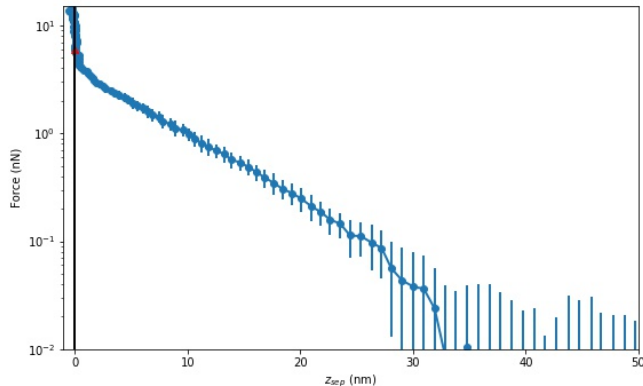


Figure 5.9 A log-linear plot of the force as a function of the Z-piezo position, highlighting the interaction phase for 0.6mM LiCl at contact site 3.

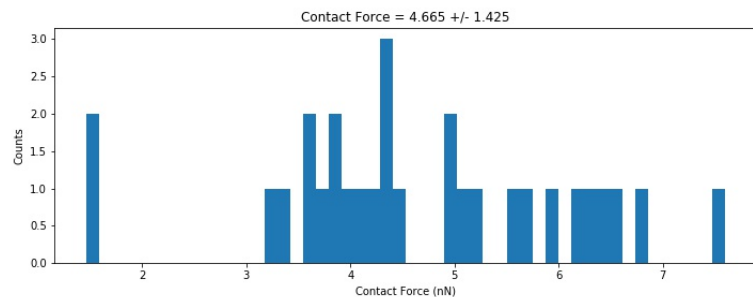


Figure 5.10 A graph demonstrating the force histogram calculated from the range of curves for 0.6mM LiCl at contact site 3. The averaged contact force with the standard deviation is given above.

5.1.7 1.6mM Site 1

Site one represents a good example of a typical well-behaved curve, where the processing is able to extract out a clear signal from the noise, and thus a clearly distributed contact force.

140 curves in total were processed. Of these processed curves the average contact force was $2.6 \text{ nN} \pm 0.6 \text{ nN}$

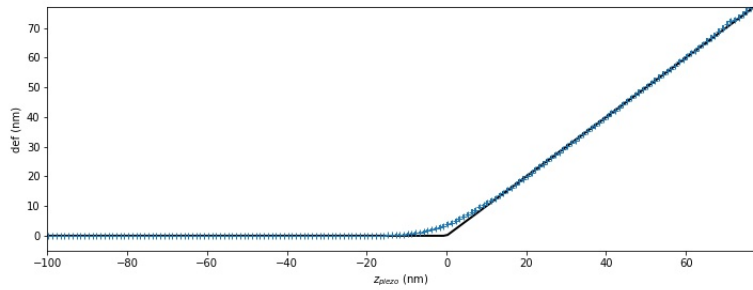


Figure 5.11 A graph demonstrating the binned average curve post fit for 1.6mM LiCl at contact site 1.

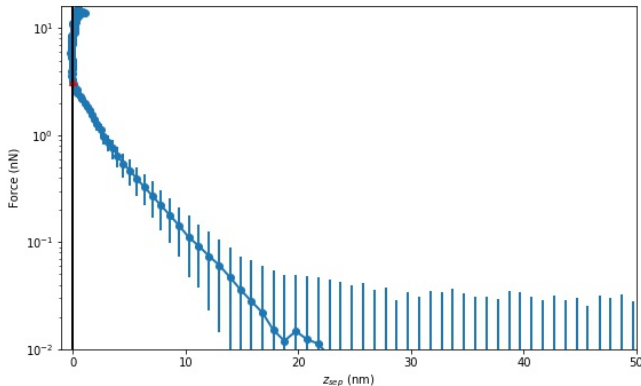


Figure 5.12 A log-linear plot of the force as a function of the Z-piezo position, highlighting the interaction phase for 1.6mM LiCl at contact site 1.

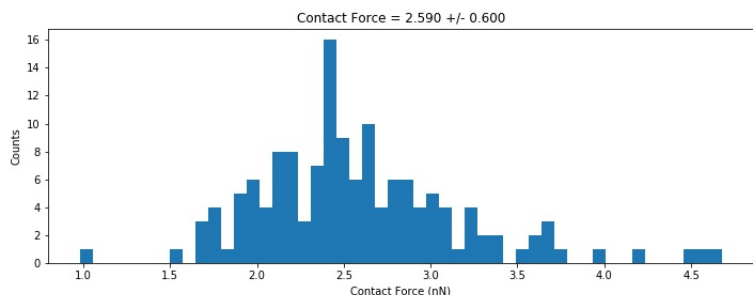


Figure 5.13 A graph demonstrating the force histogram calculated from the range of curves for 1.6mM LiCl at contact site 1. The averaged contact force with the standard deviation is given above.

5.1.8 1.6mM Site 2

Site 2 demonstrates an interesting feature - a region where there seems to be two contact phases. As DLVO doesn't explain any dual barrier features this is rather unexpected. One explanation may be that as the two surfaces approach one another some aspect (for example a small topographical protrusion or a small aggregate of ions) prevents full contact between the sphere and surface, which

then slips or is overcome, allowing full contact later. It is important to note that this feature is present throughout the dataset, and survived the binning and averaging process, and thus is a consistent feature in this site.

113 curves in total were processed. Of these processed curves the average contact force was $4.5 \text{ nN} \pm 0.5 \text{ nN}$

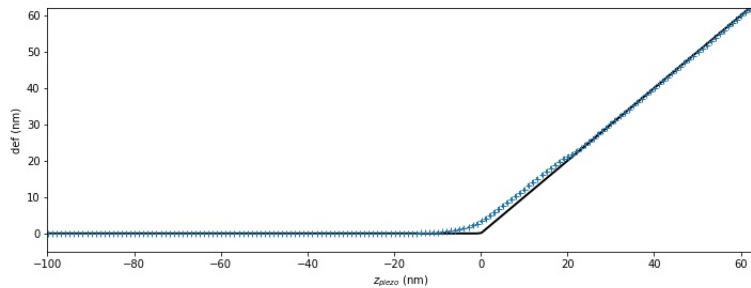


Figure 5.14 A graph demonstrating the binned average curve post fit for 1.6mM LiCl at contact site 2.

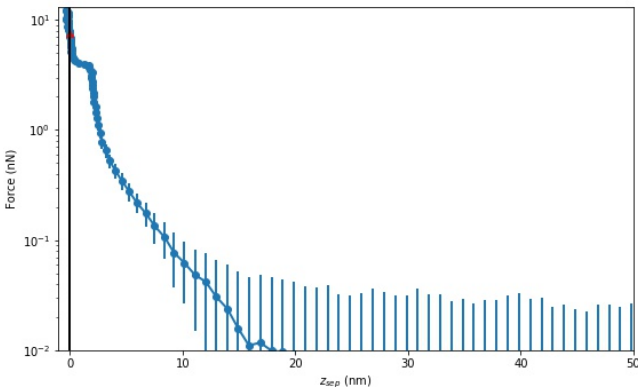


Figure 5.15 A log-linear plot of the force as a function of the Z-piezo position, highlighting the interaction phase for 1.6mM LiCl at contact site 2.

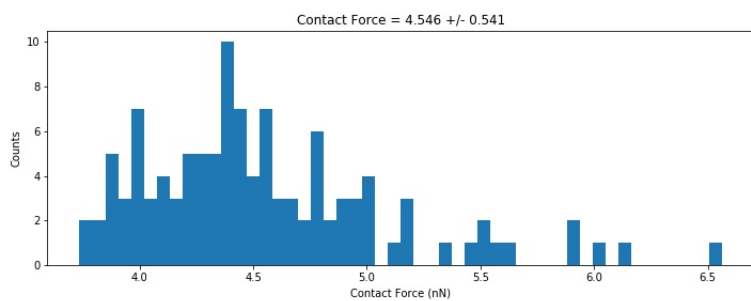


Figure 5.16 A graph demonstrating the force histogram calculated from the range of curves for 1.6mM LiCl at contact site 2. The averaged contact force with the standard deviation is given above.

5.1.9 5mM Site 1

Site one demonstrates a similar, but weaker feature seen in 1.6 mM site 2 observable in the log-lin plot. The overall binned fit demonstrates a suitable fit, so it remains to be a feature of this site. Equally, this site demonstrates the weakest repulsive force in the set.

128 curves in total were processed. Of these processed curves the average contact force was $2.2 \text{ nN} \pm 0.5 \text{ nN}$

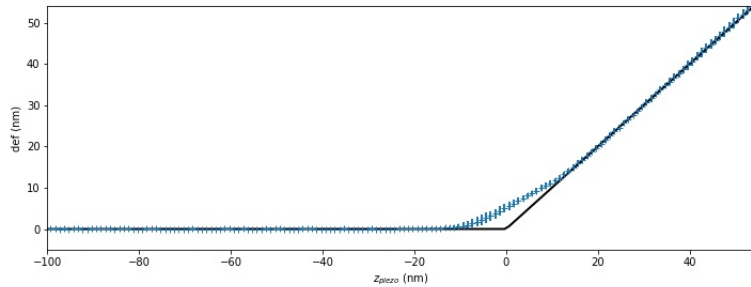


Figure 5.17 A graph demonstrating the binned average curve post fit for 5mM LiCl at contact site 1.

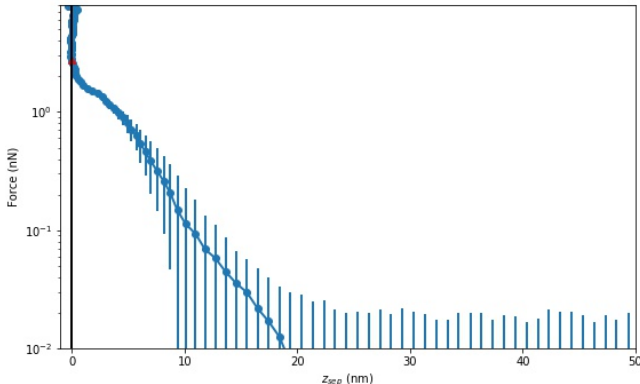


Figure 5.18 A log-linear plot of the force as a function of the Z-piezo position, highlighting the interaction phase for 5mM LiCl at contact site 1.

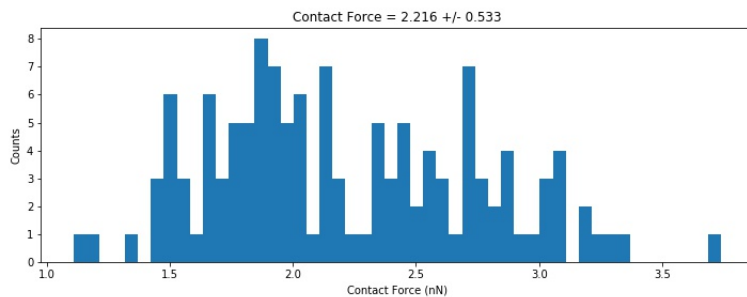


Figure 5.19 A graph demonstrating the force histogram calculated from the range of curves for 5mM LiCl at contact site 1. The averaged contact force with the standard deviation is given above.

5.1.10 5mM Site 2

Site two demonstrates the same feature, but slightly less prominent again. 110 curves in total were processed. Of these processed curves the average contact force was $3.1 \text{ nN} \pm 0.7 \text{ nN}$

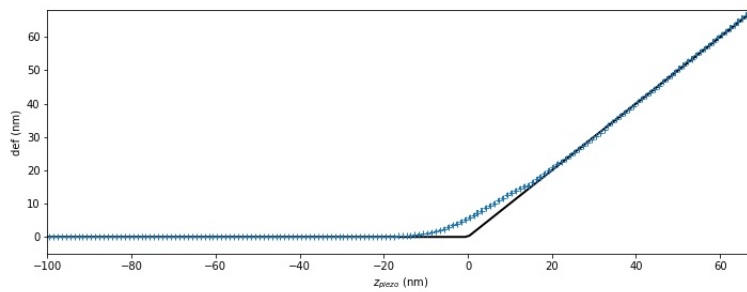


Figure 5.20 A graph demonstrating the binned average curve post fit for 5mM LiCl at contact site 2.

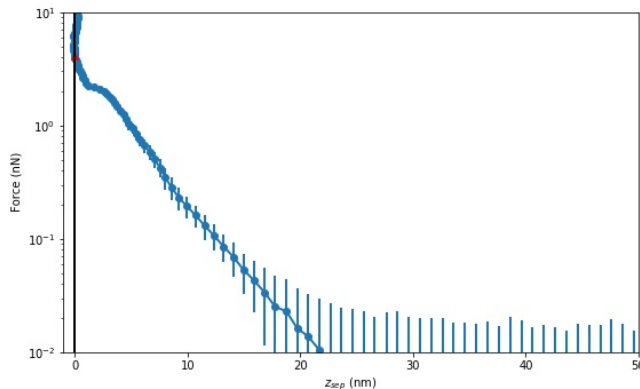


Figure 5.21 A log-linear plot of the force as a function of the Z-piezo position, highlighting the interaction phase for 5mM LiCl at contact site 2.

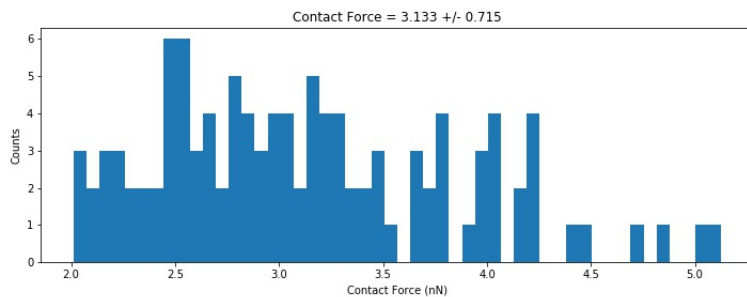


Figure 5.22 A graph demonstrating the force histogram calculated from the range of curves for 5mM LiCl at contact site 2. The averaged contact force with the standard deviation is given above.

5.1.11 5mM Site 3

Site three once again has the feature seen across all of the force curves at this concentration

114 curves in total were processed. Of these processed curves the average contact force was $3.8 \text{ nN} \pm 0.5 \text{ nN}$

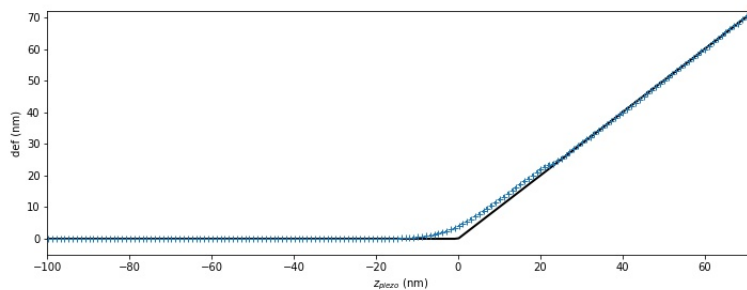


Figure 5.23 A graph demonstrating the binned average curve post fit for 5mM LiCl at contact site 3.

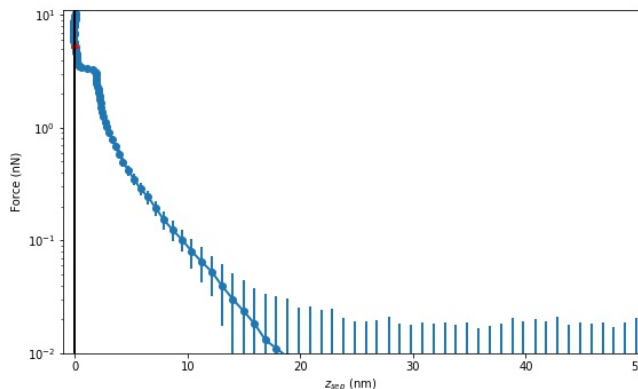


Figure 5.24 A log-linear plot of the force as a function of the Z-piezo position, highlighting the interaction phase for 5mM LiCl at contact site 3.

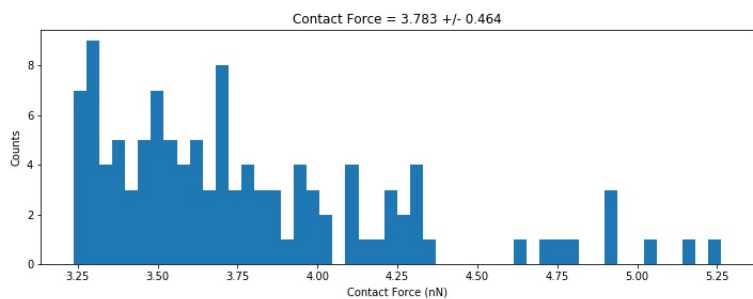


Figure 5.25 A graph demonstrating the force histogram calculated from the range of curves for 5mM LiCl at contact site 3. The averaged contact force with the standard deviation is given above.

1.6 mM site 2 and 5 mM presents an interesting and repeatable shelf seen in the force profiles across all different sites. There are a number of theories as to what this feature may be. For one If the AFM tip encounters a region of the sample with a topological feature that does not mesh well with the surface it could provide the observed barrier. This feature can then hold the tip back from fully sliding down until a threshold force determined by the surface roughness is presented. Once this threshold force is overcome it then "slips" down further into contact.

5.1.12 10mM Site 1

Site 1 demonstrates a noisy top of the graph, which can sometimes happen when the AFM oversteers and provides too much force onto the sample.

130 curves in total were processed. Of these processed curves the average contact force was $1.8 \text{ nN} \pm 1.1 \text{ nN}$

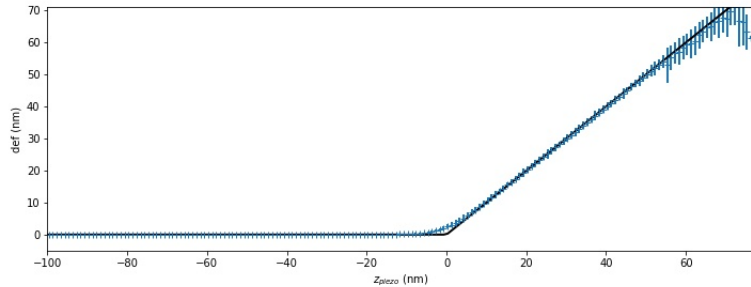


Figure 5.26 A graph demonstrating the binned average curve post fit for 10mM *LiCl* at contact site 1.

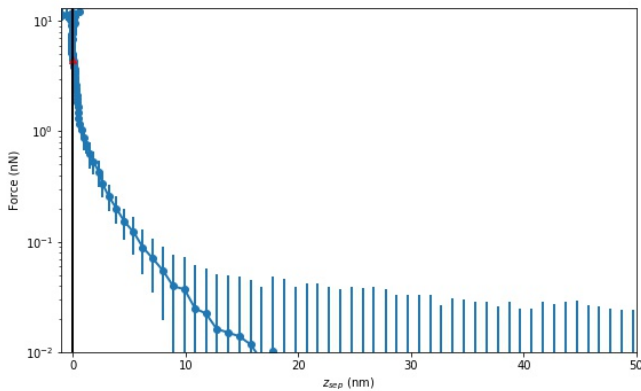


Figure 5.27 A log-linear plot of the force as a function of the Z-piezo position, highlighting the interaction phase for 10mM *LiCl* at contact site 1.

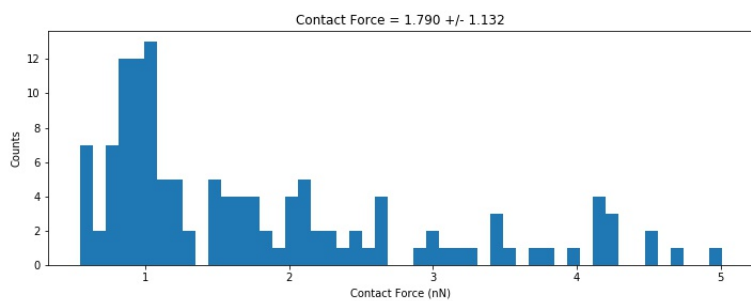


Figure 5.28 A graph demonstrating the force histogram calculated from the range of curves for 10mM *LiCl* at contact site 1. The averaged contact force with the standard deviation is given above.

5.1.13 10mM Site 2

119 curves in total were processed. Of these processed curves the average contact force was $3.8 \text{ nN} \pm 0.4 \text{ nN}$

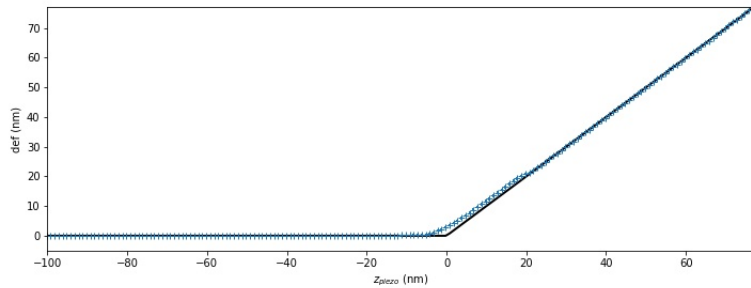


Figure 5.29 A graph demonstrating the binned average curve post fit for 10mM LiCl at contact site 2.

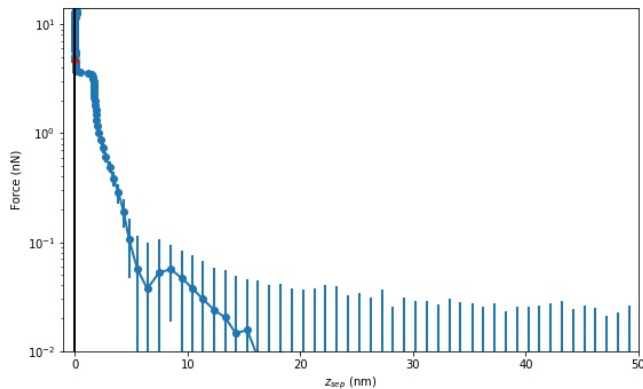


Figure 5.30 A log-linear plot of the force as a function of the Z-piezo position, highlighting the interaction phase for 10mM LiCl at contact site 2.

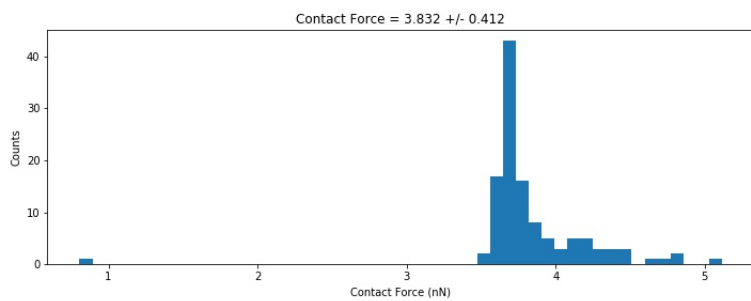


Figure 5.31 A graph demonstrating the force histogram calculated from the range of curves for 10mM LiCl at contact site 2. The averaged contact force with the standard deviation is given above.

5.1.14 10mM Site 3

124 curves in total were processed. Of these processed curves the average contact force was $4.4 \text{ nN} \pm 0.5 \text{ nN}$

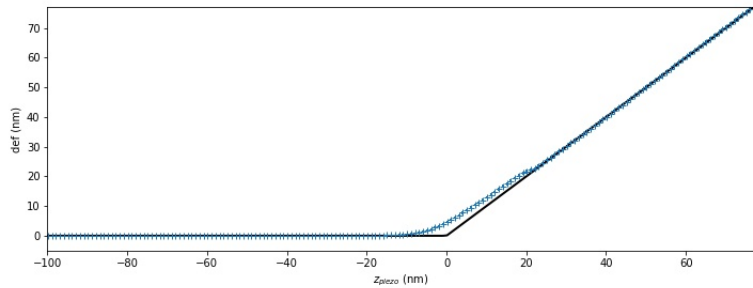


Figure 5.32 A graph demonstrating the binned average curve post fit for 10mM LiCl at contact site 3.

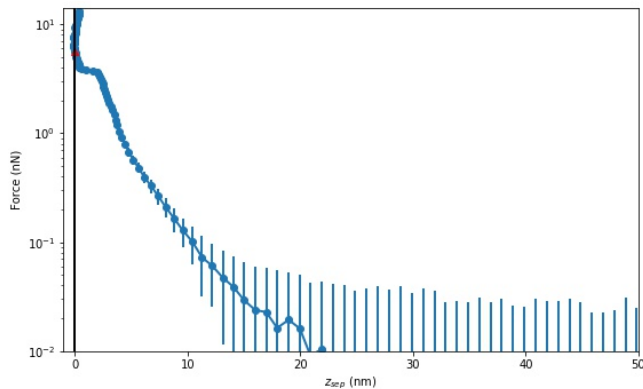


Figure 5.33 A log-linear plot of the force as a function of the Z-piezo position, highlighting the interaction phase for 10mM LiCl at contact site 3.

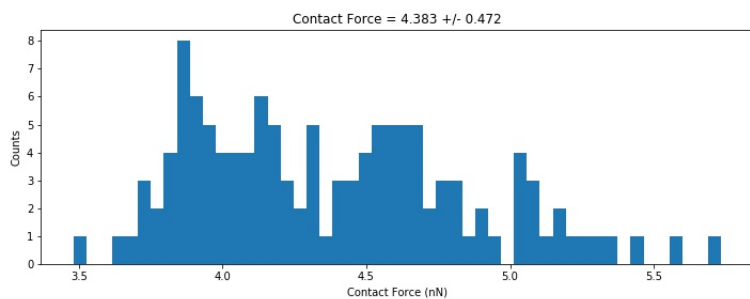


Figure 5.34 A graph demonstrating the force histogram calculated from the range of curves for 10mM LiCl at contact site 3. The averaged contact force with the standard deviation is given above.

5.1.15 25mM Site 1

Site 1 demonstrates a high degree of noise in the binned average curve and demonstrates towards what curves could be without the involved processing

144 curves in total were processed. Of these processed curves the average contact force was $2.2 \text{ nN} \pm 1.7 \text{ nN}$

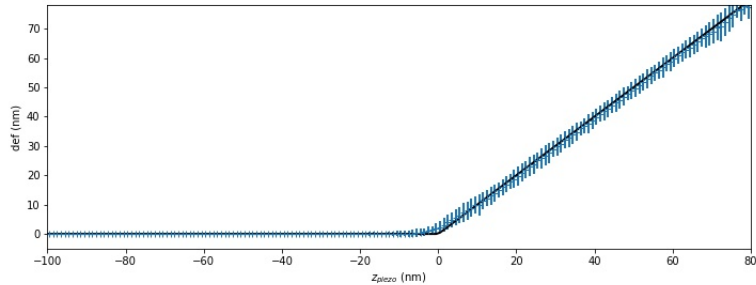


Figure 5.35 A graph demonstrating the binned average curve post fit for 25mM LiCl at contact site 1.

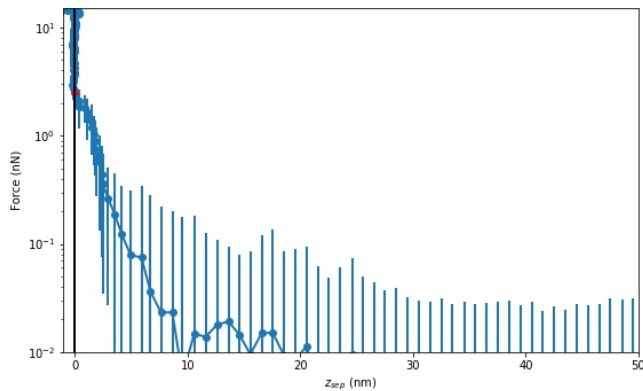


Figure 5.36 A log-linear plot of the force as a function of the Z-piezo position, highlighting the interaction phase for 25mM LiCl at contact site 1.

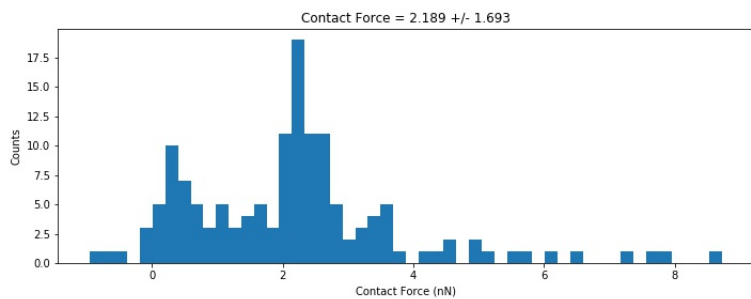


Figure 5.37 A graph demonstrating the force histogram calculated from the range of curves for 25mM LiCl at contact site 1. The averaged contact force with the standard deviation is given above.

5.1.16 25mM Site 2

Site 2 also demonstrates a shelf feature.

124 curves in total were processed. Of these processed curves the average contact force was $2.7 \text{ nN} \pm 1.1 \text{ nN}$

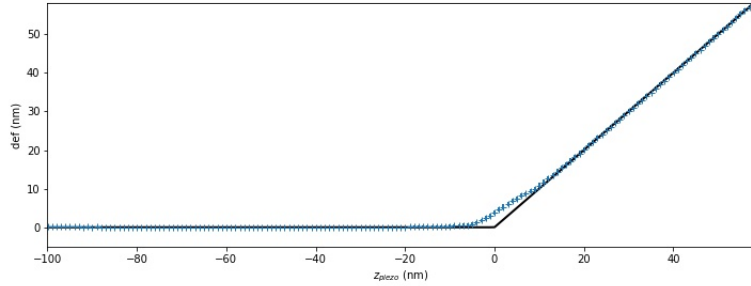


Figure 5.38 A graph demonstrating the binned average curve post fit for 25mM LiCl at contact site 2.

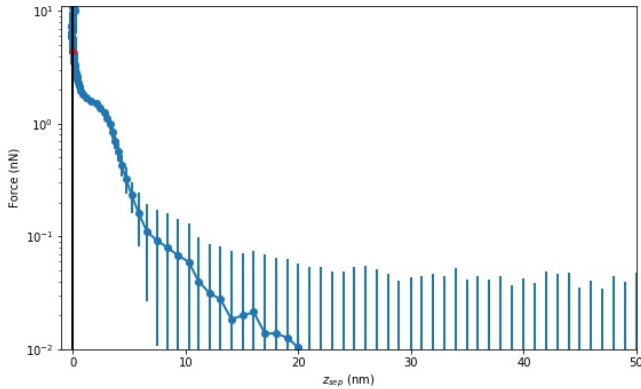


Figure 5.39 A log-linear plot of the force as a function of the Z-piezo position, highlighting the interaction phase for 25mM LiCl at contact site 2.

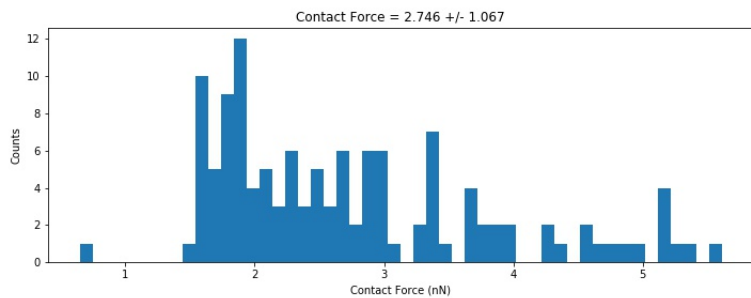


Figure 5.40 A graph demonstrating the force histogram calculated from the range of curves for 25mM LiCl at contact site 2. The averaged contact force with the standard deviation is given above.

5.1.17 25mM Site 3

76 curves in total were processed. Of these processed curves the average contact force was $3.9 \text{ nN} \pm 1.5 \text{ nN}$

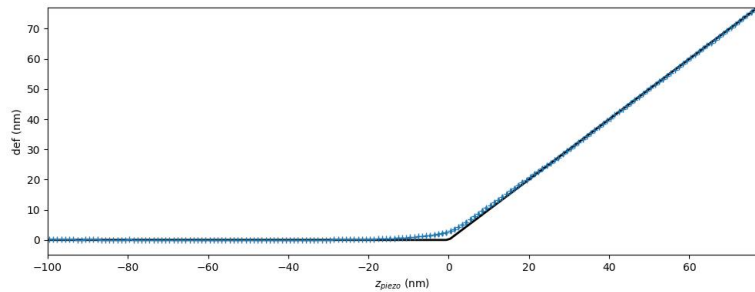


Figure 5.41 A graph demonstrating the binned average curve post fit for 25mM LiCl at contact site 3.

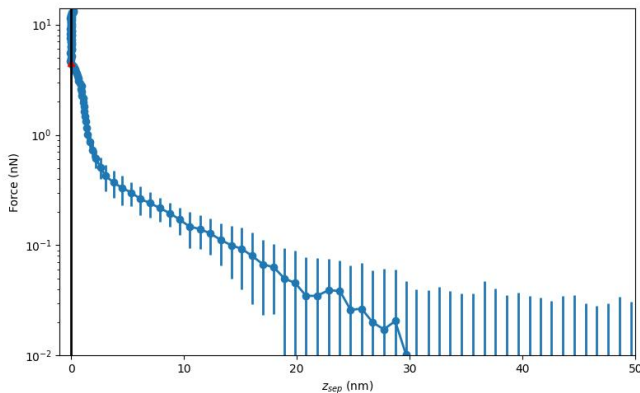


Figure 5.42 A log-linear plot of the force as a function of the Z-piezo position, highlighting the interaction phase for 25mM LiCl at contact site 3.

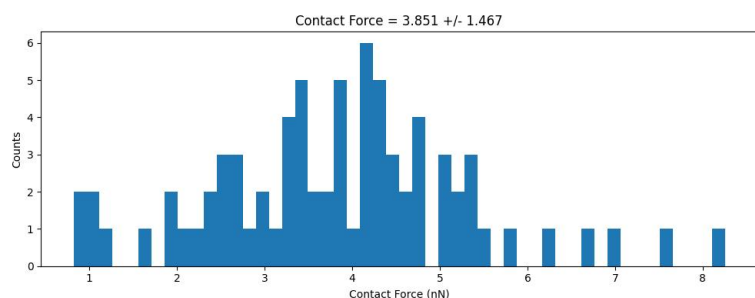


Figure 5.43 A graph demonstrating the force histogram calculated from the range of curves for 25mM LiCl at contact site 3. The averaged contact force with the standard deviation is given above.

5.1.18 50mM Site 1

50mM both demonstrates the presence of the shelf feature, as well the contact force following the trend of decreasing over time.

104 curves in total were processed. Of these processed curves the average contact force was $3.3 \text{ nN} \pm 0.6 \text{ nN}$

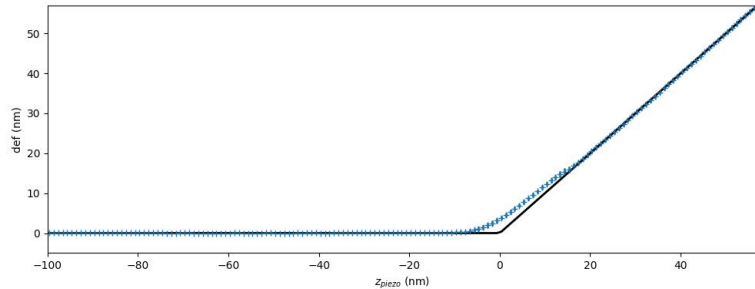


Figure 5.44 A graph demonstrating the binned average curve post fit for 50mM LiCl at contact site 1.

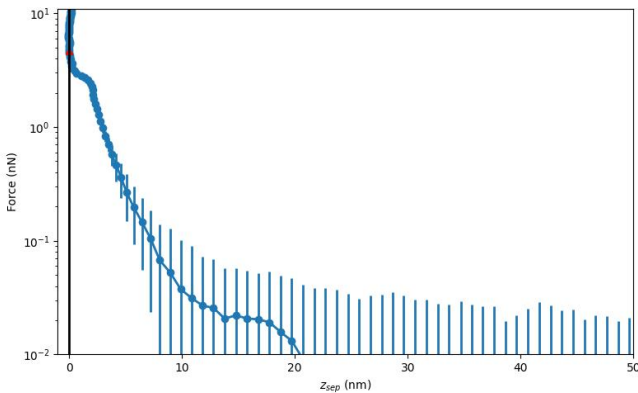


Figure 5.45 A log-linear plot of the force as a function of the Z-piezo position, highlighting the interaction phase for 50mM LiCl at contact site 1.

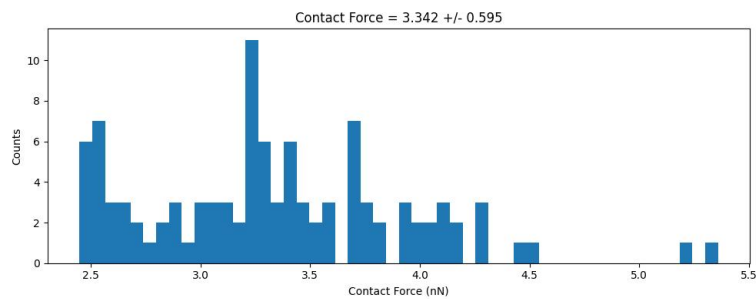


Figure 5.46 A graph demonstrating the force histogram calculated from the range of curves for 50mM LiCl at contact site 1. The averaged contact force with the standard deviation is given above.

5.1.19 50mM Site 2

105 curves in total were processed. Of these processed curves the average contact force was $2.8 \text{ nN} \pm 0.7 \text{ nN}$

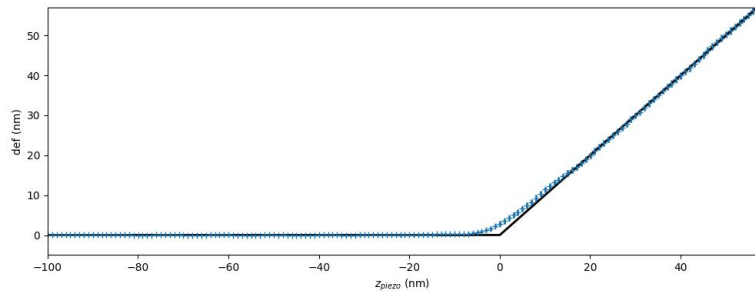


Figure 5.47 A graph demonstrating the binned average curve post fit for 50mM LiCl at contact site 2.

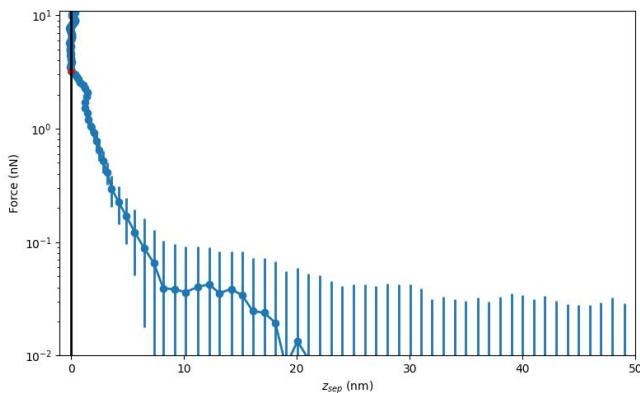


Figure 5.48 A log-linear plot of the force as a function of the Z-piezo position, highlighting the interaction phase for 50mM LiCl at contact site 2.

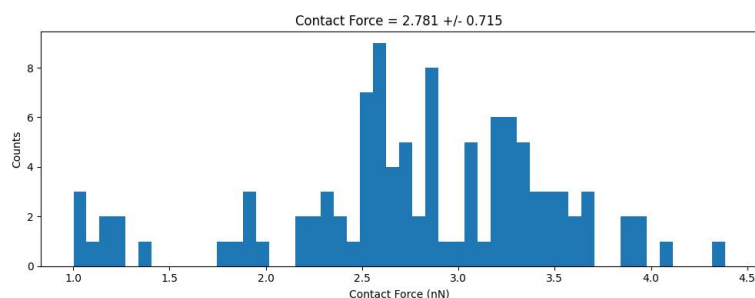


Figure 5.49 A graph demonstrating the force histogram calculated from the range of curves for 50mM LiCl at contact site 2. The averaged contact force with the standard deviation is given above.

5.1.20 230mM Site 1

230mM demonstrates the point in which the repulsive force observed is close to 0. The shelf feature observed in the 230mM data is particularly significant because it suggests a region of weak attraction following the initial contact. This feature is not consistently observed in all graphs, which could be due to variations in local surface roughness, heterogeneity in the colloidal particles, or slight differences in the approach speed of the AFM tip.

109 curves in total were processed. Of these processed curves the average contact force was $2.2 \text{ nN} \pm 0.3 \text{ nN}$

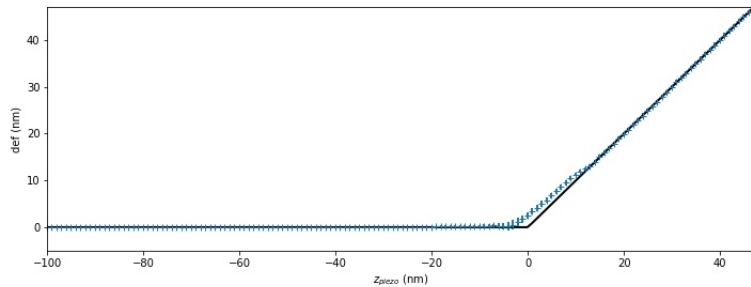


Figure 5.50 A graph demonstrating the binned average curve post fit for 230mM LiCl at contact site 1.

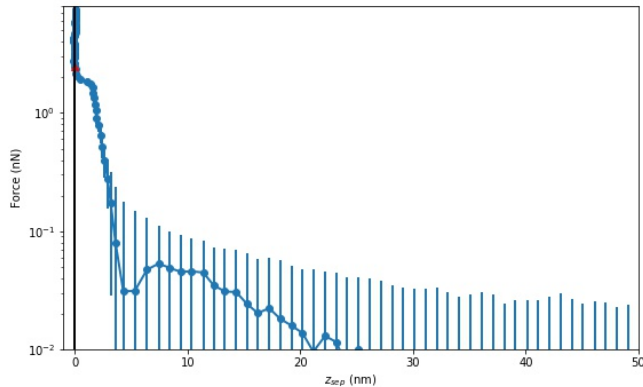


Figure 5.51 A log-linear plot of the force as a function of the Z-piezo position, highlighting the interaction phase for 230mM LiCl at contact site 1.

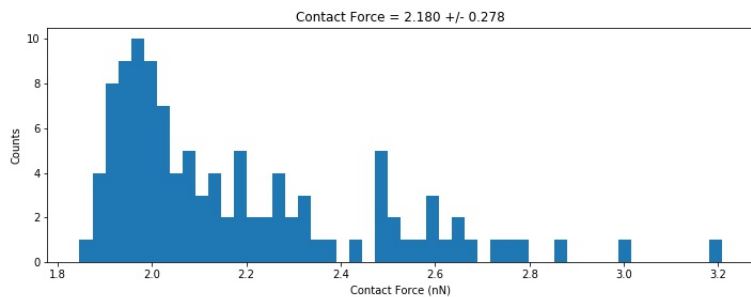


Figure 5.52 A graph demonstrating the force histogram calculated from the range of curves for 230mM LiCl at contact site 1. The averaged contact force with the standard deviation is given above.

5.1.21 230mM Site 2

84 curves in total were processed. Of these processed curves the average contact force was $0.8 \text{ nN} \pm 0.4 \text{ nN}$

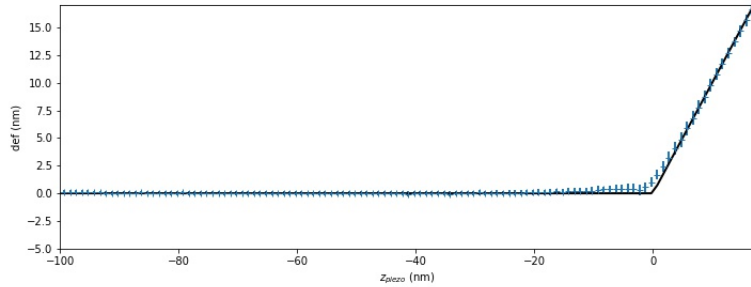


Figure 5.53 A graph demonstrating the binned average curve post fit for 230mM LiCl at contact site 2.

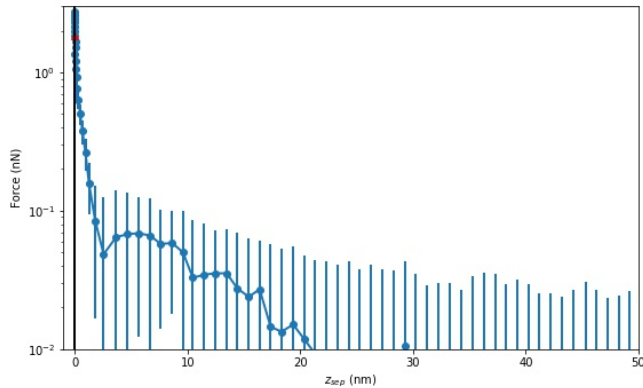


Figure 5.54 A log-linear plot of the force as a function of the Z-piezo position, highlighting the interaction phase for 230mM LiCl at contact site 2.

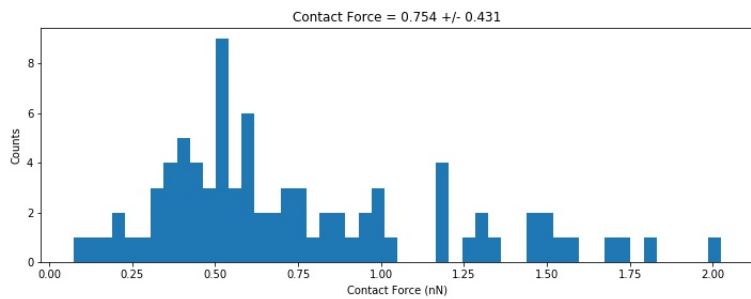


Figure 5.55 A graph demonstrating the force histogram calculated from the range of curves for 230mM LiCl at contact site 2. The averaged contact force with the standard deviation is given above.

5.1.22 550mM Site 1

500mM marks the situation where the charge screen starts to overcome the electrostatic repulsion, giving way to an attractive force instead. Interestingly the shelf effect is still observed despite the attractive nature of the two surfaces.

84 curves in total were processed. Of these processed curves the average contact force was $-0.3 \text{ nN} \pm 0.1 \text{ nN}$

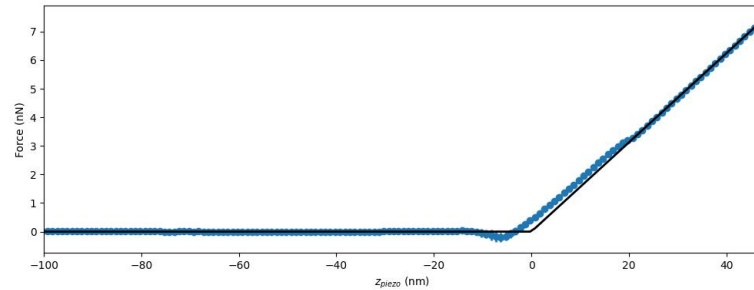


Figure 5.56 A graph demonstrating the binned average curve post fit for 550mM LiCl at contact site 1.

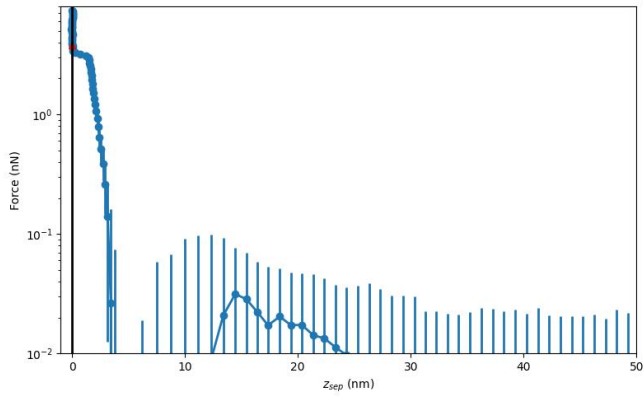


Figure 5.57 A log-linear plot of the force as a function of the Z-piezo position, highlighting the interaction phase for 550mM LiCl at contact site 1.

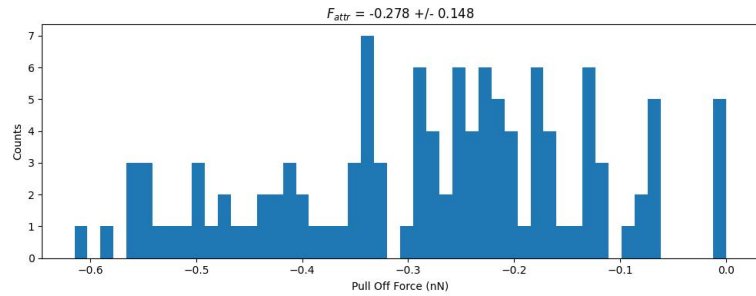


Figure 5.58 A graph demonstrating the force histogram calculated from the range of curves for 550mM LiCl at contact site 1. The averaged attractive force with the standard deviation is given above.

5.1.23 550mM Site 2

107 curves in total were processed. Of these processed curves the average contact force was $-0.1 \text{ nN} \pm 0.1 \text{ nN}$

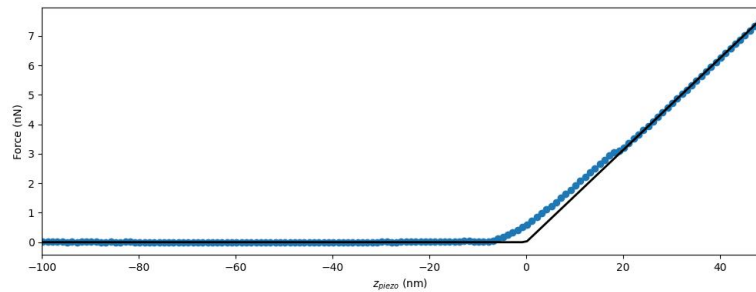


Figure 5.59 A graph demonstrating the binned average curve post fit for 550mM LiCl at contact site 2.

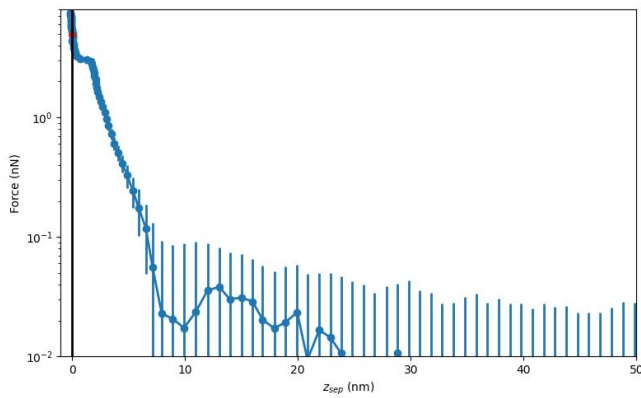


Figure 5.60 A log-linear plot of the force as a function of the Z-piezo position, highlighting the interaction phase for 550mM LiCl at contact site 2.

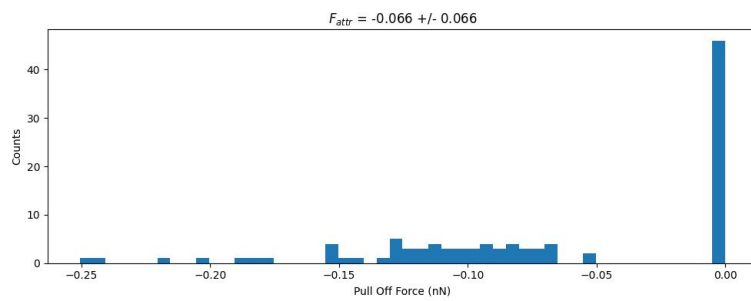


Figure 5.61 A graph demonstrating the force histogram calculated from the range of curves for 550mM LiCl at contact site 2. The averaged attractive force with the standard deviation is given above.

5.1.24 550mM Site 3

89 curves in total were processed. Of these processed curves the average contact force was $-0.1 \text{ nN} \pm 0.1 \text{ nN}$

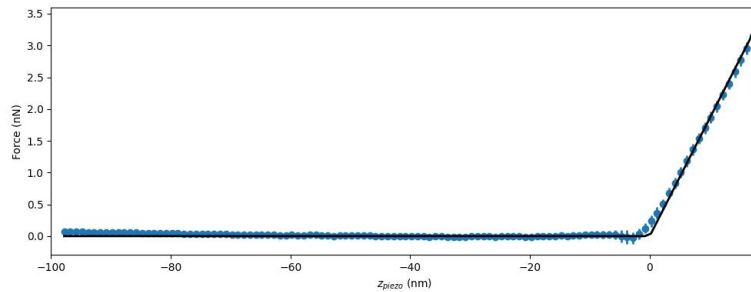


Figure 5.62 A graph demonstrating the binned average curve post fit for 550mM LiCl at contact site 3.

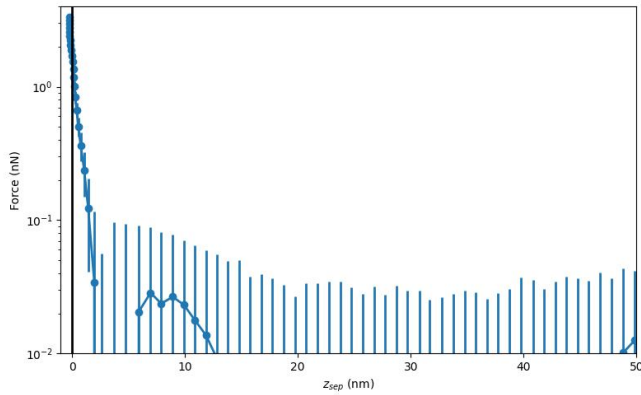


Figure 5.63 A log-linear plot of the force as a function of the Z-piezo position, highlighting the interaction phase for 550mM LiCl at contact site 3.

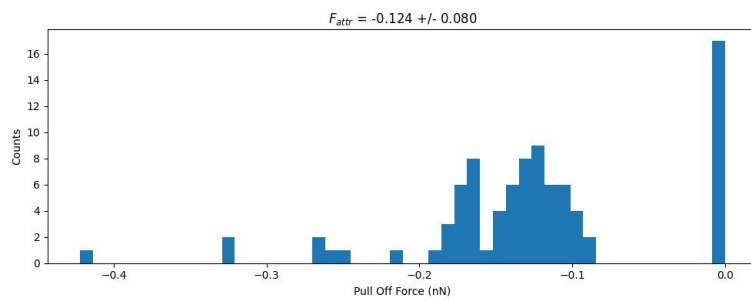


Figure 5.64 A graph demonstrating the force histogram calculated from the range of curves for 550mM LiCl at contact site 3. The averaged attractive force with the standard deviation is given above.

5.2 Overall force vs LiCl concentration graph

The forces calculated at the point of contact were subsequently plotted on a graph. For the values, the average was taken, the standard deviation was calculated by:

$$Stdev_{avg} = \sqrt{\frac{x_1^2 + x_2^2 + x_3^2}{n_{num}}} \quad (5.1)$$

Where x is the site's standard deviation and n_{num} is the number of sites in the calculation (i.e. where there were 3 sites, this value was 3).

In the case of a LiCl concentration of 550 mM, the attractive force was utilized in the plot due to the alteration in the nature of the force curve.

The overall graph demonstrate the force at contact appears to decrease with increasing LiCl concentration. The reality for each of the sites is that they were exposed to different tips and different sites. As the AFM used was unable to save site locations, site 1, 2 and 3 aren't the same spacial location on the glass between salt concentrations.

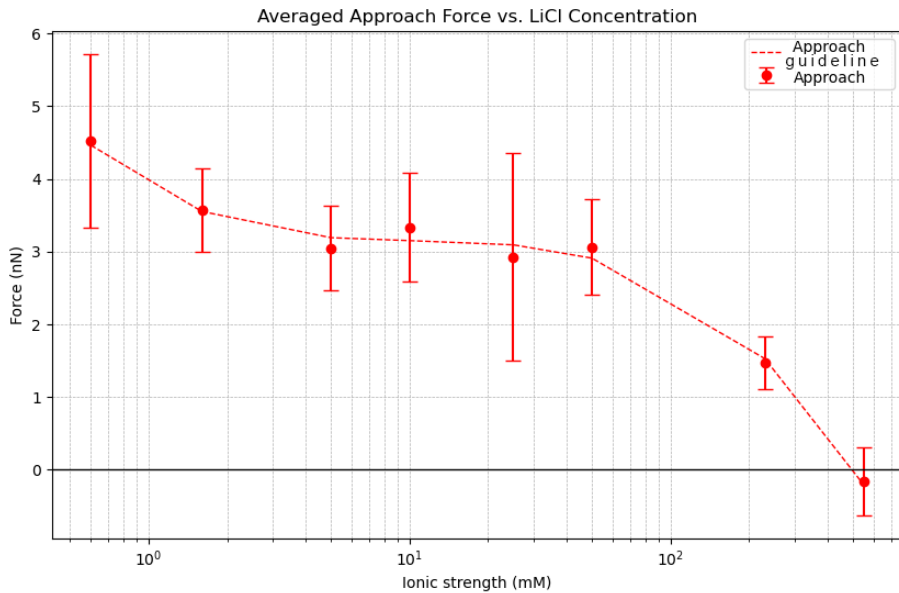


Figure 5.65 All sites' calculated force at contact with standard deviation error bars. There is an observed trend of increasing LiCl concentration leading to a decrease in repulsive force, until the repulsive force becomes attractive.

An interesting observation however is in the error bars and thus the variability or uncertainty of the measurements. Larger error bars at middling concentrations, especially noticeable at 25mM, might suggest greater variability in the interaction forces measured at these points.

The dotted line was added to guide the rough direction of the plots, which indicates that as salt concentration increases, the force requires for silica particles to come into contact decreases, eventually giving way to an attraction between the particles. This is likely due to the higher salt concentrations screening the electrostatic interactions. However, another interesting aspect is an observed plateau between 5 - 50mM ionic strengths, potentially indicating a critical ion concentration needed to disrupt the electrostatic repulsion enough in this region.

These calculated forces are then expanded upon in chapter 7, with further analysis into potential reasons as to why these trends are observed.

5.3 Discussion of Force Measurements and Salt Concentration Effects

The interaction forces between silica surfaces in electrolyte solutions have been a significant area of study in surface science, particularly in understanding the influence of varying salt concentrations on adhesion forces. The results obtained in this thesis, particularly regarding the influence of LiCl concentration on the

contact forces between silica particles, align with and extend findings from previous studies such as those by Guleryuz et al. (2012) and Kostakis et al. (2006). [53] [38]

Guleryuz et al. (2012) performed AFM measurements of forces between silica surfaces in the presence of NaCl and reported that increasing the salt concentration significantly reduces the electrostatic repulsion between the surfaces. This reduction in repulsion allowed for a more pronounced adhesion force as the surfaces approached closer under the influence of the van der Waals attraction. Specifically, their study showed that at higher pH levels, where the silica surface is more negatively charged, the presence of high NaCl concentrations reduced the Debye length, thereby diminishing the range of the electrostatic double-layer repulsion and resulting in a higher adhesion force. In the context of the findings presented in this Chapter, a similar trend was observed, with LiCl instead, where increasing concentrations led to a decrease in the repulsive forces and a corresponding increase in the adhesion forces measured between the silica particles. [38]

The work by Kostakis et al. (2006) further complements these findings by exploring the stabilization of bubbles by silica particles in high salt concentrations. They noted that at high NaCl concentrations, the surface structures, such as polysilic acid chains, collapsed, leading to a significant reduction in steric repulsion and an increase in adhesion. This observation parallels the results of Chapter 5, as it suggests that the reduced repulsive force, and thus increased contact forces observed at higher LiCl concentrations could be due to a similar collapse of surface structures on the silica particles, thereby allowing closer surface contact and stronger adhesion. [53]

The similarities in the behavior of silica surfaces in NaCl and LiCl solutions across these studies reinforce the hypothesis that the ionic strength of the solution plays a crucial role in modulating the balance between repulsive and attractive forces in colloidal systems. The increased adhesion forces observed in the presence of high salt concentrations, as reported by Guleryuz et al. and Kostakis et al., provide a valuable comparison point for the results discussed in this thesis. This comparison highlights the generality of the observed phenomena across different electrolytes, confirming that the reduction in electrostatic and steric repulsion with increasing ionic strength is a robust effect influencing contact forces in AFM measurements.

It emphasizes the importance of considering both the chemical nature of the electrolyte and the pH of the solution when analyzing AFM force profiles, which is one aspect that is expanded upon in Chapter 7. The observed increase in adhesion force with higher LiCl (salt) concentrations is consistent with the broader body of literature, and leads us into our next chapter, which focuses on the adhesive nature of the silica tip to the borosilica surface.

Chapter 6

Analysis of Retract Force Curves in Colloidal Systems

6.1 Introduction

Analysis of Silica-silica retract curves

In AFM, the study of force curves between silica surfaces in saline environments is a well explored avenue. However, the journey back from the surface—the retrace curve—is often overlooked. Standard practice in AFM analysis tends to focus on the approach curves specifically, yet with every approach curve recorded, a corresponding retrace is inherently generated. However, a review of the literature reveals a conspicuous absence of retrace curve analysis; most studies emphasize the approach while relegating the retrace to a footnote, if it is acknowledged at all [14].

This omission is understandable. Retrace curves can present a messier dataset, with the variability and complexity that derives from the chaotic nature of interactions when a tip withdraws from contact. This is due to a multitude of factors influencing the tip upon retraction: capillary forces, adhesion hysteresis, and tip contamination are but a few of the phenomena that can alter the tip's path back from the surface. While an approach curve starts from a place free of influence from the target in a stable part of a DLVO curve, the retrace starts at the point where it often is most complex.

Furthermore, DLVO theory, while capable in describing forces during the approach, can encounter hurdles when applied to the retrace curve. The symmetry of interaction predicted by DLVO when a tip approaches and retracts from a surface is often disrupted in practice. The retrace curve does not simply mirror the approach; it is influenced by history-dependent effects and irreversible changes to the tip or surface.

Within this chapter, we focus on these retrace curves, unpacking the generally noisier data in order to uncover the forces present between silica surfaces at

the nanoscale. It is here where the complex analysis software shines, allowing conclusions to be drawn from curves that would otherwise be rejected.

The chapter advocates for a more holistic view in the field of AFM study, demonstrating that the insights gleaned from retrace curves are indispensable. By embracing the full cycle of approach and retraction, a more complete picture of the interaction forces at play can be derived. The retrace curve, often overlooked, may hold the key to a deeper understanding of surface interactions, and it is time we turn our attention to this pivotal part of the AFM narrative.

6.2 MFP-1D contact force derivation

This section will overview the results for the following LiCl concentrations: 0.6mM, 1.6mM, 5mM, 10mM, 25mM, 50mM, 230mM, 550mM. For each concentration multiple sites are analysed, highlighting features of each curve in preparation for analysis. The analytical approach to processing this large dataset is given in Chapter 4.

The removal retrace curves followed the same reasoning in the previous chapter, and overlapped with the ones removed in the approach curves. This was largely due to machine errors (such as failing to connect to the surface) or from too little data within the window. The sheer volume of data more than made up for the removals however.

The graphs presented here have, once again, been meticulously selected from a broader dataset, chosen to demonstrate a good fit, to highlight the force profile and to elucidate the forces present between the interacting surfaces.

The optimization of data processing was informed by an extensive analysis of hundreds of thousands of curves. It is the same process laden with additional challenges, primarily due to the inherent noise and the diverse effects that can influence the tip upon retraction, such as capillary forces, adhesion hysteresis, or contamination. Ensuring accuracy in the retrace fit is important; a poor fit could yield erroneous curves and unreliable interpretations.

Three distinct graph types were chosen to demonstrate the fit for each of the concentrations. The retrace force curve, constructed from binned averages, depicts the aggregate behavior of the tip during retraction. Unlike its approach counterpart, the retrace curve tends to be much nosier in areas of adhesion, this is due to the variation in attractive forces within the same dataset.

The force versus the Z-piezo position reflects the forces at play as the tip disengages from the surface. It also highlights where the graph contact phase is determined.

The force histogram statistical compiles a distribution of the retrace forces encountered across multiple measurements. It provides a clear visual representation of the variability and the most probable forces during tip retraction. It also highlights the variability in the forces present.

6.2.1 0.6mM Site 1

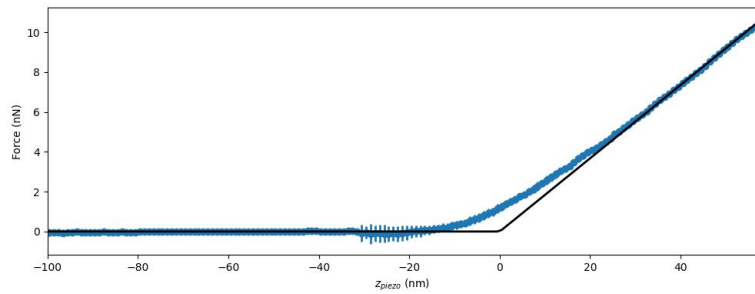


Figure 6.1 A graph demonstrating the binned average curve post fit for 0.6mM LiCl at contact site 1.

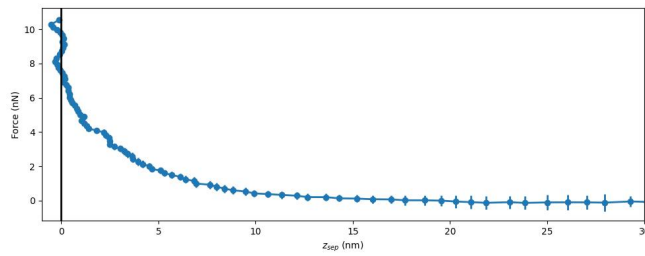


Figure 6.2 A linear plot of the force as a function of the Z-piezo position, highlighting the contact phase alignment for 0.6mM LiCl at contact site 1.

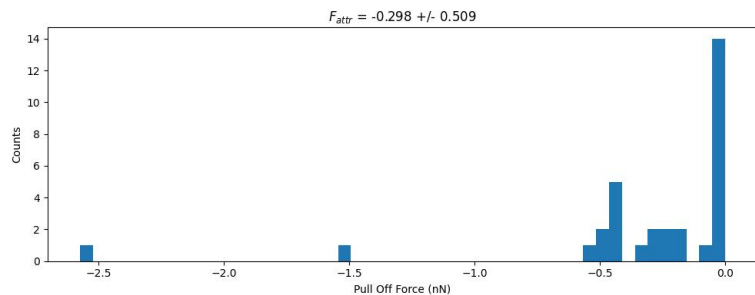


Figure 6.3 A graph demonstrating the force histogram calculated from the range of curves for 0.6mM LiCl at contact site 0.6. The averaged attractive force with the standard deviation is given above.

6.2.2 0.6mM Site 2

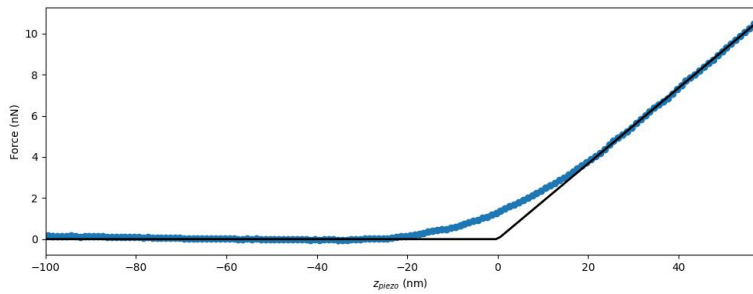


Figure 6.4 A graph demonstrating the binned average curve post fit for 0.6mM LiCl at contact site 2.

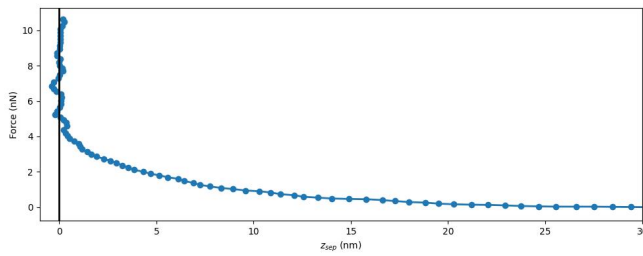


Figure 6.5 A linear plot of the force as a function of the Z-piezo position, highlighting the contact phase alignment for 0.6mM LiCl at contact site 2.

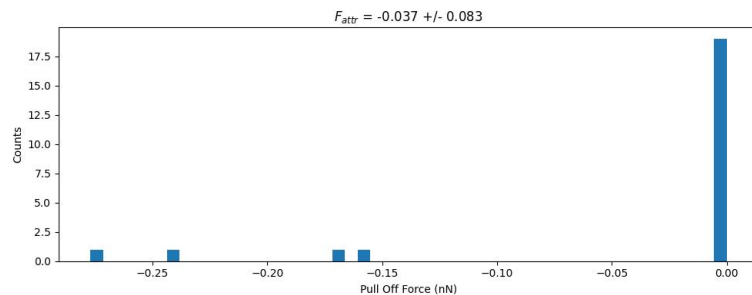


Figure 6.6 A graph demonstrating the force histogram calculated from the range of curves for 0.6mM LiCl at contact site 0.6. The averaged attractive force with the standard deviation is given above.

6.2.3 0.6mM Site 3

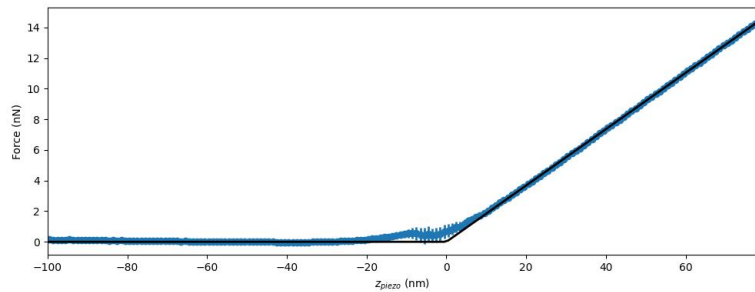


Figure 6.7 A graph demonstrating the binned average curve post fit for 0.6mM LiCl at contact site 3.

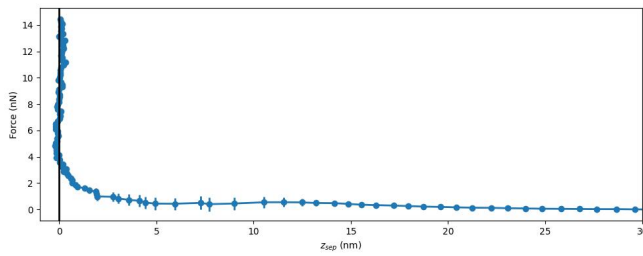


Figure 6.8 A linear plot of the force as a function of the Z-piezo position, highlighting the contact phase alignment for 0.6mM LiCl at contact site 3.

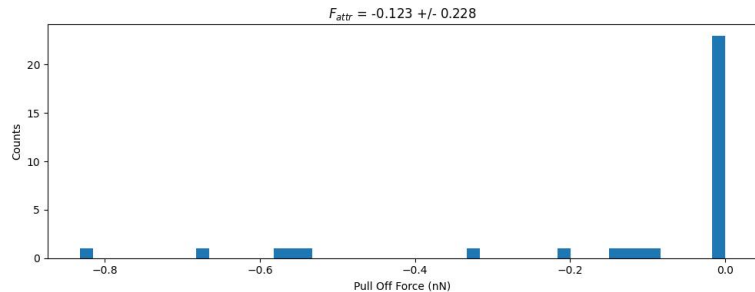


Figure 6.9 A graph demonstrating the force histogram calculated from the range of curves for 0.6mM LiCl at contact site 0.6. The averaged attractive force with the standard deviation is given above.

0.6mM demonstrates the variability present in retrace curves. Occasionally, a retrace will have a higher attractive force. In general however, 0.6mM has very little to no attractive forces between the interacting elements.

6.2.4 1.6mM Site 1

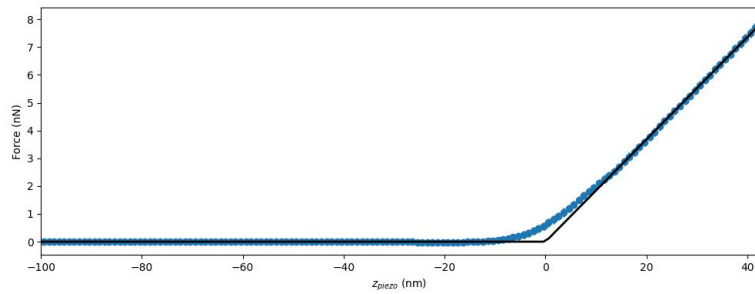


Figure 6.10 A graph demonstrating the binned average curve post fit for 1.6mM LiCl at contact site 1.

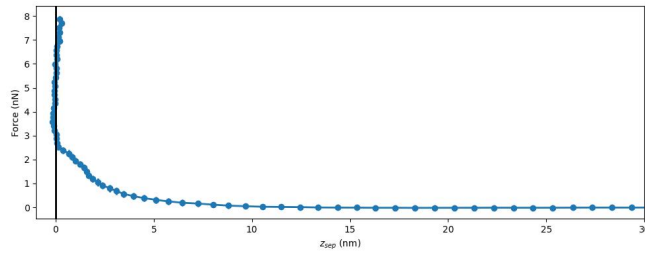


Figure 6.11 A linear plot of the force as a function of the Z-piezo position, highlighting the contact phase alignment for 1.6mM LiCl at contact site 1.

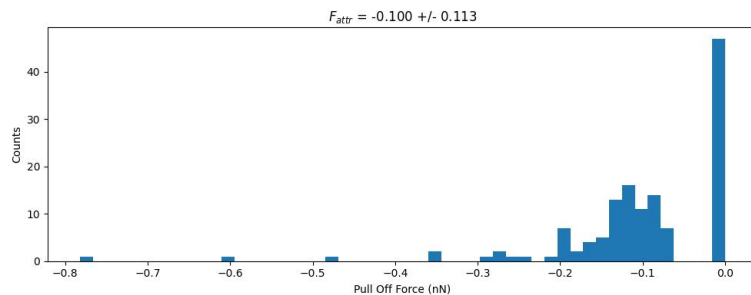


Figure 6.12 A graph demonstrating the force histogram calculated from the range of curves for 1.6mM LiCl at contact site 1.6. The averaged attractive force with the standard deviation is given above.

6.2.5 1.6mM Site 2

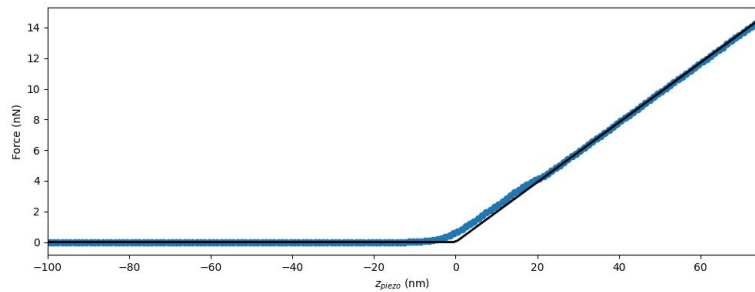


Figure 6.13 A graph demonstrating the binned average curve post fit for 1.6mM LiCl at contact site 2.

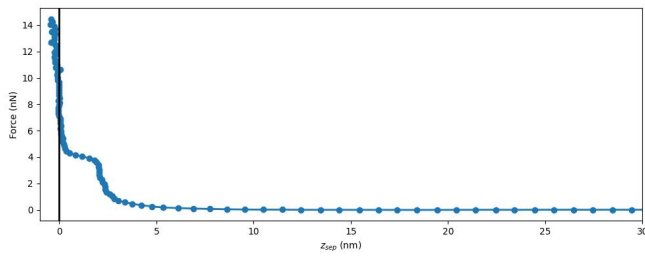


Figure 6.14 A linear plot of the force as a function of the Z-piezo position, highlighting the contact phase alignment for 1.6mM LiCl at contact site 2.

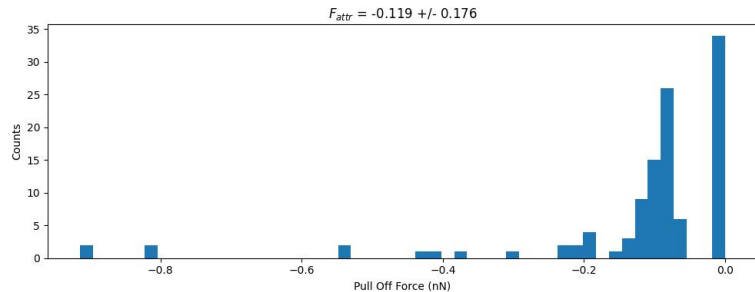


Figure 6.15 A graph demonstrating the force histogram calculated from the range of curves for 1.6mM LiCl at contact site 1.6. The averaged attractive force with the standard deviation is given above.

1.6mM has the same interesting shelf feature seen in the previous chapter. Interestingly - this shelf is largely in the same force range as the approach. Otherwise, 1.6 again has little attractive force, though notably more than 0.6mM.

6.2.6 5mM Site 1

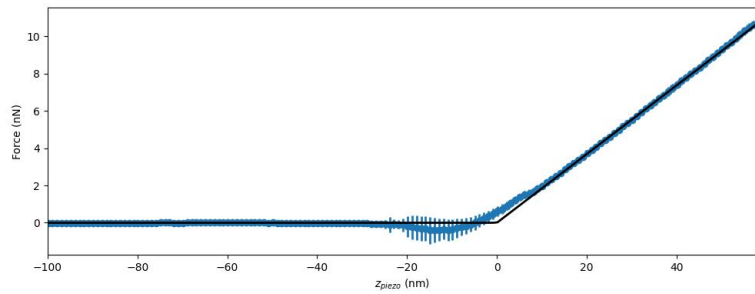


Figure 6.16 A graph demonstrating the binned average curve post fit for 5mM LiCl at contact site 1.

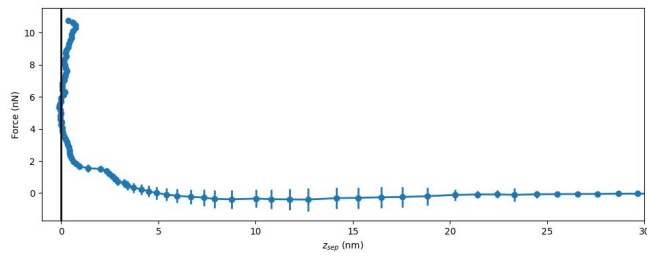


Figure 6.17 A linear plot of the force as a function of the Z-piezo position, highlighting the contact phase alignment for 5mM LiCl at contact site 1.

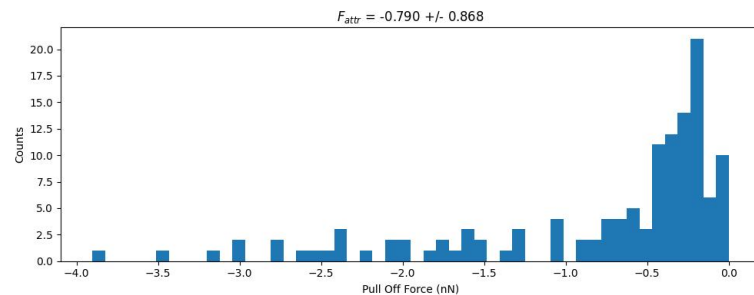


Figure 6.18 A graph demonstrating the force histogram calculated from the range of curves for 5mM LiCl at contact site 5. The averaged attractive force with the standard deviation is given above.

6.2.7 5mM Site 2

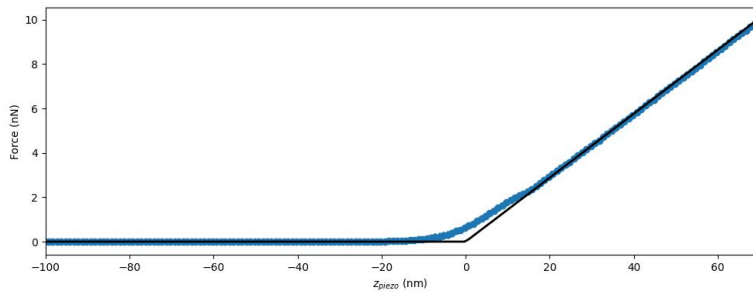


Figure 6.19 A graph demonstrating the binned average curve post fit for 5mM LiCl at contact site 2.

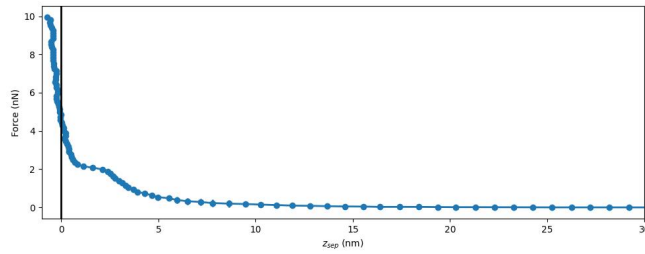


Figure 6.20 A linear plot of the force as a function of the Z-piezo position, highlighting the contact phase alignment for 5mM LiCl at contact site 2.

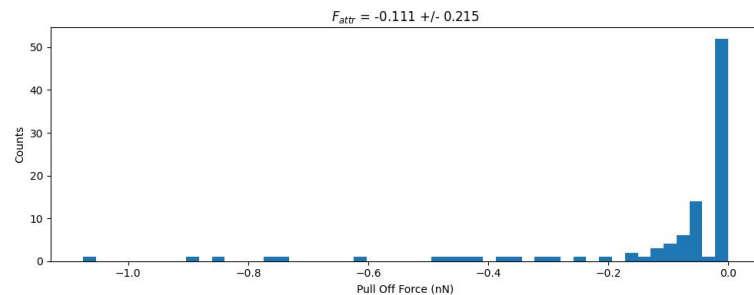


Figure 6.21 A graph demonstrating the force histogram calculated from the range of curves for 5mM LiCl at contact site 5. The averaged attractive force with the standard deviation is given above.

6.2.8 5mM Site 3

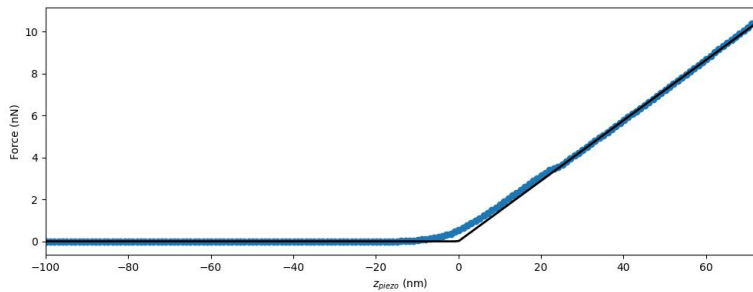


Figure 6.22 A graph demonstrating the binned average curve post fit for 5mM LiCl at contact site 3.

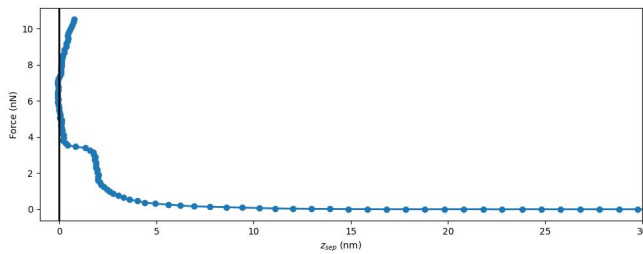


Figure 6.23 A linear plot of the force as a function of the Z-piezo position, highlighting the contact phase alignment for 5mM LiCl at contact site 3.

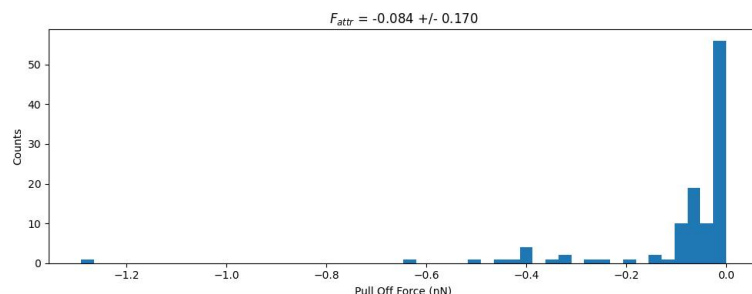


Figure 6.24 A graph demonstrating the force histogram calculated from the range of curves for 5mM LiCl at contact site 5. The averaged attractive force with the standard deviation is given above.

5mM demonstrates that as the range of pull off forces increases, so too does the variability in the binned points in the average curve post fit. This is due to the range of distances the cantilever disengages from the surface.

6.2.9 10mM Site 1

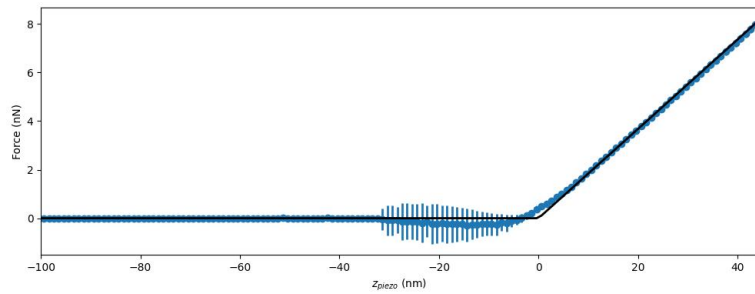


Figure 6.25 A graph demonstrating the binned average curve post fit for 10mM LiCl at contact site 1.

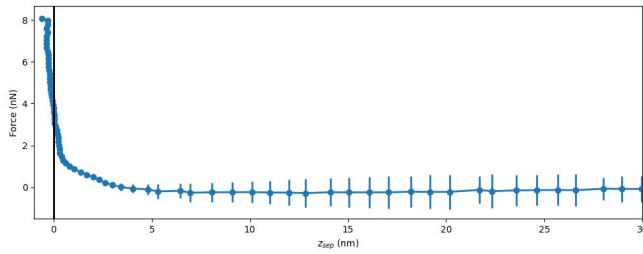


Figure 6.26 A linear plot of the force as a function of the Z-piezo position, highlighting the contact phase alignment for 10mM LiCl at contact site 1.

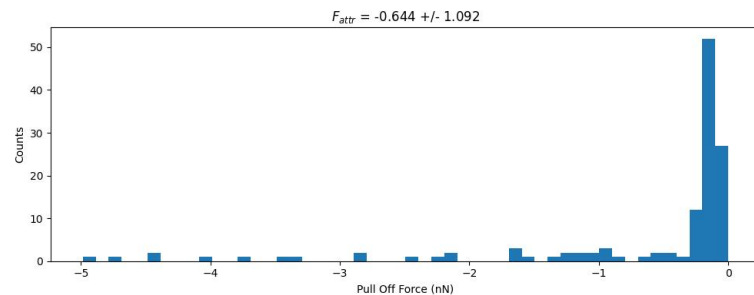


Figure 6.27 A graph demonstrating the force histogram calculated from the range of curves for 10mM LiCl at contact site 10. The averaged attractive force with the standard deviation is given above.

6.2.10 10mM Site 2

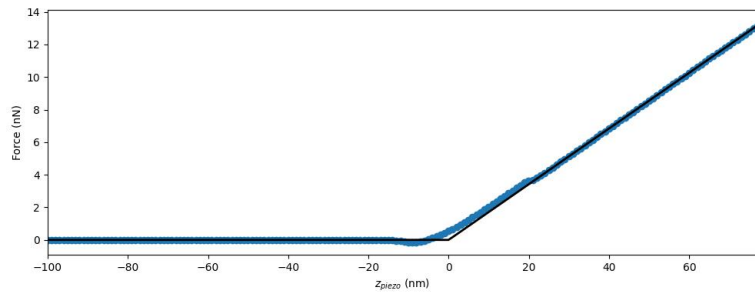


Figure 6.28 A graph demonstrating the binned average curve post fit for 10mM LiCl at contact site 2.

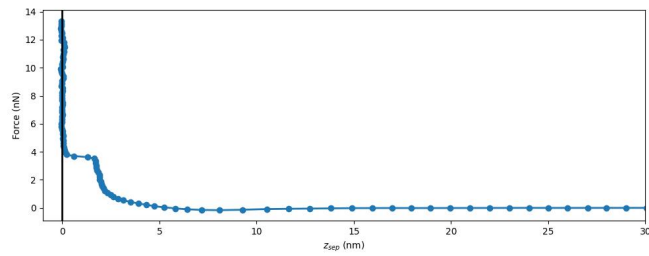


Figure 6.29 A linear plot of the force as a function of the Z-piezo position, highlighting the contact phase alignment for 10mM LiCl at contact site 2.

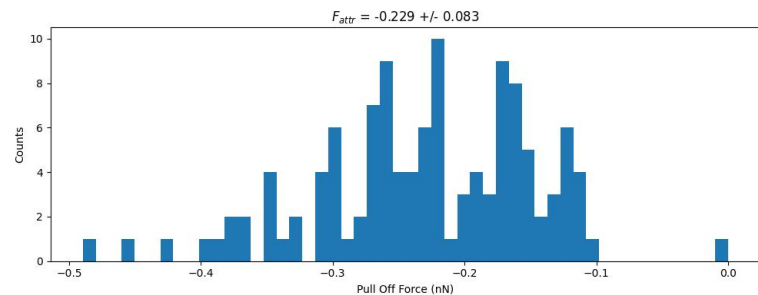


Figure 6.30 A graph demonstrating the force histogram calculated from the range of curves for 10mM LiCl at contact site 10. The averaged attractive force with the standard deviation is given above.

6.2.11 10mM Site 3

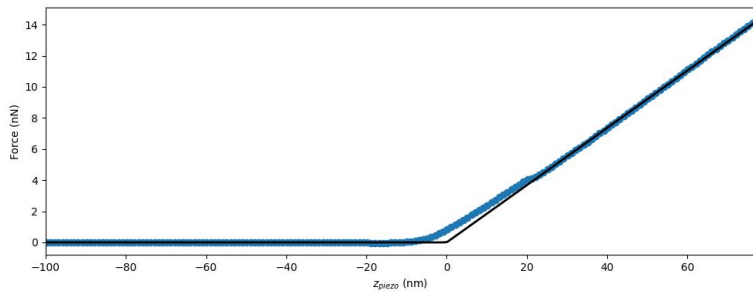


Figure 6.31 A graph demonstrating the binned average curve post fit for 10mM LiCl at contact site 3.

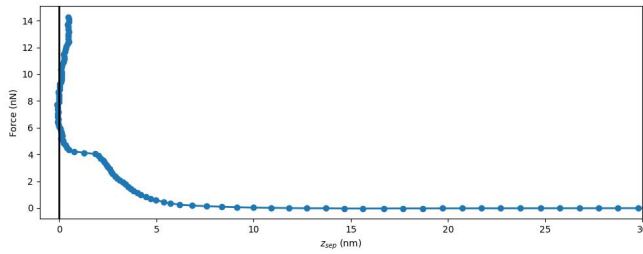


Figure 6.32 A linear plot of the force as a function of the Z-piezo position, highlighting the contact phase alignment for 10mM LiCl at contact site 3.

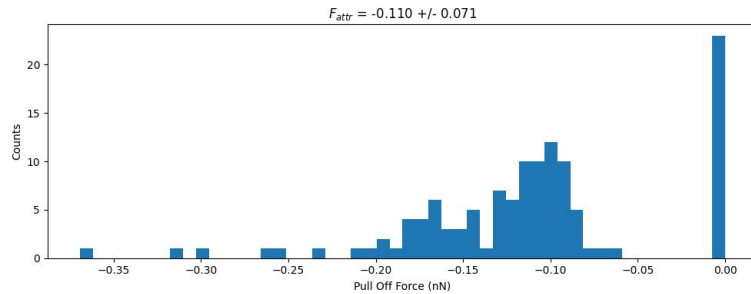


Figure 6.33 A graph demonstrating the force histogram calculated from the range of curves for 10mM LiCl at contact site 10. The averaged attractive force with the standard deviation is given above.

10mM starts to transition from a the occasional adhesive retrace curve, to a distribution of attractive ranges. Both site 2 and 3 have a a distribution similar to a normal distribution, unlike its predecessors.

6.2.12 25mM Site 1

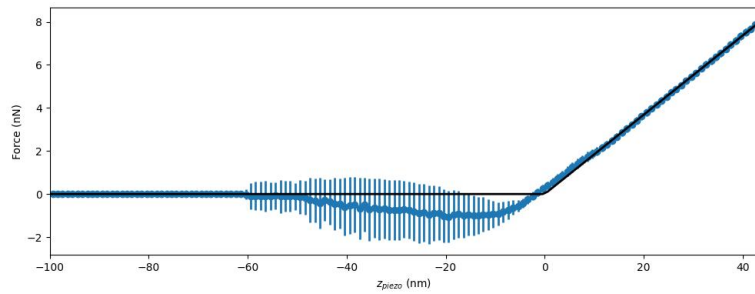


Figure 6.34 A graph demonstrating the binned average curve post fit for 25mM LiCl at contact site 1.

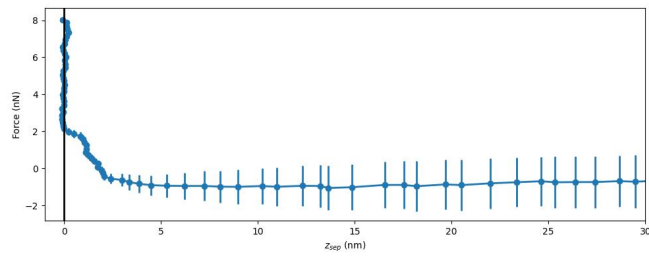


Figure 6.35 A linear plot of the force as a function of the Z-piezo position, highlighting the contact phase alignment for 25mM LiCl at contact site 1.

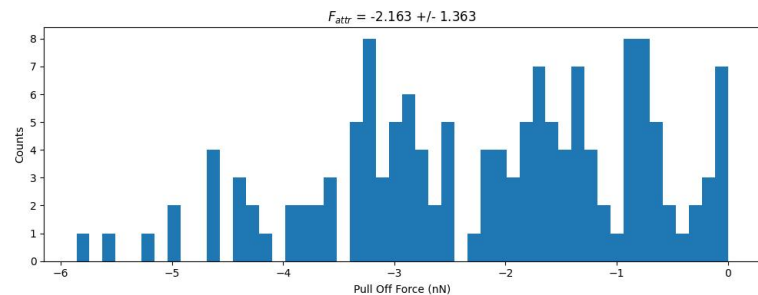


Figure 6.36 A graph demonstrating the force histogram calculated from the range of curves for 25mM LiCl at contact site 25. The averaged attractive force with the standard deviation is given above.

6.2.13 25mM Site 2

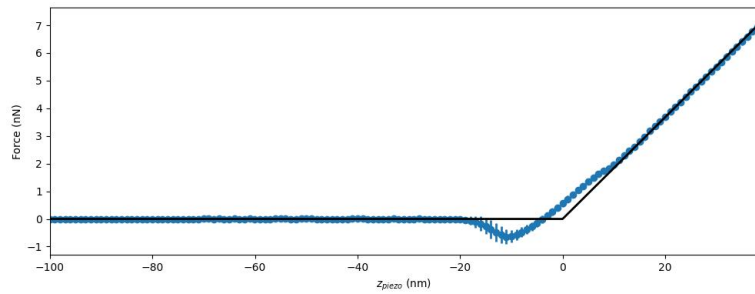


Figure 6.37 A graph demonstrating the binned average curve post fit for 25mM LiCl at contact site 2.

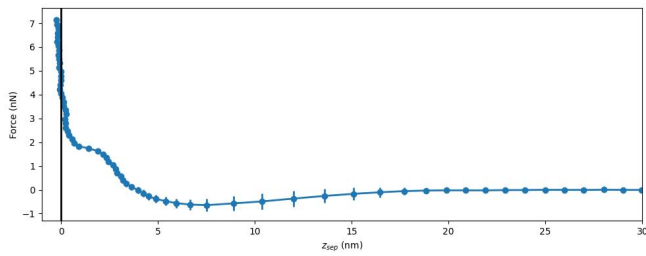


Figure 6.38 A linear plot of the force as a function of the Z-piezo position, highlighting the contact phase alignment for 25mM LiCl at contact site 2.

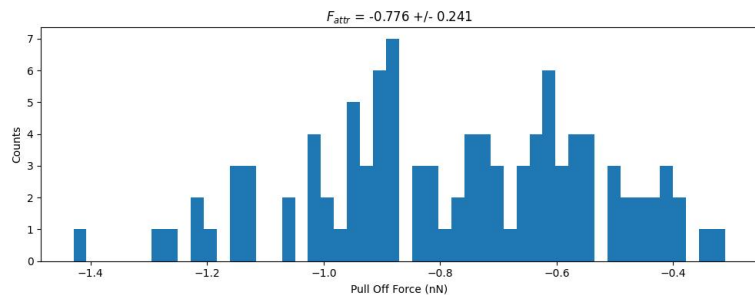


Figure 6.39 A graph demonstrating the force histogram calculated from the range of curves for 25mM LiCl at contact site 25. The averaged attractive force with the standard deviation is given above.

6.2.14 25mM Site 3

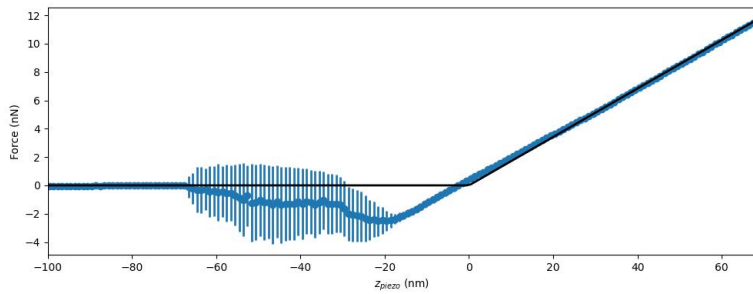


Figure 6.40 A graph demonstrating the binned average curve post fit for 25mM LiCl at contact site 3.

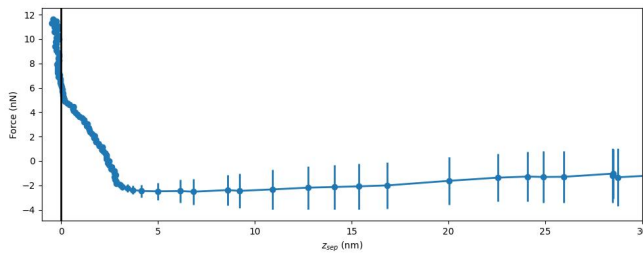


Figure 6.41 A linear plot of the force as a function of the Z-piezo position, highlighting the contact phase alignment for 25mM LiCl at contact site 3.

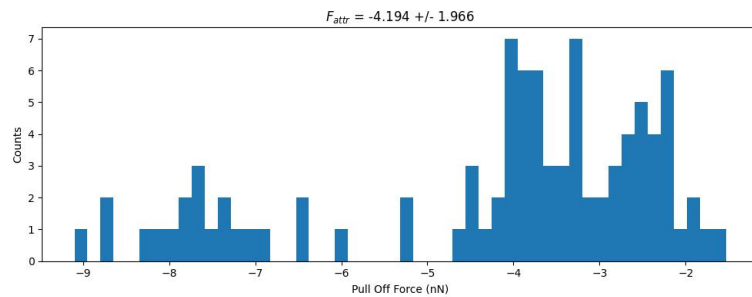


Figure 6.42 A graph demonstrating the force histogram calculated from the range of curves for 25mM LiCl at contact site 25. The averaged attractive force with the standard deviation is given above.

25mM realises the previous observation, with a more frequent distribution of a range of attractive forces. As a result, the summed data is very noisy.

6.2.15 50mM Site 1

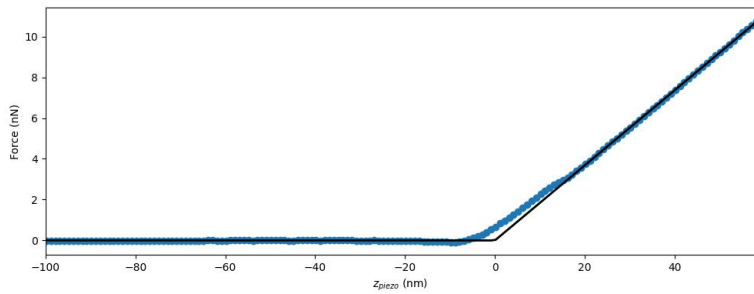


Figure 6.43 A graph demonstrating the binned average curve post fit for 50mM LiCl at contact site 1.

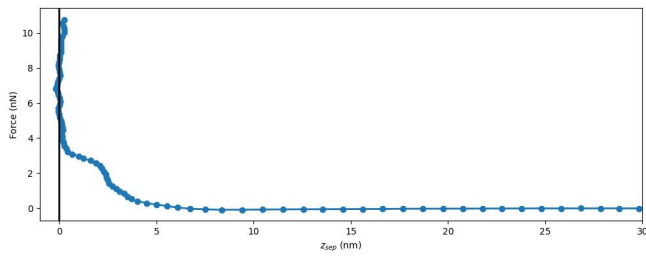


Figure 6.44 A linear plot of the force as a function of the Z-piezo position, highlighting the contact phase alignment for 50mM LiCl at contact site 1.

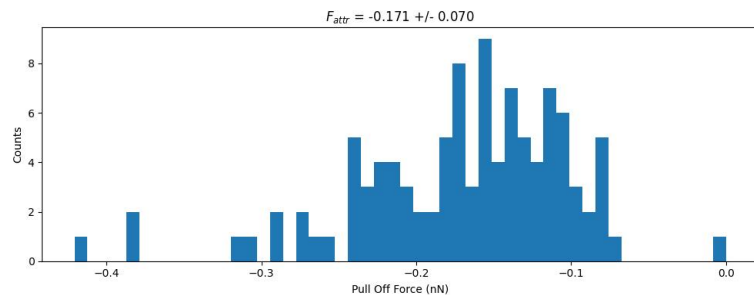


Figure 6.45 A graph demonstrating the force histogram calculated from the range of curves for 50mM LiCl at contact site 50. The averaged attractive force with the standard deviation is given above.

6.2.16 50mM Site 2

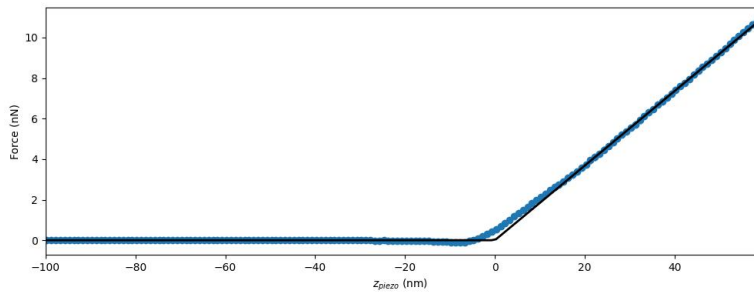


Figure 6.46 A graph demonstrating the binned average curve post fit for 50mM LiCl at contact site 2.

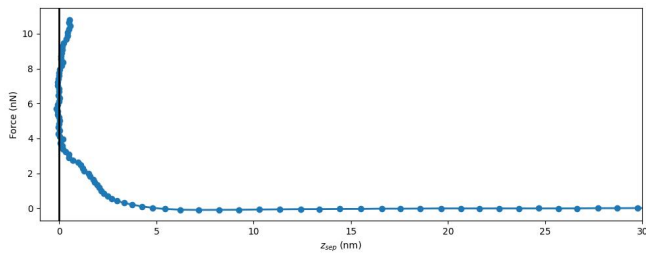


Figure 6.47 A linear plot of the force as a function of the Z-piezo position, highlighting the contact phase alignment for 50mM LiCl at contact site 2.

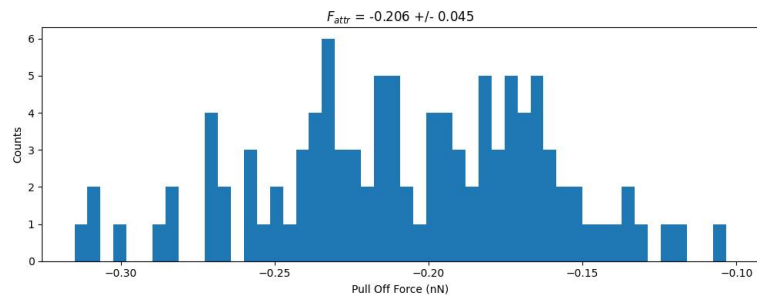


Figure 6.48 A graph demonstrating the force histogram calculated from the range of curves for 50mM LiCl at contact site 50. The averaged attractive force with the standard deviation is given above.

6.2.17 230mM Site 1

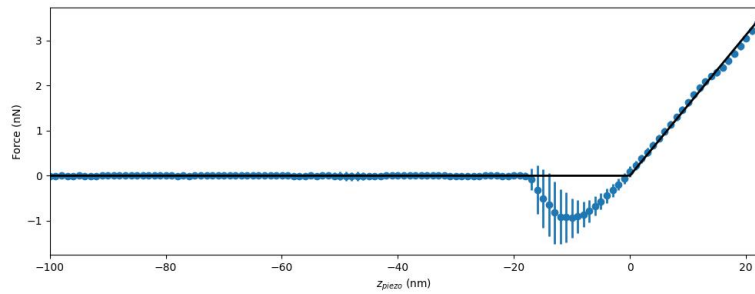


Figure 6.49 A graph demonstrating the binned average curve post fit for 230mM LiCl at contact site 1.

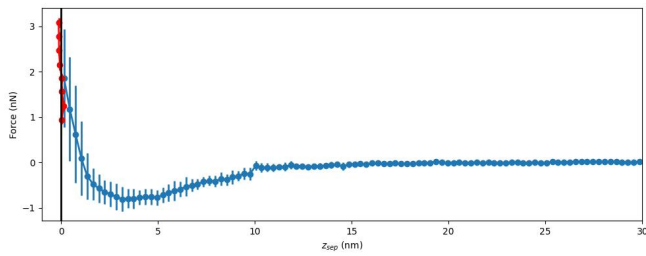


Figure 6.50 A linear plot of the force as a function of the Z-piezo position, highlighting the contact phase alignment for 230mM LiCl at contact site 1.

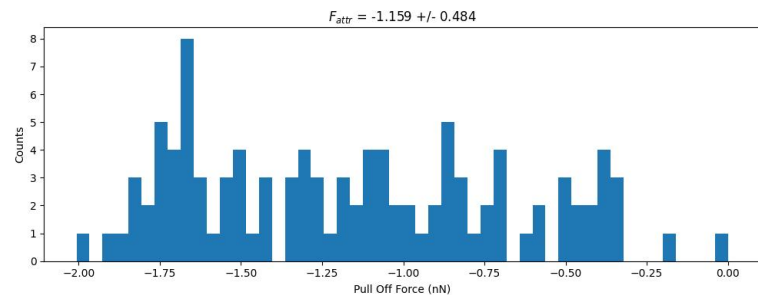


Figure 6.51 A graph demonstrating the force histogram calculated from the range of curves for 230mM LiCl at contact site 230. The averaged attractive force with the standard deviation is given above.

6.2.18 230mM Site 2

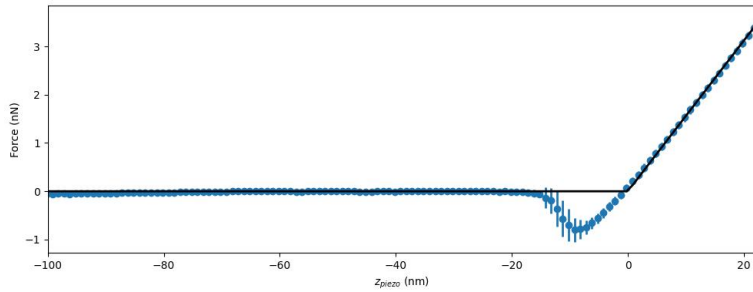


Figure 6.52 A graph demonstrating the binned average curve post fit for 230mM LiCl at contact site 2.

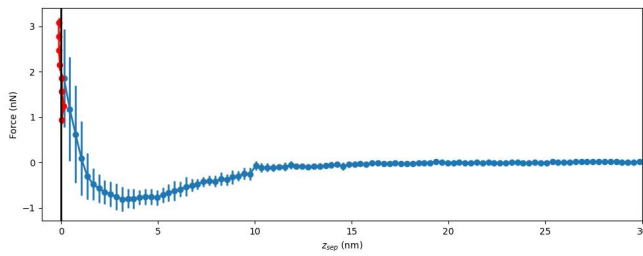


Figure 6.53 A linear plot of the force as a function of the Z-piezo position, highlighting the contact phase alignment for 230mM LiCl at contact site 2.

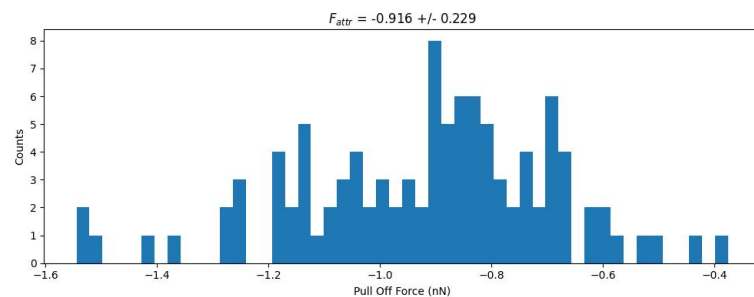


Figure 6.54 A graph demonstrating the force histogram calculated from the range of curves for 230mM LiCl at contact site 230. The averaged attractive force with the standard deviation is given above.

230mM starts to have a more coherent attractive profile as the theory starts to transition into a more attractive profile between the surfaces.

6.2.19 550mM Site 1

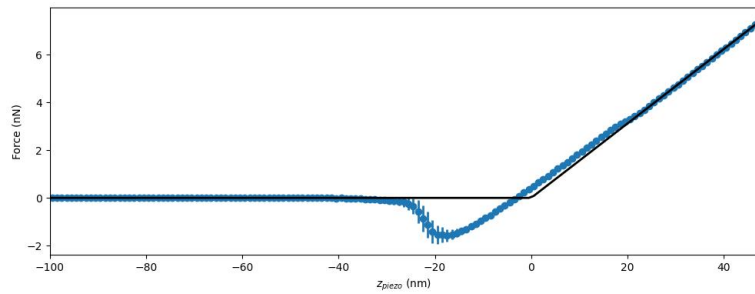


Figure 6.55 A graph demonstrating the binned average curve post fit for 550mM LiCl at contact site 1.

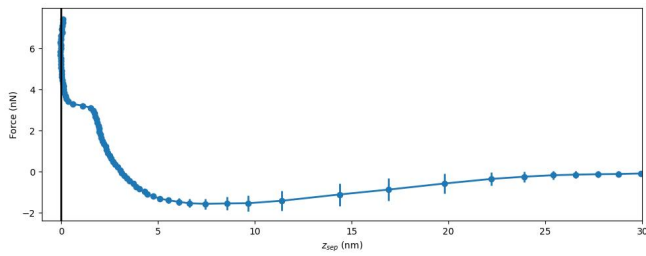


Figure 6.56 A linear plot of the force as a function of the Z-piezo position, highlighting the contact phase alignment for 550mM LiCl at contact site 1.

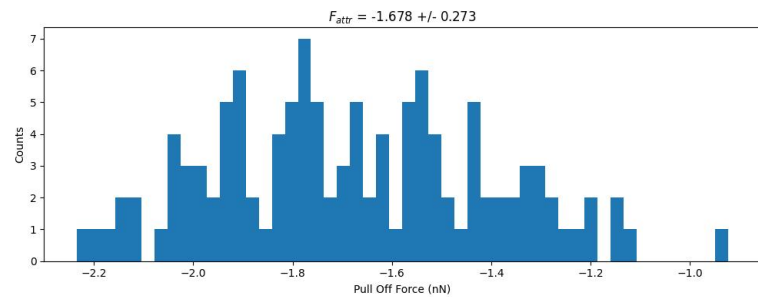


Figure 6.57 A graph demonstrating the force histogram calculated from the range of curves for 550mM LiCl at contact site 550. The averaged attractive force with the standard deviation is given above.

6.2.20 550mM Site 2

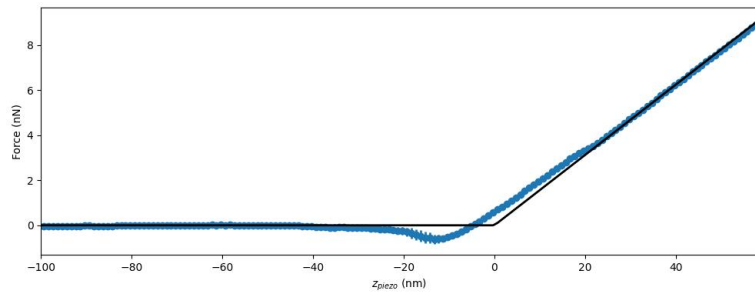


Figure 6.58 A graph demonstrating the binned average curve post fit for 550mM LiCl at contact site 2.

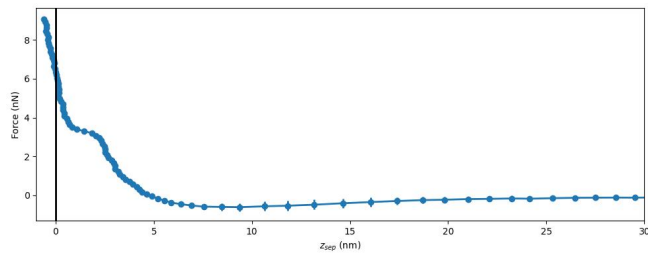


Figure 6.59 A linear plot of the force as a function of the Z-piezo position, highlighting the contact phase alignment for 550mM LiCl at contact site 2.

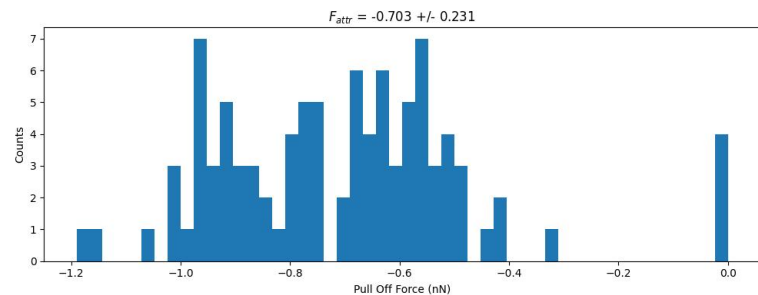


Figure 6.60 A graph demonstrating the force histogram calculated from the range of curves for 550mM LiCl at contact site 550. The averaged attractive force with the standard deviation is given above.

6.2.21 550mM Site 3

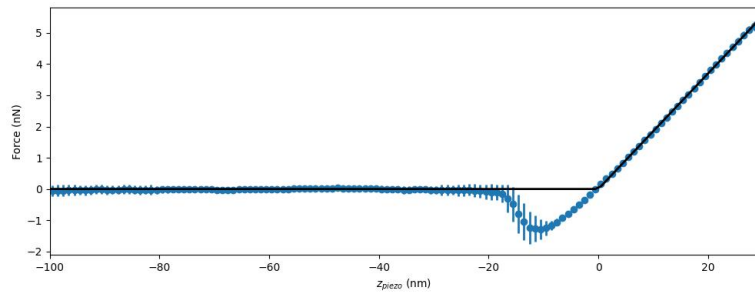


Figure 6.61 A graph demonstrating the binned average curve post fit for 550mM LiCl at contact site 3.

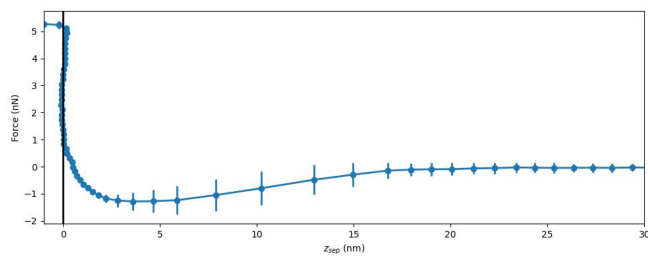


Figure 6.62 A linear plot of the force as a function of the Z-piezo position, highlighting the contact phase alignment for 550mM LiCl at contact site 3.

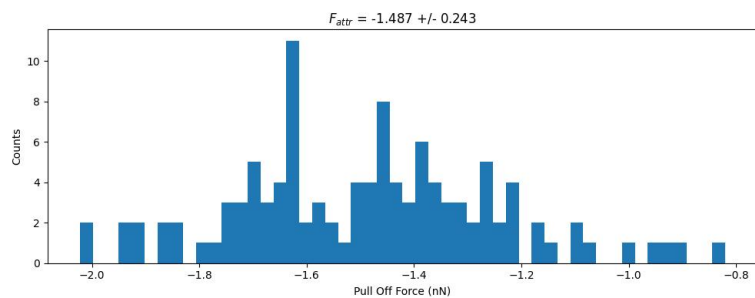


Figure 6.63 A graph demonstrating the force histogram calculated from the range of curves for 550mM LiCl at contact site 550. The averaged attractive force with the standard deviation is given above.

6.3 Overall force vs LiCl concentration graphs

The pull off forces calculated were subsequently averaged, with the standard deviation calculated using equation 5.1.

The retrace curve shown in figure 6.64 represent the attractive forces that are retained when the AFM tip is retracted from the contact with the surface

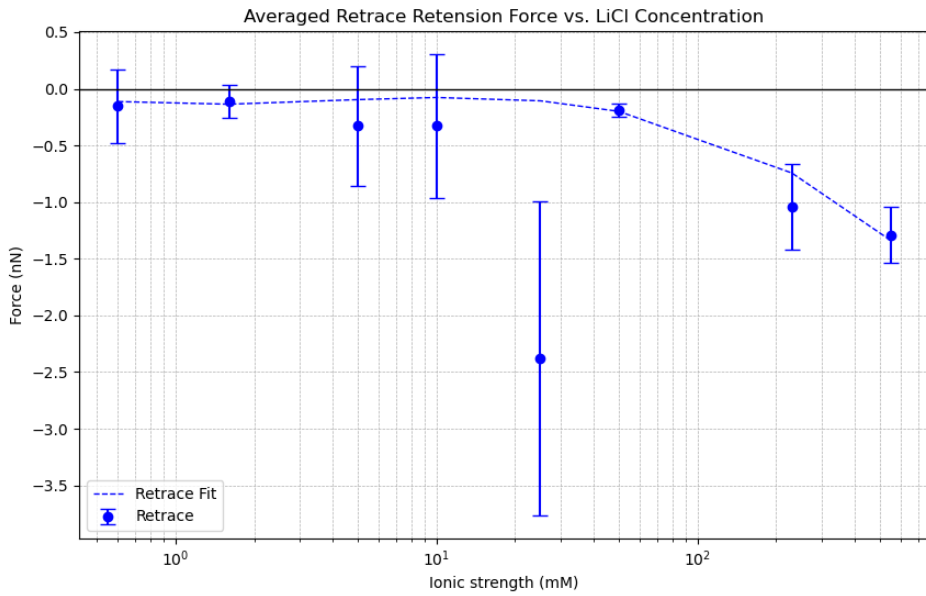


Figure 6.64 Site one calculated attractive force retained from contact with standard deviation error bars.

at different LiCl concentrations. The retrace curve shows an attractive force plateau, until a critical concentration at around 50mM where the attractive force between the tip and surface increases increasing LiCl concentration, with the force generally following a trend downwards. However 25mM is perplexing, as it demonstrates the strongest attractive force, though it is worth noting that 25mM was also a bit of an oddity in the approach curves due to its higher standard deviation. This could be due to other reasons, such as a unexpected surface perturbation providing additional friction. In general, however, there is a trend of increasing attractive force past 50mM concentration, and thus pull off force across the datapoints.

Another aspect that stands out is the prominence of the standard deviation, especially at the higher concentrations. This is typical for retrace curves due to the reasons mentioned earlier such as tip changes upon contact. It is also interesting to note that the attractive forces in retrace curves are usually not symmetrical with the approach curves due to various interactions that can occur when the tip is in contact with the surface. These interactions include adhesion hysteresis, capillary forces, and possible tip contamination or wear, which can all affect the tip as it retracts and lead to the variability observed.

One final interesting note is the observation of the 50mM tipping point present in both the approach and retrace curve, indicating that past 50mM there potentially could be some kind of mechanism that impacts the electrostatic repulsion, rather than a linear build up of ions on the surface (potentially enough ions to fully saturate the surface?).

This analysis is important for interpreting the overall behavior of the system and

for validating models of interfacial forces, which is the focus of our next chapter.

Chapter 7

Operational parameter exploration and their implications

7.1 Introduction

Building on the foundations laid by the preceding chapters, this chapter delves into a more nuanced investigation of the parametric influences on the resulting force curves obtained through Atomic Force Microscopy (AFM). When operating an AFM, it is typical to use a standard set of operational parameters. [78] These parameters are often found during operation in an exploratory manner to find a good signal to noise ratio. However, it can be prudent to examine a spectrum of force curves under varied conditions. Such an investigation enables the assessment of result consistency across diverse settings, thereby ensuring that the observed outcomes are not merely artifacts of parameter-specific minima phenomena. Additionally, a range of differing conditions can provide an insight into how other phenomena may have an effect on the observed behaviour of the curves.

A range of differing conditions were repeated with the following parameter changes: Tip speed, dwell time, solution pH and force mapping.

Tip Speed Variations

The velocity of the AFM tip's approach and retraction impacts the force measurements, potentially altering the energy landscape of particle interactions. Varying the tip speed not only affects the kinetic parameters but also provides insight into time-dependent phenomena such as lubrication forces and simple viscous drag. The adjustment of the tip's velocity probes the dynamic response of the system, shedding light on the viscoelastic properties of the medium and the rate-dependent behavior of interparticle forces.

The previous results were taken at 0.5Hz, or a tip speed of $1\mu\text{m}/\text{s}$. Two other speeds were used; 0.1Hz ($0.2\mu\text{m}/\text{s}$) and 2Hz ($4\mu\text{m}/\text{s}$). 0.1Hz was done exclusively

on 10mM.

Effect of Dwell Time

The incorporation of a 5-second dwell time between the approach and retrace allows for the relaxation of the system and the establishment of equilibrium conditions in between movements, potentially revealing the subtleties of time-dependent interactions. The extended dwell time is expected to amplify phenomena such as capillary forces and hydration layers, which are often overshadowed by more dominant forces in quicker measurements.

Solution pH Influence

The pH of the colloidal solution is a determinant of the surface charge on the silica particles, which in turn modulates the force interactions observed. The variations in pH are expected to impact the electrical double layer, thereby influencing the force profiles and interaction potentials, while retaining the same force curve profile ranges as shown previously.

Forcemapping for wide range site analysis

Forcemapping, a method of tracking force-distance curves over a defined grid area, was employed to obtain a comprehensive understanding of the force distribution across the sample. This technique is useful in discerning how heterogeneous the analysed surface is and provides a statistical interpretation of interparticle forces across a range of areas.

The exploration of these parameters serves not just as a methodical inquiry into the forces acting within colloidal dispersions, but also as a means to justify our approach to force curve analysis. The diversity of these conditions reflects the complex nature of the studied system and underscores the need for a comprehensive dataset that accurately represents the multifaceted nature of particle interactions.

The subsequent section presents the force distributions across our dataset, providing empirical evidence to the impact of these discussed factors. Finally, the section highlights the differences between the “standard” dataset and the modified parameters.

7.2 Tip speed analysis

One of the differences between the different tip speeds was the data density. For faster speed less data was taken, while slower speeds had more data taken. This was due to the rate in which the AFM takes in data - the AFM was set to take in the maximum rate of data throughout the whole process. This was done to

maximise the volume of data usable for the binning process (as seen in chapter 5).

For 0.1 and 0.5Hz frequencies, the data recording rate was sufficient to support the processing of the curves, while 2Hz had significantly less data volume, and required a more involved fitting, with generally a lower bitsize setting used in the script - increasing the noise in the averaged curve.

For each of the points, the tip speed increase was done after the initial reading, thus meaning that the sites can be directly compared across the standard dataset and this dataset (i.e. 0.5Hz dataset was recorded, then 2Hz was recorded right after in the same area).

0.6mM

For 0.6mM only one site was recorded. Interestingly 0.6mM presented the highest recorded repulsive force across the entire dataset. Due to the lower data density, and the force cap set at around 12nN, there was a small window in which to fit the contact region, leading to a higher failure rate by the script for each movement. It is interesting to note that for this concentration the retract force histogram has no attractive force associated with the return movement, possibly indicating that higher speeds do not give the system enough time to relax towards an attractive profile, or that the electrostatic component decay is time dependant.

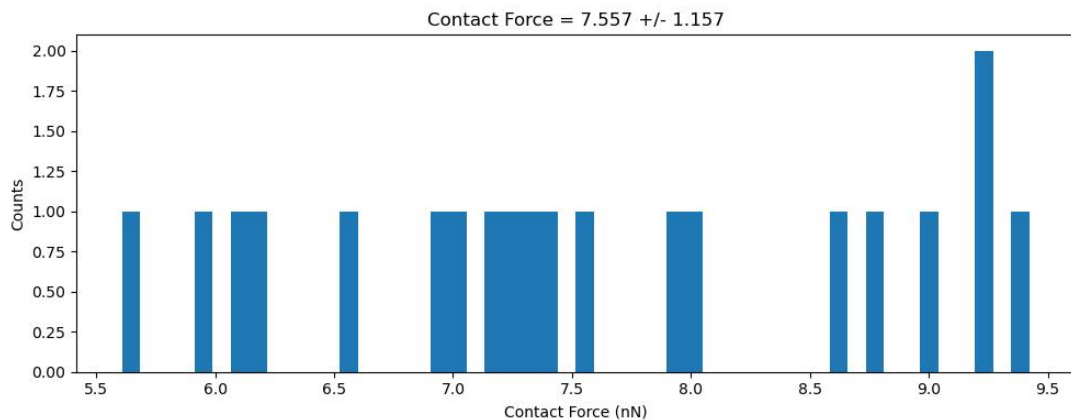


Figure 7.1 Approach force-current histogram at 0.6mM at 2Hz

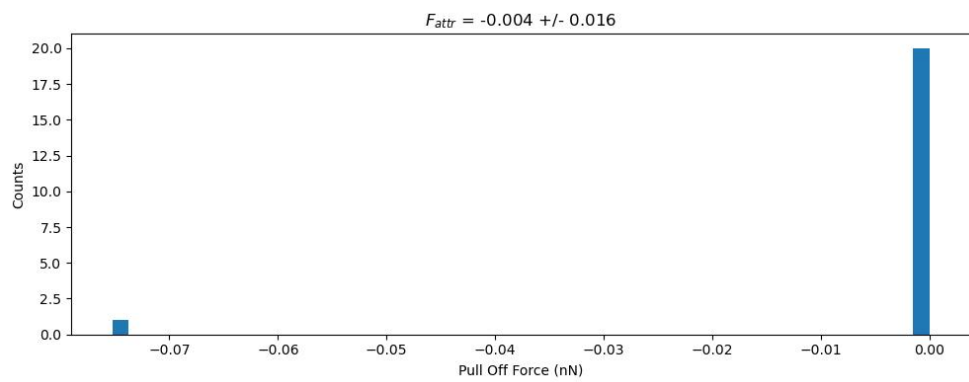


Figure 7.2 Retract force-amplitude histogram at 0.6mM at 2Hz

1.6mM

1.6mM demonstrates a return to the previously expected values as set from the previous datasets. The retract curve demonstrates a widening of the attractive force, but still a very minor attraction.

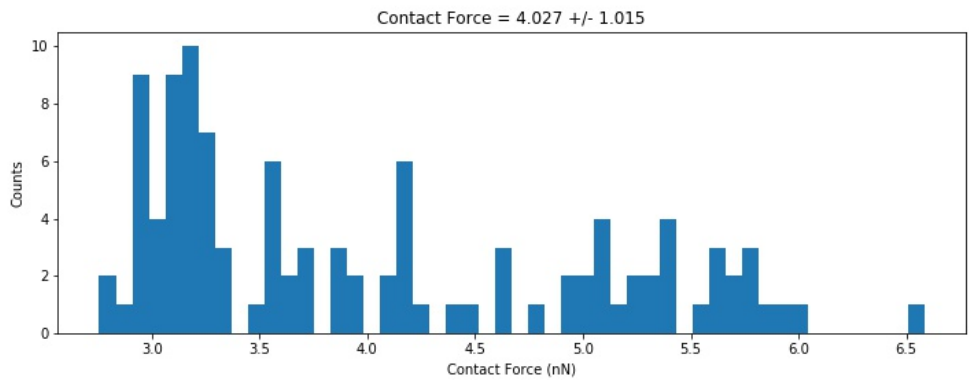


Figure 7.3 Approach curve for 1.6mM, S2 at 2Hz

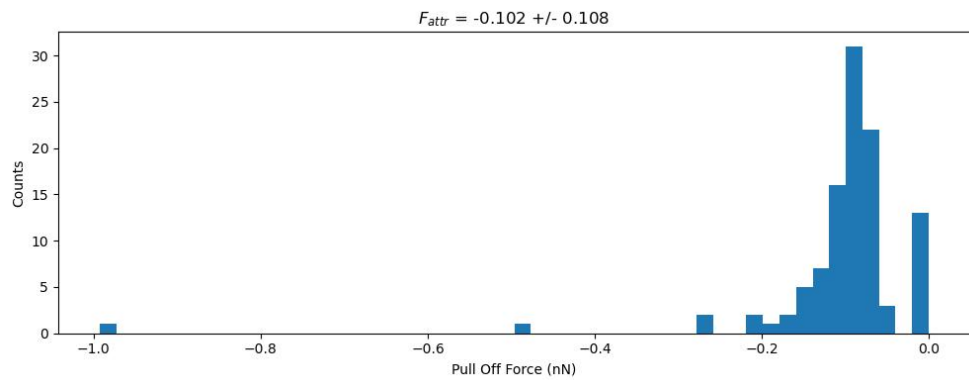


Figure 7.4 Retract curve for 1.6mM, S2 at 2Hz

5mM

5mM is the first concentration where a wider range of sites were explored. For the approach, the largest distribution was around the 2.5-4nN range, which is within expectations. For the retrace, minor instances of adhesive force was observed, but not significantly, again in line with previous results.

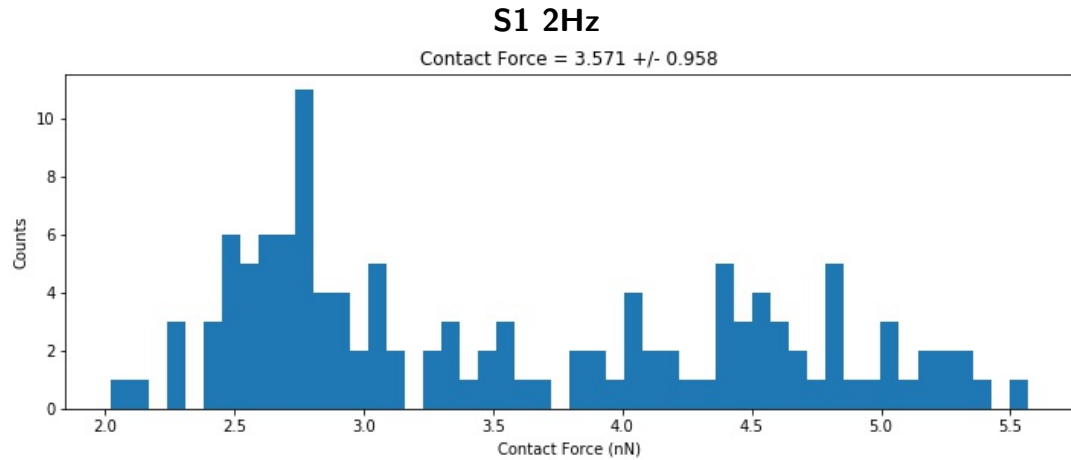


Figure 7.5 Approach curve for 5mM, S1 at 2Hz

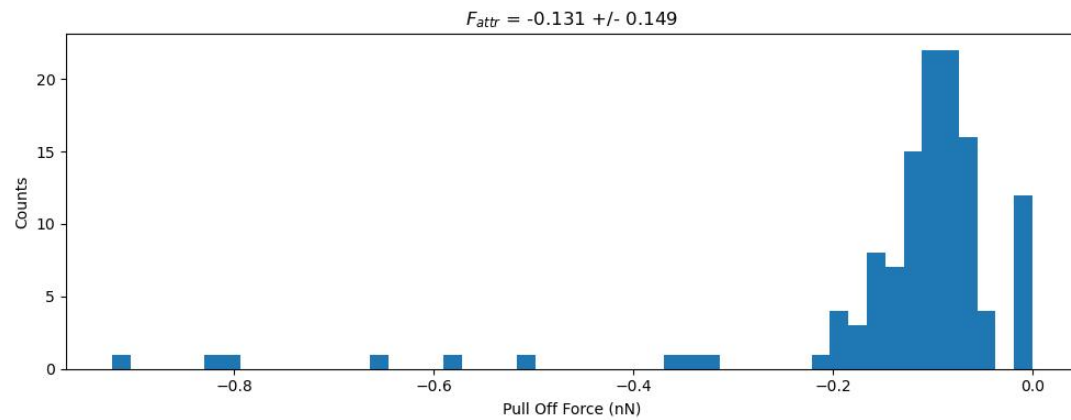


Figure 7.6 Retract curve for 5mM, S1 at 2Hz

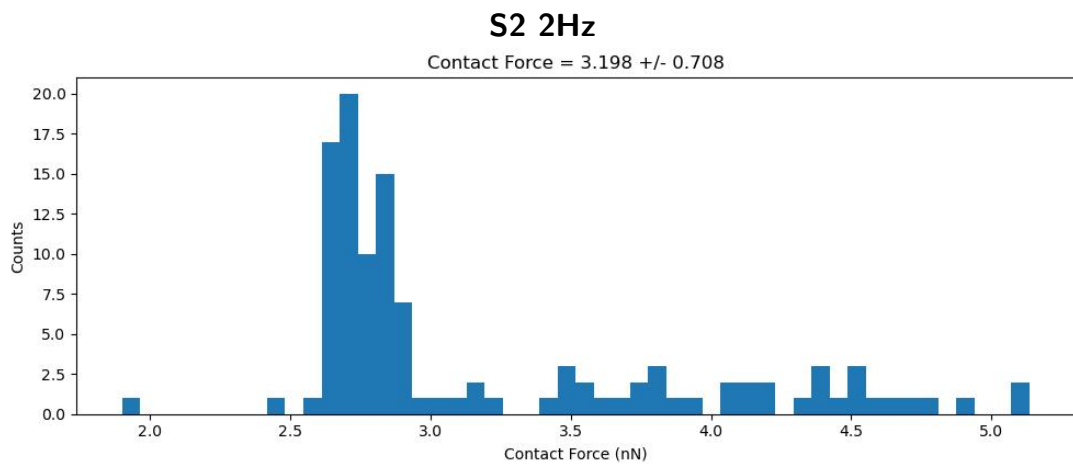


Figure 7.7 Approach curve for 5mM, S2 at 2Hz

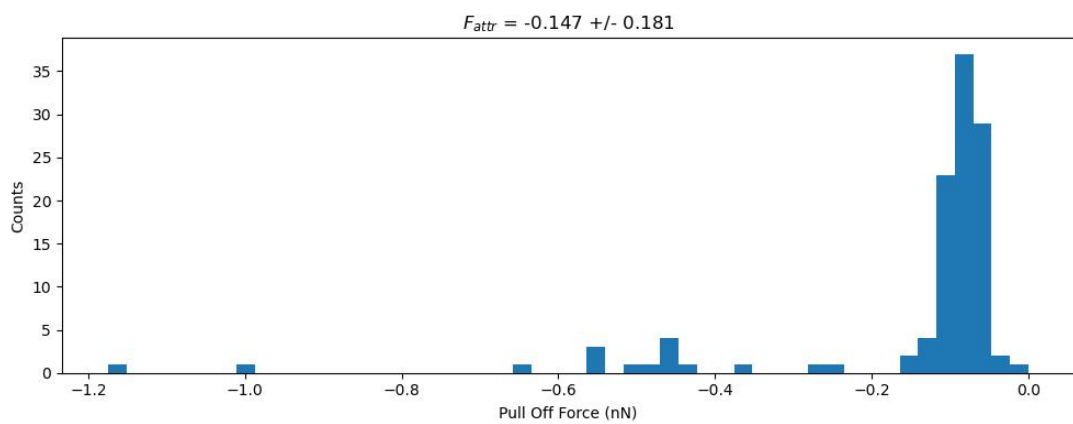


Figure 7.8 Retract curve for 5mM, S2 at 2Hz

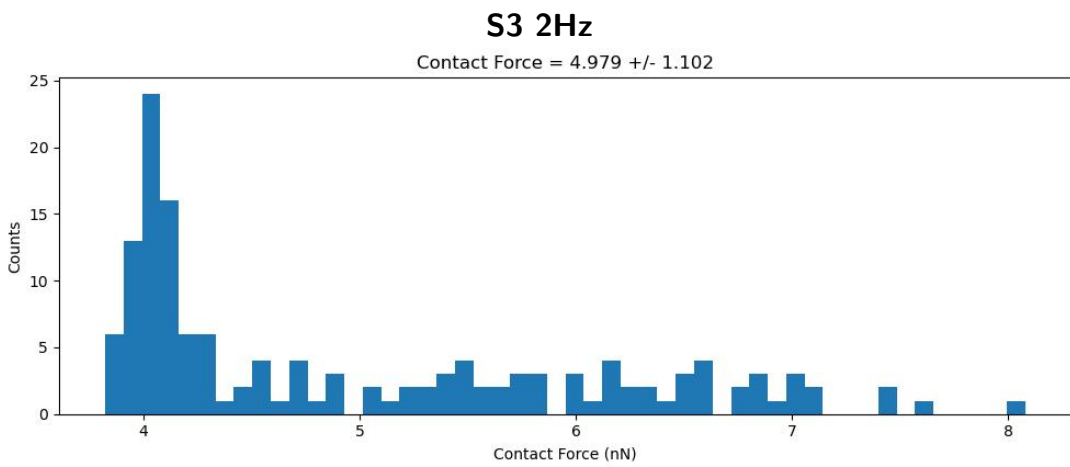


Figure 7.9 Approach curve for 5mM, S3 at 2Hz

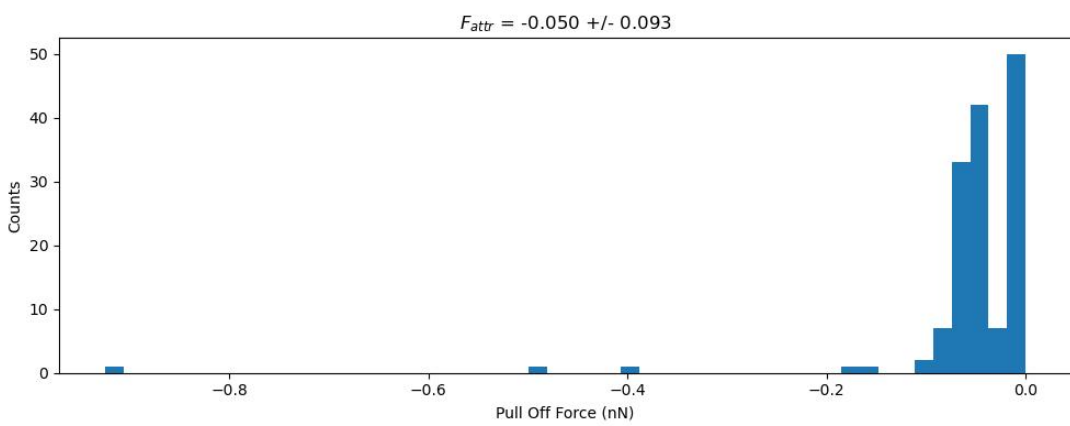


Figure 7.10 Retract curve for 5mM, S3 at 2Hz

10mM

10mM also includes an analysis of a slower tip - a tip speed of 0.1Hz. This was the only site to include a slower speed. Overall, for 0.1Hz, while 1 datapoint shows a significantly high attractive force, the other 2 largely show little to no attraction. Overall however, the 0.1Hz speed shows a slightly stronger retrace attractive force when compared to the previous data. 2Hz shows data within expected ranges from previous data.

S1 0.1Hz

Contact Force = 4.082 ± 0.748

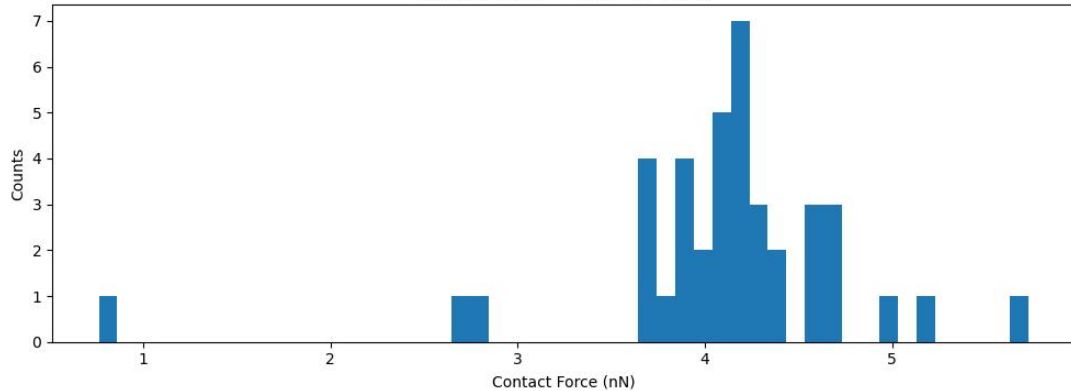


Figure 7.11 Approach curve for 10mM, S1 at 0.1Hz

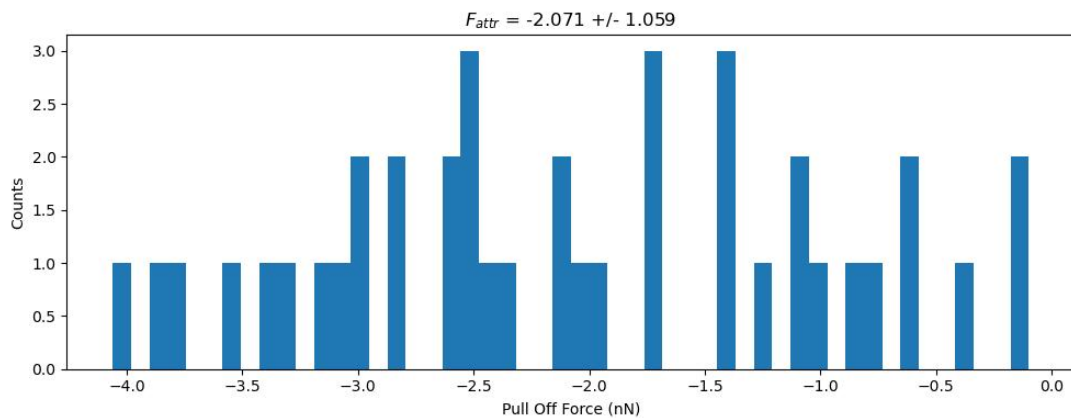


Figure 7.12 Retract curve for 10mM, S1 at 0.1Hz

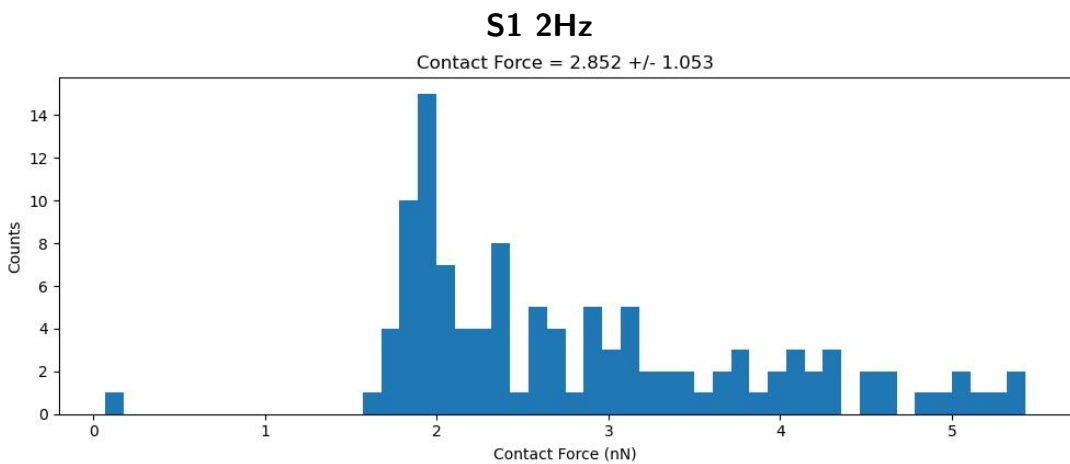


Figure 7.13 Approach curve for 10mM, S1 at 2Hz

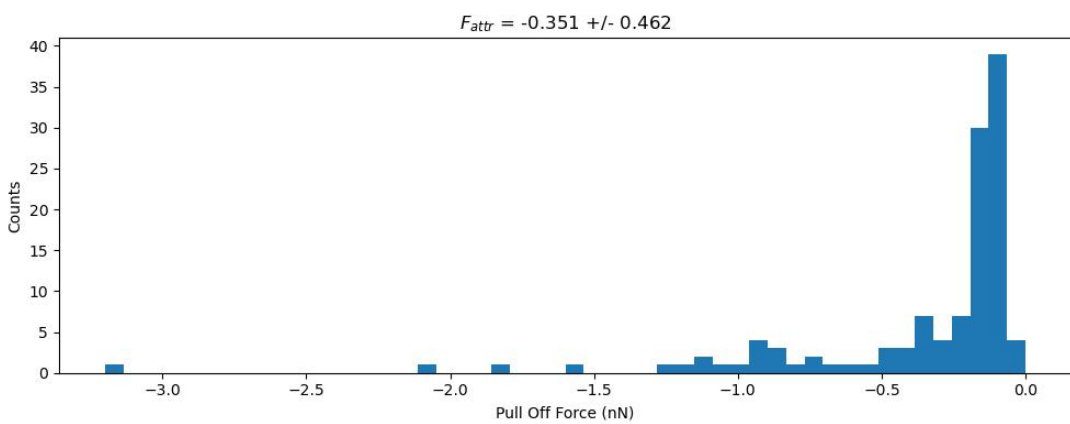


Figure 7.14 Retract curve for 10mM, S1 at 2Hz

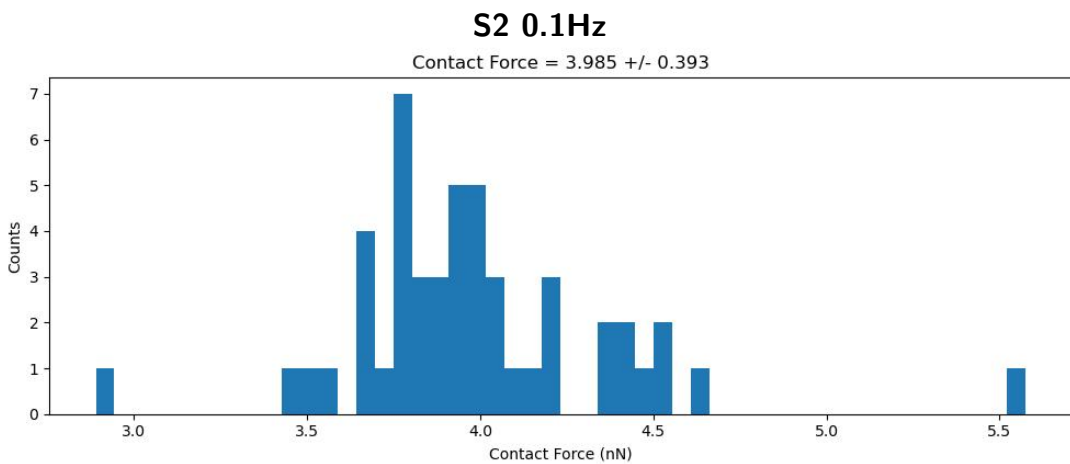


Figure 7.15 Approach curve for 10mM, S2 at 0.1Hz

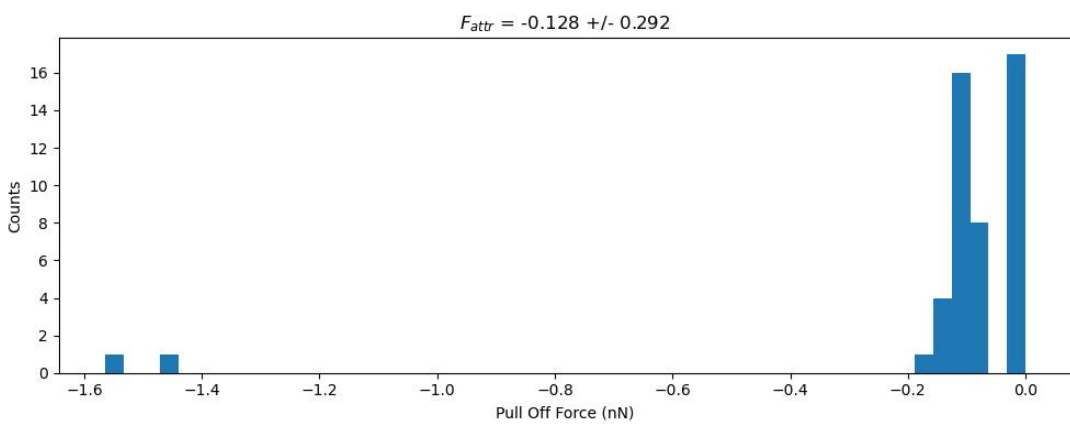


Figure 7.16 Retract curve for 10mM, S2 at 0.1Hz

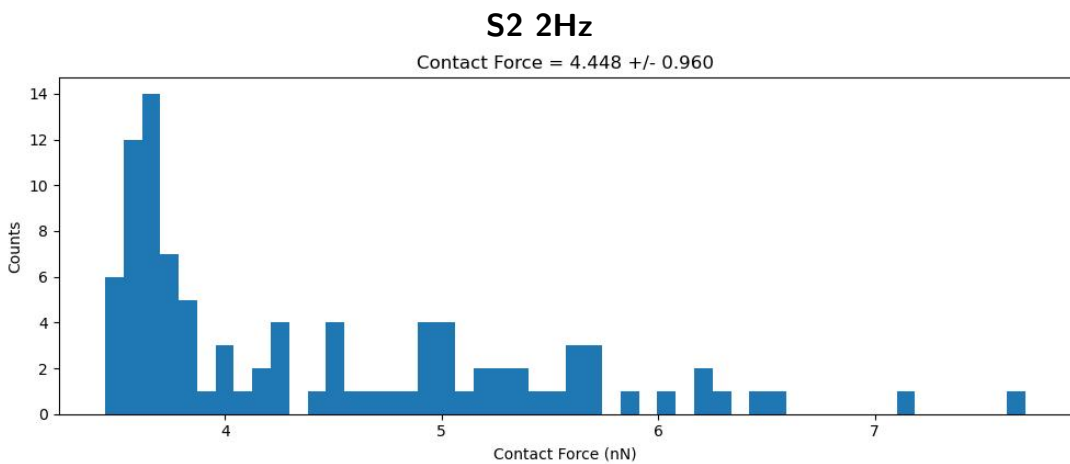


Figure 7.17 Approach curve for $10mM$, S2 at 2Hz

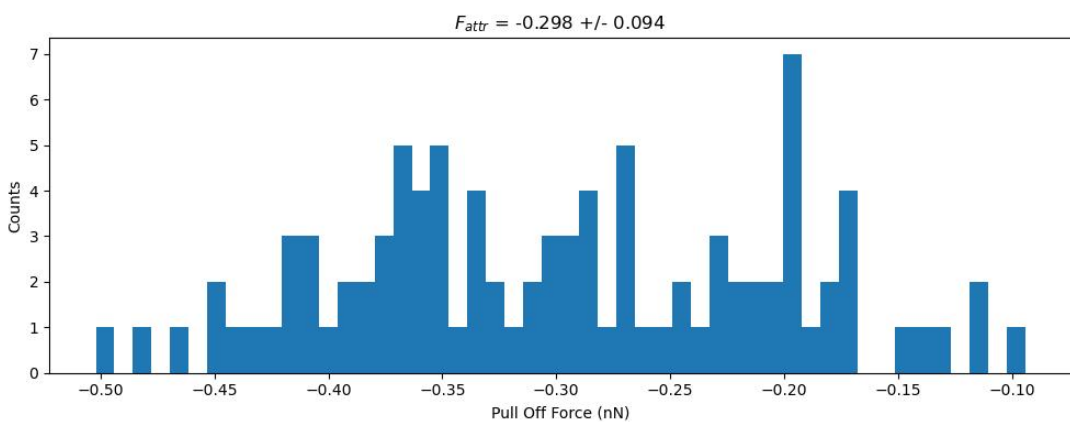


Figure 7.18 Retract curve for $10mM$, S2 at 2Hz

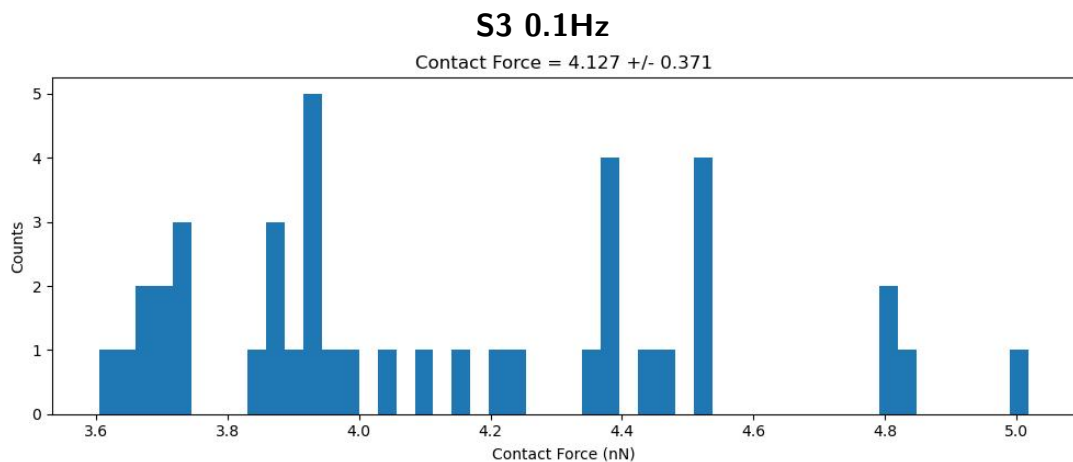


Figure 7.19 Approach curve for 10mM, S3 at 0.1Hz

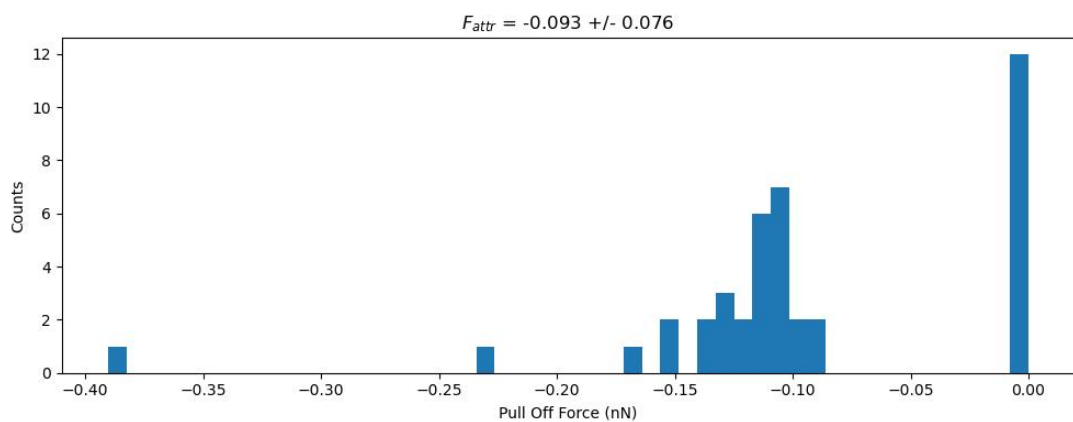


Figure 7.20 Retract curve for 10mM, S3 at 0.1Hz

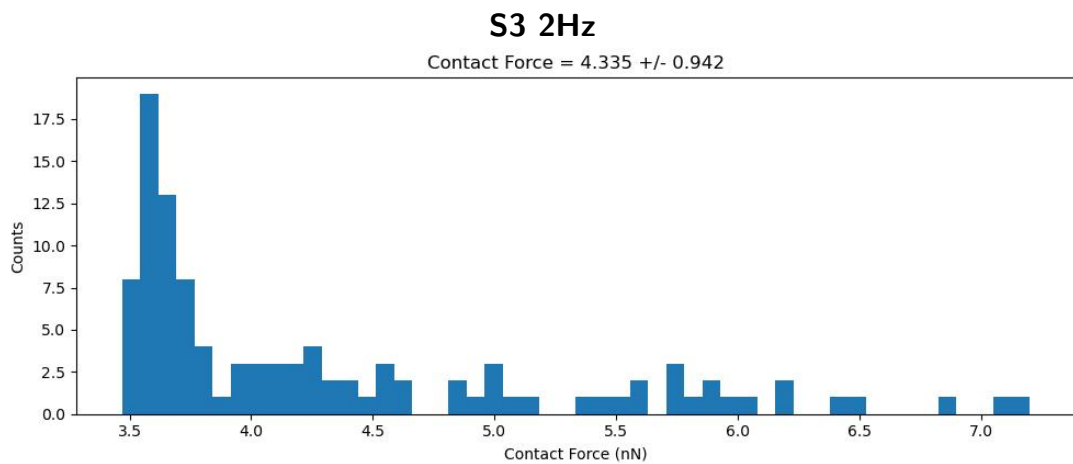


Figure 7.21 Approach curve for $10mM$, S3 at 2Hz

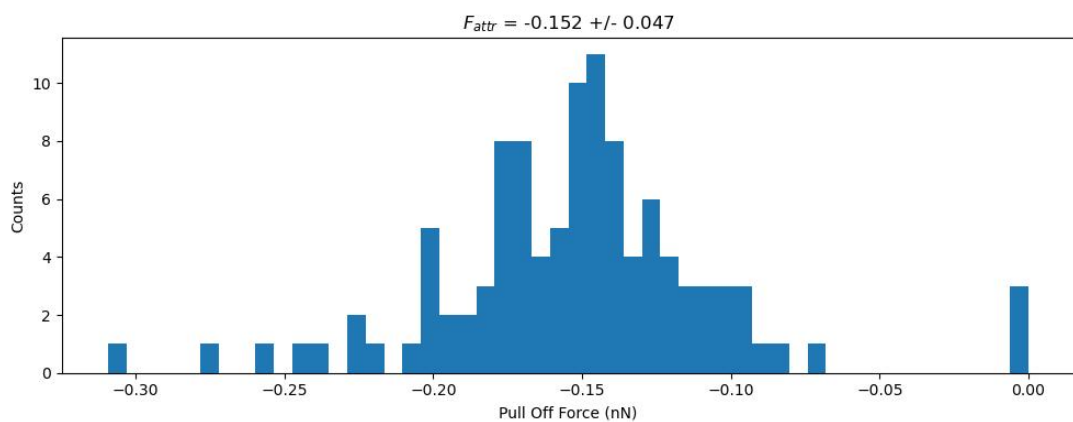


Figure 7.22 Retract curve for $10mM$, S3 at 2Hz

25mM

25mM shows data within an expected range for the approach portion of the data, whereas the retrace demonstrates a significantly reduced attractive force.

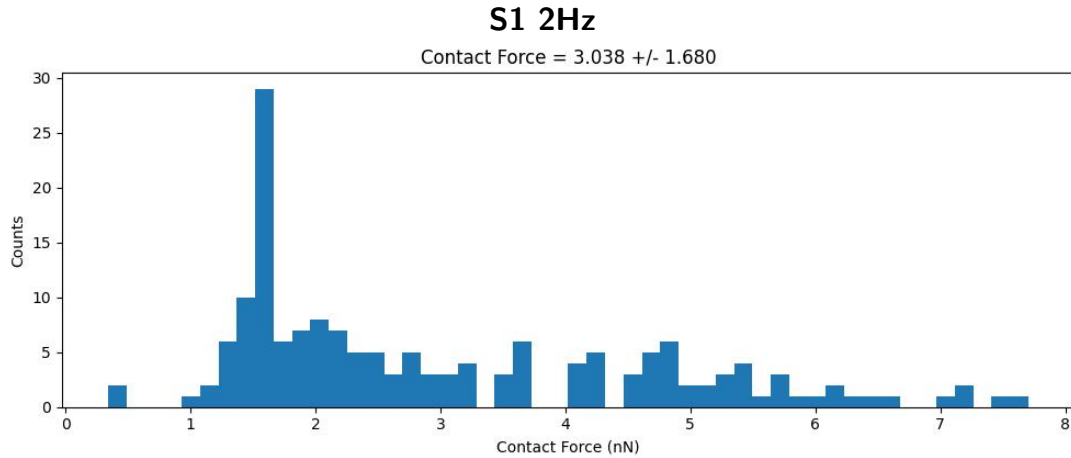


Figure 7.23 Approach curve for 25mM, S1 at 2Hz

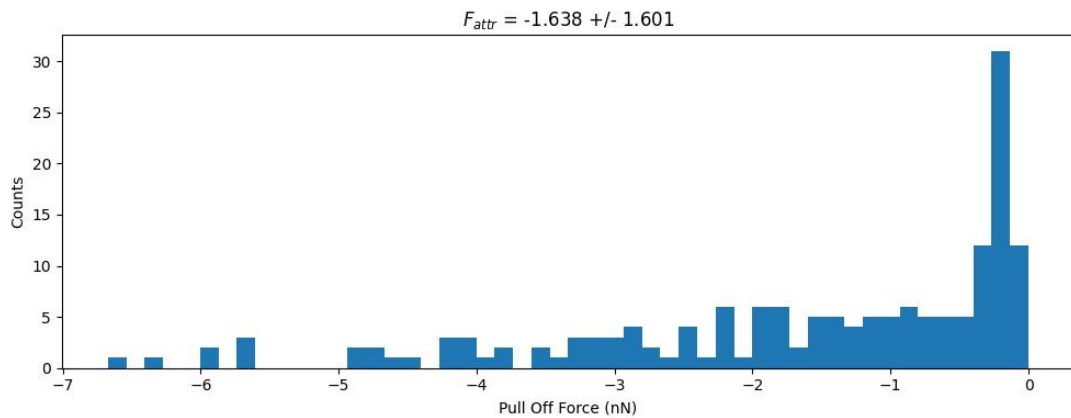


Figure 7.24 Retract curve for 25mM, S1 at 2Hz

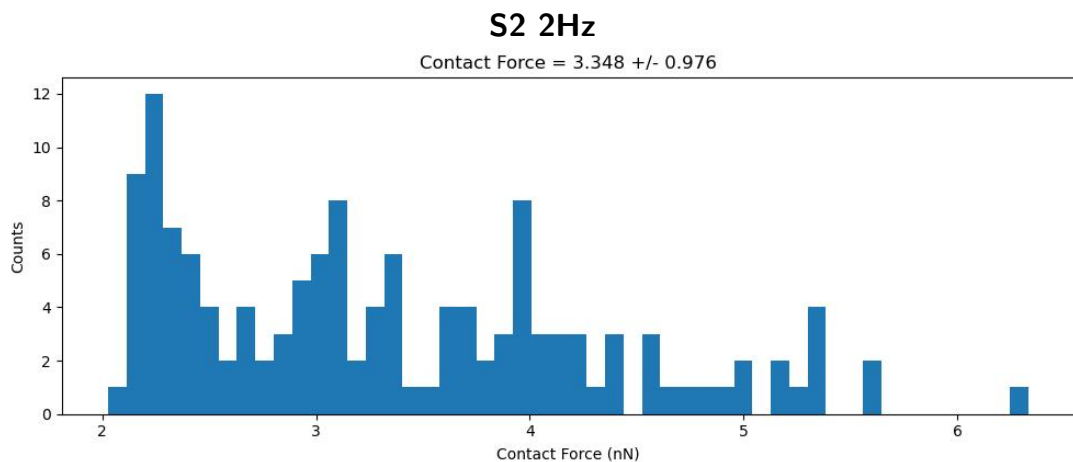


Figure 7.25 Approach curve for 25mM, S2 at 2Hz

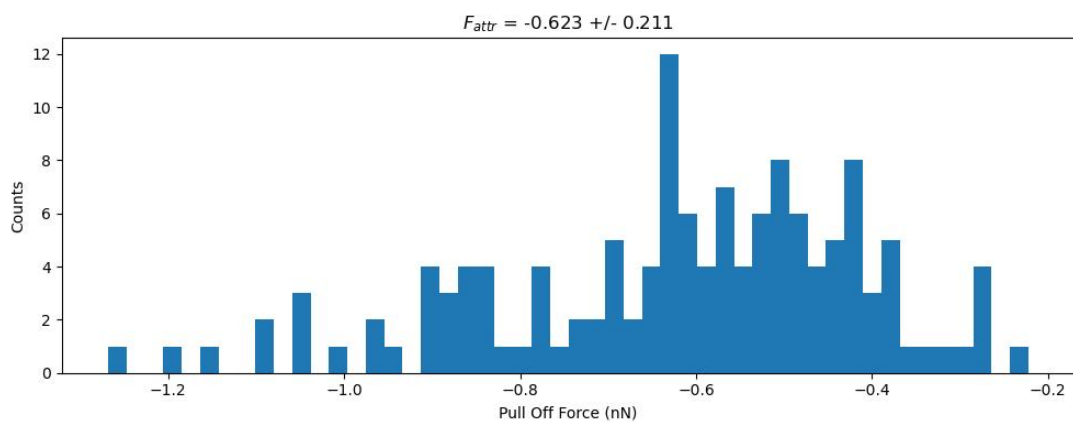


Figure 7.26 Retract curve for 25mM, S2 at 2Hz

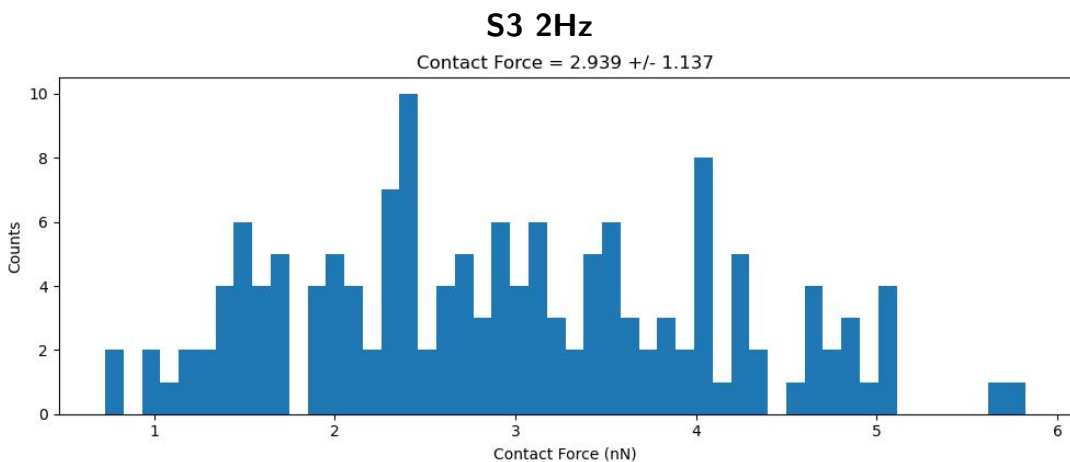


Figure 7.27 Approach curve for 25mM, S3 at 2Hz

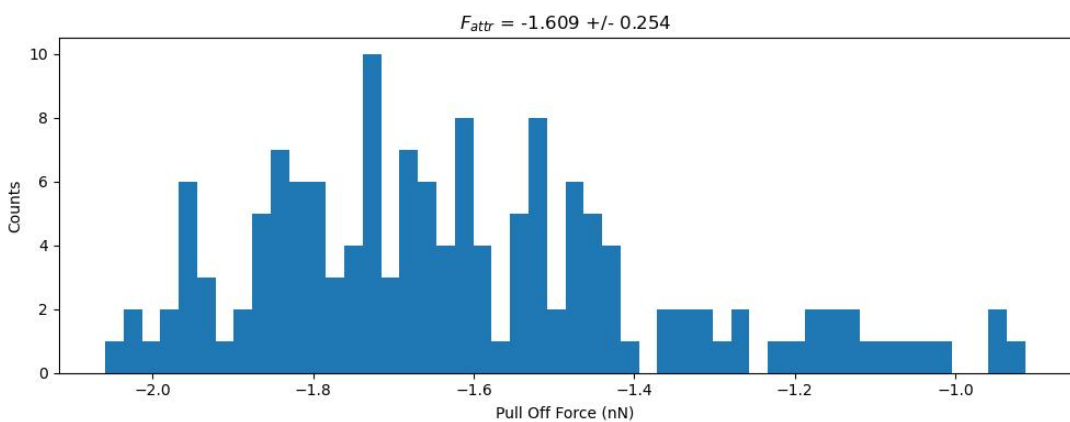


Figure 7.28 Retract curve for 25mM, S3 at 2Hz

230mM

230mM 2Hz again shows data within expected ranges, while having a slightly higher approach repulsive force. For the retrace attractive force, the results are similar, again with a slightly lower attractive force.

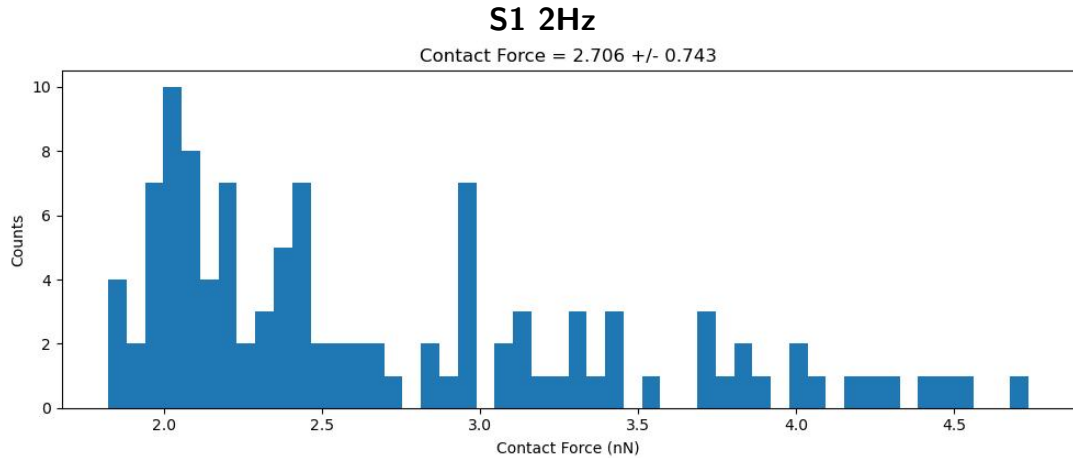


Figure 7.29 Approach curve for 230mM, S1 at 2Hz

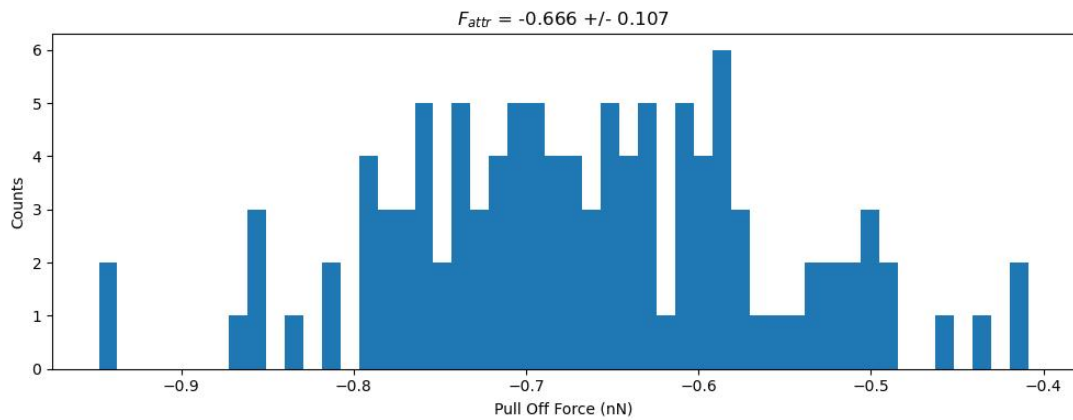


Figure 7.30 Retract curve for 230mM, S1 at 2Hz

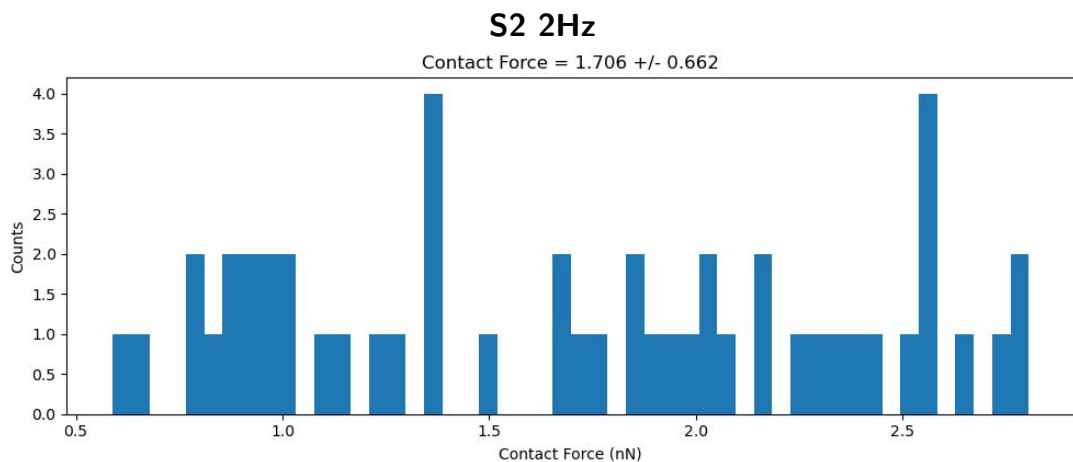


Figure 7.31 Approach curve for 230mM, S2 at 2Hz

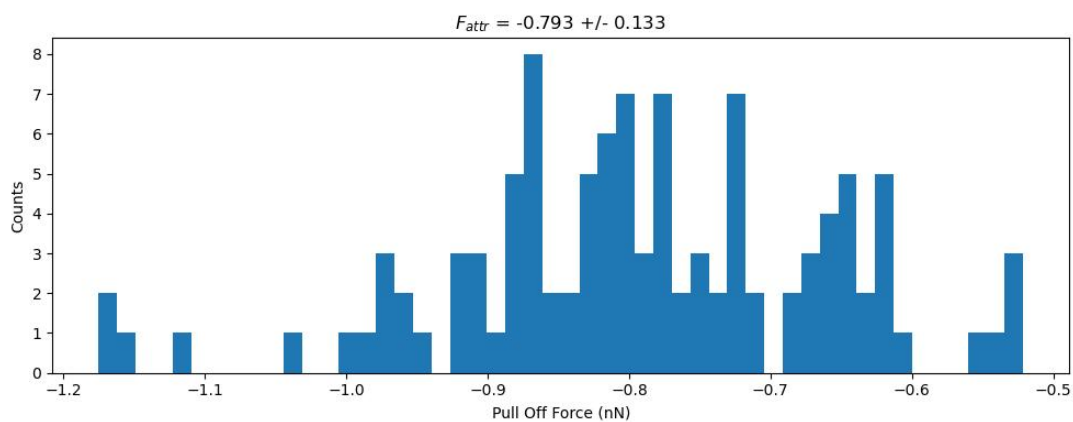


Figure 7.32 Retract curve for 230mM, S2 at 2Hz

550mM

550mM 2Hz marks a shift in approach forces towards the attractive. The results are similar again to other datapoints in this series; minorly reduced attractive force on the retrace. However, interestingly, the approach has very little attractive force.

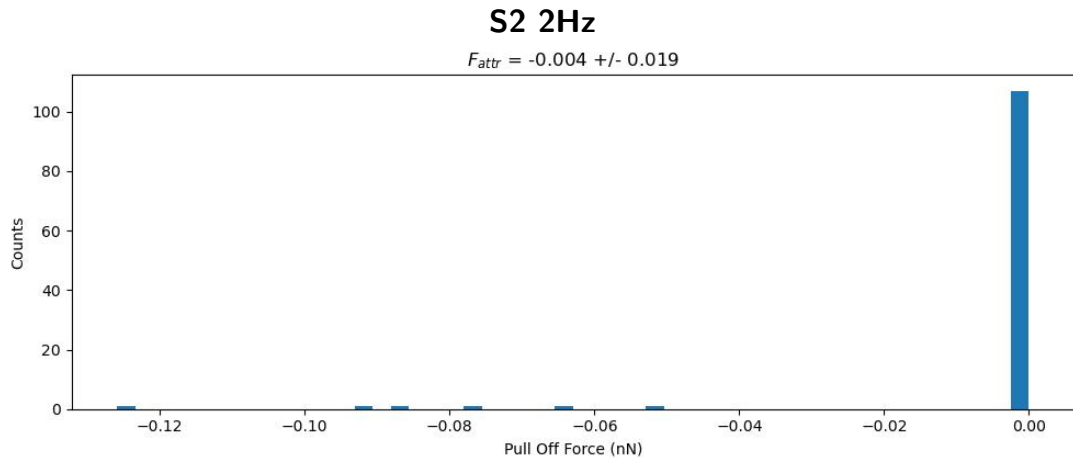


Figure 7.33 Approach curve for 550mM, S2 at 2Hz

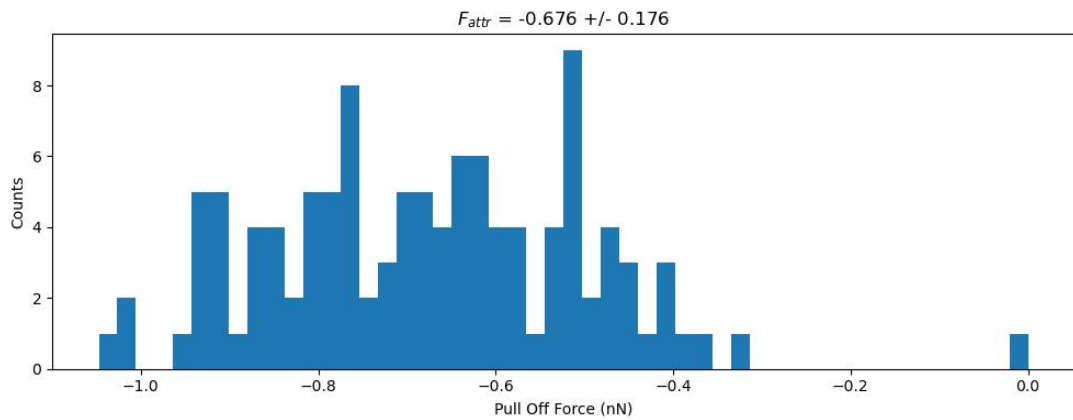


Figure 7.34 Retract curve for 550mM, S2 at 2Hz

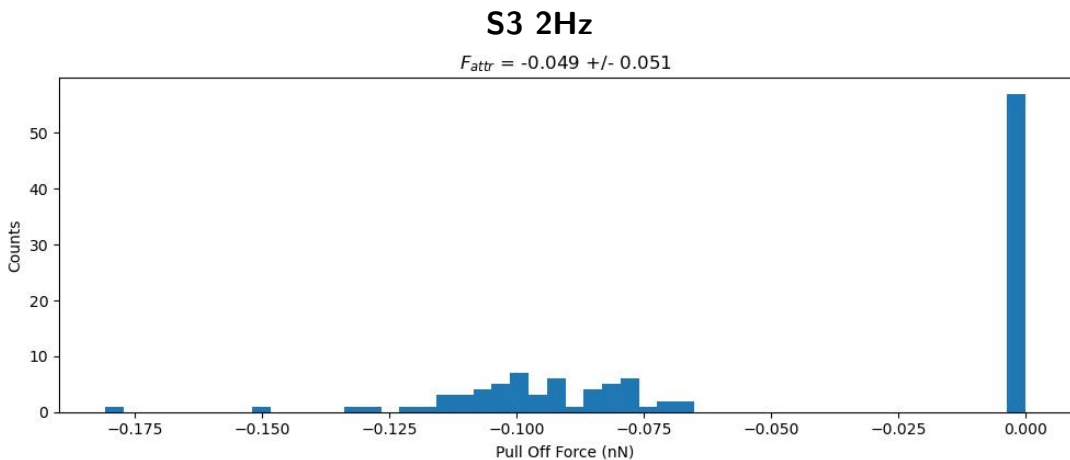


Figure 7.35 Approach curve for 550mM, S3 at 2Hz

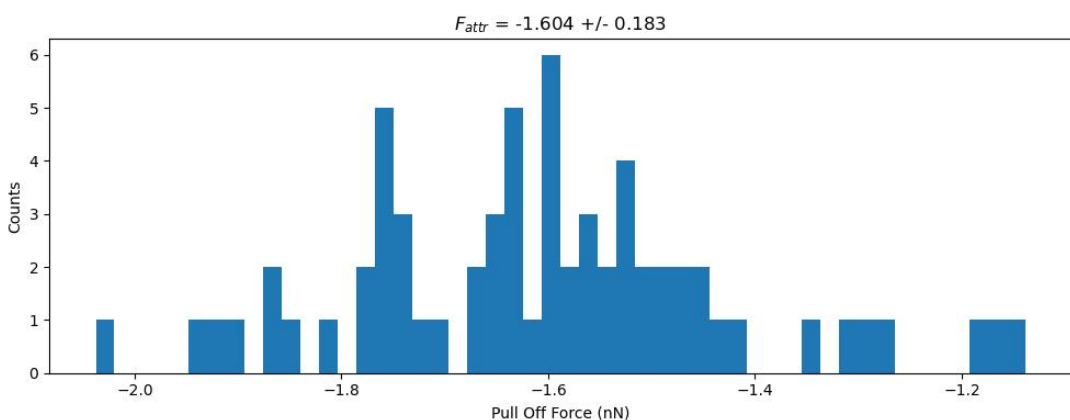


Figure 7.36 Retract curve for 550mM, S3 at 2Hz

Averaged curve of data

These datapoints were then averaged, with the standard deviations ($Stdev_{avg}$) concatenated between sites using equation 5.1

These points were then plotted against the original dataset to investigate if any noticeable overall differences between points could be discerned.

The approach curve (*Figure 7.37*) demonstrates an interesting observation: While minor, the increase in tip speed seems to indicate that the force required to bring the tip in contact increases with the speed of the tip. Possibly indicating that the system relaxes or changes in response to an approaching surface. 0.6mM is particularly interesting - as there was a significant increase in repulsive force at the higher speed, potentially indicating that tip speed has larger effects at very low ionic concentrations. 550mM is also interesting, where there was very little in the way of variation, and the approach force was nearly 0, potentially indicating that as the tip approaches, the surface was unable to relax in this way. 0.1Hz, while interestingly overlaps with the 2Hz datapoint, does not represent enough datapoints to fully make any solid conclusions.

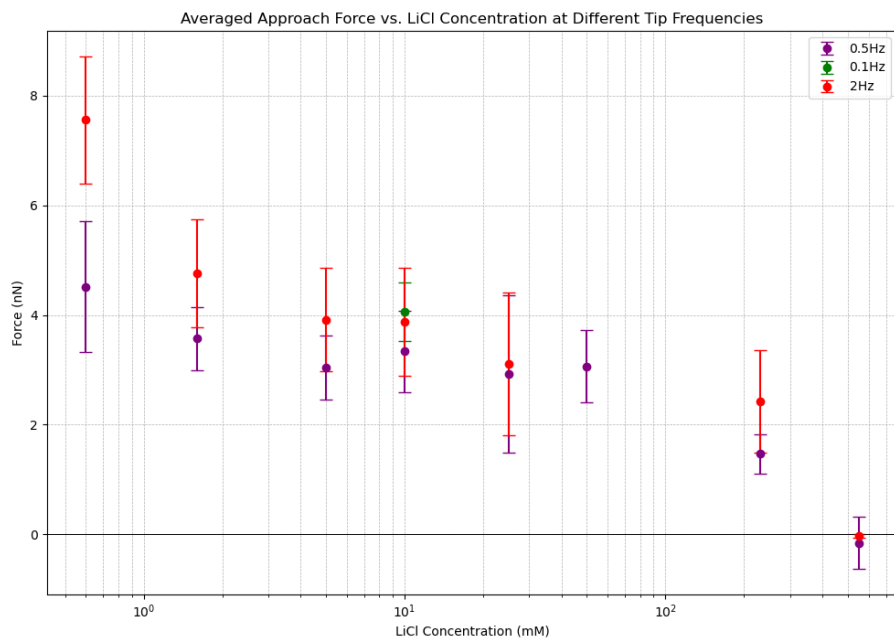


Figure 7.37 Averaged approach curve with the range of tip speeds. 0.5Hz represents the standard dataset, whereas 0.1Hz and 2Hz represent the modified speeds under investigation.

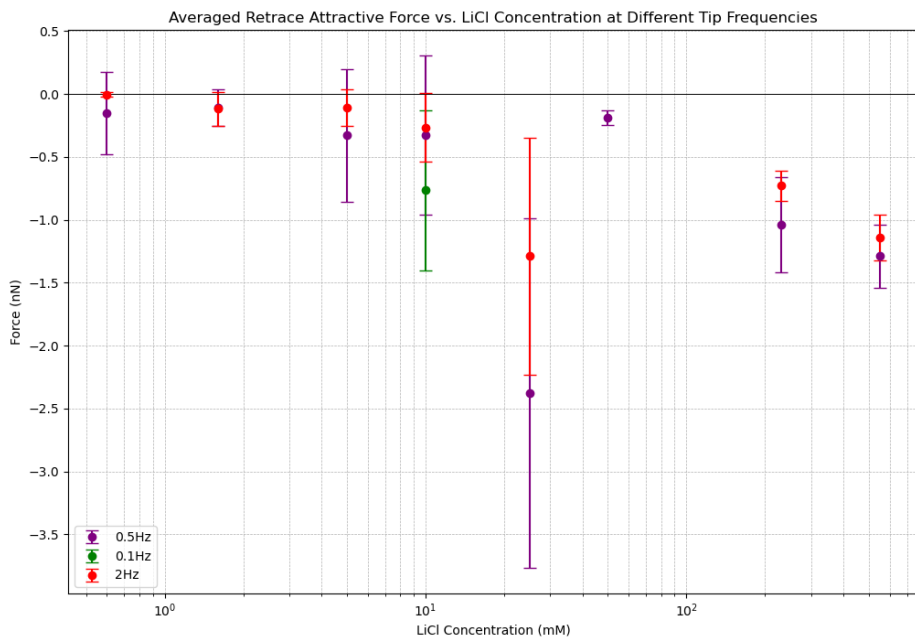


Figure 7.38 Averaged retract curve with the range of tip speeds. 0.5Hz represents the standard dataset.

The retrace curve (*Figure 7.38*) shows a similar story - the majority of each of the datapoints are slightly less attracted to the surface, and as such, are easier to disengage. This again could indicate that the potential relaxation of the system to introduced conditions. 0.6mM as well does not seem to carry over the large change seen in the retrace curve, instead giving a value within expected ranges. The 0.1Hz datapoint, also seems to indicate that as tip speed decreases, the attractive potential between tip and surface increases. Another interesting factor is the 25mM datapoints; the wide range and intrigue of a sudden spike in attractive force is retained, if muted, in the data. However, for 25mM it is important to point out that the sites for 25mM values are the same between speeds, so if the cause is due to the site location themselves that would not be changed in this case.

Another aspect of investigation worth looking into is how the speed influences the reliability of the data. As tip speed increases, the volume of data decreases, as mentioned before, and as such it stands to reason that the standard deviation of the data would increase with this phenomena too.

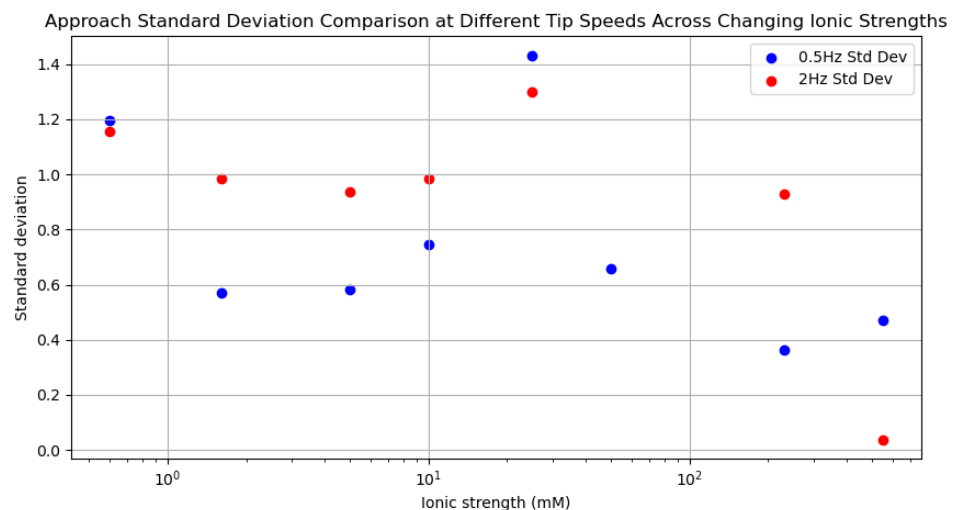


Figure 7.39 Averaged approach standard deviation between points. 0.5Hz represents the standard dataset.

For the majority of the datapoints this theory proves true (*Figure 7.39*, with 2 datapoints (0.6mM and 25mM) slightly below the slower value. The big exception however is the 550mM datapoint.

However, when we consider the retract curve (*Figure 7.40*, our expectations are flipped. For each of the datapoints there is less variation between points, indicating a faster tip leads to a more stable analysis for the retraction. This could potentially lean into the relaxation theory, where, because there is less time for the system to relax and alter, the retrace experiences a more repeatable environment.

The other question that is raised by this analysis is thus, if a tip is held in constant and allowed to relax, how would that affect the results? This leads us directly

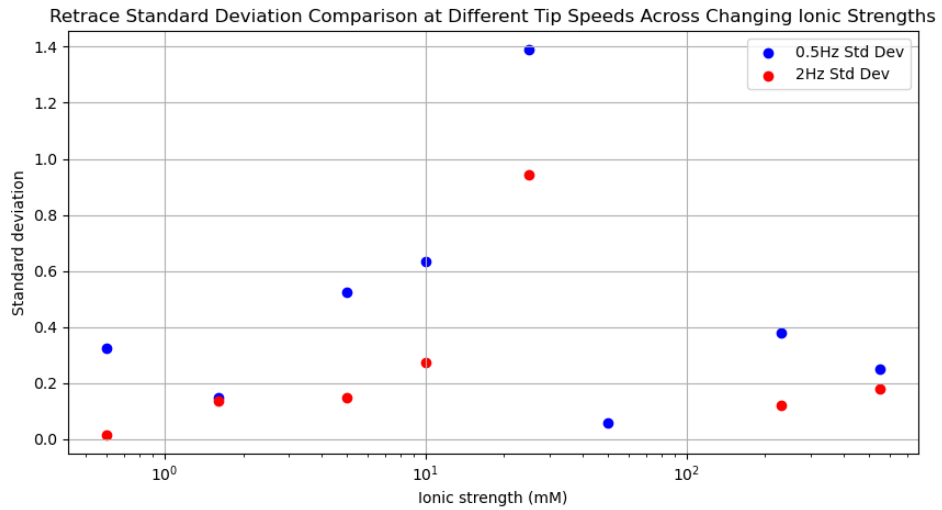


Figure 7.40 Averaged retract standard deviation between points. 0.5Hz represents the standard dataset.

into our next section, the dwell time analysis.

7.3 Dwell time

The dwell time represents the time in which the tip is held down onto the surface between the approach and retrace curves. This is usually done by the system attempting to use the feedback mechanism to keep the force applied to the tip at a constant force. This action was done for each and every curve taken on the machine for the dwell dataset.

For this series of data, only one point per concentration was done. This was due to the increased strain this often puts on the cantilever, which was an important and managed resource throughout this investigation. Overindulgence in certain aspects of the experimental protocol may lead to underindulgence or lack of exploration in other areas. As a result, a series of repeats could be performed to improve this analysis. For this case, the single dwell datapoints were compared against the averaged standard dataset points.

One other frustration seen during this operational mode was the inconsistency in data shape. This made using the analysis software particularly challenging, and is an area of potential improvement for the script. The script expects the user to provide a clear series of data with an approach and retrace aspect separated clearly, however, due to the 5 second dwell time providing a high degree of variability in forces, this can often trip up the detection method used to differentiate between the two phases. While two datapoints were successfully analysed using the script (25mM and 230mM) the other datapoints would've required a significant rewrite. As such, a simplified script was written to extract the peak force from the retrace curve, as, in theory, the only portion of the curve

affected should be the retrace due to the potential impact of dwelling only being felt during the retrace curve.

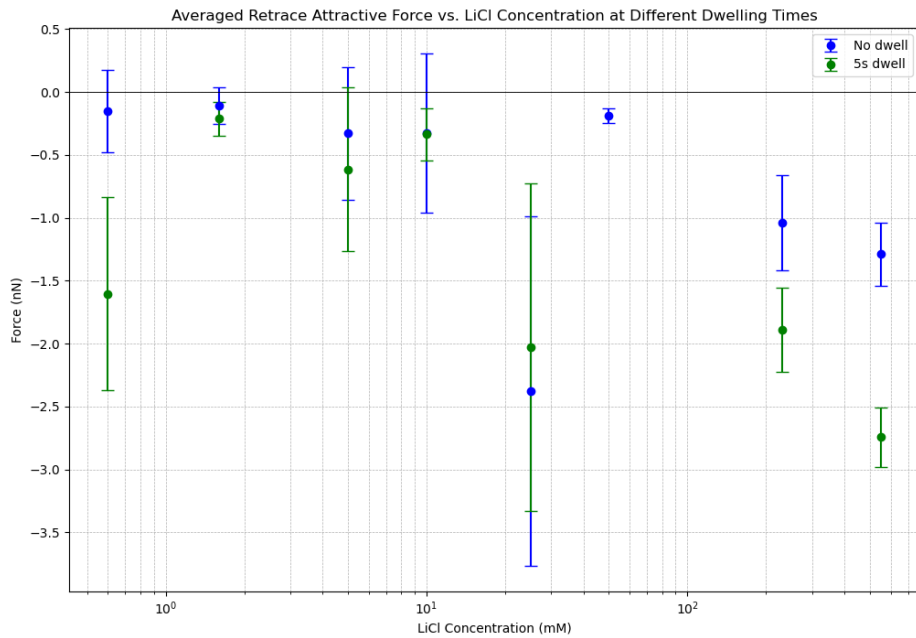


Figure 7.41 A graph demonstrating the averaged retract forces felt by the AFM tip at different LiCl concentrations with 5s dwell time and 0s dwell time respectively.

The retrace curve presents (Figure 7.41) an interesting but not unexpected conclusion: As tip exposure time increases, so too does the retentive force between the surface and tip on the retrace motion for some of the data points (0.6mM, 230mM and 550mM particularly). However, one that significantly stands out is 25mM, where the postulation is inverse. This could potentially be due to the previously proposed relaxation time, or because 25mM is consistently weird.

However, when we look at the approach curve for the 2 points (figure 7.42), we see an interesting picture. As the dwell time is increased, the time between curves is increased too, providing more time for water molecules and ions to adapt to the approaching tip, thus decreasing the repulsive force. This highlights that there is potentially hysteretic effects.

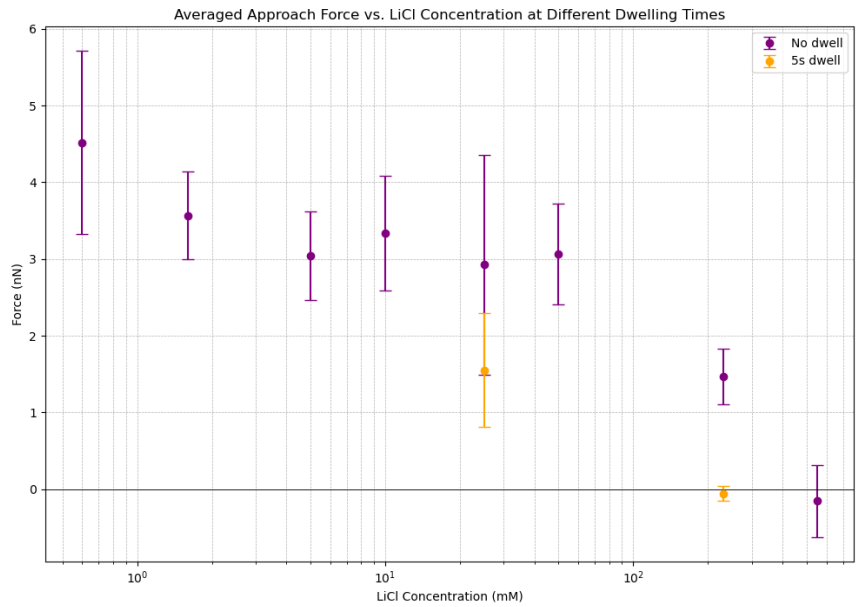


Figure 7.42 A graph demonstrating the averaged approach forces felt by the AFM tip at different LiCl concentrations with 5s dwell time and 0s dwell time respectively.

7.4 pH analysis

The pH level of a solution can significantly affect the forces between silica particles in a 50:50 water-glycerol solution due to changes in the surface charge of the silica particles. At different pH levels, the degree of ionization of silanol groups on the silica surface can vary, which impacts the electrostatic component of the total interparticle force.

Silica surfaces are known to have silanol groups that can either accept or donate protons depending on the pH. At pH 5, which is close to the isoelectric point of silica, the surface charge density is reduced. This condition is interesting for force measurements since the electrostatic repulsion between particles is minimized, allowing other forces (such as van der Waals or steric forces) to be more prominently observed. [73]

While the solutions used in the standard dataset was around pH 7 on creation the pH can drift to slightly acidic due to carbon dioxide (CO_2) from the air dissolving in the water, forming carbonic acid (H_2CO_3), which can dissociate to form bicarbonate (HCO_3^-) and hydrogen ions (H^+). Though this effect is generally quite small, it is worth investigating to see if changes in pH could've altered the resulting dataset.

For this analysis a solution made up to pH of 5 instead of the standard pH 7 was performed, with the results directly compared against the 0.6mM LiCl concentration solution.

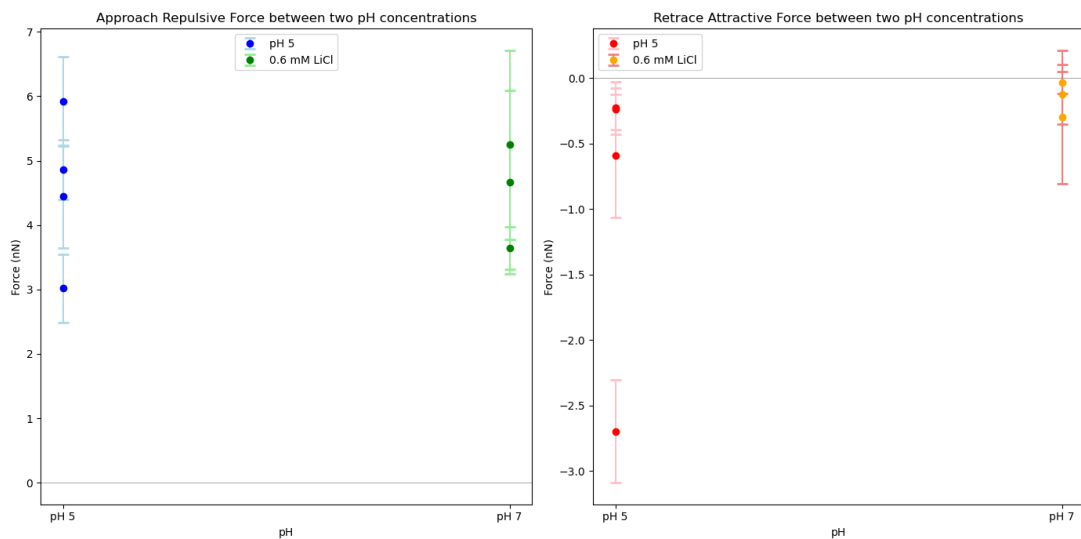


Figure 7.43 A graph demonstrating the differences in approach and retract forces at differing pHes. pH 5 is the deviation and pH 7 is the standard.

From the observed change in pH, the resulting forces are similar to what would be expected with a pH 7 environment (0.6mM LiCl), with a striking overlap between the two data series on approach. The only observable difference between the two is in the retrace curve, where one datapoint is significantly more attractive.

7.5 JPK Forcemapping

One of the limitations of using the interpretation software is that it assumes that all curves are of the same shape. This is not the case for a range of sites. While this helps highlight features (such as the shelf) across multiple repeats on the same area, it does not take into account a range of different sites. That being said, however, as long as the user does not attempt to use the software incorrectly to provide an averaged graph, the attractive/repulsive force analysis is perfectly applicable and as such was used to analyse each individual curve from the forcemapping.

Due to the differences between the AFMs, and potentially the way the AFMs were used to measure the interactions, the “shelf” seen was more of a snap to contact point in the curve. This meant that the shelf seen in the previous AFM, may have been the point in which the tip snapped to the surface, and the older AFM may not have been able to detect or measure this sudden change in the way the new one has.

Due to the limited window in which this AFM was available, it was not possible to explore this interaction further, but it is promising that this shelf feature is present across multiple AFMs and sites. The script was adapted in order to use the new data type, with a specialised script written to convert exportable JPK filetypes into the format expected by the software.

The operation of the AFM was done with the same tip and conditions, with a 16x16 grid with a 1um distance between each of the sites. Only 2 concentration could be performed during the available time: 0.6mM and 10mM.

0.6mM approach

As the script is written to concatenate a range of graphs into a single one, there were some quirks of processing. For one, the histogram shows a range of forces, but it is important to know that for this range it is across different areas of the glass, rather than a single area.

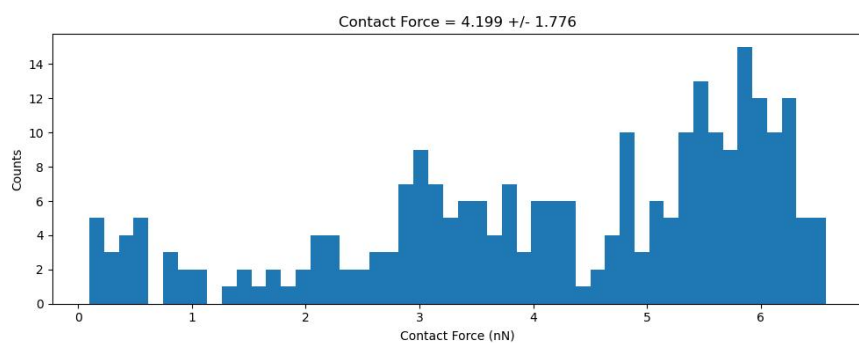


Figure 7.44 Approach force histogram for 0.5mM concentration.

The heatmap demonstrates the wide range of variability seen on a glass surface.

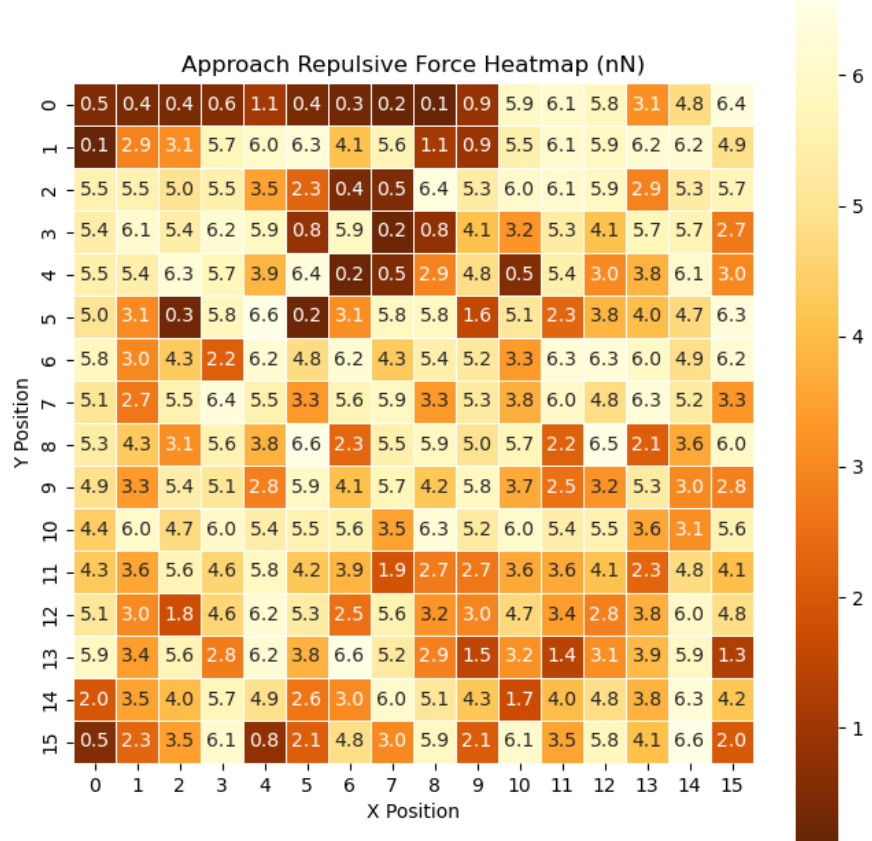


Figure 7.45 Approach heatmap for 0.5mM concentration.

This indicates that interacting surfaces is significantly dependent on local conditions of the surface. A range of forces is present, indicating variability in the interaction forces across different points on the surface. This could be due to surface heterogeneities or variations in local chemical composition and structure.

0.6mM retract

However for the retraction portion of the curve, the histogram shows the distribution of attractive forces measured during the retract phase across all different sites. Most measurements cluster around a relatively small attractive force as seen in the standard dataset, but there is an outlier showing a strong attraction. This suggests that while the retract forces are generally consistent, certain specific interactions result in much stronger attraction.

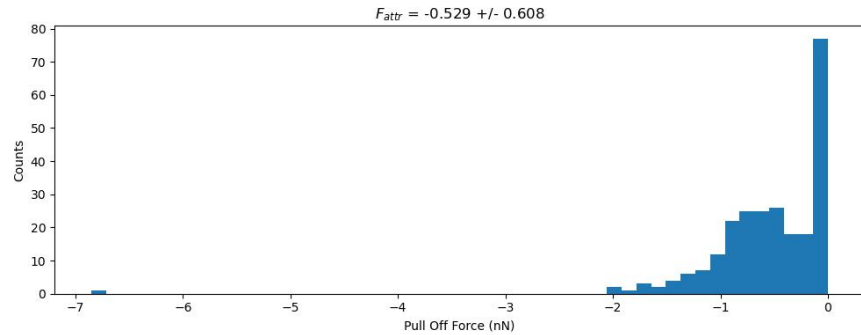


Figure 7.46 Retract force histogram for 0.5mM concentration.

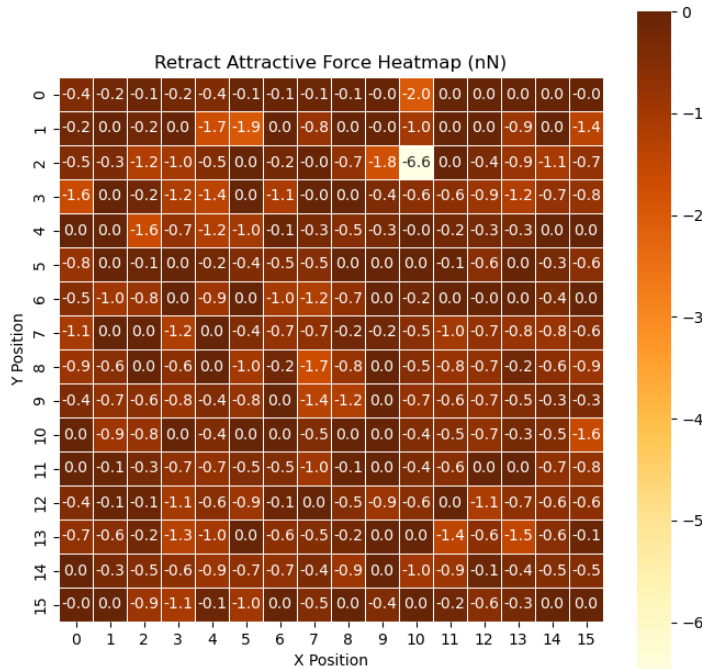


Figure 7.47 Retract heatmap for 0.5mM concentration.

10mM approach

The histogram shows a wide range of contact forces with a relatively large standard deviation. This suggests that at the 10mM concentration, there is a significant variability in the forces measured across different sites of the surface during the approach phase. Interestingly, for some curves an attractive force was observed which is unlike the standard dataset. The attractive part of the curves are generally clustered towards the top of the heatmap suggesting that the surface has regions of varying repulsive forces.

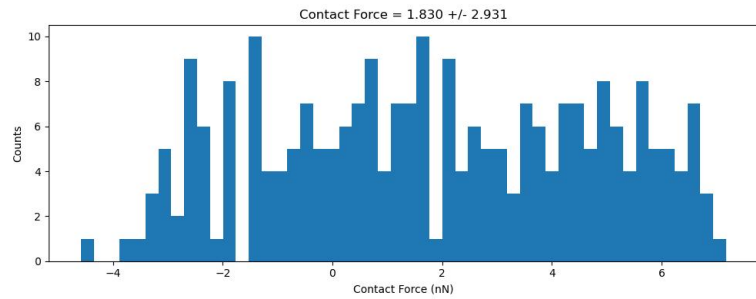


Figure 7.48 Retract heatmap for 0.5mM concentration.

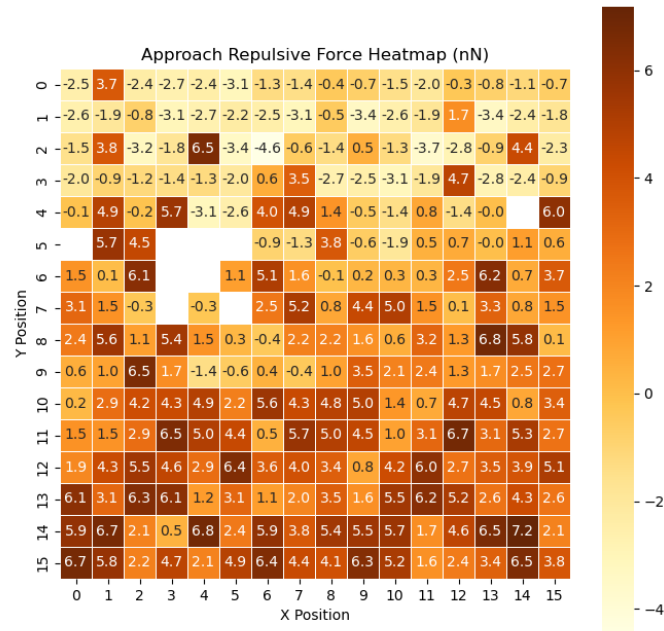


Figure 7.49 Approach heatmap for 10mM concentration.

10mM retract

The retract portion of the curve is even more unusual with a consistent attractive force recorded at about 34nN. This is unlike anything else seen in the dataset, so it is likely that the tip was contaminated or damaged, especially since the tip used was a reused one at the time.

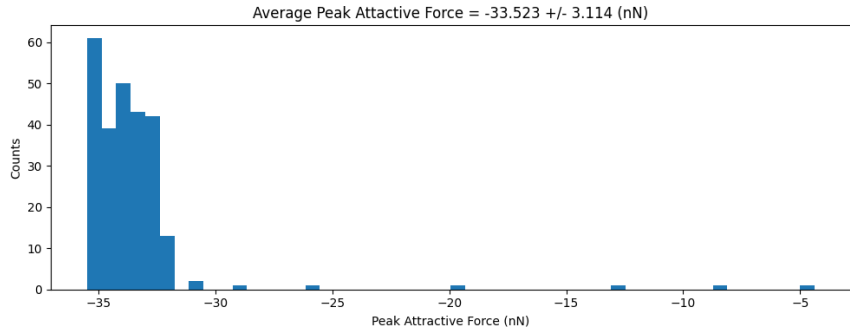


Figure 7.50 Retract heatmap for 0.5mM concentration.

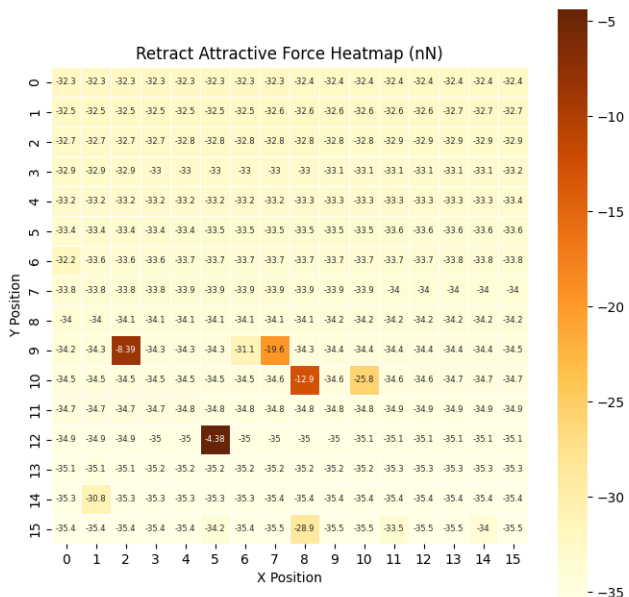


Figure 7.51 Retract heatmap for 10mM concentration.

While the 10mM results are ultimately suspicious, it does highlight the variability seen in these kinds of surfaces. As to what could possibly cause these high degrees of variability, that leads us to the next chapter: the overall analysis of all of the data presented so far.

Chapter 8

Further analysis and discussion

This chapter aims to analyse and discuss the findings presented in the previous three chapters, focusing on the intricate details and implications of Atomic Force Microscopy (AFM) force curve analysis. The preceding chapters laid a foundational understanding of the colloidal interactions and the work involved to process the raw data into a usable format. This chapter instead will focus on using the previous chapters' data to draw conclusions about colloidal systems. The force-distance profiles obtained from AFM are analysed, providing a direct and nuanced insight into the particle interactions at an individual level. The force curves, reflecting the precise nature of forces acting at the nanoscale, will be juxtaposed against the bulk property measurements to draw a more comprehensive picture of the colloidal dynamics. This analysis will not only validate but also potentially challenge and refine the conclusions drawn from the bulk measurements, offering a more holistic understanding of the colloidal systems under study. Through this integrative approach, we aim to bridge the gap between our microscopic observations and derive behaviour on the macro scale. This chapter takes the following format, firstly over viewing the approach data, then the retract data.

8.1 Approach force curves

The approach curve section of the data demonstrated a range of interesting effects and features. For one, the increase in LiCl concentration directly resulted in a decrease of the repulsive force upon the tip, likely due to the charge screening effect. At certain concentrations (550mM) this repulsive force flips into an attractive force, presumably where the electrostatic repulsion was muted enough for Van der Waals forces to predominate. However, even then, there was a notable range of attractive force, with some 550mM curves having very little attraction (550mM site 2).

The variety in the magnitude of attractive forces at this high ionic strength, especially observed in the 550mM site 2 curves, further complicates the narrative.

Such variability could be the result of surface heterogeneity, variations in ion distribution, or differing hydration layers, each of which could alter the force profile significantly.

Another interesting feature observed is the shelf. This shelf presented a sometime present energy barrier for the tip to overcome to come into contact. The presence of this shelf could possibly influence the plateau seen in the Averaged Approach Force vs LiCl Concentration graph, as the script was set to define contact as after the shelf.

Interestingly, the absence of a shelf often correlated with lower repulsive forces, suggesting a relationship between the energy barrier and the overall force profile. In the case of 550mM concentrations, where an attractive force towards the surface was noted, the presence of an energy barrier despite the attraction further adds to the complexity. It raises questions about the nature of these barriers: whether they are purely electrostatic or if other forces, such as steric or hydration forces, contribute to their formation.

8.2 Retract force curves

The retract force curves, which are often omitted due to their lack of acquiescence to DLVO, have several interesting properties too. Firstly, in general as the LiCl concentration increases, so too does the attractive force between the surface and the tip. But equally, when dwell time is applied, the attractive force additionally increases. This likely means that the mechanism holding the tip down during retrace may be dependant on ionic effects.

When dwell time is factored in, the attractive force further increases. This increment is indicative of a time-dependent process, possibly due to the reorganization of ions around the contact point, which enhances the attractive forces. The mechanism underlying this could be attributed to a combination of factors such as ion adsorption, water structuring, or surface conditioning over time, which requires further investigation.

The increasing attraction with dwell time also underscores the dynamic nature of colloidal interactions, where the history of contact and the duration of interaction significantly influence the force profiles. This temporal aspect is often not captured in instantaneous measurements and suggests a viscoelastic or time-dependent response in the colloidal system.

In addition, the retract force curves with varying LiCl concentrations provide insights into the complexity beyond what is described by classical DLVO theory. The increased attraction at higher ionic strengths contradicts the expected screening effect that should reduce the interaction forces. This anomaly could be hinting at non-DLVO interactions, such as capillary forces, hydrophobic interactions, or specific ion effects, which are not accounted for in the classical theory.

Additionally, there are some curiosities in the dataset, 25mM for example has a

dramatic spike in attractive force towards the surface. This is further compounded by the dwell time decreasing the attractive force for 25mM. The shelf feature, as seen in the approach curves, is also present in the retract curve, indicating that the energy barrier may be more akin to an energy trap, which could lead towards the potential of surface roughness/frictional forces between the tip and surface.

8.3 Shelf analysis

The shelf seen in some datapoints is a consistent feature across multiple sites, present in the majority of the curves. The only concentration that doesn't feature the shelf in any of the sites is the 0.6mM concentrations, which is equally true in both the MFP and JPK AFMs.

However the shelf was also seen in the JPK forcemaps as well - specifically the 10mM curves. Though, the shelf prominence varies between sites, some have a visible shelf that extends across multiple nanometers, while others don't. This feature is also seen in other papers from literature.[37]

However, it is prudent to ensure that the script is not the cause of this feature. As part of the curve is used to align the data into a straight line for the contact region, it is conceivable that this was introduced by the user defining said region.

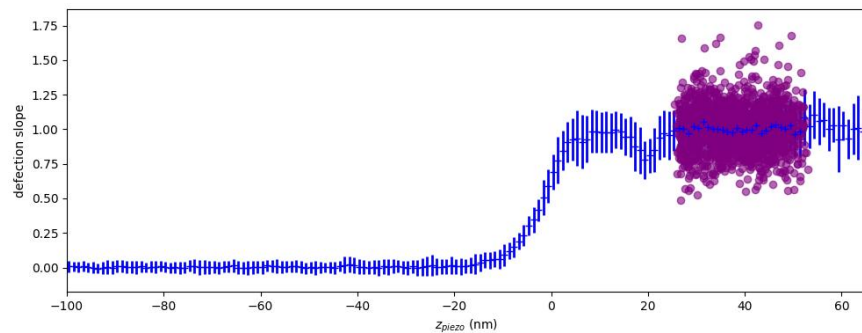


Figure 8.1 An example of a derived deflection slope vs z separation processed curve. This curve is used to help guide the user to optimise the fitting parameters. The purple region indicates the region used to define contact, and to help straighten the contact region.

From Figure 8.1 and 8.2 the fit can be seen to be right after the shelf shift. This is intentional during the fitting process - as to fit closest to the transition point. However, to ensure that the feature isn't caused by the script, lets apply the contact point to the shelf itself.

Figures 8.3 and 8.4 demonstrate that the fitting does not influence underlying features of the graphs. The shelf is still present in the curves, and the shelf is at the same expected force.

One specific paper describes an attractive force that is observed when using a counterion at intermediate salt concentrations. This force has a range of about 1

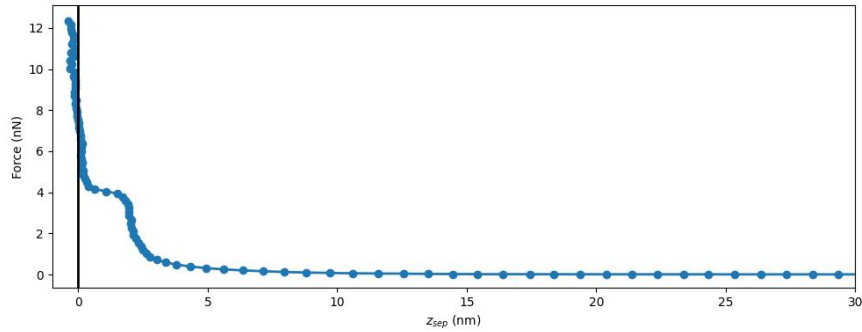


Figure 8.2 The fitted curve from the values above. The back is relatively straight.

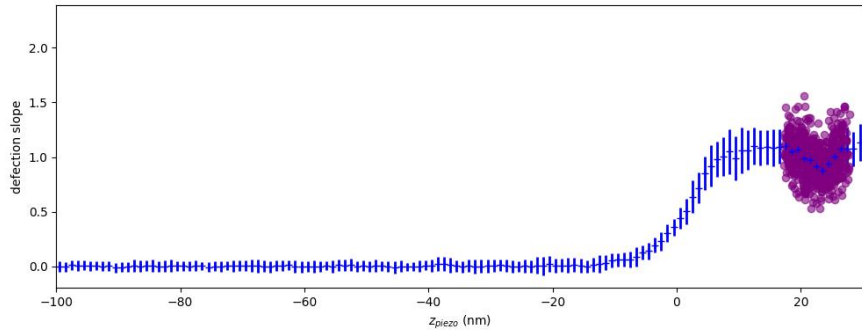


Figure 8.3 An example of a derived deflection slope vs z separation processed curve. The purple region indicates the region used to define contact, and has specifically been placed onto the shelf area.

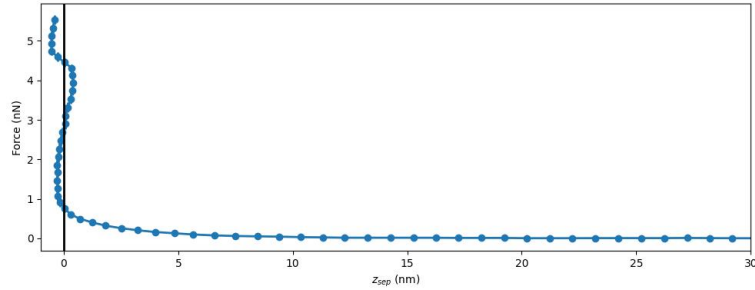


Figure 8.4 The fitted curve from the values above. The back is wonky, but the shelf feature prevails.

nm and is distinct from the forces predicted by DLVO theory. It is believed that this additional force could be due to ion-ion correlations, which are interactions that can occur between ions in solution due to their charge. However, the shelf could also be influenced by other factors such as surface charge heterogeneities (variations in the distribution of charge on the surface) or charge fluctuation forces (forces that arise from temporary changes in the distribution of charge). [81]

However one interesting point about the findings in that paper is the notation of

a roughly 1 nm range. Given that several of the graphs in the dataset feature shelves, an analysis of the shelf force (the force required for the energy barrier to yield) and an analysis of the shelf range (the width of the shelf as seen on the dataset) would serve as a useful exploration for determining overlaps between our data and theirs.

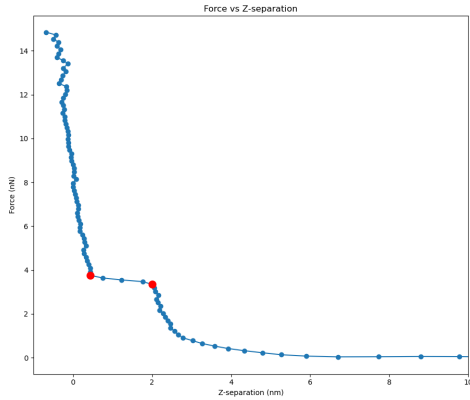


Figure 8.5 Demonstrating the fitting range for the shelf analysis. The two red dots highlight the end points of the range. The shelf force is calculated by the average force for the points within the range, and the shelf range is calculated by the width of the two points in nm.

This data was taken for all datapoints that could be extracted this way (one or two shelves were omitted due to the inability to define a firm range, i.e. the repulsive curve blended into the shelf feature, a good example of this is 25mM site 3). These points were then plotted in figure 8.6.

The results in 8.6 show that the shelf had a consistent range between 1-2nm, and the yield force was between 1.5-4nN. While the range was slightly higher in our data, our findings align with what Kilpatrick et al discusses [49]. The fact that the shelf is consistent across a broad range of salt concentrations might imply that these additional forces are present regardless of ionic strength variations, possibly due to surface charge heterogeneities or charge fluctuation forces that are less sensitive to ionic strength.

In addition to this finding, the JPK forcemapping curves demonstrated the same shelf seen across the standard dataset. As the tip moved across multiple locations, the shelf force changed, however the shelf range was relatively static.

One interesting aspect of this shelf as seen in the JPK AFM is the sudden attractive force felt by the tip. This again is in line with Kilpatrick et al.

As such our findings match Kilpatrick et al. [49], where the shelf can be attributed to additional, non-DLVO attractive forces likely related to the specific ion effects, such as ion-ion correlations, surface charge heterogeneities, or other surface-specific interactions at the water-silica interface such as hydration forces. These forces can be significant in the presence of multivalent ions, which are known to impact the surface charge and hydration layers in a manner not fully accounted for by classical DLVO theory. As such, this provides evidence towards a growing

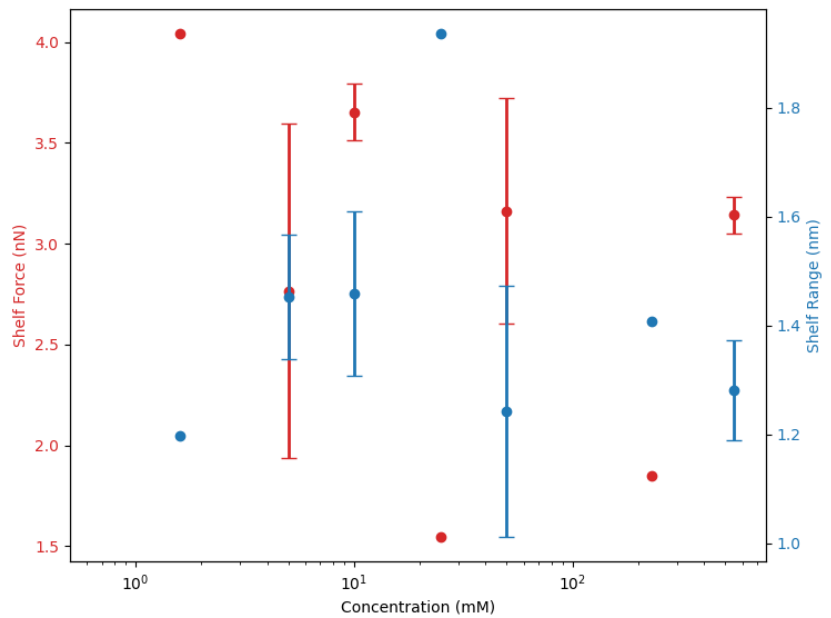


Figure 8.6 Demonstrating the range of self force and self range. For the range of data, there was no significant change in the datapoints due to salt concentration for both features.

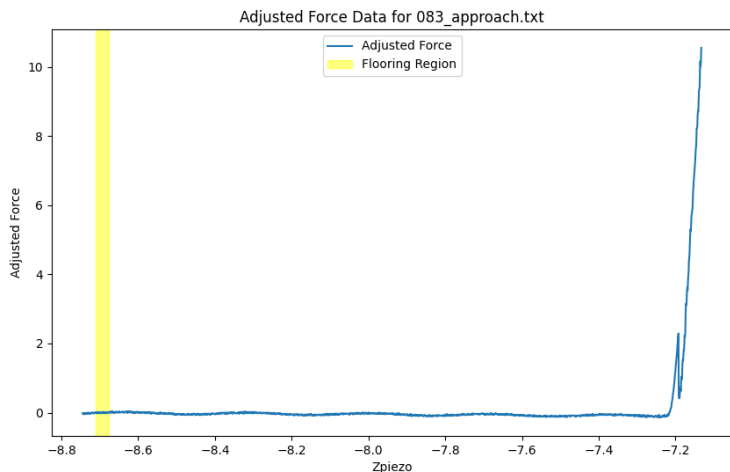


Figure 8.7 An example of an unprocessed curve (except force flooring) from the JPK forcemapping. The "shelf" can clearly be seen, with a sudden jump down to contact. The difference between this and the MFP could be due to the higher resolution the newer AFM offers.

call for improvements to the current DLVO theory.

8.4 Overcoming the noise in data

The noise in the data from MFP AFM is significant. Not all AFMs can be operated in optimal conditions such as AFMs isolated from vibrations, under peak maintenance, free from external factors, etc. Other sources of noise in AFM can stem from electronic components, particularly those involved in the detection system, such as photodiodes and amplifiers. This includes shot noise from random electron motion, Johnson noise related to thermal motion within resistors, and noise intrinsic to operational amplifiers. Additionally, mechanical vibrations and thermal fluctuations also contribute to noise, affecting the spatial and temporal resolution of measurements. [34]

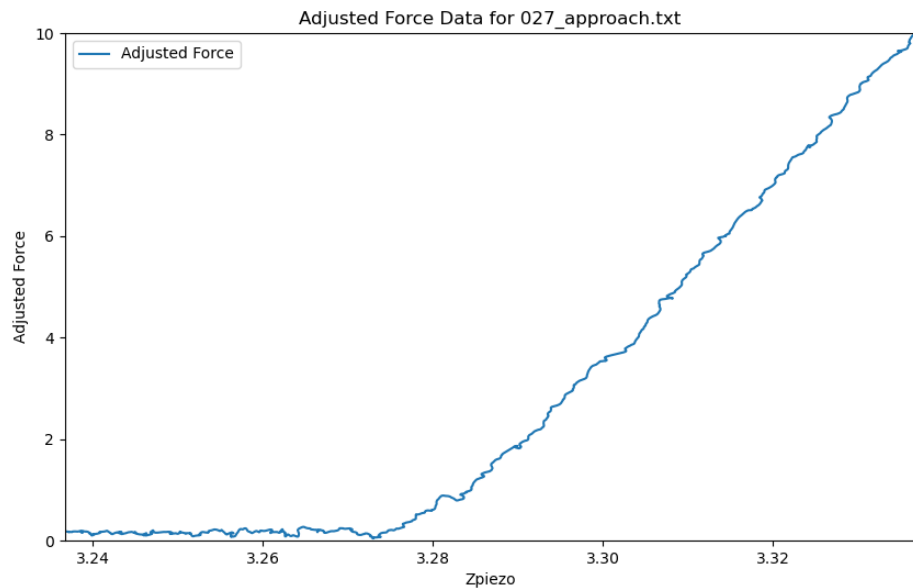


Figure 8.8 An example of a zoomed in portion of a raw curve. The noise is intense. The shelf feature can be somewhat seen in the curve, but could easily be discounted by the background noise.

These sources of noise could have impacted the resulting graphs from the age of the components in the system. Other sources of noise and frustration during the data taking process is due to the variability in the force feedback loop. It was observed that the AFM doesn't always apply consistent pressure, especially during the dwell time graphs, which was the source of difficulty during their processing. The data rate as well as the limited amount of binning that could possibly be done, as features would be lost/smoothed out.

In science there is a constant pressure to use newer equipment, when older equipment is still potentially suitable. Given that newer AFMs can brush up against the million pound mark, it is imperative to consider whether the trade-offs justify such investments. The challenge with older instruments, is that the wear and tear over time can exacerbate the inherent noise issues. Components such as

piezoelectric scanners, which are responsible for the precise movements required for imaging and force measurements, may degrade in performance, leading to drifts or instability in the collected data. Similarly, older detection systems may not be as effective in filtering out noise or may not have the same sensitivity as modern instruments.

However, the fundamental mechanics of AFM have remained relatively consistent, the primary mechanisms of force detection and image resolution are still based on the deflection of a cantilever and the distance control between the probe and the sample. Hence, an older, well-maintained AFM can still provide valuable data, particularly for applications where ultra-high resolution is not mandatory.

The software developed during this investigation provides a powerful tool for older AFMs, particularly for nosier systems. The ability to resolve the shelf feature is a significant one, as the baseline noise present in the MFP curves often hide the feature. This capability is seen throughout all of the variability in conditions seen throughout the various different sites. By utilising the scripts and methods used in this investigation, it opens up the possibility for the scientific community to extend the lifespan of older equipment, making it viable for current and future research without the immediate need for costly upgrades.

The scripts and analysis methods developed as part of this research cater to the nuanced intricacies of noise in AFM data, enabling the extraction of meaningful results even from signals that might be considered too noisy or from data that would otherwise be discarded. This notion is particularly relevant in the context of educational institutions and research facilities with limited funding, where such software enhancements can democratize access to high-quality research opportunities.

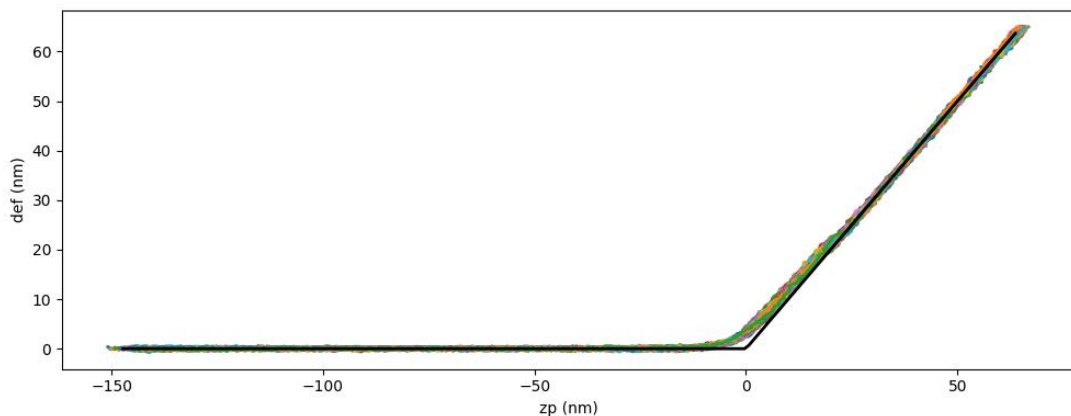


Figure 8.9 An example of an adjusted and overlapped portion of multiple curves. The shelf is clearly visible and highlighted throughout the multiple movements throughout the noise floor.

The software utilises several methods of adjusting the curves towards a more user readable graph, without impacting the underlying data, this is in addition to binning the data to reduce the noise floor, while keeping binning rates sensible to retain the features of the curve. The sum effects of the software can be clearly

seen in the extraction of the shelf features, which have previously been observed in literature [49], from otherwise convoluted curves.

By making this software open source and accessible on a git repository, the scientific community can utilise, revise and improve upon tools that allow for a greater applicability of AFM. While the software presently is modest, the potential for the wider community to contribute and grow the software to address the current issues is always present. [80]

8.5 Temporal Dynamics in Force Measurements

8.5.1 The Influence of Tip Velocity

The velocity at which the Atomic Force Microscopy (AFM) tip approaches or retracts from the colloidal surface is significant in resolving the temporal characteristics of the electrostatic forces. High tip velocities may fail to accurately reflect the nuanced development or diminution of these forces, potentially obscuring the true dynamics of the interaction. Conversely, a slower tip velocity can provide a more comprehensive temporal profile, capturing the incremental changes in electrostatic forces as the tip-surface distance changes. This distinction is crucial in colloidal systems where the electrostatic interactions are sensitive to even minute variations in distance or ionic composition.

8.5.2 Dielectric Relaxation, Ion Mobility and Measurement Fidelity

The dielectric properties of the medium through which the AFM tip traverses also warrant consideration. In instances where dielectric relaxation is a factor, the velocity of the AFM tip can modify these relaxation effects. At higher speeds, there may be insufficient time for the dielectric medium to fully relax between the tip and sample, potentially skewing the results. This could manifest in force measurements that do not fully encapsulate the dielectric response of the system. The motion of the AFM tip can instigate a redistribution of ions around the tip-sample interface, with the speed of the tip dictating the extent of this redistribution. At higher tip velocities, the ions may not have sufficient time to reorganize, that could distort the observed electrostatic force.

8.5.3 Implications for Measurement Strategy

These considerations collectively underscore the necessity of carefully selecting the tip velocity to match the specific temporal and dynamic requirements of the colloidal system under study. An optimized approach speed is paramount for ensuring that the force measurements obtained are both representative and

reproducible. The appropriate speed enhances the reliability of the data, enabling a more authentic interpretation of the colloidal system's properties and behaviors.

AFM contact force measurements and rheological behaviour of dense colloidal suspensions

The significance of the present work does not confine in the direct measurement and fundamental understanding of forces of material surfaces in close proximity within aqueous media. Moreover, it allows us to investigate a working hypothesis in the colloidal rheology community regarding the onset of shear thickening behaviour in dense colloidal suspensions. [16]

Currently it is assumed that the colloidal particles do not experience any frictional forces at low shear stresses and it is only above an “onset” stress, σ^* , that frictional contact occurs leading to shear thickening behaviour. [59] It is speculated that it is this frictional contact occurring above the onset stress that is responsible for the characteristic viscosity increase observed during shear thickening. Following this reasoning, in order for the frictional contact to occur the shear stress has to overcome the repulsive interparticle force that inhibits contact, i.e. the repulsive critical contact force, F_c , which is directly related to the shear thickening onset stress σ^* . Using Derjaguin approximation [3], a critical surface energy W^* can be associated with the critical force, F_c (as measured by AFM) experiments as follows

$$W_{AFM}^* = \frac{F_c}{\pi R_t}$$

Where W_{AFM}^* is the critical surface energy deduced from AFM fd curves and R_t is the radius of the colloidal sphere we have used in these measurements ($3.3\mu m$) at varying ionic strengths. The usage of the critical surface energy to describe the interactions has advantages as it is an intrinsic surface materials/media property and is independent of sizes. Equivalently, the shear thickening onset shear stress σ^* in rheology experiments should also be related to this critical surface energy W^* and simple dimensional analysis indicates that $W^* \propto R\sigma^*$, where R is the radius of colloidal particles used in rheological experiments. More precisely, numerical simulations have already confirmed this relationship and provide the numerical predictor [79].

$$W^* = 2.11R\sigma^*$$

Samuel C. Brown conducted systematic rheological experiments (colloidal silica spheres of radius of 0.75 m) at different ionic strengths and a set of his measurements is used to calculate the critical surface energy in Figure 8.10 where we also depict the calculated critical stress from the completely independent AFM fd curves presented in this thesis. The agreement is remarkable and indicates

strongly and directly for first time the validity of the interparticle friction origins of the shear thickening behaviour.

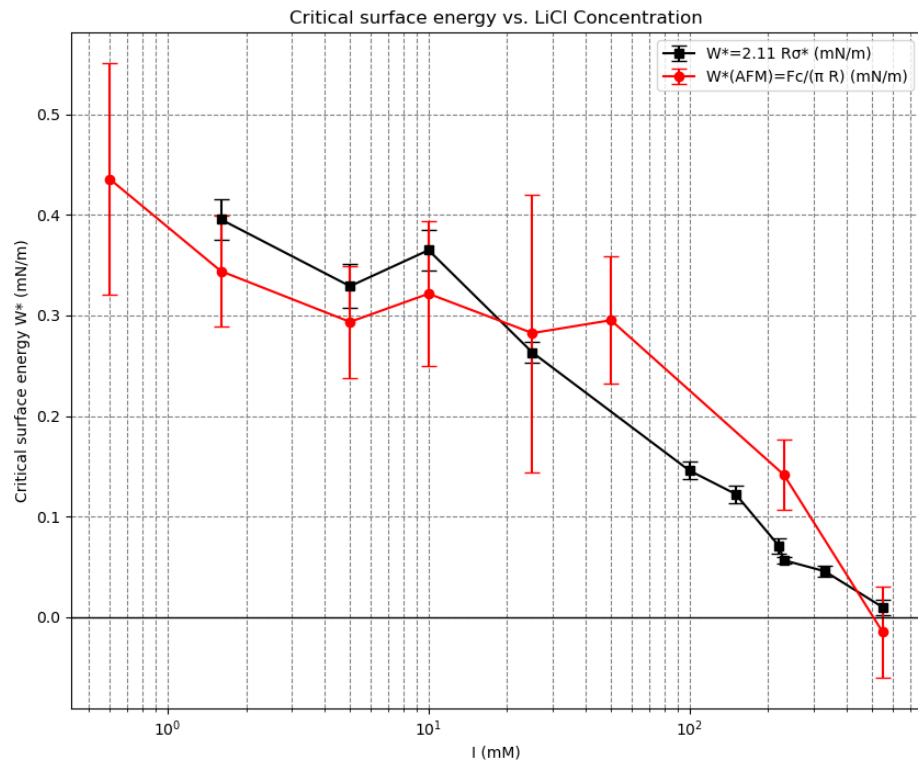


Figure 8.10 Critical surface energy values deduced from AFM (red circles) and rheological experiments (black squares) at different ionic strengths.

8.6 Comparing results to DLVO theory

The Force at Contact vs. LiCl Concentration plot is designed to show how the force at the point of contact between an Atomic Force Microscopy (AFM) tip and a sample varies with the concentration of LiCl in a 50:50 water-glycerol mixture. This relationship is important for understanding how ionic strength affects the interaction forces at the nanoscale. In order to examine our results against theory the equations from Chapter 1 were used, which represent general use equations.

Equations Used

Several equations are used in the script to model the interactions. These equations draw from chapter 1 to represent the types of equations used by those looking to model interactions. Appropriate equations were used to model sphere-plane interactions.

Debye Length: The inverse Debye length, κ , is given by

$$\kappa^{-1} = \sqrt{\frac{2N_A e^2 I}{\varepsilon_0 \varepsilon_r k_B T}},$$

where N_A is Avogadro's number, e is the elementary charge, I is the ionic strength, ε_0 is the vacuum permittivity, ε_r is the relative permittivity of the mixture, k_B is the Boltzmann constant, and T is the temperature. ϵ_r was taken from [7]

Electrostatic Repulsion Force: The electrostatic repulsion force per unit area between a sphere and a plane, taking into account the surface potential Ψ_0 , is calculated as

$$U_E(r) = 2\pi R \kappa \epsilon_0 \epsilon_r \left(\frac{k_B T}{e} \right)^2 \tanh^2 \left(\frac{e \Psi_0}{4k_B T} \right) e^{-\kappa h},$$

where R is the radius of the sphere and h is the separation distance. Ψ_0 was taken from [63].

Van der Waals Force: The van der Waals force for a sphere-plane interaction is given by

$$U_{\text{vdW}}(r) = -\frac{A_H R}{6h^2},$$

where A_H is the Hamaker constant taken from [10].

Total Interaction Energy: The total interaction energy or force at a separation h is the sum of the van der Waals and electrostatic forces. When adjusted for surface roughness, the combined rms roughnesses of the two surfaces was added to the separation distance as a simple means to model roughness.

Parameter	Value (Unit)
Relative Permittivity, ϵ_r	62 (dimensionless) [7]
Vacuum Permittivity, ϵ_0	8.854×10^{-12} F/m
Radius of the Sphere, R	3.3×10^{-6} m
Surface Potential, Ψ_0	-0.040 V [63]
Temperature, T	300 K
Avogadro's Number, N_A	6.022×10^{23} molecules/mol
Elementary Charge, e	1.602×10^{-19} C
Boltzmann Constant, k_B	$1.38064852 \times 10^{-23}$ m ² kg s ⁻² K ⁻¹
Separation Distance, h	2×10^{-9} m
Hamaker Constant A_H	0.63×10^{-20} J [10]
Valency, z_i	1 (dimensionless)
Roughness Values	$2.4 \times 10^{-10} + 6.45 \times 10^{-10}$ m (chpt 3)

Table 8.1 Parameters with their values with units

Plot Explanation

The plot displays the calculated force at contact as a function of LiCl concentration. Experimental data points are overlaid to compare the theoretical model with actual measurements. At first figure 8.11 was calculated without the consideration of surface roughness, to gain a baseline.

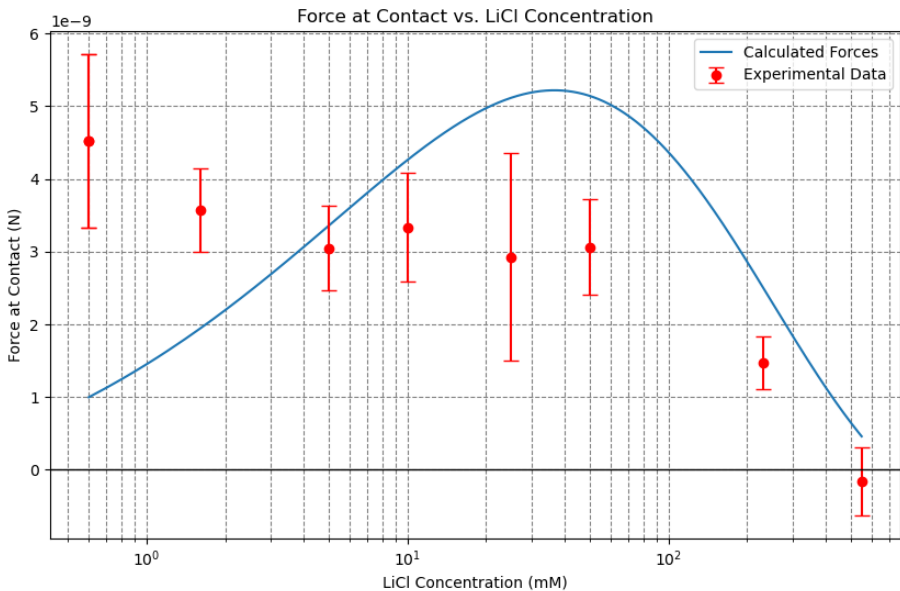


Figure 8.11 Force at contact from AFM experimental data (red circles) compared against calculated DLVO at different ionic strengths.

While the calculated fit in figure 8.11 doesn't follow the experimentally derived calculations, there are some useful aspects of this calculation. For one, the values are all roughly same order of magnitude, and the curve follows the downwards trend towards the higher concentrations. This deviation isn't entirely unexpected; DLVO has been known to break down at small lengthscales. [44]

One aspect that can easily be added is the roughnesses taken from Chapter 3 (0.24nm rms roughness and 0.64583nm rms roughness), which can then be added to the separation distance.

This addition brings down the curve into a better fit with the experimentally derived data (Figure 8.12). While this isn't definitive, as there are plenty of other issues with DLVO (such as the inability to predict the shelf seen in both AFM datasets and other papers), it does show that DLVO is sensitive to surface roughness - which we have previously proven to be significantly rough. This trait that could potentially be responsible for the larger degree of variation seen between experimental sites, which could be an avenue worth further exploration.

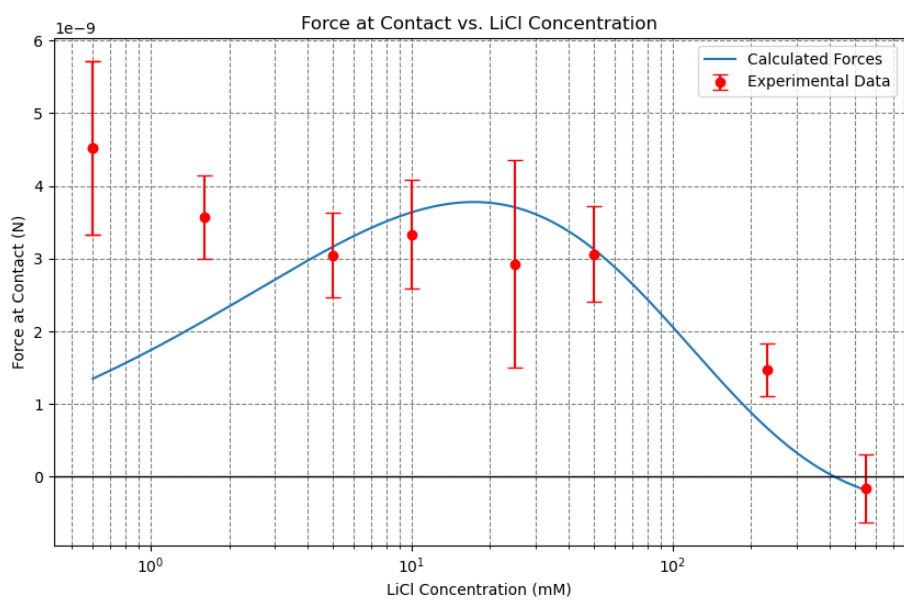


Figure 8.12 Force at contact from AFM experimental data (red circles) compared against calculated DLVO with respect to surface roughness at different ionic strengths.

Chapter 9

Conclusion

The culmination of this experimental research into the nanoscale interface of colloidal interactions, explored through the lens of Atomic Force Microscopy (AFM), presents a range of findings that both challenge and enrich our current understanding. This thesis has delved deep into the complexities of force-distance profiles, revealing the nuanced and intricate nature of particle interactions in colloidal systems. These interactions, as observed, are not only varied across different surface sites but also exhibit a remarkable sensitivity to environmental conditions, such as ionic strength and concentration of LiCl. This variability and sensitivity highlight the inherently dynamic character of colloidal systems, which has been a focal point of this study.

A detailed analysis of AFM force-distance profiles was provided, highlighting the nuanced nature of particle interactions at the nanoscale. Both approach and retract curves were analysed in a novel method of averaging several hundred curves per site. This provided a robust analysis of each site, allowing for the noise profile normally seen in AFMs to be tamed. This noise profile was mitigated to the point of extracting features otherwise unobservable (i.e. the “shelf”). The results also indicated significant variability in interaction forces across different surface sites. This variability could stem from surface heterogeneities, variations in local chemical composition, and structural differences.

From this analysis changes in ionic strength was seen to influence colloidal interactions. As concentrations increased this led to decreased repulsive forces in the approach curves, with the higher concentrations flipping to attractive forces. For retract curves, higher concentrations were seen to increase the adhesive force of the particle. For both the approach and retrace, concentrations past 50mM seemed to be a tipping point for these effects. This finding underscores the impact of ionic effects on colloidal behavior and interaction forces, and potentially provides validation for the charge screening effect theory.

The dynamic nature of colloidal interactions was highlighted from research into tip speed and dwell time analysis. The influence of tip speed highlighted that during slower speeds the AFM tip can potentially cause the surface to restructure (such as ion redistributing) in response to the gradual introduction of the tip

surface. The influence of dwell time on attractive forces between the AFM tip and surface suggests a time-dependent response in the colloidal system, possibly due to ion reorganization or surface conditioning over time.

The consistent presence of a shelf feature across various concentrations and its correlation with specific attractive forces pointed towards complex, non-DLVO interactions at play. This shelf tied into previous observations in literature [49], with our results partially validating their findings. The origin of this shelf could be a result of factors like ion-ion correlations, surface charge heterogeneities, hydration forces, or other specific ion effects.

The experimental results were validated against classical DLVO theory, revealing limitations of DLVO in explaining certain observed phenomena like the 'shelf' feature in force curves. When surface roughness was accounted for the fit with DLVO improved, though still had issues. DLVO also doesn't account for the shelf features seen at all, indicating a need for refinement in theoretical models.

Extending to the macroscopic realm, the implications of this study was considered for colloidal rheology, particularly in the context of shear thickening behavior in dense colloidal suspensions. When compared against empirical evidence [79] our data supports the theory that frictional contact is a pivotal factor in shear thickening, thus bridging the gap between nanoscale interactions and macroscopic phenomena.

In addressing the practical challenges encountered in this research, the development of software tools for enhanced AFM data analysis stands out as an achievement. These open source tools not only facilitate a more robust analysis of complex data sets, particularly from older AFM systems, but also democratize access to high-quality research opportunities by extending the functionality of existing equipment.

In summary, this thesis has not only contributed to a deeper understanding of the intricacies of colloidal interactions at the nanoscale but has also laid the groundwork for further exploration. By highlighting these areas of interest, it paves the way for a more comprehensive and accurate representation of the complex world of colloidal science. Additionally, the software provided allows other scientists to use the tools created in their own research.

9.1 Future work

This thesis has highlighted several potential avenues of further research that could be further expanded upon.

The impact of ionic strength and concentration on colloidal interactions, particularly the transition from repulsive to attractive forces, offers an interesting area of exploration. This could involve systematic experiments across a wider range of ionic conditions to map out the thresholds and dynamics of these transitions.

Two points of evidence exist to imply that surface roughness has a significant

effect on colloidal interaction on small length scales: The rheological analysis and the comparison against DLVO theory. Future research could delve deeper into the role of surface roughness, both from a rheological perspective or from better application of theoretical DLVO surface roughness models. This might involve more detailed surface characterization and modeling to understand how surface topography at the nanoscale influences colloidal behavior.

The shelf highlighted that hydration forces could play a role in the colloidal interactions observed. Future work could focus on explicitly investigating these forces, or expressly focus on investigating this observed shelf in further detail, possibly through experimental setups designed to isolate and measure hydration effects in different colloidal systems.

The influence of factors like tip speed and dwell time on force measurements indicates a dynamic and time-dependent nature of colloidal systems. Further research could explore these temporal aspects more deeply, possibly integrating rheological measurements to connect nanoscale interactions with macroscopic properties. As rheology is familiar with hysteretic effects, probing the origin of these properties on the interface can benefit both the nanoscale and macroscale.

Given the limitations of existing theories like DLVO in explaining certain phenomena observed in our data, a suitable area for further work is the refinement of these theoretical models by a theoretician. This could involve incorporating factors such as surface roughness, ion-ion correlations, and charge heterogeneities into the models. Revision of DLVO to incorporate the attractive shelf force seen in the dataset is an additional avenue open to exploration. Developing new theoretical frameworks or computational models that better capture the complex realities of colloidal interactions observed would be a significant contribution to the field.

The potential connection between nanoscale colloidal interactions and macroscopic phenomena like shear thickening in dense suspensions presents an exciting area for future research. This could involve correlating AFM measurements with bulk rheological properties to better understand the underlying mechanisms of shear thickening and other colloidal phenomena.

The software tools developed for enhanced AFM data analysis represent a significant area of interest too. Future work could involve applying these tools to a broader range of datasets, enhancing their capabilities, and possibly integrating them with other analytical methods to provide a more comprehensive analysis for a range of AFM force curves. Given that the code is available on a open source repository, there is a large potential for a range of contributors to help combat the use of proprietary software in AFM space.

In summary, this thesis, like many thesis before it, has only seemed to open up more avenues of explorations and ask more questions than it solves itself. This author, in particular, is excited to see where the future lies as a result of this investigation.

Chapter 10

Appendix

For each measurement site, a minimum of 100 force curve readings per site was taken, with the raw data saved in a single file. The full dataset is attached as a zip file for each concentration, site and parameters. Run folders correspond to approach curves, Run-ret are retract folders.

Because there are an incredible amount of images involved the dataset, the entire appendix has been provided as a comprehensive .7z file. If this 7z is missing, it's because it was too big to upload.

Bibliography

- [1] “Particle Deposition Aggregation Measurement, Modelling and Simulation.” In *Particle Deposition Aggregation*, edited by M. Elimelech, J. Gregory, X. Jia, and R.A. Williams, Woburn: Butterworth-Heinemann, 1995. <https://www.sciencedirect.com/science/article/pii/B9780750670241500182>.
- [2] Abramovitch, D. Y., S. B. Andersson, L. Y. Pao, and G. Schitter. “A Tutorial on the Mechanisms, Dynamics, and Control of Atomic Force Microscopes.” In *2007 American Control Conference*. 2007, 3488–3502.
- [3] AG, J. I. “NanoWizard NanoOptics AFM - JPK BioAFM: Bruker.”, . <https://jpk.com/products/atomic-force-microscopy/nanowizard-nanooptics>. [Online; accessed 04.05.20].
- [4] Ahmad, K., X. Zhao, Y. Pan, W. Wang, and Y. Huang. “Atomic Force Microscopy Measurement of Slip on Smooth Hydrophobic Surfaces and Possible Artifacts.” *The Journal of Physical Chemistry C* 119, 22: (2015) 12,531–12,537. <https://doi.org/10.1021/acs.jpcc.5b03426>.
- [5] Allagui, A., H. Benaoum, and O. Olendski. “On the Gouy-Chapman-Stern model of the electrical double-layer structure with a generalized Boltzmann factor.” *Physica A: Statistical Mechanics and its Applications* 582: (2022) 126,252.
- [6] Antonyuk, S., editor. *Particles in Contact: Micro Mechanics, Micro Process Dynamics and Particle Collective*. Springer, 2019.
- [7] Behrends, R., K. Fuchs, U. Kaatze, Y. Hayashi, and Y. Feldman. “Dielectric properties of glycerol/water mixtures at temperatures between 10 and 50C.” *The Journal of Chemical Physics* 124, 144512. <https://pubmed.ncbi.nlm.nih.gov/16674183/>. PMID: 16674183.
- [8] Behrens, S. H., and D. G. Grier. “The charge of glass and silica surfaces.” *The Journal of Chemical Physics* 115, 14: (2001) 6716–6721. <https://doi.org/10.1063/1.1404988>.
- [9] Belikov, S., J. Alexander, C. Wall, I. Yermolenko, S. Magonov, and I. Malovichko. “Thermal tune method for AFM oscillatory resonant imaging in air and liquid.” 2014, 1009–1014.

- [10] Bergström, L. “Hamaker constants of inorganic materials.” *Advances in Colloid and Interface Science* 70: (1997) 125–169.
- [11] Biancaniello, P. L., A. J. Kim, and J. C. Crocker. “Colloidal Interactions and Self-Assembly Using DNA Hybridization.” *Phys. Rev. Lett.* 94: (2005) 058,302. <https://link.aps.org/doi/10.1103/PhysRevLett.94.058302>.
- [12] Boersma, W., J. Laven, and H. Stein. “Shear Thickening (Dilatancy) in Concentrated Dispersions.” *AICHE Journal* 36, 3: (1990) 321–332.
- [13] Bowen, W., N. Hilal, R. W. Lovitt, and C. J. Wright. “An atomic force microscopy study of the adhesion of a silica sphere to a silica surfaceeffects of surface cleaning.” *Colloids and Surfaces A: Physicochemical and Engineering Aspects* 157, 1: (1999) 117 – 125. <http://www.sciencedirect.com/science/article/pii/S092777579900045X>.
- [14] ———. “An atomic force microscopy study of the adhesion of a silica sphere to a silica surfaceeffects of surface cleaning.” *Colloids and Surfaces A: Physicochemical and Engineering Aspects* 157, 1: (1999) 117 – 125. <http://www.sciencedirect.com/science/article/pii/S092777579900045X>.
- [15] Braga Pier Carlo, R. D. *Atomic Force Microscopy. Biomedical methods and applications*. Humana press, 2004, 1 edition.
- [16] Brown, C. S., J. French, V. Koutsos, W. C. K. Poon, and J. R. Royer. “Particle interactions and the shear thickening onset.”, 2024. In preparation.
- [17] Brown, R. “A brief account of microscopical observations made in the months of June, July and August, 1827, on the particles contained in the pollen of plants; and on the general existence of active molecules in organic and inorganic bodies.” *Edinburgh New Philosophical Journal* 5: (1827) 358–371.
- [18] Butt H-J, J. M. “Calculation of thermal noise in atomic force microscopy.” *Nanotechnology* 6: (1995) 1–7.
- [19] Bhmer, M. R. “Effects of Polymers on Particle Adsorption on Macroscopic Surfaces Studied by Optical Reflectometry.” *Journal of Colloid and Interface Science* 197, 2: (1998) 251 – 256. <http://www.sciencedirect.com/science/article/pii/S0021979797952371>.
- [20] Cannara, R. J., M. Eglin, and R. W. Carpick. “Lateral force calibration in atomic force microscopy: A new lateral force calibration method and general guidelines for optimization.” *Review of Scientific Instruments* 77, 5: (2006) 053,701. <https://doi.org/10.1063/1.2198768>.
- [21] Christenson, H. K., and N. H. Thomson. “The nature of the air-cleaved mica surface.” *Surface Science Reports* 71, 2: (2016) 367–390. [https://www.sciencedirect.com/science/article/pii/S0167572916000066](http://www.sciencedirect.com/science/article/pii/S0167572916000066).

- [22] Coussot, P. “1 - Introduction to the rheology of complex fluids.” In *Understanding the Rheology of Concrete*, edited by Nicolas Roussel, Woodhead Publishing, 2012, Woodhead Publishing Series in Civil and Structural Engineering, 3–22. <https://www.sciencedirect.com/science/article/pii/B9780857090287500017>.
- [23] Dabroś, T., and T. G. M. van de Ven. “A direct method for studying particle deposition onto solid surfaces.” *Colloid and Polymer Science* 261, 8: (1983) 694–707. <https://doi.org/10.1007/BF01415042>.
- [24] Derjaguin, B., and L. Landau. “Theory of the stability of strongly charged lyophobic sols and of the adhesion of strongly charged particles in solutions of electrolytes.” *Progress in Surface Science* 43, 1: (1993) 30 – 59. <http://www.sciencedirect.com/science/article/pii/007968169390013L>.
- [25] Dolez, P., and J. Mlynarek. “22 - Smart materials for personal protective equipment: Tendencies and recent developments.” In *Smart Textiles and their Applications*, edited by Vladan Koncar, Oxford: Woodhead Publishing, 2016, Woodhead Publishing Series in Textiles, 497–517. <https://www.sciencedirect.com/science/article/pii/B9780081005743000229>.
- [26] Ducker, W. A., Z. Xu, and J. N. Israelachvili. “Measurements of Hydrophobic and DLVO Forces in Bubble-Surface Interactions in Aqueous Solutions.” *Langmuir* 10, 9: (1994) 3279–3289. <https://doi.org/10.1021/la00021a061>.
- [27] Eisenschitz, F., R. London. “ber das Verhltnis der van der Waalsschen Krfte zu den homopolaren Bindungskrften.” *Zeitschrift fr Physik* 60.
- [28] Elbourne, A., K. Voitchovy, G. G. Warr, and R. Atkin. “Ion structure controls ionic liquid near-surface and interfacial nanostructure.” *Chem. Sci.* 6: (2015) 527–536. <http://dx.doi.org/10.1039/C4SC02727B>.
- [29] Escobar, J. V., C. Garza, and R. Castillo. “Measuring adhesion on rough surfaces using atomic force microscopy with a liquid probe.” *Beilstein journal of nanotechnology* 8: (2017) 813–825. [https://pubmed.ncbi.nlm.nih.gov/28503393. 28503393\[pmid\]](https://pubmed.ncbi.nlm.nih.gov/28503393. 28503393[pmid]).
- [30] Farr, R. S., J. R. Melrose, and R. C. Ball. “Kinetic theory of jamming in hard-sphere startup flows.” *Phys. Rev. E* 55: (1997) 7203–7211. <https://link.aps.org/doi/10.1103/PhysRevE.55.7203>.
- [31] FOSS, D. R., and J. F. BRADY. “Structure, diffusion and rheology of Brownian suspensions by Stokesian Dynamics simulation.” *Journal of Fluid Mechanics* 407: (2000) 167200.
- [32] Frasch, H., and H. Menke. “V34: Atomic Force Microscopy.”, 2013. <https://www.henrimenke.com/PPII/V34.pdf>.

- [33] Giesbers, M. *Surface Forces Studied with Colloidal Probe Atomic Force Microscopy*. Ph.D. thesis, Wageningen University, Wageningen, Netherlands, 2001.
- [34] Gittes, F., and C. F. Schmidt. *Signals and Noise in Micromechanical Measurements*, Ann Arbor, Michigan: Academic Press, 1997, volume 55, chapter 8, 129–156. <https://www.sciencedirect.com/science/article/pii/S0091679X08604069>.
- [35] Graham, T. “X. Liquid diffusion applied to analysis.” *Philosophical Transactions of the Royal Society of London* 151: (1861) 183–224. <https://royalsocietypublishing.org/doi/abs/10.1098/rstl.1861.0011>.
- [36] Griffiths, D. J. *Introduction to Quantum Mechanics*. Pearson Education, 2005, 2 edition.
- [37] Guleryuz, H., A. K. Røyset, I. Kaus, C. Filiaâtre, and M.-A. Einarsrud. “AFM measurements of forces between silica surfaces.” *Journal of Sol-Gel Science and Technology* 62, 3: (2012) 460–469.
- [38] Guleryuz, H., A. K. Ryset, I. Kaus, C. Filitre, and M.-A. Einarsrud. “AFM measurements of forces between silica surfaces.” *Journal of Sol-Gel Science and Technology* 62, 3: (2012) 460–469. <https://doi.org/10.1007/s10971-012-2750-6>.
- [39] H., E. D. *Basic Principles of Colloid science*. London: Royal Society of Chemistry, 1988, 1st ed. edition.
- [40] Hadjittofis, E., S. Das, G. Zhang, and J. Heng. “Chapter 8 - Interfacial Phenomena.” In *Developing Solid Oral Dosage Forms (Second Edition)*, edited by Yihong Qiu, Yisheng Chen, Geoff G.Z. Zhang, Lawrence Yu, and Rao V. Mantri, Boston: Academic Press, 2017, 225 – 252. Second edition edition. <http://www.sciencedirect.com/science/article/pii/B978012802447800008X>.
- [41] Halliday, D., R. Resnick, and J. Walker. *Fundamentals of Physics*. Wiley, 2013, 10th edition. Chapter on Electric Charge and Coulomb’s Law.
- [42] Hansma, P. K., J. P. Cleveland, M. Radmacher, D. A. Walters, P. E. Hillner, M. Bezanilla, M. Fritz, D. Vie, H. G. Hansma, C. B. Prater, J. Massie, L. Fukunaga, J. Gurley, and V. Elings. “Tapping mode atomic force microscopy in liquids.” *Applied Physics Letters* 64, 13: (1994) 1738–1740. <http://dx.doi.org/10.1063/1.111795>.
- [43] Heisenberg, W. “ber den anschaulichen Inhalt der quantentheoretischen Kinematik und Mechanik.” *Zeitschrift fr Physik* 43, 3-4: (1927) 172–198.
- [44] Horinek, D. *DLVO Theory*, New York, NY: Springer New York, 2014, 343–346. https://doi.org/10.1007/978-1-4419-6996-5_7.

- [45] Hunter, R. J. *Foundations of Colloid Science*. Oxford University Press, 2001, 2 edition.
- [46] Hutter, J. L., and J. Bechhoefer. “Calibration of atomicforce microscope tips.” *Review of Scientific Instruments* 64, 7: (1993) 1868–1873.
- [47] Israelachvili, J. N. *Intermolecular and Surface Forces*. Academic Press, 2011, 3 edition.
- [48] J, H. R. *Foundations of colloid science : 2nd ed.* New York: Oxford Uni. Press, 2001, 2nd ed. edition.
- [49] Kilpatrick, J. I., S.-H. Loh, and S. P. Jarvis. “Directly Probing the Effects of Ions on Hydration Forces at Interfaces.” *Journal of the American Chemical Society* 135, 7: (2013) 2628–2634. <http://pubs.acs.org>. Supported by Science Foundation Ireland (Grant 07/IN1/B931).
- [50] Kim, H.-M., C.-H. Lee, and B. Kim. “Sonochemical synthesis of silica particles and their size control.” *Applied Surface Science* 380: (2016) 305–308.
- [51] Koishi, A., S. S. Lee, P. Fenter, A. Fernandez-Martinez, and I. C. Bourg. “Water Adsorption on Mica Surfaces with Hydrophilicity Tuned by Counterion Types (Na, K, and Cs) and Structural Fluorination.” *J Phys Chem C Nanomater Interfaces* 126, 38: (2022) 16,447–16,460.
- [52] Kokkoli, E., and C. F. Zukoski. “Surface Pattern Recognition by a Colloidal Particle.” *Langmuir* 17, 2: (2001) 369–376. <https://doi.org/10.1021/la0006059>.
- [53] Kostakis, T., R. Ettelaie, and B. S. Murray. “Effect of High Salt Concentrations on the Stabilization of Bubbles by Silica Particles.” *Langmuir* 22, 3: (2006) 1273–1280. <https://doi.org/10.1021/la052193f>. PMID: 16430294.
- [54] LibreTexts. “Lennard-Jones Potential - Chemistry LibreTexts.”, 2020. https://chem.libretexts.org/Bookshelves/Physical_and_Theoretical_Chemistry_Textbook_Maps/Supplemental_Modules_%28Physical_and_Theoretical_Chemistry%29/Physical_Properties_of_Matter/Atomic_and_Molecular_Properties/Intermolecular_Forces/Specific_Interactions/Lennard-Jones_Potential.
- [55] Litton, G. M., and T. M. Olson. “Colloid Deposition Kinetics with Surface-Active Agents: Evidence for Discrete Surface Charge Effects.” *Journal of Colloid and Interface Science* 165, 2: (1994) 522 – 525. <http://www.sciencedirect.com/science/article/pii/S0021979784712586>.
- [56] Ludwig, T., R. Kirmse, and K. Poole. “Probing cellular microenvironments and tissue remodeling by atomic force microscopy.” *Pflugers Arch - Eur J Physiol* 2949.

- [57] Lpez-Esparza, R., M. A. Balderas Altamirano, E. Prez, and A. Gama Goic-ochea. “Importance of Molecular Interactions in Colloidal Dispersions.” *Advances in Condensed Matter Physics* 2015: (2015) 8. [10.1155/2015/683716](https://doi.org/10.1155/2015/683716).
- [58] Lderitz, L. A. C. *An AFM study of the interactions between colloidal particles*. Ph.D. thesis, von der Fakultt II - Technischen Universitt Berlin, 2012.
- [59] Morris, J. F. “Shear Thickening of Concentrated Suspensions: Recent Developments and Relation to Other Phenomena.” *Annual Review of Fluid Mechanics* 52: (2020) 121–144.
- [60] Moshar, A. “Force Measurements in AFM.”, 2011. https://nanohub.org/resources/11221/download/2011.02.17-AFM_Workshop-L03-Moshar.pdf.
- [61] Mulder, D. J., and T. L. Kuhl. “Polymer brushes in restricted geometries.” *Soft Matter* 6: (2010) 5401–5407. <http://dx.doi.org/10.1039/COSM00444H>.
- [62] N, I. J. *Intermolecular and surface forces*. London: Academic Press Limited, 1987, 2nd ed. edition.
- [63] nanoComposix. “Silica Physical Properties.”, 2021. <https://nanocompositix.com/pages/silica-physical-properties>. Accessed: 2024-01-07.
- [64] Naudascher, E. *Hydrodynamic Forces: IAHR Hydraulic Structures Design Manuals 3*. Routledge, 1991, 1 edition. <https://doi.org/10.1201/9780203751534>.
- [65] Neier-Deiters, A., S. Scherb, N. Beuntner, and K.-C. Thienel. “Influence of the calcination temperature on the properties of a mica mineral as a suitability study for the use as SCM.” *Applied Clay Science* 179: (2019) 105,168. <https://www.sciencedirect.com/science/article/pii/S0169131719302261>.
- [66] Newton, I. *Philosophiae Naturalis Principia Mathematica*. Joseph Streater, 1687.
- [67] Neas, D., and P. Klapetek. “Gwyddion: an open-source software for SPM data analysis.” *Central European Journal of Physics* 10: (2012) 181–188.
- [68] Ninham, B. “On progress in forces since the DLVO theory.” *Advances in Colloid and Interface Science* 83, 1: (1999) 1 – 17. <http://www.sciencedirect.com/science/article/pii/S0001868699000081>.
- [69] Ninhama, B. “On progress in forces since the DLVO theory.” *Advances in Colloid and Interface Science* 83: (1999) 1–17. Available from: www.elsevier.nl/locate/cis.

- [70] Ohshima, H. “Surface Charge Density/Surface Potential Relationship for a Spherical Colloidal Particle in a Salt-Free Medium.” *Journal of Colloid and Interface Science* 247, 1: (2002) 18–23. <https://www.sciencedirect.com/science/article/pii/S0021979701981056>.
- [71] Oliphant, T. “NumPy: A guide to NumPy.” USA: Trelgol Publishing, 2006–. <http://www.numpy.org/>. [Online; accessed 06.05.20].
- [72] Ostendorf, F., C. Schmitz, S. Hirth, A. Khnle, J. J. Kolodziej, and M. Reichling. “How flat is an air-cleaved mica surface?” *Nanotechnology* 19, 30: (2008) 305,705. <https://dx.doi.org/10.1088/0957-4484/19/30/305705>.
- [73] Pavan, C., M. Delle Piane, M. Gullo, F. Filippi, B. Fubini, P. Hoet, C. J. Horwell, F. Huaux, D. Lison, C. Lo Giudice, G. Martra, E. Montfort, R. Schins, M. Sulpizi, K. Wegner, M. Wyart-Remy, C. Ziemann, and F. Turci. “The puzzling issue of silica toxicity: are silanols bridging the gaps between surface states and pathogenicity?” *Particle and Fibre Toxicology* 16, 1: (2019) 32. <https://doi.org/10.1186/s12989-019-0315-3>.
- [74] plasma, H. “Plasma Cleaning : Henniker Plasma Treatment.”, . <https://plasmatreatment.co.uk/henniker-plasma-technology/plasma-surface-technology/plasma-technology-what-is-plasma-treatment/plasma-cleaning/>. [Online; accessed 084.05.20].
- [75] Preedy, E., S. Perni, D. Nipi, K. Bohinc, and P. Prokopovich. “Surface Roughness Mediated Adhesion Forces between Borosilicate Glass and Gram-Positive Bacteria.” *Langmuir* 30, 31: (2014) 9466–9476. <https://doi.org/10.1021/la501711t>. PMID: 25019516.
- [76] Richmond, P. “Electrical forces between particles with discrete periodic surface charge distributions in ionic solution.” *J. Chem. Soc., Faraday Trans. 2* 71: (1975) 1154–1163. <http://dx.doi.org/10.1039/F29757101154>.
- [77] Savitzky, A., and M. J. E. Golay. “Smoothing and differentiation of data by simplified least squares procedures.” *Analytical Chemistry* 36: (1964) 1627–1639.
- [78] Schirmeisen, A., B. Anczykowski, and H. Fuchs. *Dynamic Modes of Atomic Force Microscopy*, Berlin, Heidelberg: Springer Berlin Heidelberg, 2007, 737–766. https://doi.org/10.1007/978-3-540-29857-1_27.
- [79] Singh, A., R. Mari, M. M. Denn, and J. F. Morris. “A constitutive model for simple shear of dense frictional suspensions.” *Journal of Rheology* 62: (2018) 457–468.
- [80] Thalpy. “Force-curve-analysis-tool.” <https://github.com/Thalpy/Force-curve-analysis-tool>, 2023.

- [81] Valmacco, V., M. Elzbieciak-Wodka, D. Herman, G. Trefalt, P. Maroni, and M. Borkovec. “Forces between silica particles in the presence of multivalent cations.” *Journal of Colloid and Interface Science* 472: (2016) 108–115. All rights reserved.
- [82] Van Rossum, G., and F. L. Drake. *Python 3 Reference Manual*. Scotts Valley, CA: CreateSpace, 2009.
- [83] Verwey, E. J. W. “Theory of the Stability of Lyophobic Colloids.” *The Journal of Physical and Colloid Chemistry* 51, 3: (1947) 631–636. <https://doi.org/10.1021/j150453a001>.
- [84] Victor J Morris, A. P. G., Andrew R Kirby. *Atomic Force Microscopy for Biologists*. Imperial College Press, 2009, 2 edition.
- [85] van der Waals, J. D. *Over de Continuiteit van den Gas- en. Vloeistofstoestand*. Ph.D. thesis, Univ. Leiden, 1873.
- [86] Wagner, R., A. Raman, and R. Moon. “Transverse Elasticity of Cellulose Nanocrystals Via atomic Force microscopy.” 2010.
- [87] Walz, J. Y. “The effect of surface heterogeneities on colloidal forces.” *Advances in Colloid and Interface Science* 74, 1: (1998) 119 – 168. <http://www.sciencedirect.com/science/article/pii/S0001868697000420>.
- [88] Wennerstrm, H. “Electrostatic interactions in concentrated colloidal dispersions.” *Physical Chemistry Chemical Physics* 19: (2017) 23,849–23,853. <https://doi.org/10.1039/C7CP02594G>.
- [89] Yoo, S., C.-H. Ji, J.-Y. Jin, and Y.-K. Kim. “Suppression of surface crystallization on borosilicate glass using RF plasma treatment.” *Applied Surface Science* 316: (2014) 484 – 490. <http://www.sciencedirect.com/science/article/pii/S0169433214016110>.